

**Project Report  
ATC-447**

**The 2017 Buffalo Area Icing and  
Radar Study (BAIRS II)**

**E.R. Williams  
M.F. Donovan  
D.J. Smalley  
J.M. Kurdzo  
B.J. Bennett**

14 May 2020

---

**Lincoln Laboratory**  
MASSACHUSETTS INSTITUTE OF TECHNOLOGY  
*LEXINGTON, MASSACHUSETTS*



---

This material is based upon work supported by the  
Federal Aviation Administration under Air Force  
Contract No. FA8702-15-D-0001.

DISTRIBUTION STATEMENT A. Approved for public  
release. Distribution is unlimited.

This report is the result of studies performed at Lincoln Laboratory, a federally funded research and development center operated by Massachusetts Institute of Technology. This material is based upon work supported under Air Force Contract No. FA8702-15-D-0001. Any opinions, findings, conclusions or recommendations expressed in this material are those of the author(s) and do not necessarily reflect the views of the Federal Aviation Administration.

© 2020 Massachusetts Institute of Technology

Delivered to the U.S. Government with Unlimited Rights, as defined in DFARS Part 252.227-7013 or 7014 (Feb 2014). Notwithstanding any copyright notice, U.S. Government rights in this work are defined by DFARS 252.227-7013 or DFARS 252.227-7014 as detailed above. Use of this work other than as specifically authorized by the U.S. Government may violate any copyrights that exist in this work.

**Massachusetts Institute of Technology  
Lincoln Laboratory**

**The 2017 Buffalo Area Icing and Radar Study  
(BAIRS II)**

*E.R. Williams  
Massachusetts Institute of Technology*

*M.F. Donovan  
D.J. Smalley  
J.M. Kurdzo  
B.J. Bennett  
Group 43*

**Project Report ATC-447  
14 May 2020**

**DISTRIBUTION STATEMENT A. Approved for public  
release. Distribution is unlimited**

**Lexington**

**Massachusetts**

**This page intentionally left blank.**

## ABSTRACT

The second Buffalo Area Icing and Radar Study (BAIRS II) was conducted during the winter of 2017. The BAIRS II partnership between Massachusetts Institute of Technology (MIT) Lincoln Laboratory (LL), the National Research Council of Canada (NRC), and Environment and Climate Change Canada (ECCC) was sponsored by the Federal Aviation Administration (FAA). It is a follow-up to the similarly sponsored partnership of the original BAIRS conducted in the winter of 2013. The original BAIRS provided in situ verification and validation of icing and hydrometeors, respectively, within the radar domain in support of a hydrometeor-classification-based automated icing hazard algorithm. The BAIRS II motivation was to:

- Collect additional in situ verification and validation data,
- Probe further dual polarimetric radar features associated with icing hazard,
- Provide foundations for additions to the icing hazard algorithm beyond hydrometeor classifications, and
- Further characterize observable microphysical conditions in terms of S-band dual polarimetric radar data.

With BAIRS II, the dual polarimetric capability is provided by multiple Next Generation Weather Radar (NEXRAD) S-band radars in New York State, and the verification of the icing hazard with microphysical and hydrometeor characterizations is provided by NRC's Convair-580 instrumented research plane during five icing missions covering about 21 mission hours. The ability to reliably interpret the NEXRAD dual polarization radar-sensed thermodynamic phase of the hydrometeors (solid, liquid, mix) in the context of cloud microphysics and precipitation physics makes it possible to assess the icing hazard potential to aviation. The challenges faced are the undetectable nature of supercooled cloud droplets (for S-band) and the isotropic nature of Supercooled Large Drops (SLD). The BAIRS II mission strategy pursued was to study and probe radar-identifiable, strongly anisotropic crystal targets (dendrites and needles) with which supercooled water (and water saturated conditions) are physically linked as a means for dual polarimetric detection of icing hazard.

BAIRS II employed superior optical array probes along with state and microphysical instrumentation; and, using again NEXRAD-feature-guided flight paths, was able to make advances from the original BAIRS helpful to the icing algorithm development. The key findings that are given thorough treatment in this report are:

- Identification of the radar-detectable “crystal sandwich” structure from two anisotropic crystal types stratified by in situ air temperature in association with varying levels of supercooled water
  - with layer thicknesses observed to 2 km,
  - over hundred-kilometer scales matched with the mesoscale surveillance of the NEXRAD radars,

- Development and application of a multi-sensor cloud phase algorithm to distinguish between liquid phase, mixed phase, and glaciated (no icing) conditions for purposes of a “truth” database and improved analysis in BAIRS II,
- Development of concatenated hydrometeor size distributions to examine the in situ growth of both liquid and solid hydrometeors over a broad size spectrum; used, in part, to demonstrate differences between maritime and continental conditions, and
- The Icing Hazard Levels (IHL) algorithm’s verification in icing conditions is consistent with previous work and, new, is documented to perform well when indicating “glaciated” (no icing) conditions.

## ACKNOWLEDGEMENTS

Mengistu Wolde of NRC and Alexei Korolev of ECCC played key roles in organizing, instrumenting, and participating in all five Convair-580 flights of BAIRS II, with great assistance from the NRC team (Konstantin Baibakov, Matthew Bastian, Cuong Nguyen, Eric Roux and Thit Tun) and the ECCC team (Mike Harwood and Jason Iwachow). The Convair-580 pilots (Anthony Brown, Paul Kissman and Rob Erdos) did their utmost to go after observations in hazardous conditions of greatest interest. Jessica Schultz of the NEXRAD Radar Operations Center supported engagement with the National Weather Service's Buffalo, NY Weather Forecast Office (David Zaff) for coordination of radar scan strategies during BAIRS II. The radar operators at NEXRAD sites Buffalo, NY NEXRAD (KBUF); Binghamton, NY NEXRAD (KBGM); and Montague, NY NEXRAD (KTYX) were all very helpful in accommodating our aircraft plans. We also thank Valery Melnikov, Alexander Ryzhkov, and Tsuneya Takahashi for valuable discussions pertaining to the crystal sandwich. The BAIRS II effort also benefitted greatly from the ECCC's Weather Radar Validation Experiment (WERVEX) team (Dave Hudak, Peter Rodriguez, Vlado Stojanovic, Sudesh Boodoo and David Sills), especially during the February 7 mission. Alexei Korolev has been exceedingly helpful throughout this project with the provision of aircraft data and the discussion on its interpretation. Final acknowledgment goes to Steve Kim at the FAA who was able to support the icing missions understanding the merit of and need for in situ measurements to verify and validate.

**This page intentionally left blank.**

# TABLE OF CONTENTS

	<b>Page</b>
ABSTRACT	iii
ACKNOWLEDGEMENTS	v
List of Illustrations	ix
List of Tables	xxiii
1. INTRODUCTION	1
2. METHODOLOGY	5
2.1 Convair-580 Aircraft Instruments	5
2.2 Ground-Based NEXRAD Radars (KBUF, KBGM, KTYX)	10
2.3 Spatial–Temporal Comparisons between Aircraft Observations and Ground-Based Radar Measurements	10
2.4 Differential Reflectivity Offset Adjustments to Account for System Bias	12
2.5 Analysis Tools	17
3. FLIGHT DESCRIPTIONS	27
3.1 Overview of Five Flights	27
3.2 10 January 2017, 13:22–17:45 UTC	28
3.3 24 January 2017, 02:30–06:52 UTC	32
3.4 7 February 2017, 16:05–19:20 UTC	38
3.5 24 March 2017, 09:33–14:15 UTC	41
3.6 25 March 2017, 11:00–16:00 UTC	45
4. PRINCIPAL FINDINGS AND RESULTS	51
4.1 Characterization of Cloud Phase	51
4.2 The Crystal Sandwich: A Dual Pol Signature for Icing Hazard	55
4.3 Reflectivity Level of Crystal Snowstorms and Implications for the Presence of Supercooled Water and Aircraft Icing Conditions	90
4.4 SLD in a Maritime Synoptic Regime: Comparisons with Flights in a Continental Regime	94
4.5 Further Considerations of Ice Multiplication and the Association of Needle Crystals with Supercooled Water	125
4.6 Search for Dual Polarimetric Distinctions between Glaciated and Supercooled Environments	133
4.7 IHL Performance Using Cloud Phase Estimates for Verification	141
5. DISCUSSION	145

**TABLE OF CONTENTS**  
**(Continued)**

	<b>Page</b>
6. CONCLUSIONS	149
7. SUGGESTIONS FOR FUTURE WORK	151
7.1 Crystal Sandwich	151
7.2 Unrimed Dendritic and Needle Crystals	151
7.3 Ascent Rates along Frontal Boundaries	151
7.4 Radar Bright Band and the Environment Below the Melting Layer in Winter Storms	152
7.5 Cloud Condensation Nuclei	152
7.6 Comparison of $N^*r$ in Snowstorms and in Thunderstorms	152
7.7 Embryos for Graupel Particles	152
APPENDIX A	
INTER-COMPARISON OF AIRCRAFT AND RADAR VARIABLES FOR FIVE FLIGHTS	155
APPENDIX B	
SYNOPTIC ANALYSIS OF RADAR SITUATION WITH +ZDR BRIGHT BANDS	163
APPENDIX C	
CLOUD PHASE ESTIMATE TIMELINES FOR FIVE FLIGHTS	167
Glossary	173
References	177

## LIST OF ILLUSTRATIONS

Figure No.		Page
1	Illustration of possible icing hazard scenarios observed in winter weather systems and the likelihood of detectability with an S-band dual polarimetric radar.	2
2	Illustration of the majority of probes mounted beneath the left (top) and right (bottom) wings of the Convair-580 aircraft.	5
3	Summary of hydrometeor imaging probes and scattering probes available in BAIRS II, including the dynamic range of their respective size resolution. The upper limit of the imaging probes can be extended during processing. Instruments for measuring supercooled water concentration are also included near the top. Image courtesy of Dr. Mengistu Wolde (NRC).	8
4	Illustration showing examples of a physical-sized window with increasing range and from which an aircraft observation is compared to ground-based radar measurements. Window boxes are shown at 10 km range intervals out to 120 km along the 45° azimuth angle. The azimuthal width associated with each example box is shown to the right of each window box. The range length of each box is fixed at 1.25 km.	11
5	Time series plots of the running average ZDR error estimated for KBUF (top), KBGM (center), and KTYX (bottom) radars during the 24 January 2017 mission flight between 02:00–07:00 UTC. The error estimates shown in blue were computed from the dry snow method. Estimates from the rain and Bragg methods were not obtainable due to an unfavorable meteorological scenario. The value in the upper-right corner of each plot represents the average ZDR error over the entire flight interval.	13
6	Frequency histogram plots showing a comparison of ZDR values between adjacent NEXRADs, KBUF (abscissa) and KBGM (ordinate), for radar bins residing within a small common overlapping range-azimuth window centered at the mid-point range between the two radars for the interval 02:30–07:00 UTC on 24 January 2017. Only radar bins matched close in time and space are considered. The distribution plot on the left shows the ZDR values measured in real time. The distribution on the right shows the post-processed ZDR values after an adjustment of 0.4 dB was added (subtracted) to KBUF (KBGM) data. The correlation line is shown as a red dashed line.	15
7	Four-panel PPI plots showing ZDR comparisons between the KBUF (left column) and KBGM (right column) radars centered at the mid-range bin for products generated in real time (top row) and from post-processing after a +0.4 and -0.4 dB offset was applied to the ZDR values (bottom row), respectively. All PPI images are from the 0.5° scan on 24 January 2017 at 05:21:53 (left) and 05:22:57 UTC (right).	16

## LIST OF ILLUSTRATIONS (Continued)

Figure No.		Page
8	<p>Nine-panel PPI plot of ZDR with the center plot matched nearest in time (volume time 15:25:12 UTC) and space (elevation angle 8.0°) to the Convair-580 position at 15:30:40 UTC on 10 January 2017. The row (column) of plots show adjacent elevation angles (volume times) increasing from bottom to top (left to right), respectively. A five-minute history of the flight path color-coded according to the estimated cloud phase encountered is shown as red (mixed) in the center image with the northern most point representing the current location. The phase category at this location is also indicated to the right of the image along with the mean ZDR value computed among the valid data points within the physical-sized window matched and centered at this location.</p>	18
9	<p>Six-panel time series plots of five-second averaged in situ measurements collected by the Convair-580 and mean radar product data for the 10-minute interval 03:30–03:40 UTC on 24 January 2017. The plots show particle-type frequency distributions of Spheres, Needles, Dendrites, and Irregulars (SNDI) derived from the 2D-C (first plot) and PIP (second plot) OAP imagery. The color-coded squares at the top of the 2D-C plot denote estimates of the cloud phase type encountered. The third plot shows in situ temperature (blue), aircraft altitude (red), slant range distance of aircraft from KBGM radar (magenta), and mode of KBGM HCA detected class at top of panel. Nevzorov LWC (blue), Nevzorov TWC (green), FSSP LWC (black) and RID frequencies (magenta) are shown in the fourth plot. The fifth and sixth plots show the aircraft X-band mean reflectivity (black) and mean KBGM reflectivity (magenta), ZDR (blue), CC (red), and KDP (black). The mean and mode KBGM products were computed among all valid values within the physical-sized window associated with and centered on the aircraft position.</p>	20
10	<p>Illustration of a four-panel plot generated from a utility used to analyze features observed between two NEXRAD products. PPI images of Z (upper left), ZDR (upper right), one-hour RAP model temperature forecast (lower left), and scatterplot of Z and ZDR values (lower right) within the three highlighted arc sectors are shown for the KBOX 9.9° elevation angle at 08:01:25 UTC on 9 December 2017. Ice crystal growth regions of dendrites and needles and an adjacent region void of a needle signature are identified by the user and shown on the PPI images as a black, red, and green arc sector, respectively.</p>	22
11	<p>Multi-parameter plot of the slant range distance of the Convair-580 position from the KBUF (blue), KBGM (green), and KTYX (red) NEXRADs, the aircraft altitude (dashed line), and in situ temperature (color-coded circles) at three-minute intervals for the 24 January 2017 flight between 02:30–07:00 UTC. The vertical gray shaded columns denote time intervals when the aircraft performed a spiral maneuver descent and ascent.</p>	23

## LIST OF ILLUSTRATIONS (Continued)

Figure No.		Page
12	Distributions of concatenated hydrometeor spectra showing particle concentrations derived from the FSSP, 2D-C, and PIP probes on 10 January 2017 for the interval 14:00–18:00 UTC. Timelines of MVD from each probe are shown in black (FSSP), green (2D-C), and red (PIP). Five-second averages of the in situ temperature are shown in blue.	25
13	One-hour RAP NWP model profile forecast of temperature (top) and relative humidity (bottom) for the model bins associated with the Convair-580 aircraft position on 24 January 2017 between 02:35–06:40 UTC. The magenta line shows the altitude of the aircraft along the flight track.	26
14	Illustration of the display utility used during the BAIRS II campaign providing real-time data and communication from the PLANET Iridium system. A chat log is shown on the left detailing conversations among airborne and on-the-ground participants. The icons on the right-hand-side allow various overlays to be displayed such as navigational aids and local ground-based radar reflectivity. The geomarker box in the upper left was used by MIT LL staff to propose locations for Convair-580 flight transects. Radar reflectivity is shown with the aircraft located just north of the KBUF NEXRAD on 25 March 2017 at 13:56 UTC.	28
15	Surface analysis over the continental U.S. valid at 15:00 UTC on 10 January 2017. The large black arrows denote past and future projection of the surface low pressure center presently located over central Iowa. The black rectangle shows the region of interest where in situ measurements were taken during the BAIRS II campaign.	29
16	Flight track taken by the Convair-580 aircraft on 10 January 2017 between 13:22-17:45 UTC. The locations of the KBUF, KBGM, and KTYX NEXRADs are shown in cyan. The overlays and base map were displayed using the GR2Analyst radar display program developed by Gibson Ridge Software.	30
17	Surface analysis over the continental U.S. valid at 03:00 UTC on 24 January 2017. The large black arrows denote past and future projection of the surface low pressure centers in the eastern U.S. The black rectangle shows the region of interest where in situ measurements were taken during the BAIRS II campaign.	33
18	Flight track taken by the Convair-580 aircraft on 24 January 2017 between 02:30–06:52 UTC. The overlays and base map were displayed using the GR2Analyst radar display program developed by Gibson Ridge Software.	34

## LIST OF ILLUSTRATIONS (Continued)

Figure No.		Page
19	Image showing the accumulation of supercooled raindrops frozen onto the side window of the Convair-580.	36
20	Surface analysis over the continental U.S. valid at 18:00 UTC on 7 February 2017. The large black arrows denote past and future projection of the surface low-pressure center presently located in southern Lake Michigan. The black rectangle shows the region of interest where in situ measurements were taken during the BAIRS II campaign.	38
21	Flight track taken by the Convair-580 aircraft on 7 February 2017 between 16:05–19:20 UTC. The overlays and base map were displayed using the GR2Analyst radar display program developed by Gibson Ridge Software.	39
22	Surface analysis over the continental U.S. valid at 12:00 UTC on 24 March 2017. The large black arrows denote past and future projection of the surface low-pressure centers in the central U.S. The black rectangle shows the region of interest where in situ measurements were taken during the BAIRS II campaign.	42
23	Flight track taken by the Convair-580 aircraft on 24 March 2017 between 09:33–14:15 UTC. The overlays and base map were displayed using the GR2Analyst radar display program developed by Gibson Ridge Software.	43
24	Surface analysis over the continental U.S. valid at 15:00 UTC on 25 March 2017. The large black arrows denote past and future projection of the surface low-pressure center presently located over Missouri. The black rectangle shows the region of interest where in situ measurements were taken during the BAIRS II campaign.	46
25	Flight track taken by the Convair-580 aircraft on 25 March 2017 between 11:00–16:00 UTC. The overlays and base map were displayed using the GR2Analyst radar display program developed by Gibson Ridge Software.	47
26	Flowchart illustrating the methodology used to estimate the cloud phase encountered by the Convair-580 aircraft at five-second observation intervals. The data preprocessing steps are shown in row 1. Determination of the initial phase type is based on probe measurements from the Nevzorov LWC, TWC, and LWC/TWC ratio (row 2), the FSSP concentration (row 3), and crystal habit classification frequencies generated by the SNDI algorithm (row 4). Several steps are then performed to assign an unknown phase type, validate the initial type, and identify SLD intervals.	53

## LIST OF ILLUSTRATIONS (Continued)

Figure No.		Page
27	An example of a six-panel time series plot generated from a tool used in the evaluation of the cloud phase estimate methodology for the interval 15:30–15:40 UTC on 10 January 2017. From top to bottom, the panels show probe measurements from the Nevzorov LWC, TWC, and LWC/TWC ratio (panel 1), FSSP concentration (panel 2), SNDI crystal habit classifications derived from the 2D-C and PIP probes (panels 3 and 4), RID frequency (panel 5), and particle types observed in the CPI imagery (left axis) with temperature (right axis)(panel 6).	55
28	The crystal habit diagram based on laboratory diffusion chamber measurements of Bailey and Hallett [1]. The sloping red line represents the condition of water saturation. Also encircled are the three crystal types of fundamental importance for the crystal sandwich: the flat crystals on the left (including dendrites and flat-plate hexagonal crystals) in a temperature range from $-9^{\circ}$ to $-16^{\circ}\text{C}$ and the needle crystals on the right in a temperature range from $-4^{\circ}$ to $-7^{\circ}\text{C}$ .	57
29	Vertical profile of LWC and samples of the 2D-C hydrometeor imagery at two temperature levels in the profile while porpoising between 18:31–18:37 UTC on 28 February 2013. A maximum in LWC is evident between the two crystal layers.	59
30	Nine-panel plot of KBUF differential reflectivity (ZDR) with the center plot matched nearest in time and space to the Convair-580 position at 18:34:22 UTC for the crystal sandwich case on 28 February 2013. The row (column) of plots show adjacent elevation angles (volume times) increasing from bottom to top (left to right), respectively.	60
31	Nine-panel plot of KBUF reflectivity (Z) with the center plot matched nearest in time and space to the Convair-580 position at 18:34:22 UTC for the crystal sandwich case on 28 February 2013. The row (column) of plots show adjacent elevation angles (volume times) increasing from bottom to top (left to right), respectively.	61
32	Nine-panel plot of KBUF hydrometeor classification (HC) with the center plot matched nearest in time and space to the Convair-580 position at 18:34:22 UTC for the crystal sandwich case on 28 February 2013. The rows (columns) of plots show adjacent elevation angles (volume times) increasing from bottom to top (left to right), respectively. Abbreviations of the HC categories include Biological (BI), Ground Clutter (GC), Ice Crystals (IC), Dry Snow (DS), Wet Snow (WS), Rain (RA), Heavy Rain (HR), Big Drops (BD), Graupel (GR), Hail-rain mix (HA), Unknown (UK), and Range Folding (RF).	62

## LIST OF ILLUSTRATIONS (Continued)

Figure No.		Page
33	Six-panel plot showing records from the SNDI algorithm (top two panels), in situ temperature, aircraft altitude, Nevzorov LWC and TWC, RID frequency, and FSSP LWC (middle two panels), and onboard X-band radar reflectivity and dual polarimetric quantities from KBUF (bottom two panels) radar for the interval 15:20–15:30 UTC on 10 January 2017.	63
34	Vertical profile of LWC and samples of the 2D-C hydrometeor imagery at two temperature levels in the profile during a spiral ascent between 15:20–15:34 UTC on 10 January 2017.	64
35	Nine-panel plot of KBUF differential reflectivity (ZDR) with the center plot matched nearest in time and space to the Convair-580 position at 15:32:05 UTC for the crystal sandwich case on 10 January 2017. The row (column) of plots show adjacent elevation angles (volume times) increasing from bottom to top (left to right), respectively.	65
36	Nine-panel plot of KBUF reflectivity (Z) with the center plot matched nearest in time and space to the Convair-580 position at 15:32:05 UTC for the crystal sandwich case on 10 January 2017. The row (column) of plots show adjacent elevation angles (volume times) increasing from bottom to top (left to right), respectively.	66
37	Nine-panel plot of KBUF hydrometeor classification (HC) with the center plot matched nearest in time and space to the Convair-580 position at 15:32:05 UTC for the crystal sandwich case on 10 January 2017. The row (column) of plots show adjacent elevation angles (volume times) increasing from bottom to top (left to right), respectively. Abbreviations of the HC categories include Biological (BI), Ground Clutter (GC), Ice Crystals (IC), Graupel (GR), Hail–Rain mix (HA), Unknown (UK), and Range Folding (RF).	67
38	Six-panel plot showing records from the SNDI algorithm (top two panels), in situ temperature, aircraft altitude, Nevzorov LWC and TWC, RID frequency, and FSSP LWC (middle two panels), and onboard X-band radar reflectivity and dual polarimetric quantities from KBUF (bottom two panels) radar for the interval 10:40–10:50 UTC on 24 March 2017.	68
39	Vertical profile of LWC and samples of the 2D-C hydrometeor imagery at two temperature levels in the profile during a spiral descent between 10:42–10:50 UTC on 24 March 2017.	69

## LIST OF ILLUSTRATIONS (Continued)

Figure No.		Page
40	Nine-panel plot of KBUF differential reflectivity (ZDR) with the center plot matched nearest in time and space to the Convair-580 position at 10:48:32 UTC for the crystal sandwich case on 24 March 2017. The row (columns) of plots show adjacent elevation angles (volume times) increasing from bottom to top (left to right).	70
41	Nine-panel plot of KBUF reflectivity (Z) with the center plot matched nearest in time and space to the Convair-580 position at 10:48:32 UTC for the crystal sandwich case on 24 March 2017. The row (column) of plots show adjacent elevation angles (volume times) increasing from bottom to top (left to right), respectively.	71
42	Nine-panel plot of KBUF hydrometeor classification (HC) with the center plot matched nearest in time and space to the Convair-580 position at 10:48:32 UTC for the crystal sandwich case on 24 March 2017. The row (column) of plots show adjacent elevation angles (volume times) increasing from bottom to top (left to right), respectively. Abbreviations of the HC categories include Biological (BI), Ground Clutter (GC), Ice Crystals (IC), Dry Snow (DS), Wet Snow (WS), Rain (RA), Heavy Rain (HR), Big Drops (BD), Graupel (GR), Hail–Rain mix (HA), Unknown (UK), and Range Folding (RF).	72
43	Six-panel plot showing records from the SNDI algorithm (top two panels), in situ temperature, aircraft altitude, Nevzorov LWC and TWC, RID frequency, and FSSP LWC (middle two panels), and onboard X-band radar reflectivity and dual polarimetric quantities from KBUF (bottom two panels) radar for the interval 14:10–14:20 UTC on 25 March 2017.	73
44	Vertical profile of LWC and samples of the 2D-C hydrometeor imagery at two temperature levels in the profile during a spiral ascent between 14:15–14:21 UTC on 25 March 2017.	74
45	Nine-panel plot of KBUF differential reflectivity (ZDR) with the center plot matched nearest in time and space to the Convair-580 position at 14:15:40 UTC for the crystal sandwich case on 25 March 2017. The row (column) of plots show adjacent elevation angles (volume times) increasing from bottom to top (left to right), respectively.	75
46	Nine-panel plot of KBUF reflectivity (Z) with the center plot matched nearest in time and space to the Convair-580 position at 14:15:40 UTC for the crystal sandwich case on 25 March 2017. The row (column) of plots show adjacent elevation angles (volume times) increasing from bottom to top (left to right), respectively.	76

## LIST OF ILLUSTRATIONS (Continued)

Figure No.		Page
47	Nine-panel plot of KBUF hydrometeor classification (HC) with the center plot matched nearest in time and space to the Convair-580 position at 14:15:40 UTC for the crystal sandwich case on 25 March 2017. The row (column) of plots show adjacent elevation angles (volume times) increasing from bottom to top (left to right), respectively. Abbreviations of the HC categories include Biological (BI), Ground Clutter (GC), Ice Crystals (IC), Dry Snow (DS), Wet Snow (WS), Rain (RA), Heavy Rain (HR), Big Drops (BD), Graupel (GR), Hail–Rain mix (HA), Unknown (UK), and Range Folding (RF).	77
48	Evidence for crystal sandwich structure in vertical profiles of LWC (black), reflectivity (red), ZDR (blue), and LDR (linear depolarization ratio; orange) from the AIRS-II aircraft campaign on 11 November 2003 (Wolde et al. [92]).	78
49	Four-panel PPI plot of reflectivity (upper left), ZDR (upper right), CC (lower left), and KDP (lower right) for the KBOX 9.9° elevation angle at 08:01:25 UTC on 9 December 2017.	81
50	Four-panel PPI plot of reflectivity (upper left), ZDR (upper right), CC (lower left), and KDP (lower right) for the KMRX 19.5° elevation angle at 15:21:02 UTC on 20 December 2017.	82
51	Four-panel PPI plot of reflectivity (upper left), ZDR (upper right), CC (lower left), and KDP (lower right) for the KMHX 9.9° elevation angle at 16:52:55 UTC on 27 December 2017.	83
52	Four-panel PPI plot of reflectivity (upper left), ZDR (upper right), CC (lower left), and KDP (lower right) for the KBOX 19.5° elevation angle at 15:40:58 UTC on 7 February 2018.	84
53	Schematic illustration of the crystal sandwich structure, including profiles of supercooled liquid water (left) and ground-based radar differential reflectivity (right).	89
54	Relationship between snowfall rate $S$ (mm/hr) and ascent speed $W$ (m/s) based on Eq. 7. Rough boundaries on three snowstorm regimes discussed in the text are also shown. The snowfall rate along the ordinate is liquid water equivalent.	92
55	Five flight history of MVD derived from the FSSP. The red dashed line denotes the critical threshold diameter for runaway coalescence and the formation of drizzle from smaller cloud droplets.	96

## LIST OF ILLUSTRATIONS (Continued)

Figure No.		Page
56	Concatenated hydrometeor size distributions showing particle concentrations derived from the FSSP, 2D-C, and PIP probes on 10 January 2017 for the interval 14:00–18:00 UTC. Timelines of MVD are shown in black (FSSP), green (2D-C), and red (PIP). Five-second averages of the in situ temperature are shown in blue.	98
57	Concatenated hydrometeor size distributions showing particle concentrations derived from the FSSP, 2D-C, and HVPS probes on 24 January 2017 for the interval 02:30–07:00 UTC. Timelines of MVD are shown in black (FSSP), green (2D-C), and red (HVPS). Five-second averages of the in situ temperature are shown in blue.	99
58	Concatenated hydrometeor size distributions showing particle concentrations derived from the FSSP, 2D-S, and PIP probes on 7 February 2017 for the interval 16:00–19:30 UTC. Timelines of MVD are shown in black (FSSP), green (2D-S), and red (PIP). Five-second averages of the in situ temperature are shown in blue.	100
59	Concatenated hydrometeor size distributions showing particle concentrations derived from the FSSP, 2D-C, and HVPS probes on 24 March 2017 for the interval 09:30–14:30 UTC. Timelines of MVD are shown in black (FSSP), green (2D-C), and red (HVPS). Five-second averages of the in situ temperature are shown in blue.	101
60	Concatenated hydrometeor size distributions showing particle concentrations derived from the FSSP, 2D-C, and HVPS probes on 25 March 2017 for the interval 11:00–16:00 UTC. Timelines of MVD are shown in black (FSSP), green (2D-C), and red (HVPS). Five-second averages of the in situ temperature are shown in blue.	102
61	Distributions of cloud extinction coefficient measured during four of five flights. The extinction meter was not operable on the 10 January flight.	104
62	Scatterplot of LWC versus extinction coefficient with evidence of needle crystals for four of five flights. The extinction meter was not operable on the 10 January flight.	105
63	CPI imagery for 16:17:07–16:17:40 UTC on 10 January 2017. Each image is labeled with a time stamp (above) and particle size (bottom; in $\mu\text{m}$ ).	110
64	CPI imagery for 05:59:12–05:59:21 UTC on 24 January 2017. Each image is labeled with a time stamp (above) and particle size (bottom; in $\mu\text{m}$ ).	112

## LIST OF ILLUSTRATIONS (Continued)

Figure No.		Page
65	CPI imagery for 17:18:11–17:18:47 UTC on 7 February 2017. Each image is labeled with a time stamp (above) and particle size (bottom; in $\mu\text{m}$ ).	114
66	2D-S imagery for 17:18–17:19 UTC on 7 February 2017. The number of seconds past the minute is shown to the left of each image.	115
67	CPI imagery for 18:48:16–18:48:45 UTC on 7 February 2017. Each image is labeled with a time stamp (above) and particle size (bottom; in $\mu\text{m}$ ).	116
68	CPI imagery for 10:51:51–10:52:14 UTC on 24 March 2017. Each image is labeled with a time stamp (above) and particle size (bottom; in $\mu\text{m}$ ).	118
69	CPI imagery for 12:57:20–12:57:40 UTC on 24 March 2017. Each image is labeled with a time stamp (above) and particle size (bottom; in $\mu\text{m}$ ).	120
70	CPI imagery for 12:53:59–12:54:11 UTC on 25 March 2017. Each image is labeled with a time stamp (above) and particle size (bottom; in $\mu\text{m}$ ).	122
71	CPI imagery for 14:30:31–14:30:52 UTC on 25 March 2017. Each image is labeled with a time stamp (above) and particle size (bottom; in $\mu\text{m}$ ).	124
72	Needle crystal concentrations for dates and times when the fraction of needle crystals in the SNDI algorithm exceeded 90%. Data points are labeled by the date of the BAIRS II flight and by mean crystal size. Data from one flight in BAIRS I (28 February 2013) were also added. The placement of the points along the abscissa is not indicative of the amount of SLW present.	127
73	CPI imagery covering a transition from rimed columns (and small graupel particles) (15:18:39–15:19:02 UTC) to unrimed needles (15:20:22–15:20:45 UTC) on 10 January 2017.	129
74	CPI imagery on 24 March 2017 (13:37:13–13:37:27 UTC) with rimed needles in the presence of supercooled water in small droplet form.	130
75	Histogram of $N^*r$ values for all dendrite crystals under the condition that >90% of crystals in the SNDI algorithm are Dendrites.	132
76	Histogram of $N^*r$ values for all needle crystals under the condition that >90% of crystals in the SNDI algorithm are Needles.	133

## LIST OF ILLUSTRATIONS (Continued)

Figure No.		Page
77	Convair-580 X-band 450 m mean reflectivity (side) for all BAIRS II missions separated by glaciated (blue) and SLD (cyan) phases.	134
78	NEXRAD mean reflectivity for all BAIRS II missions separated by glaciated (blue) and SLD (cyan) phase.	135
79	NEXRAD hydrometeor classification (HC) mode for all BAIRS II missions separated by glaciated (blue) and SLD (cyan) phases. Abbreviations of the HC categories include Biological (BI), Ground Clutter (GC), Ice Crystals (IC), Dry Snow (DS), Wet Snow (WS), Rain (RA), Heavy Rain (HR), Big Drops (BD), Graupel (GR), Hail–Rain mix (HA), and Unknown (UK).	136
80	NEXRAD mean differential phase for all BAIRS II missions separated by glaciated (blue) and SLD (cyan) phases.	137
81	NEXRAD mean correlation coefficient for all BAIRS II missions separated by glaciated (blue) and SLD (cyan) phases.	138
82	NEXRAD mean differential reflectivity for all BAIRS II missions separated by glaciated (blue) and SLD (cyan) phases.	139
83	In situ temperature for all BAIRS II missions separated by glaciated (blue) and SLD (cyan) phases.	140
84	Categorical breakdown of all aircraft–radar beam comparisons for observations categorized as an icing hazard (top row) and no-icing (bottom row) encountered by the Convair-580 relative to the KBUF (left column), KBGM (center column), and KTYX (right column) radars.	144
85	Select distributions of Convair-580 measurements (top row) and spatial–temporal matched KBUF radar estimates (bottom row) for the duration of the 10 January 2017 flight. The top row shows temperature (left), Nevzorov LWC (center; log scale), and FSSP MVD (right). The bottom row shows mean reflectivity (left), mean ZDR (center), and HC mode (right). Abbreviations of the HC categories include Biological (BI), Ground Clutter (GC), Ice Crystals (IC), Dry Snow (DS), Wet Snow (WS), Rain (RA), Heavy Rain (HR), Big Drops (BD), Graupel (GR), Hail–Rain mix (HA), Unknown (UK), and Range Folding (RF).	157

## LIST OF ILLUSTRATIONS (Continued)

Figure No.		Page
86	Select distributions of Convair-580 measurements (top row) and spatial–temporal matched KBUGM radar estimates (bottom row) for the duration of the 24 January 2017 flight. The top row shows temperature (left), Nevzorov LWC (center; log scale), and FSSP MVD (right). The bottom row shows mean reflectivity (left), mean ZDR (center), and HC mode (right). Abbreviations of the HC categories include Biological (BI), Ground Clutter (GC), Ice Crystals (IC), Dry Snow (DS), Wet Snow (WS), Rain (RA), Heavy Rain (HR), Big Drops (BD), Graupel (GR), Hail–Rain mix (HA), Unknown (UK), and Range Folding (RF).	158
87	Select distributions of Convair-580 measurements (top row) and spatial–temporal matched KBUF radar estimates (bottom row) for the duration of the 7 February 2017 flight. The top row shows temperature (left), Nevzorov LWC (center; log scale), and FSSP MVD (right). The bottom row shows mean reflectivity (left), mean ZDR (center), and HC mode (right). Abbreviations of the HC categories include Biological (BI), Ground Clutter (GC), Ice Crystals (IC), Dry Snow (DS), Wet Snow (WS), Rain (RA), Heavy Rain (HR), Big Drops (BD), Graupel (GR), Hail–Rain mix (HA), Unknown (UK), and Range Folding (RF).	159
88	Select distributions of Convair-580 measurements (top row) and spatial–temporal matched KBUF radar estimates (bottom row) for the duration of the 24 March 2017 flight. The top row shows temperature (left), Nevzorov LWC (center; log scale), and FSSP MVD (right). The bottom row shows mean reflectivity (left), mean ZDR (center), and HC mode (right). Abbreviations of the HC categories include Biological (BI), Ground Clutter (GC), Ice Crystals (IC), Dry Snow (DS), Wet Snow (WS), Rain (RA), Heavy Rain (HR), Big Drops (BD), Graupel (GR), Hail–Rain mix (HA), Unknown (UK), and Range Folding (RF).	160
89	Select distributions of Convair-580 measurements (top row) and spatial–temporal matched KBUF radar estimates (bottom row) for the duration of the 25 March 2017 flight. The top row shows temperature (left), Nevzorov LWC (center; log scale), and FSSP MVD (right). The bottom row shows mean reflectivity (left), mean ZDR (center), and HC mode (right). Abbreviations of the HC categories include Biological (BI), Ground Clutter (GC), Ice Crystals (IC), Dry Snow (DS), Wet Snow (WS), Rain (RA), Heavy Rain (HR), Big Drops (BD), Graupel (GR), Hail–Rain mix (HA), Unknown (UK), and Range Folding (RF).	161

## LIST OF ILLUSTRATIONS (Continued)

Figure No.		Page
90	Time series plot of cloud phase (above panel 1) estimated from the data components displayed in the six panels for the 14:00–18:00 UTC interval on 10 January 2017. From top to bottom, the panels show probe measurements from the Nevzorov LWC, TWC, and LWC/TWC ratio (panel 1), FSSP concentration (panel 2), SNDI crystal habit classifications derived from the 2D-C and PIP probes (panels 3 and 4), RID frequency (panel 5), and particle types observed in the CPI imagery (left axis) with temperature (right axis)(panel 6).	167
91	Time series plot of cloud phase (above panel 1) estimated from the data components displayed in the six panels for the 02:30–07:00 UTC interval on 24 January 2017. From top to bottom, the panels show probe measurements from the Nevzorov LWC, TWC, and LWC/TWC ratio (panel 1), FSSP concentration (panel 2), SNDI crystal habit classifications derived from the 2D-C and PIP probes (panels 3 and 4), RID frequency (panel 5), and particle types observed in the CPI imagery (left axis) with temperature (right axis)(panel 6).	168
92	Time series plot of cloud phase (above panel 1) estimated from the data components displayed in the six panels for the 16:00–19:30 UTC interval on 7 February 2017. From top to bottom, the panels show probe measurements from the Nevzorov LWC, TWC, and LWC/TWC ratio (panel 1), FSSP concentration (panel 2), SNDI crystal habit classifications derived from the 2D-C and PIP probes (panels 3 and 4), RID frequency (panel 5), and particle types observed in the CPI imagery (left axis) with temperature (right axis)(panel 6).	169
93	Time series plot of cloud phase (above panel 1) estimated from the data components displayed in the six panels for the 09:30–14:30 UTC interval on 24 March 2017. From top to bottom, the panels show probe measurements from the Nevzorov LWC, TWC, and LWC/TWC ratio (panel 1), FSSP concentration (panel 2), SNDI crystal habit classifications derived from the 2D-C and PIP probes (panels 3 and 4), RID frequency (panel 5), and particle types observed in the CPI imagery (left axis) with temperature (right axis)(panel 6).	170
94	Time series plot of cloud phase (above panel 1) estimated from the data components displayed in the six panels for the 11:00–16:00 UTC interval on 25 March 2017. From top to bottom, the panels show probe measurements from the Nevzorov LWC, TWC, and LWC/TWC ratio (panel 1), FSSP concentration (panel 2), SNDI crystal habit classifications derived from the 2D-C and PIP probes (panels 3 and 4), RID frequency	

**LIST OF ILLUSTRATIONS**  
**(Continued)**

<b>Figure No.</b>	<b>Page</b>
(panel 5), and particle types observed in the CPI imagery (left axis) with temperature (right axis)(panel 6).	171

## LIST OF TABLES

Table No.		Page
1	ZDR Bias Offset Values Used to Reprocess the ZDR Products during Playback for Use in the Aircraft–Radar Comparisons for each NEXRAD and BAIRS II Mission Date	17
2	NEXRAD Radar Evidence for Crystal Sandwiches	79
3	Dual Polarimetric Parameters for Four Crystal Sandwich Cases on NEXRAD Radars	85
4	Z-S Relationships for Snowfall and Precipitation Rate (mm/hr Liquid Water Equivalent) for 10 dBZ, and Corresponding Ascent Value based on Figure 54	93
5	Two Hypotheses for Presence of Large Droplets (>24 $\mu\text{m}$ ) Just Above the 0°C Level for Purposes of Enabling an Ice Multiplication Process	108
6	Number of Observations Characterized as Icing and No-Icing based on an Assessment of Cloud Phase when the Convair-580 Aircraft was within 200 km of each Radar and the Performance of the IHL Algorithm Measured in Terms of POD and FAR	143
7	Summary of Cases Examined for Lifting Mechanism with Associated Maximum Composite Reflectivity	164

**This page intentionally left blank.**

# 1. INTRODUCTION

This study is concerned with the in situ validation of the icing hazard in winter storms by aircraft and with the identification of S-band dual polarimetric Next Generation Weather Radar (NEXRAD) methods to localize that hazard in space and time. This work in the second Buffalo Area Icing and Radar Study (BAIRS II) follows on the earlier BAIRS I study in 2013 (Williams *et al.* [84]) in the same general location with NEXRAD radars in New York (NY) State, but now with improved characterization of supercooled water, sharper imagery on rimed hydrometeors, and the implementation of five long-duration flights in winter storms of 2017. Project partners in this work again included the National Research Council of Canada (NRC), Environment and Climate Change Canada (ECCC), and the Massachusetts Institute of Technology (MIT) Lincoln Laboratory (LL). The Canadian counterpart of this research effort was called Weather Radar Validation Experiment (WERVEX).

The direct observation of the icing hazard (supercooled water) with S-band dual polarimetric radar is challenging at the outset because this hazard is often in undetectable small (cloud) droplet form, and even when in supercooled large drop (SLD) (and drizzle drop) form, it is still comprised of spherical hydrometeors that present isotropic targets. Accordingly, the general strategy adopted in BAIRS II has been to identify strongly anisotropic ice crystal targets (dendrites and needles) with which the radar-elusive supercooled water is physically linked, and then make use of the dual polarimetric methods (most notably differential reflectivity) to find these special crystals' radar signatures. Fortuitously, the habits of incipient ice crystals often organize themselves by temperature and supersaturation with respect to liquid and solid water and so crystal layers can be identified in the atmosphere with verified layers of supercooled water in their immediate vicinity. The organization of distinct needle and dendritic crystal layers on the mesoscale, often bounding a layer of supercooled water, has been named the "crystal sandwich" here, and can be localized in routine NEXRAD volume scans over areas of tens of thousands of square kilometers important to commercial aviation.

There are many winter weather icing hazard scenarios that are a function of the vertical temperature and moisture profiles, synoptic conditions, microphysical processes, and the evolution thereof. BAIRS II, with its five missions and 21 hours of winter weather investigation, cannot possibly completely sample all the possible scenarios. Many of the winter weather scenarios, though, do have commonality to varying degrees. The purpose of the BAIRS II missions was to probe those commonalities as they present and relate to S-band dual polarization radar features (in particular, the differential reflectivity (ZDR)). The high-level, takeaway-message schematic shown in Figure 1 is designed to highlight some commonalities in winter weather systems, their relation to likelihood of an icing hazard, and their detectability with S-band dual polarization radar.

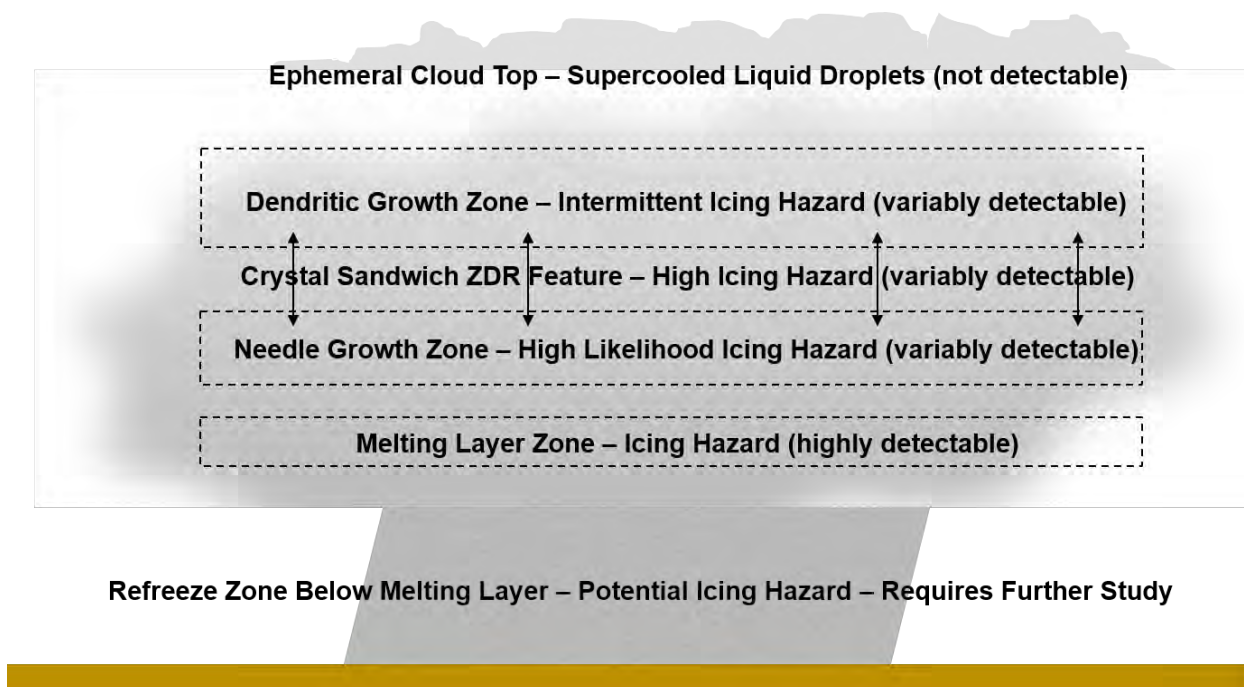


*Figure 1. Illustration of possible icing hazard scenarios observed in winter weather systems and the likelihood of detectability with an S-band dual polarimetric radar.*

Throughout this BAIRS II report, detailed analysis and discussion will be focused on what was found during the in situ missions relating to the commonalities shown in Figure 1. There is no guarantee that all these shown are present at one time and, if they are, that the storm will maintain such for the duration. Starting from top down, at the top altitudes above a winter storm, a layer of supercooled water droplets (clouds) are known to be present by in situ probing and optical methods (the observed glory). This layer is not detectable by the NEXRAD S-band dual polarization radar. The next significant common zone is the dendritic growth zone that is characterized by an intermittent icing hazard and variable NEXRAD detectability. At lower (warmer but below freezing) altitudes, the needle growth zone is characterized by a highly likely icing hazard zone and variable NEXRAD detectability. Its detectability (reminder: in ZDR) is in part a function of precipitate aggregation passing through from above zones. These crystal zones are termed “positive ZDR bright bands” or +d ZDR BB (for dendrites) and +n ZDR BB (for needles) in this report. Those form the bounds of a new feature studied in the BAIRS II (and other) data termed the “crystal sandwich”. That feature often is observed to have a maximum of supercooled liquid water and is therefore an icing hazard threat. Crystals in this zone vary and could also include precipitate from above, leading to a mixed S-band returns’ picture. The ZDR signature in this area is a relative diminishment from that of the sandwiching crystal zones (if present). At lower altitudes, the zone just above and into the melting layer is very apparent in many S-band data fields. With the water species supported and transitioning about in solid, liquid, and gaseous forms, this is a known, rich layer of icing hazard. Many of the 21 BAIRS II flight mission hours were focused from around the dendritic growth zone through the melting layer zone with

salient points discussed throughout the report. An important potential icing hazard zone resides beneath the melting layer. This refreeze zone was not well studied and only notably intercepted once in BAIRS II.

The general organization of this report runs as follows: The methodology is covered in Section 2 and includes discussion of the instrumentation and capabilities of the Convair-580 aircraft that is relied upon again in BAIRS II, operated by NRC out of Ottawa, Canada. This project also made expanded use of the NEXRAD radars, and three of them (Buffalo, NY NEXRAD (KBUF), Binghamton, NY NEXRAD (KBGM), and Montague, NY NEXRAD (KTYX)) are discussed in Section 2.2. Procedures for the careful inter-comparison of aircraft and ground-based dual polarimetric radar observations are addressed in Section 2.3. Interest in accurate measurements of differential reflectivity motivated offset checks for all three radars in Section 2.4. The development of analysis tools to facilitate the presentation of findings and results are summarized in Section 2.5.

Section 3 includes the synoptic context for each flight and a discussion of both operational and scientific highlights over each of five flight tracks. The principal findings and results of this study are collected in Section 4. A major improvement in BAIRS II in the specification of “mixed” phase conditions and their distinction with “glaciated” and non-icing conditions is presented in Section 4.1.

The collective evidence (from diffusion cloud chamber, aircraft and radar) for crystal sandwich structure, a key advance from the BAIRS I conceptualization around the positive differential reflectivity “bright band” (+ZDR BB) that focused only on dendritic crystals (see also Kennedy and Rutledge [39]), is presented in Section 4.2. This robust feature in winter storms is supported with calculations in Section 4.3 of snowfall rates in “crystal storms”, which by definition are lacking in the aggregation of ice crystals, and with synoptic scale assessments (Appendix B) of the warm and cold frontal contexts that provide for the gentle ascent needed to form laterally extensive layers of crystals each with a single predominant crystal type.

One of five BAIRS II storms (24 January 2017) was shown in the synoptic analysis to ingest mainly maritime air, with notable effects on median volume droplet diameter, concatenated droplet size distributions, and optical extinction. This maritime case is contrasted with the other four flights in Section 4.4.

Given the importance of ice multiplication as a possible modulator of icing conditions and the important role of columnar/needle crystals as a product of ice multiplication, the relationship between rich needle populations and supercooled water is examined in Section 4.5.

Finally, and in keeping with the overriding goal to identify icing hazard with dual polarimetric radar, efforts were made to find distinguishing radar signatures for “mixed phase with SLD” and purely “glaciated” situations (documented by aircraft) in a wide variety of dual polarimetric observations. These findings are included in Section 4.6. The Federal Aviation Administration’s (FAA) operational NEXRAD Icing Hazard Levels (IHL) algorithm is assessed in a new way for BAIRS II, as described in Section 4.7.

Section 5 and Section 6 are devoted to discussion of the main findings and conclusions, respectively. Section 7 contains suggestions for future work.

**This page intentionally left blank.**

## 2. METHODOLOGY

### 2.1 CONVAIR-580 AIRCRAFT INSTRUMENTS

#### 2.1.1 Aircraft Measurements for BAIRS II

The general use of the Convair-580 in the BAIRS II study (in winter 2017) closely followed the same procedures earlier in the BAIRS I campaign (winter 2013, Williams *et al.* [84]). All flights originated at the NRC in Ottawa, Canada and ferried to selected storms of interest in the vicinity of the KBUF NEXRAD radar in Buffalo, NY and occasionally two additional radars in Binghamton, NY (KBGM) and Montague, NY (KTYX). Although there is much overlap in the aircraft instrumentation suite from BAIRS I to BAIRS II, some important improvements were implemented in BAIRS II that deserve some discussion. Figure 2 shows most but not all of the probes mounted beneath the wings of the Convair-580.

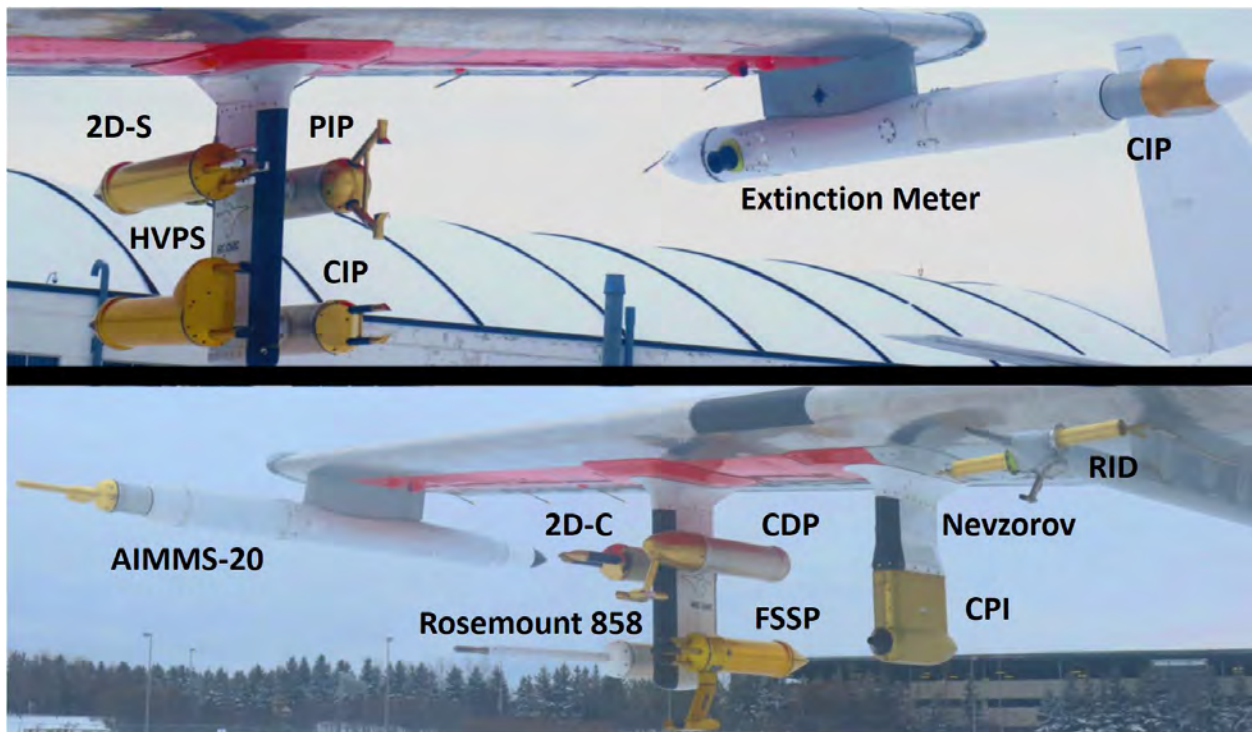


Figure 2. Illustration of the majority of probes mounted beneath the left (top) and right (bottom) wings of the Convair-580 aircraft.

## 1. Use of the Cloud Particle Imager (CPI) hydrometeor probe

On account of its superior spatial resolution (2.3  $\mu\text{m}$  per pixel), this instrument provided unambiguous detection of two key phenomenon: the existence of riming by small cloud droplets on ice particles and the existence of spherical particles in supercooled form, down to a critical diameter of 18 microns. The Particle Measuring Systems (PMS) two-dimensional cloud (2D-C) and two-dimensional precipitation (2D-P) imagery available earlier in BAIRS I lacked these capabilities. The use of the CPI probe for distinguishing rimed from unrimed needle crystals was particularly effective in BAIRS II (Williams *et al.* [87], [89]).

## 2. Integrated use of all hydrometeor probes to span full size range

During BAIRS I, the hydrometeor datasets were examined individually. In BAIRS II, the size spectra from different instruments (see Figure 3) were concatenated together to produce size distributions over the full dynamic range available for all the instruments. This enabled analysis of coalescence and riming processes that extend upward in scale from cloud droplet sizes to raindrops and graupel particles.

Three size ranges are used to make up concatenated spectra to cover the full size range shown in Figure 3. These ranges and the instruments used for each are as follows:

- |     |                     |  |
|-----|---------------------|--|
| (a) | Cloud droplets      | FSSP (Forward Scattering Spectrometer Probe)<br>CDP (Cloud Droplet Probe)                              |
| (b) | Small ice particles | 2D-S (two-dimensional Stereo Probe)<br>2D-C (two-dimensional Cloud Probe)<br>CIP (Cloud Imaging Probe) |
| (c) | Precipitation size  | HVPS (High Volume Precipitation Spectrometer)<br>PIP (Precipitation Imaging Probe)                     |

Complete spectra are updated with one-second resolution. The general rules for use are as follows: if all systems are operational, the probe that performed the best during the flight was chosen for each size range in the list above. No attempt is made to do averaging of different probe data. For size ranges (b) and (c), the first 2–3 size bins are deleted and that has the effect of creating a roll off toward smaller size for that range. No attempt is made to match results in the overlap regions. For mixed-phase clouds, the spectra are smoother across boundaries than for ice clouds only.

### 2.1.2 Characterization of Supercooled Liquid Water

Liquid water content (LWC) at sub-freezing temperatures, the so-called supercooled liquid water (SLW), is the root of the aircraft icing problem and so is arguably the most important quantity measured by the aircraft in this second validation campaign. The principle instrument for this purpose in BAIRS II is the Nevzorov probe (Korolev *et al.* [40]). This instrument performs exceptionally well when all the SLW is in cloud droplet form, with a low-end sensitivity in the range 0.003–0.005  $\text{g}/\text{m}^3$ . This notable sensitivity provides a more effective means than the temperature and humidity measurements in assessing the presence/absence of a water saturation condition in situ, a key condition for consideration of icing conditions linked with needle and with dendritic crystals (see Section 4 on results). Complete distributions

of the mean Nevzorov LWC measurements collected over five-second intervals for each flight are provided in Appendix A.

In addition to SLW, the Nevzorov probe also measures total water content (TWC; ice and liquid particles). However, one key limitation is that small ice particles can alias for liquid water (Korolev *et al.* [40]) on this probe, and so in mixed and glaciated conditions, the ice water content influences the noise floor for the SLW measurement. This condition was ignored in the BAIRS I analysis (Williams *et al.* [84]), where it was assumed that the threshold condition for SLW and icing conditions was a Nevzorov reading of  $0.005 \text{ g/m}^3$ . Korolev *et al.* [40] found that on average, 10–15% of ice water content (IWC) was manifest as SLW. (Variations in this percentage range from 2–3% (Nevzorov and Shugaev [58]) to 20% (Cober *et al.*, unpublished)). Accordingly, in the improved BAIRS II characterization of microphysical conditions, a ratio of LWC/TWC of 0.85 is used as one criterion for an all liquid condition. To characterize fully glaciated conditions, a ratio of LWC/TWC of 0.25 was selected based on earlier studies of Cober *et al.* [14].

The Rosemount icing detector (RID; Cober *et al.* [13]) was also operating during BAIRS II. Normally, this sensor has a sensitivity to LWC in all water clouds of  $0.002 \text{ g/m}^3$ , but the instrument available for this project was not operating at full resolution. Furthermore, the RID instrument could be unreliable under certain temperature and LWC conditions in which the Ludlam limit (Ludlam [54]) has been reached. This limitation can occur when the accumulation of supercooled droplets freezing onto the probe is sufficient to raise the temperature of the ice surface to  $0^\circ\text{C}$ . Accordingly, the Nevzorov probe was selected over the Rosemount probe as the main instrument pertaining to supercooled water and for use in the algorithm for cloud microphysical characterization in Section 4.1.

### **2.1.3 Characterization of Radar-Detectable Hydrometeors**

The validation of ground-based NEXRAD dual polarimetric methods with the in situ aircraft measurements requires the characterization of the hydrometeor shapes and sizes that influence the radar returns. This requires measurement over a large dynamic range in size, as shown in Figure 3. As noted in Section 2.1.1 (2), many of the probes listed here (FSSP, CDP, 2D-S, 2D-C, CIP, HVPS, and PIP) are used to produce the concatenated spectra over the available dynamic range of size. The Stratton Park Engineering Company (SPEC) CPI probe (Lawson *et al.* [50]) was not used in this task to quantify particle concentrations, but was often consulted for final assessment on the microphysical nature of the hydrometeors (valid water spheres, riming needles, and dendrites) on account of its superior spatial resolution to all other probes. The SPEC 2D-S probe (Lawson *et al.* [51]) found special benefit in a separate study of machine-learning investigation of clustering because of its access to supercooled water particle concentrations in both the small droplet and in the SLD and drizzle category. It was also used as an important check on the presence of supercooled water in small droplet form in the microphysical characterization in Section 4.1.

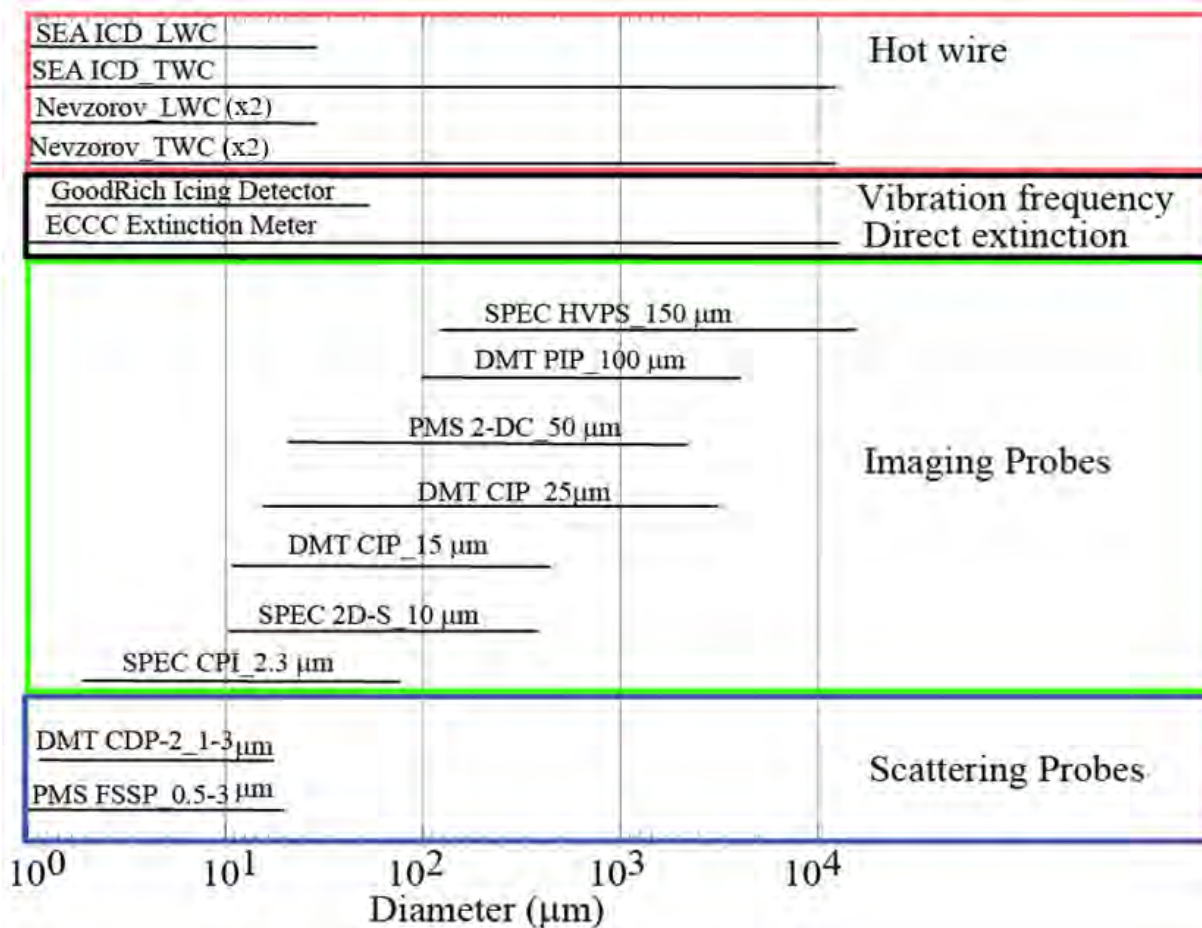


Figure 3. Summary of hydrometeor imaging probes and scattering probes available in BAIRS II, including the dynamic range of their respective size resolution. The upper limit of the imaging probes can be extended during processing. Instruments for measuring supercooled water concentration are also included near the top. Image courtesy of Dr. Mengistu Wolde (NRC).

### 2.1.4 Characterization of Supercooled Cloud Droplets

The most frequent manifestation of SLW in the atmosphere is in the form of cloud droplets. A convenient physical cutoff diameter for cloud droplets is the size needed for runaway coalescence in collisions, requiring a droplet diameter of 25 μm (e.g., Freud *et al.* [21]). This size range is below the pixel resolution of the PMS Optical Array probes (see Figure 3), thereby requiring a separate instrument for their documentation. The Convair-580 was equipped with one FSSP instrument (Gayet *et al.* [24]) for this purpose. The output of the FSSP-002 provides the cloud droplet size distribution from 3–45 μm in 3 μm intervals, also indicated in Figure 3. The median volume diameter (MVD) is also a standard output from the FSSP probe. See Appendix A for complete distributions of the mean FSSP MVD measurements collected over five-second intervals for each flight.

Droplet counts per  $\text{cm}^3$  are standard output from the FSSP instruments. Since cloud droplets form on cloud condensation nuclei (CCN) at water saturated conditions, the FSSP counts are representative of the CCN populations where they form. These CCN concentrations are typically orders of magnitude smaller than the ice nuclei on which ice particles form. Accordingly, the FSSP concentrations can be used to distinguish supercooled droplet clouds from clouds of small ice particles. Korolev *et al.* [43] reported FSSP concentrations in the range of 2–5 per  $\text{cm}^3$  in glaciated conditions. More recently, Alexei Korolev (personal communication, 2018) is using a threshold for glaciated conditions of 1 per  $\text{cm}^3$ . These values form the basis for a selection rule of 3 per  $\text{cm}^3$  in the algorithm for in situ microphysical characterization (Cober *et al.* [14]; Section 4.1).

### 2.1.5 Thermodynamic Measurements

The in situ verification of sub-freezing conditions in winter storms is a critical aspect of the aircraft validation studies. The ambient static temperature is measured on the Convair-580 with two de-iced Rosemount temperature probes and a reverse flow temperature probe shown in previous campaigns to agree within  $\pm 1^\circ\text{C}$  (Cober *et al.* [13]). For BAIRS II, the temperature and dew point probes were accurate to  $0.5^\circ\text{C}$ . Humidity measurements were carried out with an EdgeTech dew point hygrometer and with LICOR 7000 and LICOR 840A instruments. Temperature–humidity measurements on the aircraft are generally insufficiently accurate to establish the water saturation conditions that dictate the habits of ice crystals, so greater reliance was placed on the Nevzorov probe to establish this condition. Temperature measured to the stated accuracy here are useful for identifying sub-freezing conditions. Complete distributions of the mean temperature recorded during each flight are provided in Appendix A.

### 2.1.6 SNDI Algorithm for Aircraft Hydrometeor Classification

The characterization of the hydrometeors that are NEXRAD dual polarimetric radar targets is vital to the in situ validation of the radar-based hydrometeor classification algorithm (HCA) (Park *et al.* [59]) in this study. A principal tool for the characterization of the hydrometeors is the SNDI algorithm (Korolev and Sussman [41]). Based on automated analysis of the black and white particle images from the Droplet Measurement Technologies (DMT) PIP probe (100 to 8500  $\mu\text{m}$ , Figure 3) and from the PMS 2D-C probe (50 to 6500  $\mu\text{m}$ , Figure 3), this algorithm identified four categories of particles: “Spheres”, “Needles”, “Dendrites”, and “Irregulars” (SNDI) (read as “Cindy”). The Spheres category is aimed at liquid drops, but quasi-spherical ice particles like lump graupel and quasi-circular hexagonal flat plates can also enter this category (Korolev and Sussman [41]). The Needles category includes elongated shapes with aspect ratios  $>3$ . Columnar ice crystals are the main contributor. The Dendrites category includes dendritic crystals, stellar crystals, and aggregates of dendritic crystals (i.e., snowflakes). The Irregular category includes all particles having an irregular or random shape. Every one second of flight time, the automated SNDI algorithm produces estimates for the relative prevalence of hydrometeors in these four categories. Unfortunately, the SNDI algorithm in its present form does not produce absolute concentrations of specific crystal types. For that reason, SNDI categories were used for times when specific crystal types exceeded 90% of the total to obtain concentration estimates of needles and dendrites (see Section 4.5 on ice multiplication).

Though SNDI results in BAIRS II were based on an additional set of hydrometeor imagery (PIP) not available in BAIRS I, no improvements in the algorithm itself were achieved in BAIRS II.

## **2.2 GROUND-BASED NEXRAD RADARS (KBUF, KBGM, KTYX)**

An overriding goal of this FAA-sponsored study has been the exploitation of dual polarimetric radar observations for the assessment of aircraft icing hazard. Accordingly, concerted efforts were made to secure aircraft observations on verified hazard in proximity to ground-based NEXRAD S-band dual polarimetric radars. The flight paths were defined in real time in large part from targeting Convair-580 probing on radar features of interest. In BAIRS I, attention was focused in all three flights on storms in proximity to the KBUF NEXRAD in Buffalo, NY. In BAIRS II, interest in aircraft probing over a larger area in five flights led to the use of three separate NEXRAD radars. In addition to KBUF, KBGM (Binghamton, NY) and KTYX (Montague, NY) were involved. The locations of all three radars are shown in each of the flight track maps in Section 3.

## **2.3 SPATIAL–TEMPORAL COMPARISONS BETWEEN AIRCRAFT OBSERVATIONS AND GROUND-BASED RADAR MEASUREMENTS**

The procedures used to match the aircraft observations to the ground-based NEXRAD data both in space and time were identical to the methods used in BAIRS I and described in Williams *et al.* [84]. The aircraft positional data (latitude, longitude, and altitude) are first referenced to a position within the ground-based radar coordinate system in terms of slant range distance, azimuth angle, and elevation beam angle. Separation distances between the positions on the Convair-580 flight track and the fixed radar location were computed using the Haversine method (Sinnott [71]). These distances equate to the slant range distance relative to the radar. Using the slant range and the altitude difference between the aircraft and the radar antenna height, the radar elevation beam angle in which the aircraft resides is then determined. If the aircraft position intersects multiple elevation angles for the radar volume coverage pattern (VCP) scanning strategy in operation, the elevation angle associated with the aircraft position is the angle having the minimum distance between the aircraft altitude and beam center height. Conversely, when the aircraft position did not reside within the pulse resolution volume among any elevation angle, an aircraft–radar comparison was not made. These situations occurred most often at far radar ranges when the Convair-580 was en route to regions of interest or transiting back to home base. Finally, an arctangent formula was used to determine bearing, which translates to azimuth angle.

The Convair-580 in situ measurements were collected at a one-second sampling rate. For consistency with BAIRS I analyses, the one-second data were used to spatially match the aircraft position to the best-matched NEXRAD elevation angle. All probe measurement data were then averaged over five-second intervals and temporally matched to the approximate time of the associated NEXRAD azimuth angle. The time of each radar azimuth angle is not known, but can be estimated since the start time for the radar volume, first azimuth angle of each elevation scan, and the duration of the VCP in operation are all available. The time difference between the five-second aircraft time stamp and the estimated azimuth time associated with the Convair-580 position was computed for all radar volumes scanned during the mission window. The smallest time difference determines which radar volume to use in the aircraft–radar comparisons.



Within each comparison area, aircraft observations are compared to the NEXRAD reflectivity (Z), ZDR, cross-correlation coefficient (CC), differential phase (PHI), specific differential phase (KDP), and hydrometeor classification (HC) products. The statistical metrics computed among all valid range bin values within each window include mean, median, standard deviation, 10th and 90th percentiles, and HC mode. Complete distributions of the radar mean Z, mean ZDR, and HC mode associated with the position of each aircraft observation for each of five flights are provided in Appendix A.

## 2.4 DIFFERENTIAL REFLECTIVITY OFFSET ADJUSTMENTS TO ACCOUNT FOR SYSTEM BIAS

The calibration state of the KBUF, KBGM, and KTYX NEXRADs were monitored prior to and throughout each BAIRS II flight mission to observe for any evidence in operational degradation, particularly in the ZDR product. These conditions become noticeable, signifying a potential issue with calibration, when there is an abundance of measured ZDR radar values below 0 dB (negative or cold bias), an absence of negative values (positive or warm bias), and distinct differences among measured values scanned within a common region between adjacent radars whose radar bins are matched reasonably well in altitude and time. An assessment of each radar's operating ZDR bias was performed and used to generate artificially calibrated ZDR products within the NEXRAD Open Radar Product Generator (ORPG) playback system. The modified products were then used in all subsequent aircraft–radar comparisons.

ZDR error can be monitored using a utility that computes error estimates from three different methods and sends the information to a log file for ORPG system status at the completion of each radar volume. In the first method, called the “dry snow” method (Zittel *et al.* [94]), the ZDR error is the difference between the average ZDR value among all radar bins in the volume (elevation angles  $>1^\circ$ ) that are classified as “Dry Snow” by the NEXRAD HCA and reside within one kilometer from the top of the melting layer (ML), and the expected ZDR value in dry aggregated snow (0.2 dB). The second method, referred to as the “rain” method (Cunningham *et al.* [15]; Zittel *et al.* [94]), compares the median of ZDR values, associated with six reflectivity (Z) arrays in 2 dB width intervals centered between 20–30 dBZ to the climatological median ZDR for that array for all radar bins located in an expected uniform rain region more than one kilometer below the ML bottom. The climatological median ZDR data values were derived from disdrometer data collected in Oklahoma (Schuur *et al.* [69], [70]). The ZDR error estimate is the average of differences between the measured and climatological median values among the six arrays. In the third method, data filters are applied to a number of radar products in search for radar bins containing characteristics of the Bragg scattered signal (Cunningham *et al.* [15]; Zittel *et al.* [94]). Precipitation and statistical filters are applied to remove non-Bragg returns and with only select VCPs and elevation angles between  $2.4\text{--}4.5^\circ$  being considered. The ZDR bias is then estimated among the mode of the ZDR values remaining after all thresholds and criteria have been met. The final ZDR error estimate from each of the methods is averaged over 12 radar volumes to reduce short-term variability.

Time series plots of the ZDR error estimates obtained from the ORPG system status logs are shown in Figure 5 for the 24 January 2017 mission between 02:00–07:00 Universal Time Coordinated (UTC) for the KBUF, KBGM, and KTYX radars from top to bottom, respectively. The blue line represents a running average of the estimates determined from the dry snow method. Error estimates could not be determined from the rain or Bragg methods during this interval. The values shown in the upper right of each plot are the average errors computed from all estimates over the entire interval for the specific method. The dashed

horizontal line at 0 dB implies a state of calibrated ZDR measurements whereas positive (negative) values imply the ZDR measurements are too high (low). The plots show that the ZDR error estimates were consistent during the interval with the KBUF and KTYX radars both operating too low (negative bias) near -0.4 and -0.2 dB, respectively, while the KBGM ZDR measurements were estimated to be too high at +0.4 dB (positive bias).

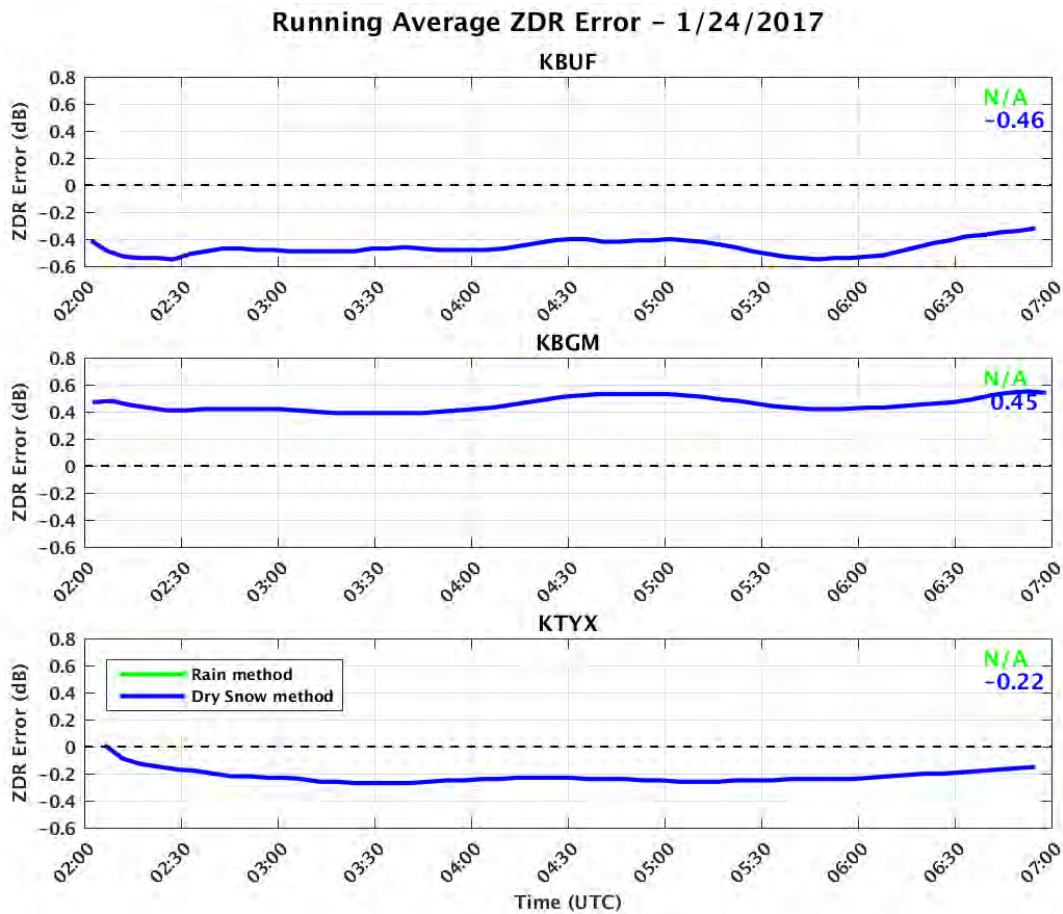


Figure 5. Time series plots of the running average ZDR error estimated for KBUF (top), KBGM (center), and KTYX (bottom) radars during the 24 January 2017 mission flight between 02:00–07:00 UTC. The error estimates shown in blue were computed from the dry snow method. Estimates from the rain and Bragg methods were not obtainable due to an unfavorable meteorological scenario. The value in the upper-right corner of each plot represents the average ZDR error over the entire flight interval.

A post-processing utility within the ORPG system allows the preprocessed ZDR data to be adjusted with a user-defined offset value. For BAIRS II, the ZDR data in real-time were adequate qualitatively for interpretation of differential reflectivity features horizontally or vertically to be useful guides of the Convair-580 to targeted feature probing. As Figure 5 illustrates, the three neighboring NEXRADs exhibited different ZDR magnitude bias errors based on the dry snow method. These biases also differed between the five flight missions. No attempts were made to verify with the imaging probes that the dry snow method was, in fact, appropriate to use. It would be ideal for all NEXRADs to have a 0 dB bias for ZDR. The motivation for the ORPG utility is to provide a pseudo-method towards that ideal. Its application in this

report is to “improve” the ZDR data and their agreement among these three radars. The utility only adjusts the ZDR data. The horizontal reflectivity are left unadjusted. It should be understood, then, that the utility is assigning all bias error to the vertical reflectivity (not an explicit, available data field in the ORPG). Furthermore, adjustments in ZDR will potentially alter some downstream products such as the hydrometeor classes derived from the HCA given that ZDR is one of six variables used in the classification scheme.

Using the ZDR error estimates obtained in real time, the utility was used during playback of each mission radar dataset to create a series of ZDR products each generated with an increasing 0.1 dB offset applied to the measured ZDR value in the opposite direction and up to the absolute magnitude as determined from the error estimates. The adjusted ZDR values from one radar were then compared to the adjusted values from an adjacent radar over a common overlap region to observe the correlation between the two product datasets. A radar comparison tool displays a scatterplot of the ZDR values among the radar bins within a small-range azimuth window centered at the mid-point range bin between the two radars. Radar bin values are only compared among elevation angles when the difference between beam center heights at the mid-point radar bin is less than 1000 feet and the difference in radar volume time is less than 120 seconds.

Figure 6 contains frequency histogram plots of ZDR values for the common overlapping radar bins between KBUF (abscissa) and KBGM (ordinate) NEXRADs on 24 January 2017 for the same time interval shown in Figure 5. Comparisons shown on the left are for the radar products generated in real time (no adjustments applied) and the plot on the right shows comparisons between the products after the ZDR values were adjusted in the opposite direction to the ZDR error estimated from the dry snow method (i.e., 0.4 dB was added for KBUF and 0.4 dB was subtracted for KBGM to account for the low and high bias, respectively). The mean ZDR difference among all the bins compared is shown in the upper-left portion of each plot. The applied offsets result in the cluster of values being more evenly distributed along the red dashed correlation line and with a substantially lower mean difference compared to the product data generated in real time with no adjustments.

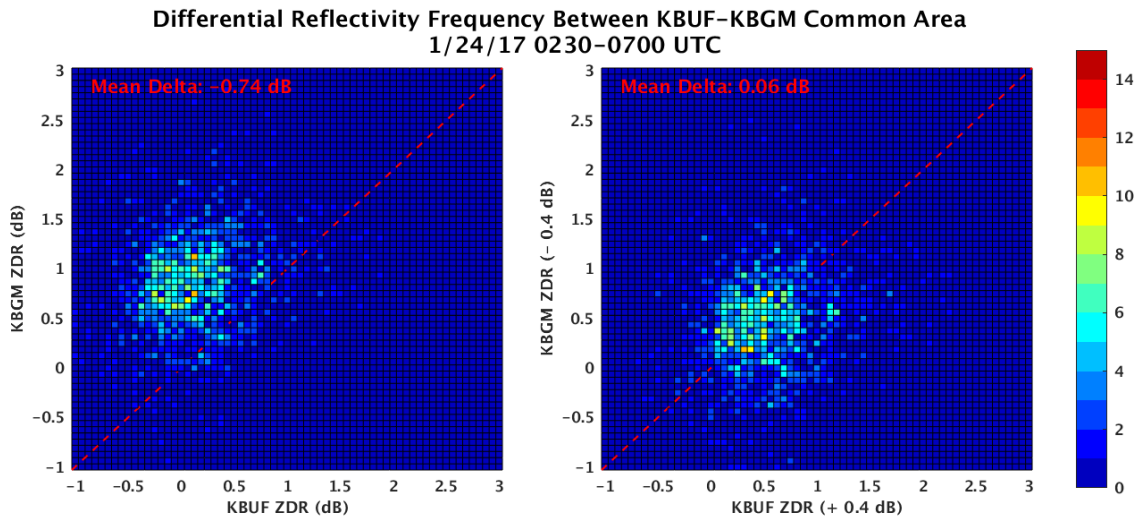


Figure 6. Frequency histogram plots showing a comparison of ZDR values between adjacent NEXRADs, KBUF (abscissa) and KBGM (ordinate), for radar bins residing within a small common overlapping range-azimuth window centered at the mid-point range between the two radars for the interval 02:30-07:00 UTC on 24 January 2017. Only radar bins matched close in time and space are considered. The distribution plot on the left shows the ZDR values measured in real time. The distribution on the right shows the post-processed ZDR values after an adjustment of 0.4 dB was added (subtracted) to KBUF (KBGM) data. The correlation line is shown as a red dashed line.

Figure 7 contains an illustration that highlights the impact of the ZDR adjustments over the common area between the KBUF (left) and KBGM (right) radars in a four-panel plan position indicator (PPI) format for the 0.5° elevation scans at 05:21:53 and 05:22:57 UTC, respectively. The top row shows ZDR with no offset applied and the bottom row shows ZDR after the +0.4 dB and -0.4 dB offsets were applied to KBUF and KBGM, respectively. The offsets produce a much-improved agreement between the product fields over the small comparison region in the center of each image.

The ZDR bias offset values used to reprocess the ZDR products during playback for use in the aircraft–radar comparisons is provided in Table 1 for each NEXRAD and BAIRS II mission date. These values produce a reasonable agreement among the ZDR values qualitatively and match the average bias offsets estimated from the various bias methods described above. No values were determined for KBGM on 7 February 2017 because the Convair-580 flight trajectory was beyond 250 km from the radar.

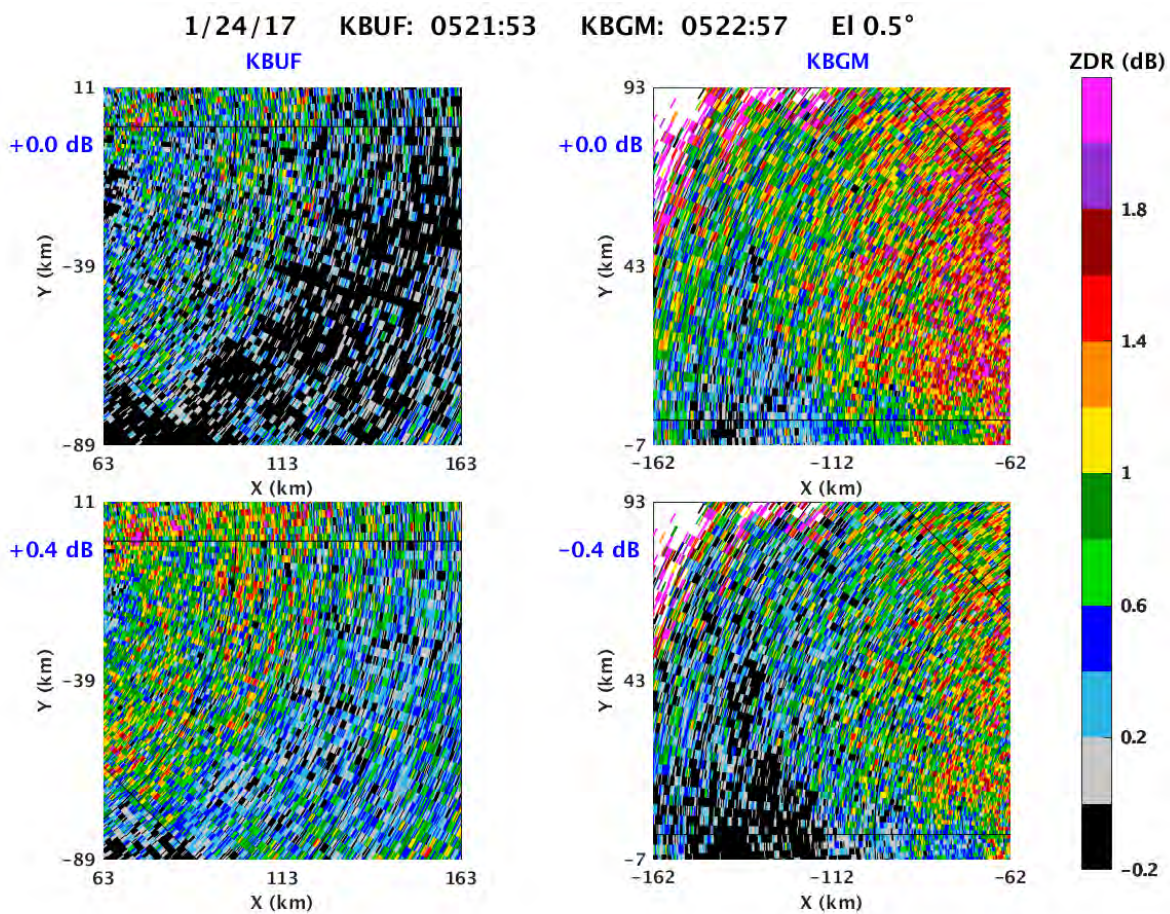


Figure 7. Four-panel PPI plots showing ZDR comparisons between the KBUF (left column) and KBGM (right column) radars centered at the mid-range bin for products generated in real time (top row) and from post-processing after a +0.4 and -0.4 dB offset was applied to the ZDR values (bottom row), respectively. All PPI images are from the 0.5° scan on 24 January 2017 at 05:21:53 (left) and 05:22:57 UTC (right).

**TABLE 1**  
**ZDR Bias Offset Values Used to Reprocess the ZDR Products during Playback for Use in the Aircraft–Radar Comparisons for each NEXRAD and BAIRS II Mission Date**

ZDR Bias Offset Values (dB)			
Mission Date	KBUF	KBGM	KTYX
10 January 2017	+0.1	-0.2	+0.2
24 January 2017	+0.4	-0.4	+0.2
7 February 2017	+0.1		+0.2
24 March 2017	-0.1	-0.3	+0.2
25 March 2017	-0.1	-0.2	+0.2

No bias estimate is provided for KBGM on 7 February 2017 because the Convair-580 aircraft flight trajectory was beyond 250 km from the radar.

## 2.5 ANALYSIS TOOLS

Numerous display tools and utilities were developed primarily in the MATLAB (Matrix Laboratory) programming language to facilitate comparisons between the Convair-580 in situ measurements and the spatial- and temporal-matched ground-based NEXRAD radar product data. Each program reads spreadsheet files that link the five-second averaged aircraft data to the radar volume space (i.e., slant range distance, azimuth angle, elevation angle) and nearest volume time as derived by the methods described in Section 2.3. In addition, some of the utilities were written to help determine which aircraft data were of the best quality among the measurements collected from redundant probe systems designed by different manufacturers. A description of the primary tools used in the aircraft–radar comparisons follows.

### 2.5.1 Aircraft Location in Radar Field

A capability to display the Convair-580 position onto underlying NEXRAD level-3 product data in PPI format was developed for the purpose of determining how often the aircraft intercepted certain identifiable features within the radar data (such as the ML) and positive ZDR enhancements (bright bands) associated with the dendritic and needle ice crystal growth zones) with estimates of the cloud phase type encountered. The tool produces a nine-panel PPI plot configured to show radar data from the elevation angle and volume matched closest in time and space to the aircraft location. Adjacent elevation angles and radar volumes are also displayed to reveal the depth and evolution of any radar feature observed.

Figure 8 shows an example of an aircraft-radar comparison on 10 January 2017 for the Convair-580 observation at 15:30:40 UTC. Each sub-panel shows a PPI plot of the ZDR product from the KBUF NEXRAD zoomed to 50 km<sup>2</sup> and centered on the aircraft position. The center plot (outlined with red axes) shows the aircraft position spatially and temporally matched to the nearest radar elevation angle (8.0° in this case) and volume time (15:25:12 UTC) based on the derived azimuth angle time. The bottom and top

row plots represent the adjacent elevation angles below ( $6.4^\circ$ ) and above ( $10.0^\circ$ ) the elevation angle shown in the center row plots, respectively. Likewise, the left and right columns of plots show the previous (15:20:12 UTC) and subsequent (15:29:53 UTC) radar volumes relative to the volume time shown in the center column plots.

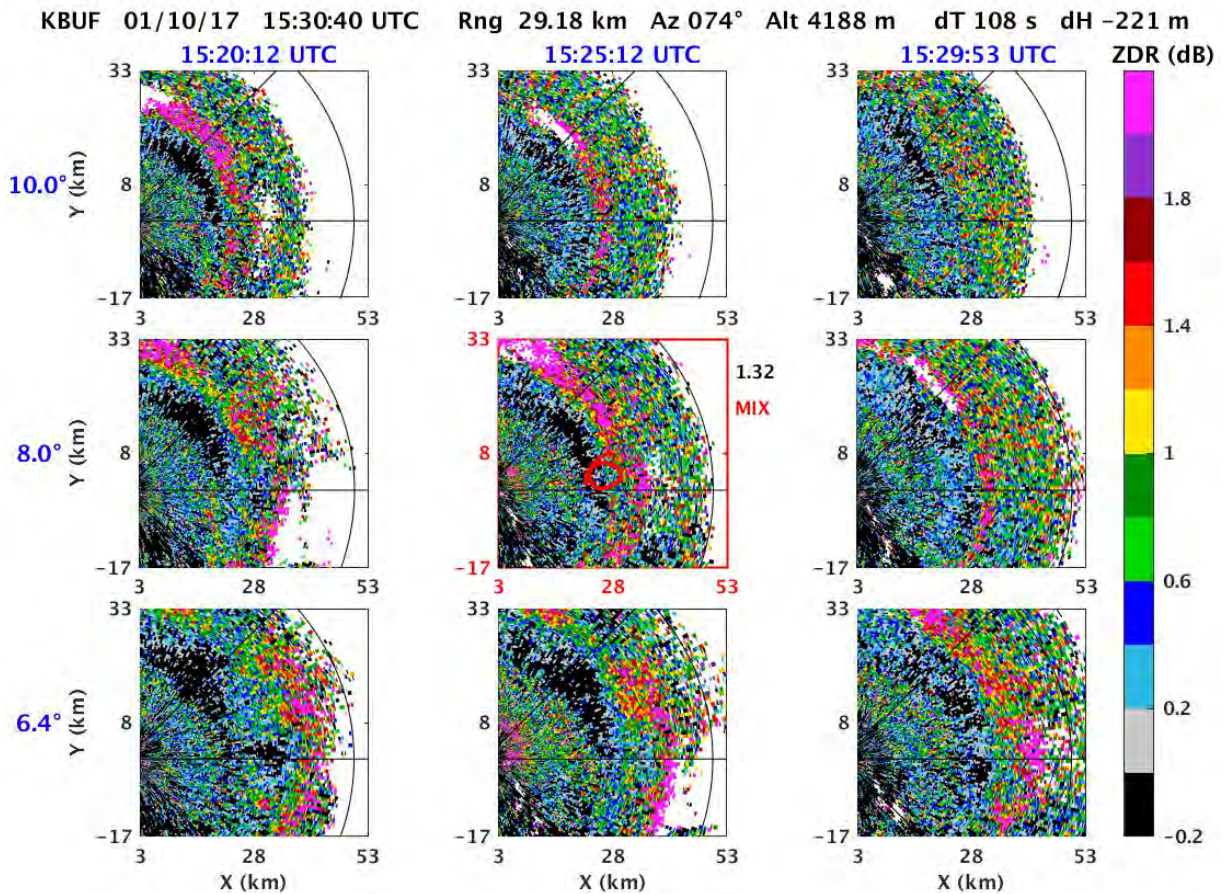


Figure 8. Nine-panel PPI plot of ZDR with the center plot matched nearest in time (volume time 15:25:12 UTC) and space (elevation angle  $8.0^\circ$ ) to the Convair-580 position at 15:30:40 UTC on 10 January 2017. The row (column) of plots show adjacent elevation angles (volume times) increasing from bottom to top (left to right), respectively. A five-minute history of the flight path color-coded according to the estimated cloud phase encountered is shown as red (mixed) in the center image with the northern most point representing the current location. The phase category at this location is also indicated to the right of the image along with the mean ZDR value computed among the valid data points within the physical-sized window matched and centered at this location.

An overlay of the flight path over the previous five minutes is shown in the center plot with the northern-most point denoting the current aircraft position at 15:30:40 UTC. The path is color-coded based on the cloud phase type estimated from the cloud phase algorithm (described in Section 4.1) and is shown as red indicating a sustained period of mixed phase conditions at sub-freezing temperatures ( $-10^\circ\text{C}$ ). A positive ZDR bright band (+ZDR BB) oriented arc of values greater than 1.0 dB is readily visible in the radar data at this observation time. Within this 10-minute radar volume history, the ZDR feature is

pronounced early in the interval at the 10.0° elevation angle (top left, top center) and evolves to an increasing signature later in the interval at the lower 6.4° angle (bottom center, bottom right). Mixed phase is widespread just beneath the feature (closer in range) and in a region of lower ZDR values (center sandwich zone).

### **2.5.2 Multi-Parameter Time Series**

Comparisons between the onboard microphysical measurements, airborne radar data, and ground-based NEXRAD product data were made possible with a utility that displays the data in a time series format over user-selected time intervals. The data format helps to quickly identify noteworthy intervals in which a more thorough analysis of additional sensor information could be studied. Generally, 10-minute time series plots were the preferred interval over which much of the analyses were performed and plots were generated for each radar operating in the BAIRS II domain.

An example of a six-panel five-second time series plot for the interval 03:30-03:40 UTC on 24 January 2017 is shown in Figure 9. The NEXRAD product data shown are from the KBGM radar. The top two panels show the particle type frequency distributions of Spheres (burnt red), Needles (cyan), Dendrites (blue), and Irregulars (gold) derived from the 2D-C and PIP optical array probes (OAP) and determined by the SNDI algorithm (Korolev and Sussman [41]). At the top of the 2D-C SNDI plot, the line of color-coded squares represents the cloud phase type of each observation time estimated from an assessment of multiple probes. The color of the phase type categories listed above the line relate to the color-coded squares.

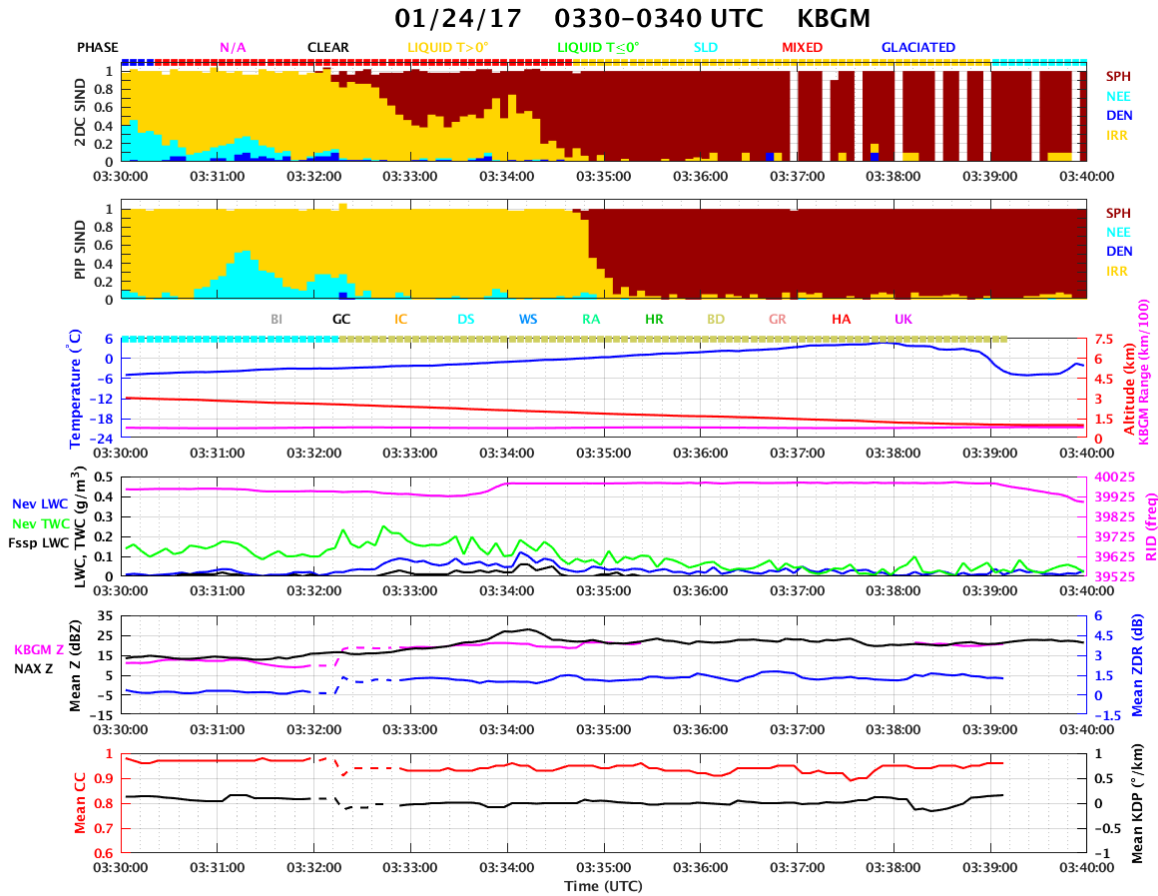


Figure 9. Six-panel time series plots of five-second averaged in situ measurements collected by the Convair-580 and mean radar product data for the 10-minute interval 03:30–03:40 UTC on 24 January 2017. The plots show particle-type frequency distributions of Spheres, Needles, Dendrites, and Irregulars (SNDI) derived from the 2D-C (first plot) and PIP (second plot) OAP imagery. The color-coded squares at the top of the 2D-C plot denote estimates of the cloud phase type encountered. The third plot shows in situ temperature (blue), aircraft altitude (red), slant range distance of aircraft from KBGM radar (magenta), and mode of KBGM HCA detected class at top of panel. Nevzorov LWC (blue), Nevzorov TWC (green), FSSP LWC (black) and RID frequencies (magenta) are shown in the fourth plot. The fifth and sixth plots show the aircraft X-band mean reflectivity (black) and mean KBGM reflectivity (magenta), ZDR (blue), CC (red), and KDP (black). The mean and mode KBGM products were computed among all valid values within the physical-sized window associated with and centered on the aircraft position.

The third subplot shows the in situ temperature measurements (blue, left axis), altitude (red, right axis), and the KBGM slant range distance of the aircraft scaled by 100 (magenta, right axis). The color-coded squares at the top of this plot denote the mode of the NEXRAD HC among all classifications within the physical-sized window associated with and centered on the aircraft position. Abbreviations of the class categories (with assigned color designations) are listed above the line and include “Biological” (BI), “Ground Clutter” (GC), “Ice Crystals” (IC), “Dry Snow” (DS), “Wet Snow” (WS), “Rain” (RA), “Heavy Rain” (HR), “Big Drops” (BD), “Graupel” (GR), “Hail-rain” mix (HA), and “Unknown” (UK).

In the fourth subplot, measurements collected from the Nevzorov LWC, Nevzorov TWC, and FSSP LWC probes are shown as blue, green, and black lines, respectively. Frequencies measured by the RID oscillation probe are shown in magenta.

The last two plots in the figure contain mean radar product values. The black line in the fifth plot shows the mean  $Z$  measured with the onboard horizontally pointed X-band radar 450 m away from the aircraft and is provided to compare with the mean horizontal-channel  $Z$  values from the S-band KBGM NEXRAD (magenta). The KBGM mean value line plots for  $Z$  and the other dual polarimetric products were computed among the values within the physical-sized window associated with the aircraft position. Mean (rectified) ZDR (blue, right axis) is shown in the fifth plot, with CC (red, left axis) and KDP (black, right axis) shown in the sixth plot. The solid (dashed) lines of the mean NEXRAD values indicate the difference between the Convair-580 observation time and the NEXRAD azimuth angle time was less (more) than 120 seconds.

### 2.5.3 Feature Analysis Tool

An analysis tool was developed that allows the user to identify and demarcate regions of interest observed among two NEXRAD radar products. The tool was used primarily to isolate reflectivity and enhanced ZDR features associated with the growth zones for dendrite and needle crystals, radar evidence that bounds the crystal sandwich structure (described in Section 4.2). A scatterplot comparison among the product values within each zone is generated. Figure 10 shows an example of the utility output for the non-BAIRS II crystal sandwich case observed at the  $9.9^\circ$  elevation angle from the KBOX (Norwood, MA) NEXRAD at 08:01:25 UTC on 9 December 2017.

The upper-left, upper-right, and lower-left panels contain PPI images of the  $Z$ , (not rectified) ZDR, and the one-hour temperature forecast from the rapid refresh (RAP) numerical weather prediction (NWP) model valid at the radar volume time and interpolated to polar format, respectively. The black and red sector overlays northwest of the radar highlight a local angular diminishment in  $Z$  and enhancement in ZDR associated with the respective dendrite and needle ZDR bright bands. Modeled temperatures within these sectors are in the range of  $-10^\circ$  to  $-16^\circ\text{C}$  and  $-6^\circ$  to  $-8^\circ\text{C}$ , respectively. The green sector overlay southwest of the radar is located in an altitude and temperature layer adjacent to the needle feature denoted in the red sector but with contrasting response in  $Z$  (enhancement) and ZDR (diminishment). This area is referred to as the needle “background” region and is presumed to be a zone in which ice crystal aggregates dominate and overwhelm the needle crystal growth signature. The lower-right panel contains a scatterplot of all reflectivity and ZDR values within all three sectors.

KBOX 12/09/17 08:01:25 UTC EI 9.9°

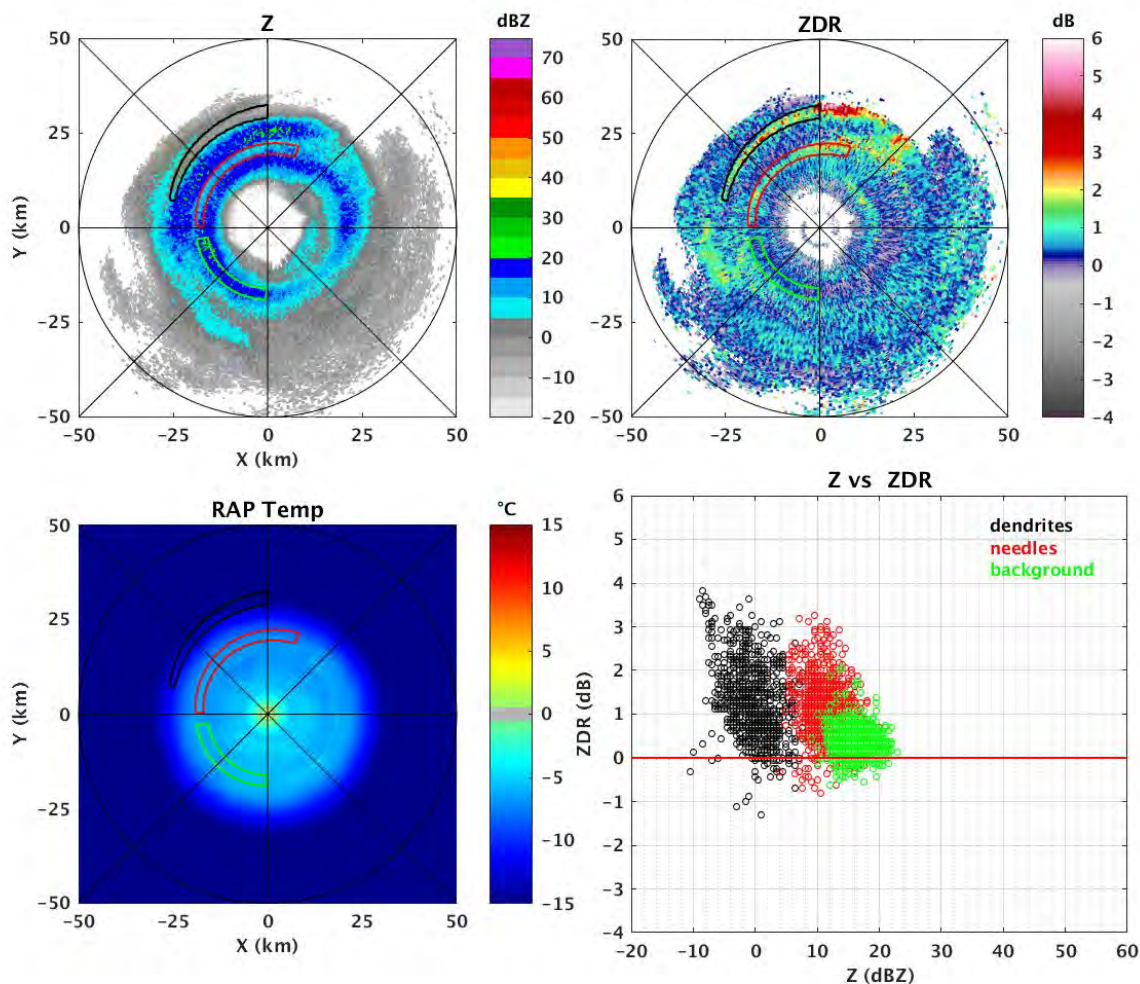


Figure 10. Illustration of a four-panel plot generated from a utility used to analyze features observed between two NEXRAD products. PPI images of Z (upper left), ZDR (upper right), one-hour RAP model temperature forecast (lower left), and scatterplot of Z and ZDR values (lower right) within the three highlighted arc sectors are shown for the KBOX 9.9° elevation angle at 08:01:25 UTC on 9 December 2017. Ice crystal growth regions of dendrites and needles and an adjacent region void of a needle signature are identified by the user and shown on the PPI images as a black, red, and green arc sector, respectively.

#### 2.5.4 Aircraft Proximity to NEXRAD

Analysis aides were developed to quickly identify the proximity of the Convair-580 aircraft relative to each NEXRAD within the BAIRS II domain and the optimum time intervals over which comparisons were performed. Figure 11 provides an illustration of such an aide showing three line plots of the slant range distance of the aircraft position from the KBUF (blue), KBGM (green), and KTYX (red) radars for the mission interval 02:30-0:700 UTC on 24 January 2017. During this flight, the aircraft probed in regions

predominantly closer to the KBGM and KTYX radars (02:45–04:45 UTC) with a shorter interval closer to KBUF late in the mission (04:54–06:06 UTC). Comparisons made for distances exceeding 150 km from the radar become less meaningful due to radar beam broadening and increased pulse resolution volume size. The figure also provides notable intervals in which the aircraft performed spiral ascents or descents (gray vertical shadings), aircraft altitude (dashed line), and color-coded temperature measurements (circles) shown along the altitude curve at three-minute intervals. Spiral maneuvers and circular flight patterns are also noted by the short-amplitude, high-frequency changes in slant range distance. The temperature observations along the altitude line clearly shows the aircraft encountered a refreezing layer (blue circles) below the ML (green circles) during the spiral descent at 03:39 UTC and remained within the layer for approximately 14 minutes.

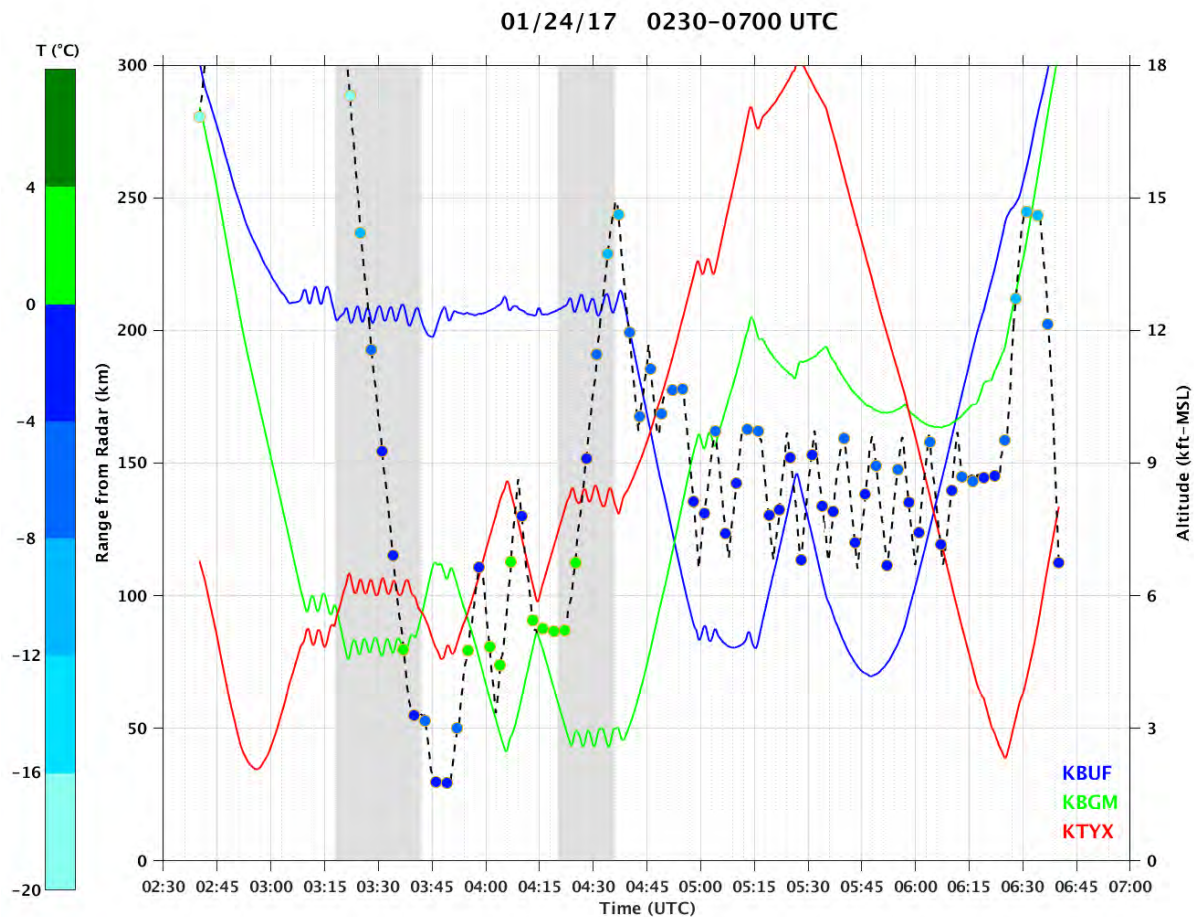


Figure 11. Multi-parameter plot of the slant range distance of the Convair-580 position from the KBUF (blue), KBGM (green), and KTYX (red) NEXRADs, the aircraft altitude (dashed line), and in situ temperature (color-coded circles) at three-minute intervals for the 24 January 2017 flight between 02:30–07:00 UTC. The vertical gray shaded columns denote time intervals when the aircraft performed a spiral maneuver descent and ascent.

### 2.5.5 Concatenated Hydrometeor Spectra

A significant post-processing effort was performed by ECCC to generate concatenated particle size distributions from the best performing OAP and the FSSP probe for each of the five flights. Three probes each having specific responses to cloud and precipitation particles over distinct size distribution ranges were selected to create the full spectra of number concentration values. The number concentration (in units of number per liter per micron) of each size spectral bin, the MVD, and in situ temperature were combined to help characterize the particles, identify the type of icing hazard encountered, and to compare and contrast the environmental conditions observed during the flights.

Figure 12 shows the concatenated hydrometeor spectra over the entire flight on 10 January 2017 for the interval 14:00–18:00 UTC. The number concentrations of particles shown were derived from the FSSP over the size range 3.5–45.5  $\mu\text{m}$ , the 2D-C probe over the size range 50–1000  $\mu\text{m}$ , and the PIP over the size range 1000–12800  $\mu\text{m}$ . Timelines of MVD for each of the respective probes are shown in black, green, and red. Five-second averages of the in situ temperature are shown in blue (right scale) at the bottom of the figure with a dashed blue line added to indicate 0°C. The dashed black line at 25  $\mu\text{m}$  signifies the threshold diameter for runaway coalescence leading toward formation of drizzle from smaller cloud droplets. Given the absence of high ice particle size concentrations, the intervals showing maximum concentrations in excess of 1000/L/ $\mu\text{m}$  (orange shading), associated MVDs near or less than 25  $\mu\text{m}$ , and maxima measured by the Nevzorov LWC probe (not shown) are indicative of an icing hazard in cloud droplet form.

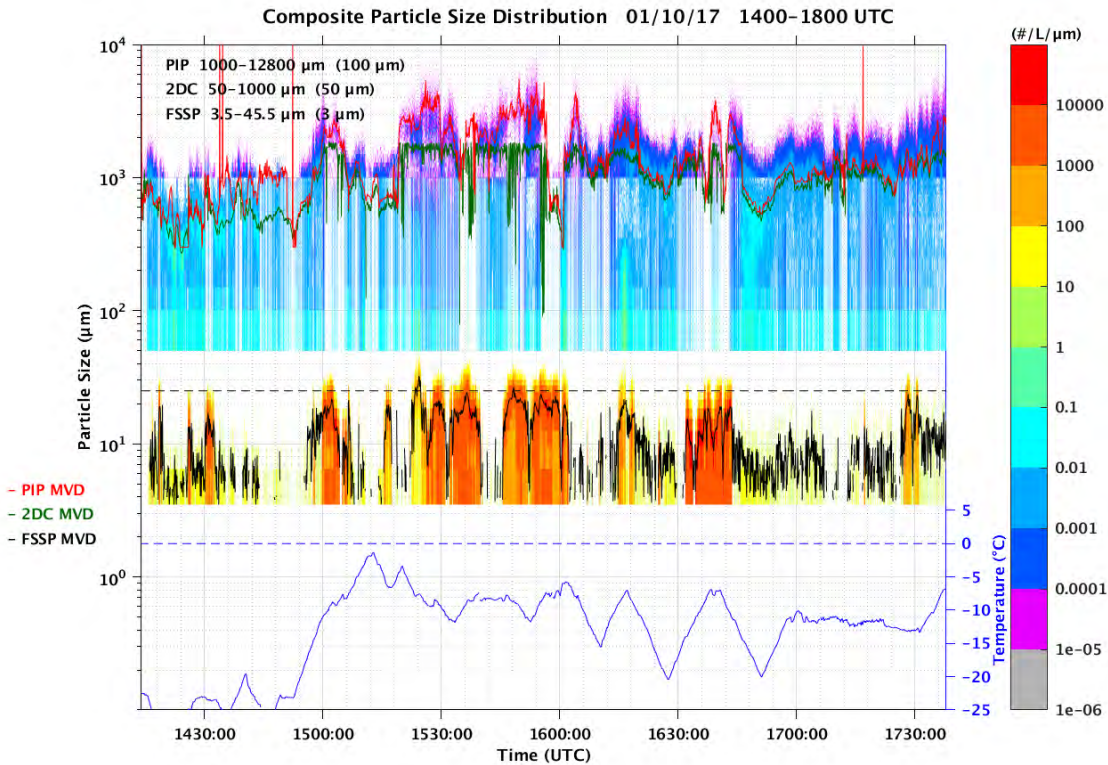


Figure 12. Distributions of concatenated hydrometeor spectra showing particle concentrations derived from the FSSP, 2D-C, and PIP probes on 10 January 2017 for the interval 14:00–18:00 UTC. Timelines of MVD from each probe are shown in black (FSSP), green (2D-C), and red (PIP). Five-second averages of the in situ temperature are shown in blue.

### 2.5.6 Numerical Weather Prediction Model Profile

A utility was developed to extract and generate RAP NWP model cross-section forecast profiles of temperature and relative humidity matched nearest in time and space to the Convair-580 flight path during the BAIRS II missions. These useful plots provide an assessment of the modeled full thermodynamic and moisture environment along and adjacent to the flight trajectory. The location of the short-term model temperature one-hour forecasts of the 0°C isotherm(s) compared remarkably well with the in situ measurements collected during the aircraft descents and ascents through this level. An example of the NWP model profile timeline for the entire flight on 24 January 2017 is shown in Figure 13. The top and bottom cross-section plots show one-hour forecasts of the model temperature and relative humidity vs. height, respectively. A trace of the Convair-580 altitude path is shown in magenta. The figure reveals that the aircraft flew through a moisture-rich layer throughout much of the mission, then performed a spiral descent (03:20–03:50 UTC) through the ML and into a near-surface sub-freezing layer. Thereafter, the aircraft spent a significant portion of time flying in a porpoising pattern a short distance above the ML in a temperature layer between 0° and -4°C.

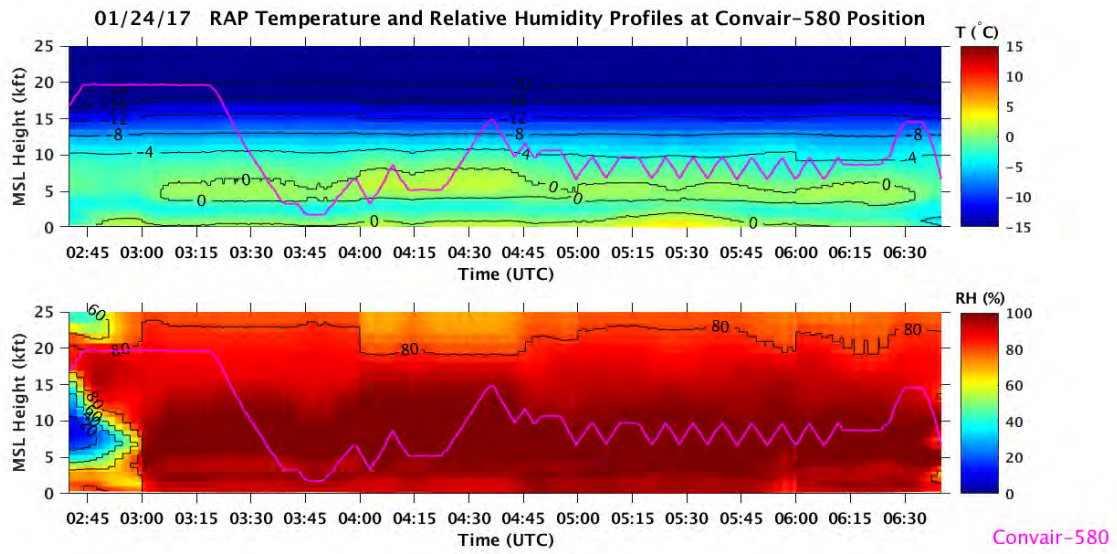


Figure 13. One-hour RAP NWP model profile forecast of temperature (top) and relative humidity (bottom) for the model bins associated with the Convair-580 aircraft position on 24 January 2017 between 02:35–06:40 UTC. The magenta line shows the altitude of the aircraft along the flight track.

### 3. FLIGHT DESCRIPTIONS

#### 3.1 OVERVIEW OF FIVE FLIGHTS

Similar to the BAIRS I field campaign, the base of research operations for BAIRS II was conducted at Ottawa International Airport in Ottawa, Canada. The duration of the operational period spanned nearly three months, from 10 January to 31 March 2017; however, the NRC Convair-580 aircraft was not available for operations for two and a half weeks interspersed throughout the period due to other previously scheduled research commitments. Five flights were conducted on the dates: 10 January, 24 January, 7 February, 24 March, and 25 March 2017, totaling just over 21 flight hours including time to account for transit to and from the air space in the vicinity of the KBUF radar in Buffalo, NY.

Starting in late December 2016, staff meteorologists at MIT LL were responsible for monitoring various short- and long-term NWP models on a daily basis to identify opportunistic winter weather synoptic events that were expected to propagate through the western and central regions of New York state. Weather forecasts were assembled and briefed daily to the NRC, ECCC, and MIT LL project participants and prospective inflight mission periods were identified. Using the work of Bernstein *et al.* [5] as a guide, in which associations are made between the incidence and location of pilot reports (PIREP) of icing relative to synoptic scale features (low, occluded low, warm front, cold front, occluded front, arctic front), the targeting strategy focused on identifying events in which the KBUF radar scanning domain would be in an optimal location for encountering regions of the synoptic system most conducive of a high icing potential. Additionally, upstream presentation of the winter system in NEXRAD radars was accessed at times to assess the potential for radar features of interest when the system advected to the Buffalo mission area.

Preflight and inflight procedures were also briefed by MIT LL staff the day of and during each mission. While in flight, communication between MIT LL personnel on the ground and onboard scientists, technicians, and pilots was conducted with a system developed by Atmosphere called the Plane Network for Weather Data Exchange (PLANET). The reliability and functionality of this system was much improved over the communication system used during BAIRS I. Figure 14 shows an illustration of the PLANET display utility used on 25 March 2017 at 13:56 UTC. The utility provides a geo-referenced pictorial of the flight mission in progress with the flight track overlaid onto NEXRAD or Canadian base reflectivity radar data and a five-channel chat dialog box containing a log of the communication among ground and airborne participants. The PLANET system also contains a valuable geomarker tool box that, when coupled with an overlay of the waypoint locations, allowed proposed flight segments to be highlighted and regions to be denoted where the MIT LL staff wanted the aircraft to collect in situ measurements based on live radar feature presentations and trends. Both BAIRS I and II are unique in that the dual polarization radar features from the NEXRAD network were the primary determinant in specifying the flight tracks during the live missions.

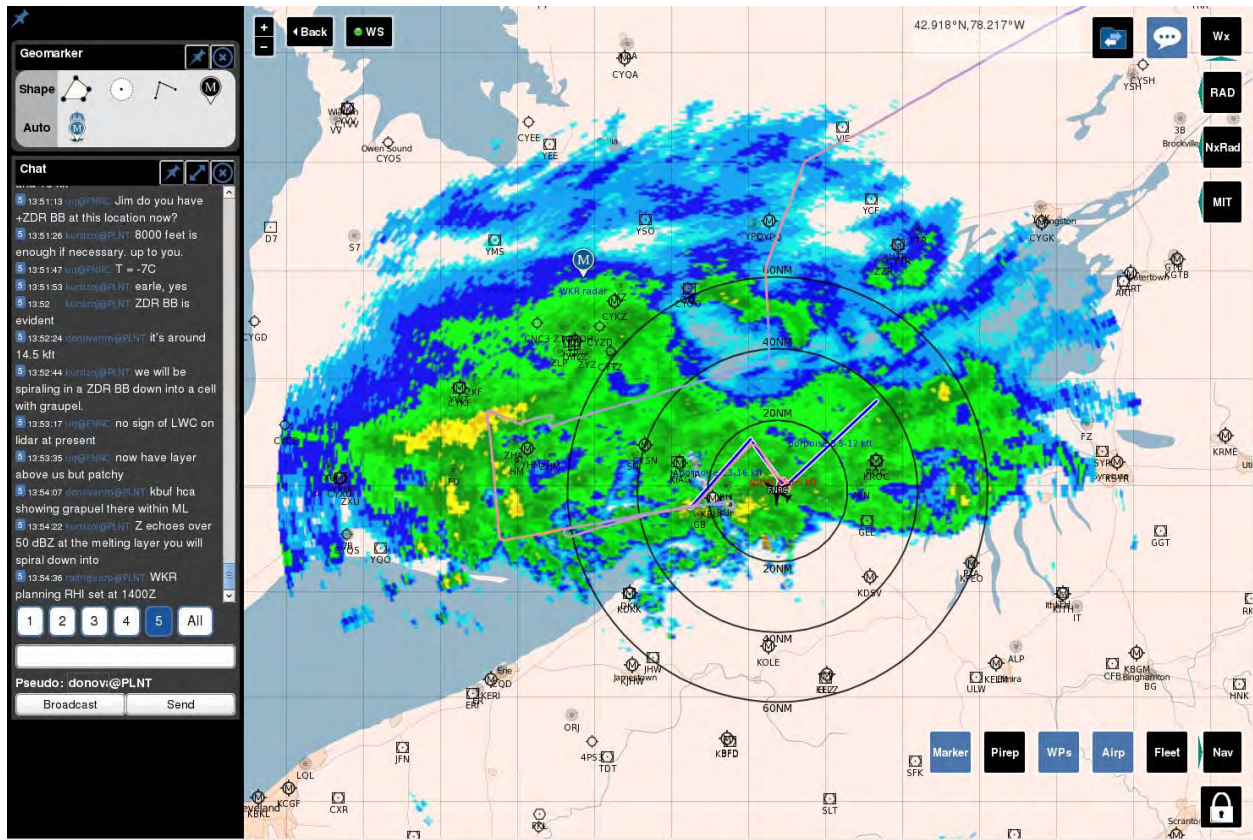


Figure 14. Illustration of the display utility used during the BAIRS II campaign providing real-time data and communication from the PLANET Iridium system. A chat log is shown on the left detailing conversations among airborne and on-the-ground participants. The icons on the right-hand-side allow various overlays to be displayed such as navigational aids and local ground-based radar reflectivity. The geomarker box in the upper left was used by MIT LL staff to propose locations for Convair-580 flight transects. Radar reflectivity is shown with the aircraft located just north of the KBUF NEXRAD on 25 March 2017 at 13:56 UTC.

The overall weather pattern during the operational period in winter 2017 was relatively consistent in that weak to moderate surface synoptic systems moved onshore from the Pacific Ocean into the western United States, propagated over the Rocky Mountains, reorganized in the western Plains states, and moved northeast through the western and central Great Lakes. A description of the synoptic scenarios and reasoning behind the flight tracks conducted by the Convair-580 for each of the five mission flights follows. A more detailed chronology along each flight track, with some highlighted observations, follows the depiction of each flight track.

### 3.2 10 JANUARY 2017, 13:22–17:45 UTC

#### Synoptic Context

A surface low-pressure system over southern Colorado moved east toward the western Plains states and later northeast toward the western Great Lakes. The storm track was influenced by the upper-level flow

(500 mb level) of the long-wave trough. A large surface high-pressure cell moved east toward the western Atlantic Ocean. A strong pressure gradient between the two systems set up a large warm air advection pattern through the central and eastern Great Lakes states extending eastward through New York. A surface analysis map valid on 10 January 2017 at 15:00 UTC, approximately the mid-point time of the flight mission, is shown in Figure 15. Within this figure and all subsequent surface analysis maps in this section, the large dashed arrow denotes the past and future trajectory of the surface low and the rectangle highlights the BAIRS II domain of interest encompassing the KBUF, KBGM, and KTYX NEXRADs. This synoptic scenario was chosen for a flight mission because the western New York region was expected to be situated within a cyclone sector well ahead (north) of an advancing warm frontal boundary, a region conducive to icing in the Bernstein scheme.

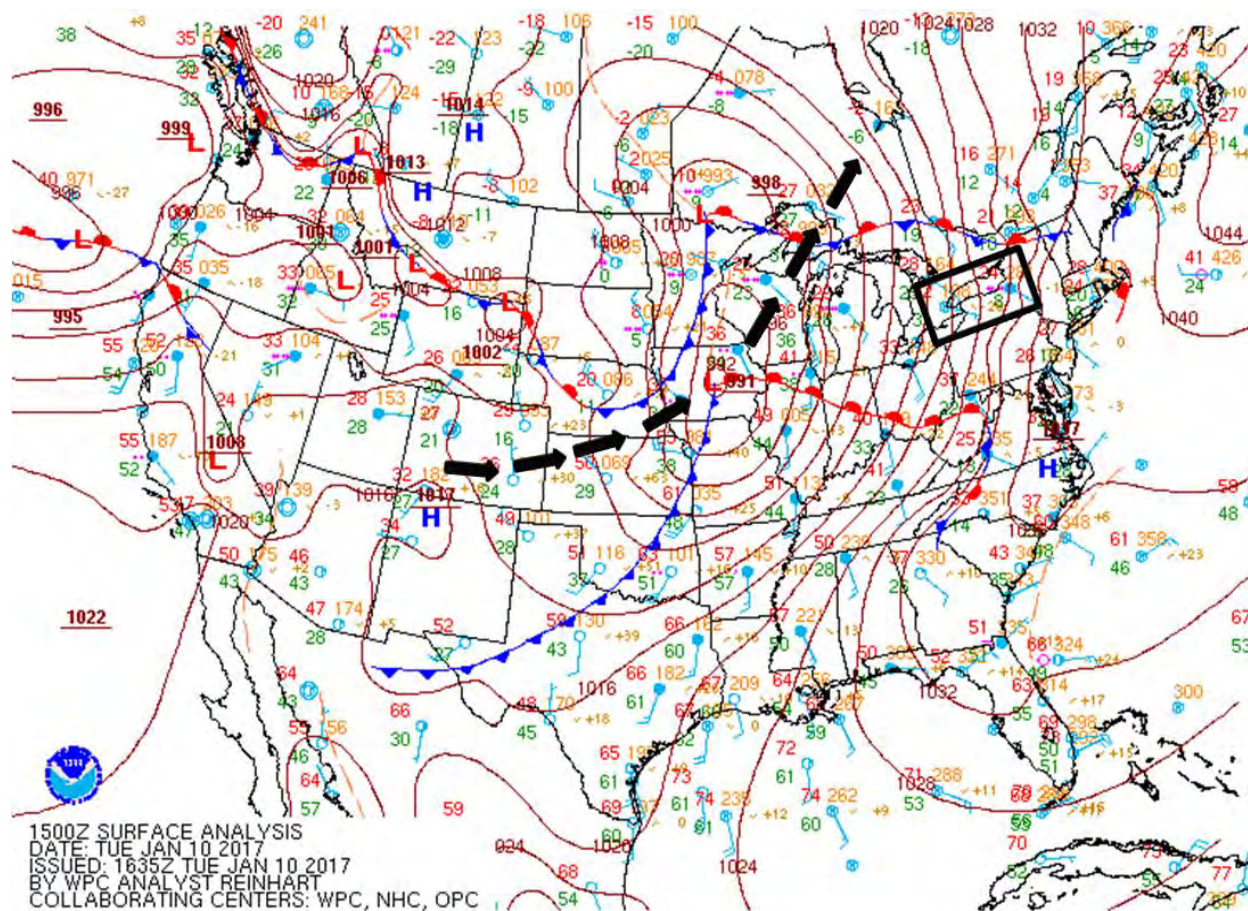


Figure 15. Surface analysis over the continental U.S. valid at 15:00 UTC on 10 January 2017. The large black arrows denote past and future projection of the surface low pressure center presently located over central Iowa. The black rectangle shows the region of interest where in situ measurements were taken during the BAIRS II campaign.

The NWP forecasts predicted a large swath of overrunning snowfall to advance northeast into the KBUF area by early morning and transition to rainfall with a warm frontal passage by early afternoon local time. Based on these projections, the initial strategy to conduct probing was to have the Convair-580

approach west of the KBUF radar near the Niagara River by mid-morning. The proposed strategy would capture in situ measurements in a zone ahead and parallel to the warm front. Figure 16 shows an overlay of the Convair-580 flight track over an underlying base map provided by the GR2Analyst radar display utility.

After executing the initial pre-planned proposal to spiral west of KBUF (shown as a small cluster of circles), the aircraft conducted several north-to-south porpoising transects within various flight layers in order to probe a similarly oriented region of precipitation with some embedded higher reflectivity elements that propagated eastward with time. Highlights of observations within the flight and in the context of Figure 16 are discussed below.

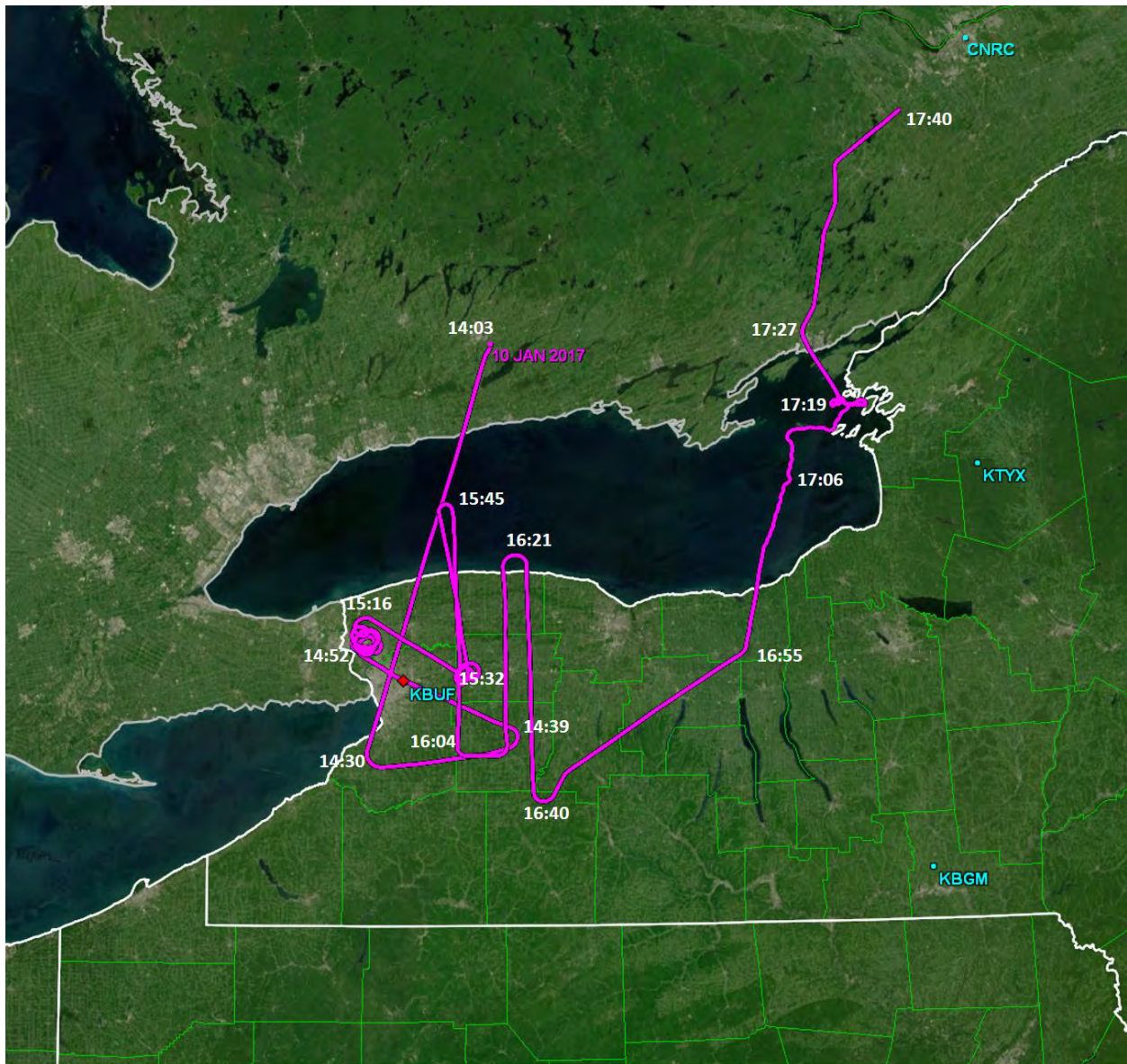


Figure 16. Flight track taken by the Convair-580 aircraft on 10 January 2017 between 13:22-17:45 UTC. The locations of the KBUF, KBGM, and KTYX NEXRADs are shown in cyan. The overlays and base map were displayed using the GR2Analyst radar display program developed by Gibson Ridge Software.

## Flight Summary/Overview

This first flight of the 2017 winter storm season, in the coldest atmosphere of all five flights, ran in daytime from 13:22 to 17:45 UTC. This flight also provided the longest near-continuous period of icing conditions, running from 15:22 to 15:40 UTC. Unlike the warmer cases later in the winter season (24 and 25 March) characterized by laterally extensive high Z melting layers, this day exhibited (on the basis of the onboard X-band radar) only intermittent bright bands near 1.8 km altitude and with modest maximum reflectivities (20–25 dBZ). The initial storm targets lay just east of Buffalo, NY, but an abrupt failure of the electrical power system on the Convair-580 en route from Ottawa prevented further communication between the aircraft and ground crews for the remainder of the flight. As a result, all decisions regarding flight transects, maneuvers, and flight altitudes were executed onboard.

While the aircraft was still en route and at higher altitude ( $T = -24^{\circ}$  to  $-29^{\circ}\text{C}$ ), some valuable observations of optical sun dogs were made at 14:23 and 14:29 UTC. Simultaneous observations of hexagonal flat-plate crystals (unrimed) in the CPI imagery (and with no ambiguity for a spherical shape in the SNDI algorithm), confirmed the contention that such crystals are essential for sun dog optics (Greenler [27]).

A nearly monotonic aircraft spiral descent was initiated at 14:52 UTC ( $T = -24^{\circ}\text{C}$ ) and completed at 15:12 UTC ( $T = -2^{\circ}\text{C}$ ) when the plane was below cloud base and Niagara Falls came into view from the aircraft window. This descent over a wide span of atmospheric temperatures, all in a confined space, provided one of the best documentations of the crystal sandwich during BAIRS II. A distinct layer of supercooled water (max LWC  $0.3\text{ g/m}^3$ ) was traversed between a dominance of dendritic crystals aloft ( $T = -13^{\circ}\text{C}$ ) and needle crystals at lower altitude ( $T = -4^{\circ}\text{C}$ ). The pilot reported “frosted slush” on the windscreen at 15:01 UTC ( $T = -11^{\circ}\text{C}$ ). Large numbers of supercooled droplets were noted in the CPI imagery at this time.

Concern was voiced in real time about the aircraft’s proximity to the KBUF radar’s “cone of silence”, but in the end, the scanning geometry was favorable to showing the aircraft context (see Section 4.2).

The sloped ascent from 15:13 to 15:33 UTC provided a return, second look at crystal sandwich structure (as detailed in Section 4.2 of this report), with needles prevalent at 15:14–15:15 UTC ( $T = -6^{\circ}\text{C}$ ) and dendrites gaining prominence ( $T = -11^{\circ}\text{C}$ ) at 15:31–15:33 UTC where supercooled water (thus, mixed phase) conditions were prevalent. Windscreen icing was reported by the pilot at 15:28 UTC, and a rough ride was noted in the same timeframe (15:30 UTC). By the end of this episode, the aircraft was heading north toward Lake Ontario, just northeast of the KBUF radar.

From 16:00 to 16:11 UTC the aircraft ascended along a straight-line track, heading north to the lake, finding first a rich population of needle crystals (and supercooled water) from 16:00 to 16:01 UTC, and then encountering dendrites (but without supercooled water; thus, glaciated) at  $T = -15^{\circ}\text{C}$ . The evidence for crystal sandwich structure is adequate enough, though less strong than if a spiral ascent at the same location were undertaken.

Following this maneuver, porpoising resumed (16:18 to 16:57 UTC) with larger temperature amplitude ( $T = -7.5^{\circ}$  to  $-21^{\circ}\text{C}$ ), slightly too cold to secure evidence for needles. Nevertheless, in the interval

16:32 to 16:44 UTC ( $T = -13^{\circ}$  to  $-7^{\circ}\text{C}$ ), supercooled water was evident and beneath a zone of prominent dendritic crystals (at  $T = -12^{\circ}\text{C}$ ) near the upper limit of the layer of supercooled water. This would be the center (prominent icing hazard region) of the crystal sandwich structure.

This portion of the flight took the aircraft back over the eastern end of Lake Erie, where it was then engaged for long series of roll maneuvers (while still over the lake water) to provide for calibration of the onboard W-band radar. Following the crossing of the lake, the aircraft returned to Ottawa.

### **3.3 24 JANUARY 2017, 02:30–06:52 UTC**

#### **Synoptic Context**

On 23 January, a large occluded surface low moved east across the northern Mississippi Valley states. The low was embedded within a progressive but slow-moving, high-amplitude, north-south oriented long wave trough also closed at 500 mb near western Virginia. The NWP models forecast the occluded system to remain occluded with hints of a new surface low development along the Mid-Atlantic coastline before moving northward up the East Coast. The 500 mb low was forecast to elongate slightly as the low slowly rotated north-northeast toward Pennsylvania (PA). The general synoptic scenario unfolded as predicted. However, the coastal surface low was slower to develop and move northward. This setup led to a deep surface-to-mid-level fetch of easterly winds off the Atlantic Ocean, resulting in a wide east–west oriented band of precipitation moving onshore from New Jersey to western PA that lifted slowly north with time. This movement of presumably clean oceanic air into the region of aircraft observations was later recognized to have a profound effect on a variety of cloud microphysical measurements for this flight.

Choosing the optimal departure time for the Convair-580 to intercept the precipitation band as it moved into central NY was challenging. Further complications arose when it became apparent the precipitation was going to be delayed advancing into western NY and near the KBUF radar due to the low-level dry air below 800 mb. This discussion of the evolving synoptic situation was shared by the ground control crew with the onboard crew with the restored, functional PLANET system. A synoptic surface analysis of the situation at 03:00 UTC (30 minutes after departure time) on 24 January 2017 is shown in Figure 17. The black arrows over southern Tennessee show the movement of the occluded low. The large black dot identifies the location of the new surface low along the North Carolina coastline and subsequent movement along the East Coast as it begins to occlude. A tight pressure gradient between the coastal low and strong high pressure over southeastern Canada helped to establish the onshore easterly fetch well inland. Light rain was predicted in central NY initially, but transitioned with time to mixed precipitation (sleet, snow, and freezing rain) due the development of a near surface sub-freezing layer caused by evaporational cooling as the precipitation intensity became heavier and advection of colder air being drawn down from southern Canada.

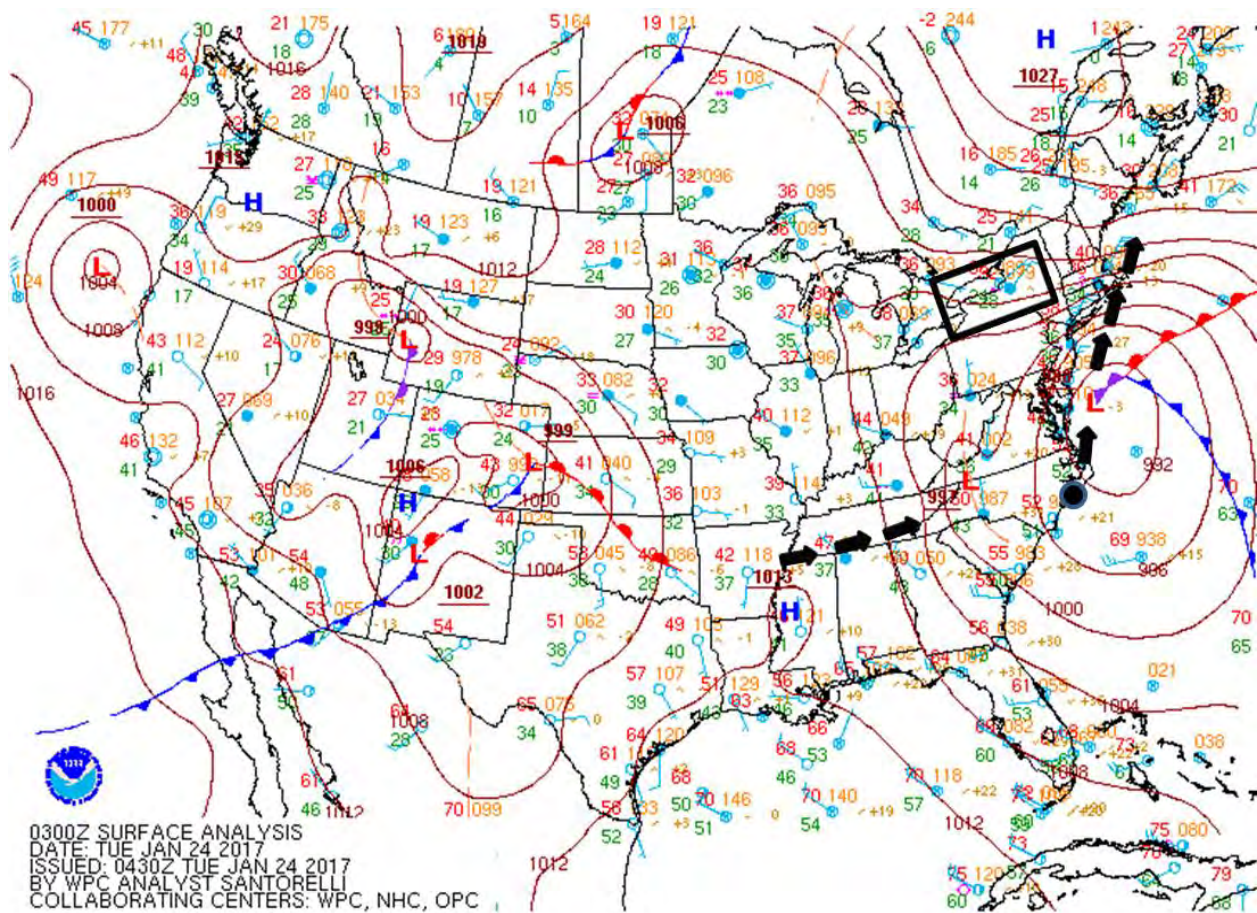


Figure 17. Surface analysis over the continental U.S. valid at 03:00 UTC on 24 January 2017. The large black arrows denote past and future projection of the surface low pressure centers in the eastern U.S. The black rectangle shows the region of interest where in situ measurements were taken during the BAIRS II campaign.

Figure 18 shows the flight path taken during this mission. The initial target was for the Convair-580 to transit out to the mid-point region between the KBUF and KBGM radars. However, given the slow advancement of moisture into the western half of the region, a decision was made shortly after departure to fly south near Syracuse, NY. Further details on observations over this flight track are discussed in the next section.

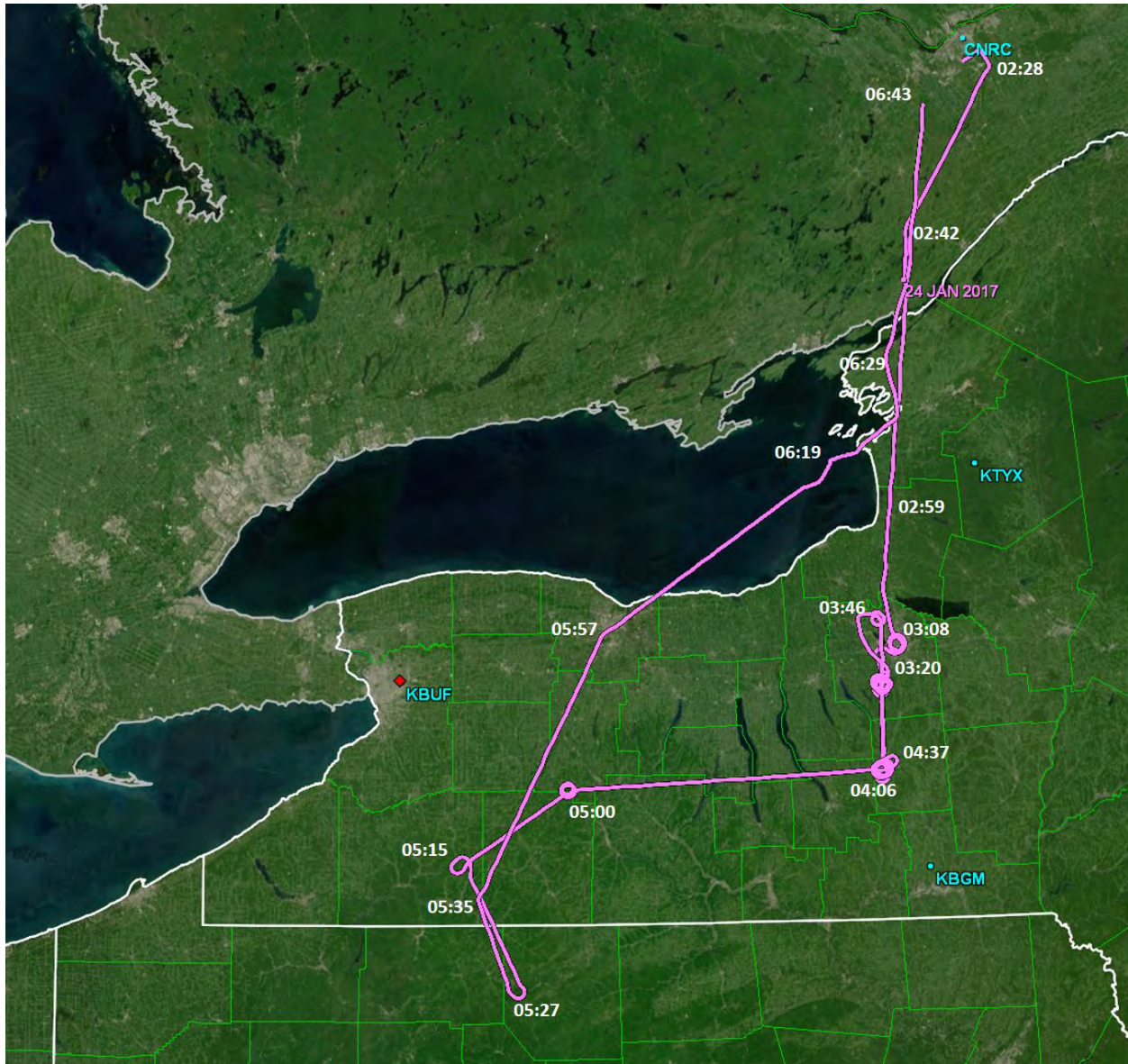


Figure 18. Flight track taken by the Convair-580 aircraft on 24 January 2017 between 02:30–06:52 UTC. The overlays and base map were displayed using the GR2Analyst radar display program developed by Gibson Ridge Software.

### Flight Summary/Overview

This evening and overnight flight ran from 02:30 to 06:52 UTC, and stands out uniquely among the five flights of BAIRS II because of the distinct maritime characteristics in aircraft observables, including larger-than-usual median volume droplet diameter, smaller-than-usual FSSP droplet concentration, and smaller-than-usual optical extinction, all of which are elaborated on in Section 4.4. These anomalous characteristics were remarked on during the debrief for this flight and were followed up strongly during the

analysis for this report. In general, the maritime characteristics for this flight support Bernstein's earlier suggestions that aerosol concentration may be the most important consideration for assessing aircraft icing hazard potential. As with the later flight on 25 March 2017, a nearly continuous bright band signature was evident in the onboard X-band reflectivity observations during the entire flight, though its typical Z level was substantially less than for the 25 March case in notably warmer atmospheric conditions.

The initial storm target was adjusted after takeoff from Ottawa to the Syracuse, NY area. En route ferrying at  $T = -23^{\circ}\text{C}$  (6.5 km altitude) showed an abundance of beautiful unrimed rosette crystals in the CPI imagery. The first appearance of the ML radar bright band (max reflectivity 28 dBZ) beneath the aircraft (03:00 UTC) coincided with the finding of some long chains of connected ice crystals in CPI imagery when the plane passed the eastern end of Lake Ontario headed due south for Syracuse.

A long spiral descent was initiated near 03:20 UTC a short distance south-southwest of Syracuse, with intention to traverse the ML. The X-band radar echo top at this time was near 8 km, and we expected to find dendritic crystals, but only irregular shapes were found in the temperature range expected for dendrites in a region largely devoid of supercooled water. At lower altitude during this spiral ( $-6^{\circ}$  to  $-3^{\circ}\text{C}$ ), a rich population of needle crystals was found in association with supercooled water above the radar bright band in the form of large cloud droplets up to 100  $\mu\text{m}$  in diameter. The  $0^{\circ}\text{C}$  isotherm was traversed at 03:35 UTC with a distinctly bumpier ride noted. Below this level, now realizing in a temperature inversion (or refreeze zone beneath the inversion top), supercooled raindrops were encountered after the aircraft leveled off around 1000 m altitude ( $T = -3^{\circ}\text{C}$ ) and remained beneath the bright band until 03:56 UTC. The ground lights of Syracuse were visible from 03:43 to 03:47 UTC, indicating that the aircraft was below cloud base in this interval. Requests to fly lower in altitude to search for a second  $0^{\circ}\text{C}$  crossing in the temperature profile were denied. It was quickly verified that the surface temperature in Syracuse beneath was  $0^{\circ}\text{C}$ . The Nevzorov probe was noted to be ineffectual in registering the supercooled cloud water in this large drop form. The pilots reported at 03:54 UTC that the "whole side window was frozen over" by virtue of the vigorous large drop icing in this time interval and captured by camera in Figure 19.



*Figure 19. Image showing the accumulation of supercooled raindrops frozen onto the side window of the Convair-580.*

Remarks were made by the MIT LL ground crew monitoring and improvising the flight track about the similarity of these pseudo-isothermal icing conditions to the tragic crash of Colgan Air Flight 3407 on 12 February 2009 near Buffalo, NY.

At the extreme southeast location of the flight track shown in Figure 18, the aircraft initiated a spiral ascent at 04:21 UTC up through the bright band near 0°C and on up to  $T = -11^{\circ}\text{C}$  (4.5 km). The reflectivity bright band beneath the aircraft (36–40 dBZ) was the strongest of the entire flight. Some needle crystals were encountered at  $T = -4^{\circ}\text{C}$  and some dendrites in low concentrations were noted at  $T = -11^{\circ}\text{C}$ , but the great majority of ice particles throughout the ascent were characterized as Irregulars based on the SNDI algorithm. So once again, just as during the spiral descent earlier in the flight, no substantial evidence for crystal sandwich structure was noted in this storm ingesting clean maritime air. Largely glaciated conditions were documented here above the ML with TWC values reaching  $0.4 \text{ g/m}^3$ .

The final porpoising strategy for this flight, implemented following the previous spiral ascent ending at 04:35 UTC and continuing until 06:15 UTC (more than half the entire flight), involved a small

temperature amplitude ( $T = -1^{\circ}$  to  $-5^{\circ}\text{C}$ ) in close proximity above the bright band that was above the refreeze layer at the lower altitude limit. This strategy remained in effect through all the remaining straight line segments of the flight track in Figure 18, including the straight leg heading northeast across Lake Ontario. A weak radar bright band (generally in the Z range 20–30 dBZ) beneath this porpoise track was evident throughout this long period. The evidence for icing conditions in the chat log was mixed for this long period, ranging from “persistent drizzle conditions” to “juiciest conditions thus far” to “out of mixed phase”. The Nevzorov probe may not have been responsive to the large cloud droplets that contributed much to the supercooled water content.

During several of the aircraft descents (downward legs of the porpoising) toward the radar bright band during this period, cloud droplets were detected in the CPI imagery that exceeded the diameter for runaway coalescence ( $D = 25 \mu\text{m}$ , Freud *et al.* [21]). The concatenated particle size spectra also showed the development of strong (yellow in color) “tails” (herein referred to as yellow tails) toward larger droplet sizes. This was taken as evidence for active coalescence in a layer of supercooled droplets just above the ML. (An alternative explanation for the origin of these supercooled droplets immediately above the ML has been proposed by Korolev *et al.* [45]). Examples of this behavior to be elaborated on in Section 4.4 were noted at 05:00, 05:07, 05:36, 05:44, 05:52, 06:00, and 06:07 UTC. An explosion of needle crystals occurred just prior to the 06:00 UTC bright band proximity, at 05:58 to 06:00 UTC when the supercooled water concentration surged to  $0.28 \text{ g/m}^3$ . However, for the majority of ascents into a temperature domain in which needle crystals would have been expected, only sparse populations were found and the ice particle population was largely dominated by irregular ice particles. Examples are 05:03 UTC, 05:11 to 05:16 UTC, 05:24, 05:40, 05:48, and 05:56 UTC. Evidence for supercooled droplets in CPI imagery was found in some of these periods, but not in others.

Beginning at 06:16 UTC when the aircraft remained over the eastern end of Lake Ontario, a long sequence of aircraft rolls was initiated, with the goal to calibrate the onboard W-band radar (Wolde *et al.* [93]). This calibration continued until 06:21 UTC. Following a final 15-minute period (06:21 to 06:36 UTC) when the aircraft was positioned over the radar bright band, and irregular ice particles were prevalent, the aircraft continued to the northeast to return to Ottawa.

### 3.4 7 FEBRUARY 2017, 16:05–19:20 UTC

#### Synoptic Context

The synoptic conditions expected in western and central NY on this date were very similar to those on 10 January. Figure 20 shows an analysis of the synoptic features at 18:00 UTC, two hours after the Convair-580 departed from Ottawa. A large, moderate-strength cyclone moved east into the Plains states before heading northeast toward the Great Lakes. The western NY region was again in a position to receive overrunning precipitation ahead of the warm front in a favorable zone for icing aloft. The main difference with this event was that the center of the surface low was forecast to pass much further east over southern Lake Huron and just west of the KBUF radar before continuing into southeast Canada. Model forecasts of the thermodynamic profile near KBUF one hour prior to departure indicated a near 0°C isothermal layer from the surface to 750 mb with a deep saturated layer from the surface to 200 mb. Shortly after departure, a 1-km thick warm nose layer was forecast to develop just above the surface. Mixed precipitation (primarily sleet) was forecast to transition to rain, but remain mixed for an extended period of time over and north of Lake Ontario due to the proximity of cold air associated with a high-pressure cell located northeast of Quebec City, Canada.

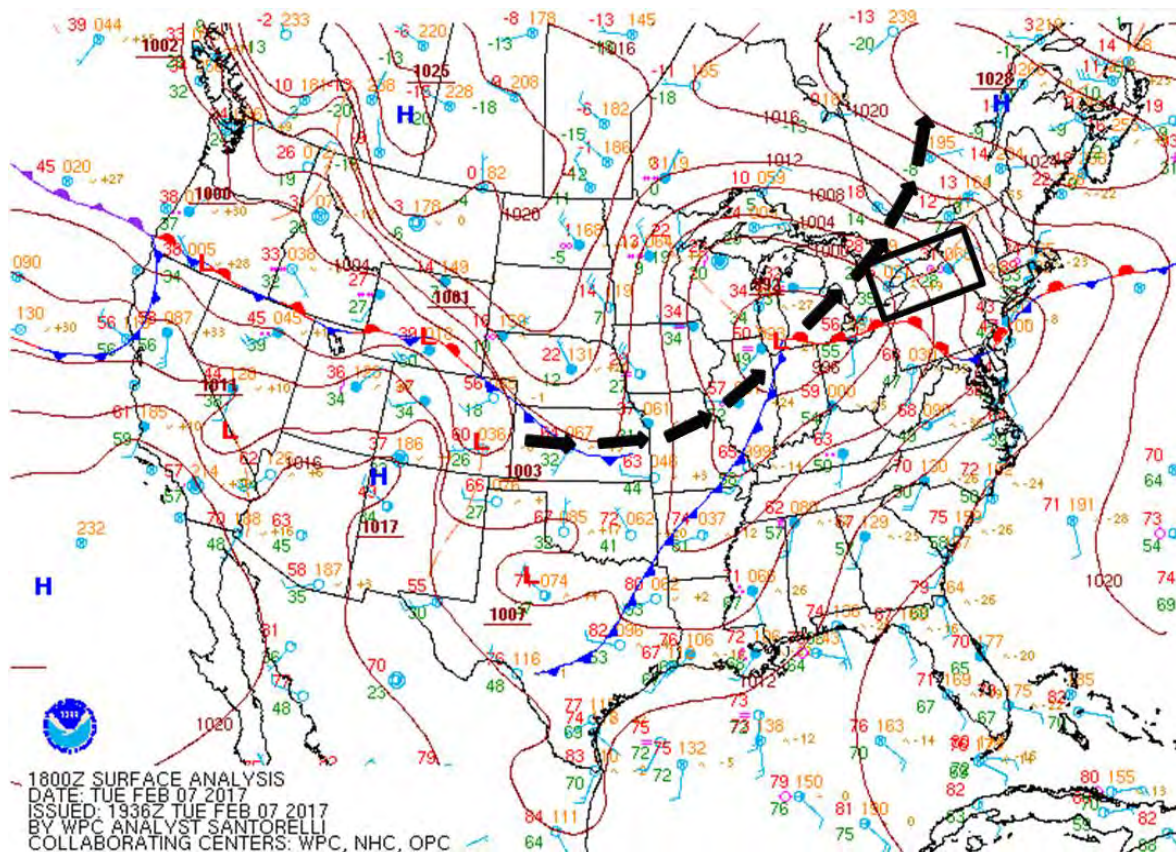


Figure 20. Surface analysis over the continental U.S. valid at 18:00 UTC on 7 February 2017. The large black arrows denote past and future projection of the surface low-pressure center presently located in southern Lake Michigan. The black rectangle shows the region of interest where in situ measurements were taken during the BAIRS II campaign.

The plan was to collect in situ measurements north and northwest of KBUF over Lake Ontario for several hours ahead of and prior to the anticipated passage of the warm front through the KBUF area by mid-afternoon. An illustration showing the flight track of the Convair-580 is shown in Figure 21. For the final hour of this flight (18:00 to 19:00 UTC), the aircraft porpoised through a 1500 m thick layer (over a temperature range between 0° to -12°C) primarily above the ML in a crisscross fashion to peruse the band of precipitation advancing north ahead of the active warm front and in a zone where the predominate hydrometeors were expected to be wet snow. Further details and observational highlights over the entire flight track are discussed in the next section.

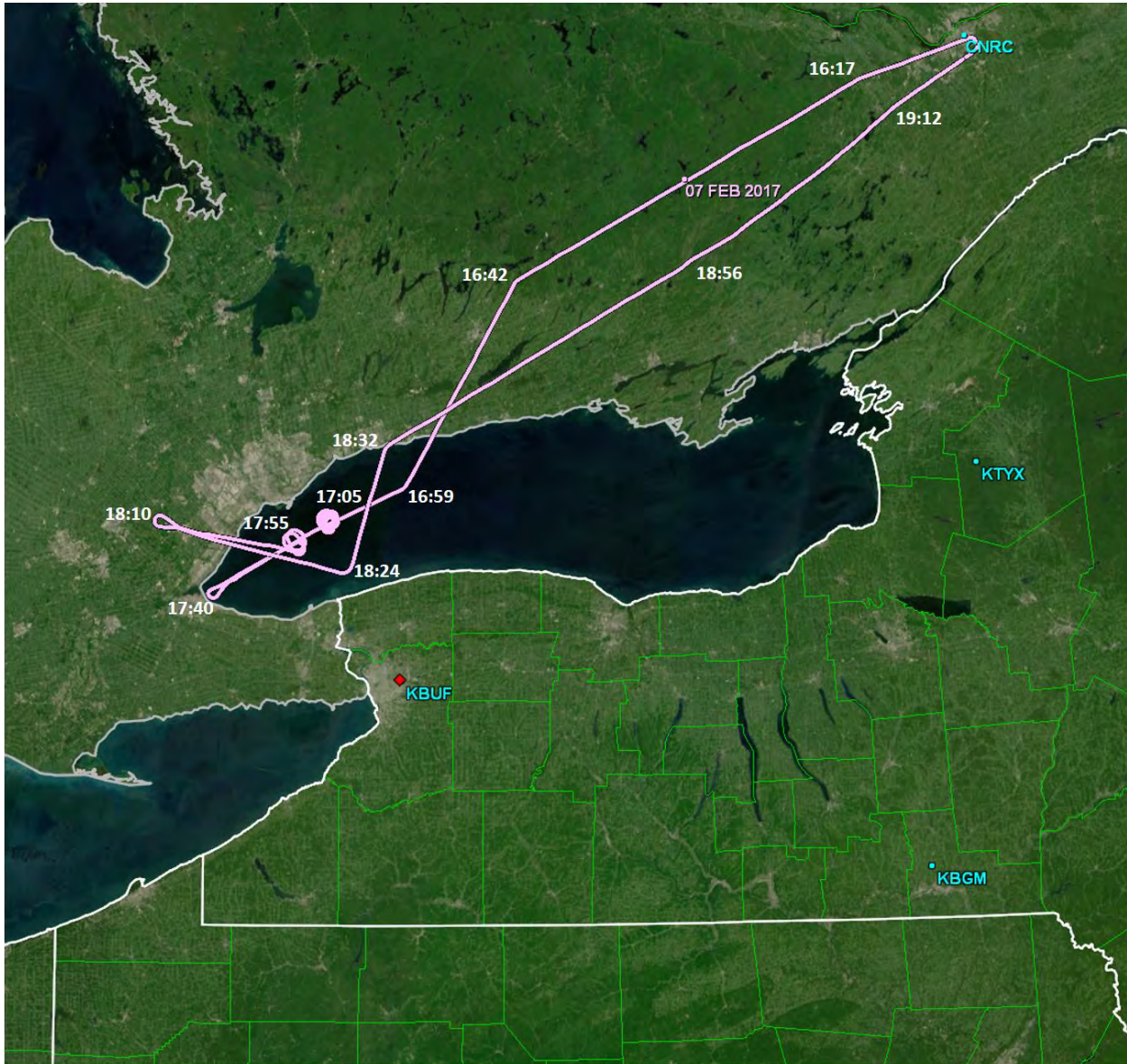


Figure 21. Flight track taken by the Convair-580 aircraft on 7 February 2017 between 16:05–19:20 UTC. The overlays and base map were displayed using the GR2Analyst radar display program developed by Gibson Ridge Software.

## Flight Summary/Overview

This daytime WERVEX-related flight ran from 16:05 to 19:20 UTC, the shortest mission in BAIRS II. Main targets for this flight were west-east lines of precipitation in the Toronto area and within range of the Canadian King City radar (just north of western Lake Ontario), whose team assisted in the coordination. The ferrying from Ottawa, aimed at Toronto, took place near 5.5 km altitude ( $T = -17^{\circ}$  to  $-20^{\circ}\text{C}$ ), in an elevated pre-warm front anvil cloud characterized by weak reflectivity levels (-5 to 5 dBZ). Rosette polycrystals with riming were common in the CPI imagery during this period.

The flight track (Figure 21) deviated southward toward Lake Ontario at 16:42 UTC, and after arrival over the lake, the first indication of a radar bright band was detected beneath the aircraft (2.3 km altitude), with the onboard X-band radar, when the cloud top altitude (smooth) was  $\sim 7$  km.

At 17:06 UTC, a spiral descent was initiated offshore near Toronto through a temperature range in which both dendrites and needles would have been expected. Neither crystal type was found in the hydrometeor observations during this descent. Instead, irregular shapes dominated the SNDI analysis until the  $0^{\circ}\text{C}$  isotherm was encountered at 17:19 UTC. The bright band was delicate ( $Z = 20$  dBZ) and thin. A layer of supercooled water (peak value  $0.45\text{ g/m}^3$ ) was found just above the ML with droplet sizes in the CPI imagery up to  $65\text{ }\mu\text{m}$ .

The aircraft then executed a porpoising maneuver up through the bright band to  $T = -6^{\circ}\text{C}$  near the western extremity of Lake Ontario, with weak indications of unrimed needle crystals (in a sea of more abundant irregular crystals) on porpoising ascent, and some rimed needles with indications of supercooled water on descent. On subsequent ascent back across the ML (22 dBZ) at 17:43 UTC, needle crystals were encountered at 17:45 UTC as the plane leveled off in a layer of supercooled water (17:48–17:54 UTC) with abundant drizzle and SLD (peak LWC value  $0.36\text{ g/m}^3$ ) and some droplet diameters  $300\text{--}400\text{ }\mu\text{m}$  at  $T = -8^{\circ}\text{C}$ . This region was characterized in the flight log as “juicy mixed phase”.

Aircraft descent from this mixed phase layer at 18:00 UTC initiated an irregular porpoising sequence for one additional hour (18:00–19:00 UTC). The porpoising continued along the straight line tracks as evident in Figure 21, well beyond the segments over the lake and especially along the long track north of the lake heading back to Ottawa, with five ascents alternating with four descents with a maximum temperature amplitude of  $0^{\circ}$  to  $-10^{\circ}\text{C}$ . The initial descent entered a rich layer of (mostly unrimed) needle crystals, the richest by far in this flight. The mean differential reflectivity on the KBUF radar ran positive during this needles episode, as expected, but was undramatic in magnitude with mean value of order  $+0.3$  dB. The in situ temperature limits for these needles were  $-7^{\circ}$  to  $-3^{\circ}\text{C}$ . The TWC values were high (max  $0.5\text{ g/m}^3$ ), but with some indication of weak supercooled water, though in amounts much reduced from the layer encountered earlier at somewhat higher altitude. All things considered, the evidence from the interval 17:58–18:10 UTC is suggestive of the lower portion of a crystal sandwich, but with only brief indication of dendritic crystals on top (at 17:59 UTC).

Though inadequate to span the temperature range expected for the full crystal sandwich, the remaining porpoising descents to near  $0^{\circ}\text{C}$  were examined for the presence of needle crystals and their association with supercooled water. Though the needle populations in the SNDI analysis were frequently dwarfed by irregular ice particles, the systematic pairing of needles/SLW was documented at 18:14–

18:19 UTC, 18:31–18:36 UTC, 18:42–18:49 UTC, and 18:53–18:59 UTC (with up to 244  $\mu\text{m}$  supercooled drops). In this initial needles sequence, an abundance of short columns was noted at lower temperatures in a layer that was likely above the needle region noted in the interval 18:14–18:19 UTC. The radar bright band beneath the aircraft was most conspicuous (up to 40 dBZ) for the entire flight in the interval 18:37–18:41 UTC, between two needle/SLW episodes in the porpoising sequence.

Following the final porpoising descent at 18:58 UTC, and with no reflectivity remaining in the X-band profile, the aircraft returned to Ottawa.

### **3.5 24 MARCH 2017, 09:33–14:15 UTC**

#### **Synoptic Context**

The prospects of a mission flight on this date hinged on the accuracy of the NWP models prediction of an overrunning precipitation event to develop and become enhanced over the Great Lakes region and within the clockwise flow behind a large, slow-moving high-pressure cell exiting the U.S. East Coast. The BAIRS II domain would again be in an advantageous location (north of a warm/stationary front) for potential icing aloft. The scenario eventually came to fruition but many challenges were encountered during the operation.

A surface analysis map of the synoptic features valid at 12:00 UTC (approximately midway into the mission) is shown in Figure 22. A large surface low over southern Colorado, with an associated stationary front extending northeast into Iowa, strengthened as it moved very slowly southeast and began to occlude beneath a slow-moving upper low closed at 500 mb. A weak low pressure center developed along the stationary front providing the mechanism for a warm frontal boundary to develop and extend east over the upper Midwest States. Influenced by an arctic high-pressure cell moving southeast out of Manitoba Province, and by the expansive high pressure along the East Coast, the low-pressure center over Iowa was expected to move east and weaken as it moved along the boundary that became stationary with time. A widespread precipitation band moved from west to east ahead of the low-pressure center and through the BAIRS II domain in early to mid-morning.

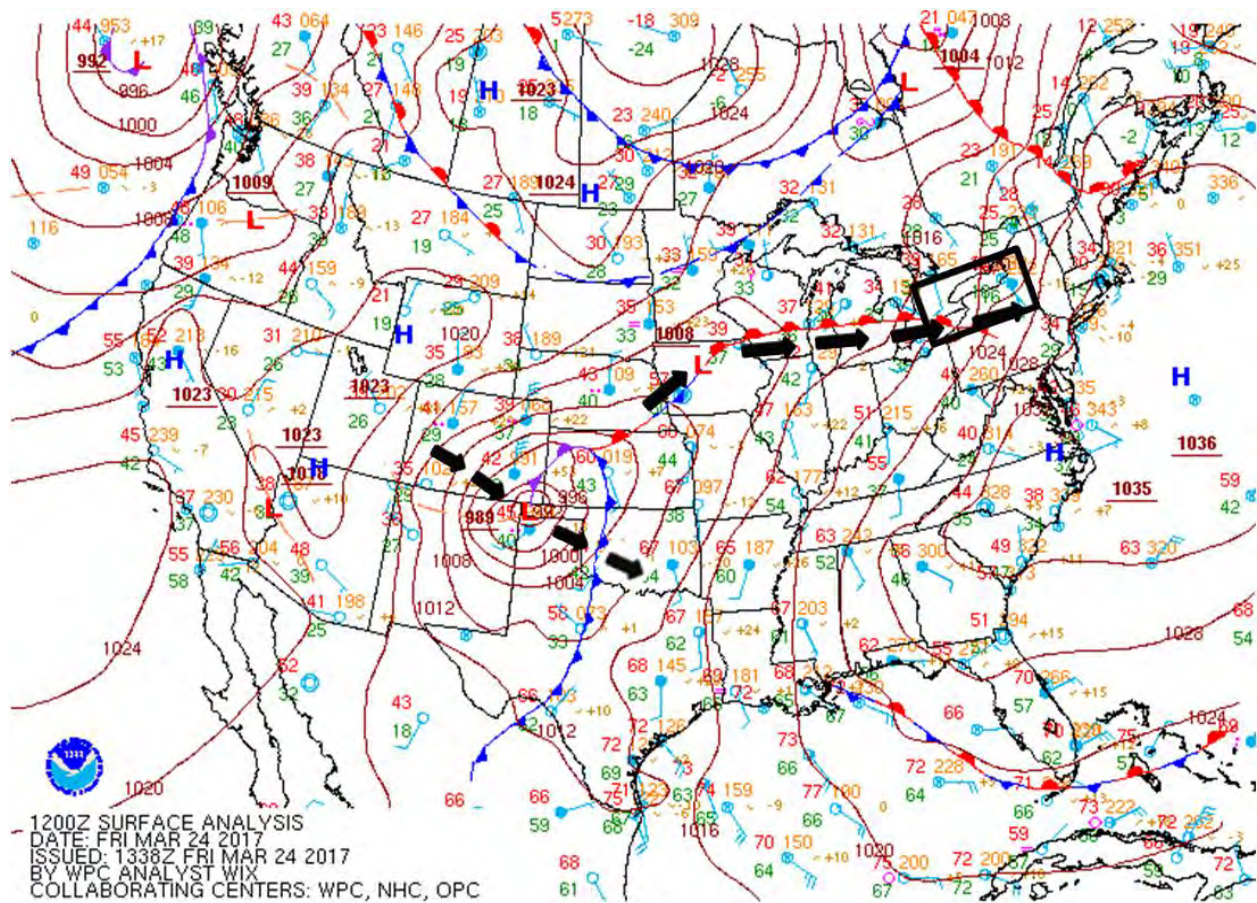


Figure 22. Surface analysis over the continental U.S. valid at 12:00 UTC on 24 March 2017. The large black arrows denote past and future projection of the surface low-pressure centers in the central U.S. The black rectangle shows the region of interest where in situ measurements were taken during the BAIRS II campaign.

As mentioned above, several challenges were encountered during the flight. The precipitation began to overspread the region of interest slightly sooner than forecast by the models. In addition, an area of snowfall with enhanced reflectivity up to 35 dBZ developed unexpectedly west of Ottawa and was anticipated to impact the airport close to the intended departure time. The Convair-580 was readied quickly and departed the airport just before the onset of heavy snow showers, thus avoiding the extra cost and delay involved with de-icing the aircraft.

Figure 23 shows the path of the Convair-580 throughout this mission. Once the aircraft approached Lake Ontario, the plan was to execute a spiral descent north of KBUF and then porpoise back and forth within the middle of the southwest–northeast-oriented precipitation band.

Although the initial intent was to have the aircraft remain near the KBUF radar for a longer period of time, attention was directed toward cells approaching the Rochester and Syracuse areas as the mission evolved. Other challenging factors during the operation include rapid erosion of the precipitation from the west due to the approach of mid-level dry air, and raising the porpoising altitude flight block with time (and

with Air Traffic Control (ATC) approval) to account for the deepening layer of warmer air approaching from the south and subsequent increase in the melting level altitude. A more detailed discussion of the key findings along the flight track is found in the next section.

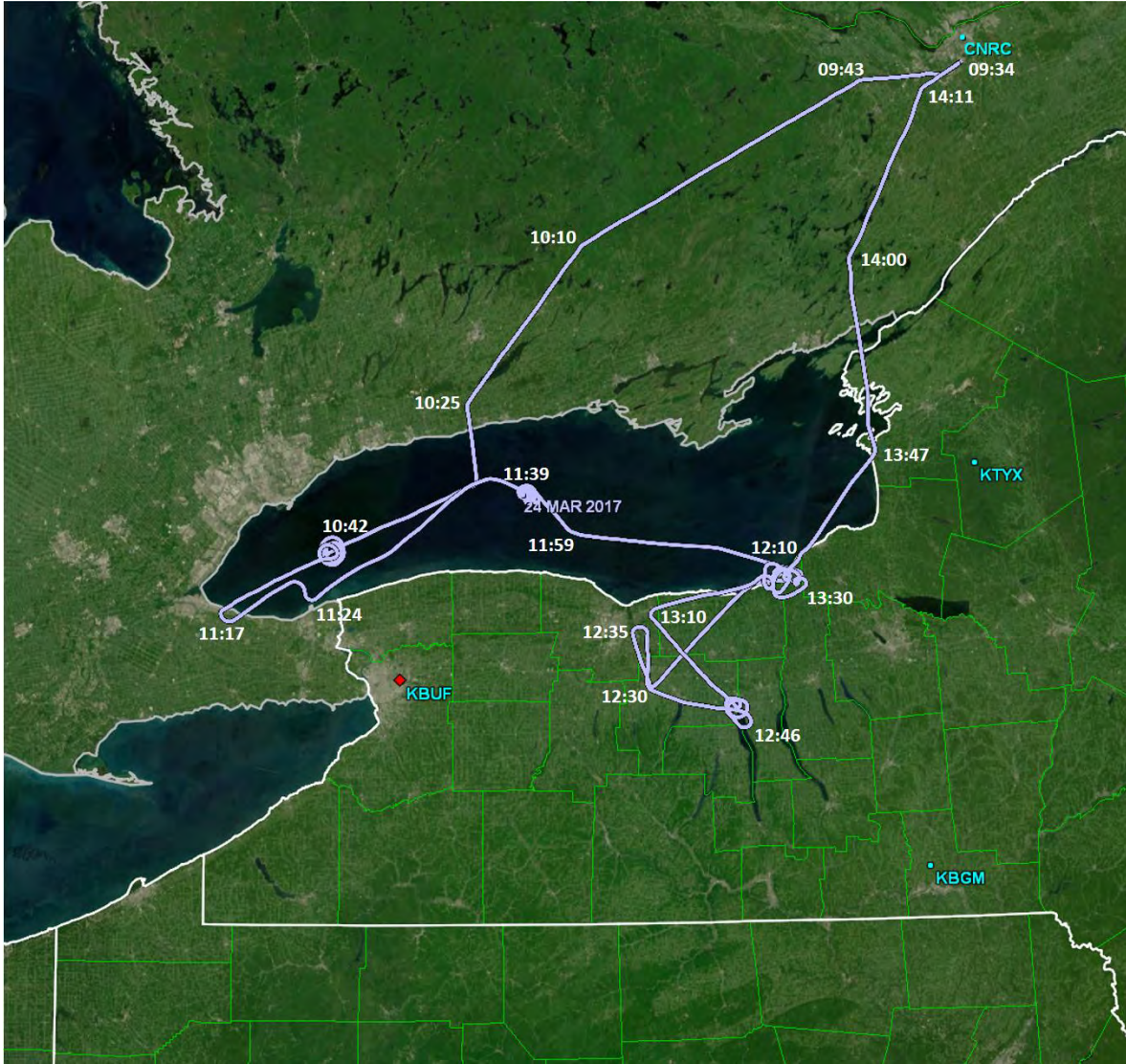


Figure 23. Flight track taken by the Convair-580 aircraft on 24 March 2017 between 09:33–14:15 UTC. The overlays and base map were displayed using the GR2Analyst radar display program developed by Gibson Ridge Software.

## Flight Summary/Overview

This nearly five-hour daytime flight (09:33–14:15 UTC) involved a large number of traversals through the melting layer/radar bright band. The documentation of needle crystals above the ML was extensive but the typical porpoising amplitude in temperature ( $+2^{\circ}$  to  $-8^{\circ}\text{C}$ ) did not enable documentation of the crystal sandwich.

Initial storm targets were near the western end of Lake Ontario. A porpoising strategy was executed en route from Ottawa (and on approach to Lake Ontario) with a modest temperature amplitude ( $-12^{\circ}$  to  $-15^{\circ}\text{C}$ ) over the time period 10:00–10:45 UTC (see Figure 23). The aircraft was already in cloud in this stretch, as St. Elmo's fire (blue corona discharge from aircraft surface) was detected on two occasions: the first at 09:39 UTC when the aircraft was gaining altitude out of Ottawa ( $T = -8^{\circ}\text{C}$  and  $\text{TWC} = 0.4 \text{ g/m}^3$ , mostly ice, irregular shapes), and later at 10:19 UTC ( $T = -15^{\circ}\text{C}$ ,  $\text{TWC} 0.1$  to  $0.2 \text{ g/m}^3$ , mostly ice with irregular shapes). The cloud profile in the vertically pointed X-band beam indicated  $\sim 7$  km tops and evidence of convection in both cases, so it is possible that the cause of the St. Elmo's fire arose from processes other than the charging of the aircraft by ice particle collisions. Beginning around 10:15 UTC, a continuous radar bright band/melting layer was evident beneath the aircraft flight track.

Following the initial shallow en route porpoising, and when located over Lake Ontario opposite Toronto, the aircraft spiraled down from a minimum temperature of  $-15^{\circ}\text{C}$  and traversed the ML at 10:55 UTC. This single in-place sounding provided a good look at crystal sandwich structure for the event documented in greater detail in Section 4.2.3. An onboard decision to conduct another spiral within a strong reflectivity core northwest of KBUF was denied by the Toronto Center due to congestion on approach to Toronto International Airport. Thereafter, the porpoising continued over the lake and above the melting layer with three additional spiral maneuvers performed within higher reflectivity cores containing stronger updraft speeds and evidence of graupel by the HCA. The objective of spiral probing was to support methods for distinguishing graupel and rimed ice crystal aggregates in the ground-based radar products. However, it was challenging to direct the aircraft to the desired locations with the cells moving rapidly from west to east.

The descent below the ML at 10:55 UTC initiated a long ( $\sim 2$  hours, 10:55–13:05 UTC) porpoising/spiraling sequence in a quasi-fixed temperature interval ( $+2^{\circ}\text{C}$  to  $-7^{\circ}\text{C}$ ) that catered to an investigation of the microphysics of the bright band. In the flight track shown in Figure 23, the leg of the flight began with the initial spiral over western Lake Ontario and ended with the fourth spiral near the southern shoreline of the lake southwest of Oswego. Some indication of the bright band's presence was evident in the onboard X-band radar observations throughout this period. Some indication of needle crystals was evident in each of seven repetitive ascents into the appropriate temperature range for this crystal type, but the lower temperature range was not sufficient to investigate a possible crystal sandwich structure in this time interval (above the needles). The clear presence of supercooled water accompanied the most conspicuous needle occurrences, at 11:12, 11:29, 12:20, 12:39, and 12:52–12:56 UTC. Supercooled water was not conspicuous when needle populations were also less distinct, such as 11:46 UTC. In general, these results support the association of supercooled water with needles, consistent with the laboratory diffusion chamber measurements (e.g., Bailey and Hallett [1]), even though the complete two-layer crystal sandwich was not documentable because of the limitations on the porpoising amplitude.

It should also be noted that during this long interval, the pilot deviated from a straight-line projection on the ground to explore regions displaying greater radar reflectivity in the onboard display of the NEXRAD observations. The strongest reflectivities encountered (48 dBZ) occurred at and beneath the ML (~2.5 km altitude) during the interval 12:02–12:04 UTC as the aircraft approached the southern shore of Lake Ontario. The cloud top altitude was ~7 km. Immediately after this high reflectivity encounter, a double ML became evident in the X-band reflectivity data, the original one at 2.4 km altitude and the second lower one near 1.1 km that persisted from 12:06 to 12:18 UTC with mean reflectivity 38 dBZ.

Altitude changes during the last 50 minute period on-station (and in the vicinity of the eastern end of Lake Ontario; but with minimum in situ temperatures no colder than  $-8^{\circ}\text{C}$ ) enabled four additional encounters with needle crystals (mixed with irregulars in the SNDI classification), all associated with supercooled water (13:12–13:14 UTC, 13:23–13:28 UTC, 13:36–13:39 UTC, and 13:58–14:01 UTC) and documented with the RID and Nevzorov probes.

At 13:39 UTC, the decision was made to return to Ottawa. During this last segment, at 13:50 UTC the optical glory was observed in the cloud top (supporting the existence of supercooled water near  $T = -7^{\circ}\text{C}$ ) as the aircraft dipped in and out of cloud (the ephemeral cloud zone noted in Figure 1). At 13:55 UTC, evidence for runback icing was noted by Alexei Korolev (onboard scientist from ECCC) on the starboard wing of the aircraft. The pilot confirmed icing on the windscreen (13:59 UTC).

### **3.6 25 MARCH 2017, 11:00–16:00 UTC**

#### **Synoptic Context**

The prospect to fly on this day was first discussed while the Convair-580 was returning to base during the previous day's flight. The favorable synoptic situation occurring on 24 March was forecast to continue, though with some distinct differences. A depiction of the synoptic conditions at 15:00 UTC (one hour prior to the end of the mission) is shown in the surface analysis map in Figure 24. The slow-moving occluded low in southern Oklahoma began to lift northeast toward the western Great Lakes and weaken with time. The associated warm front that extended eastward into NY and shifted slightly north of Lake Ontario on the 24th turned into a stationary front and drifted south to a position just south of Lake Erie by 15:00 UTC on the 25th as a result of strong arctic high pressure moving southeast from central Ontario Province. The boundary between the advancing arctic air and warm air south of the stationary front contributed to a narrow west–east-oriented band of precipitation on the north side of the front. NWP model forecasts of the scenario were accurate and the precipitation band was expected to move south of the BAIRS II domain by early afternoon.

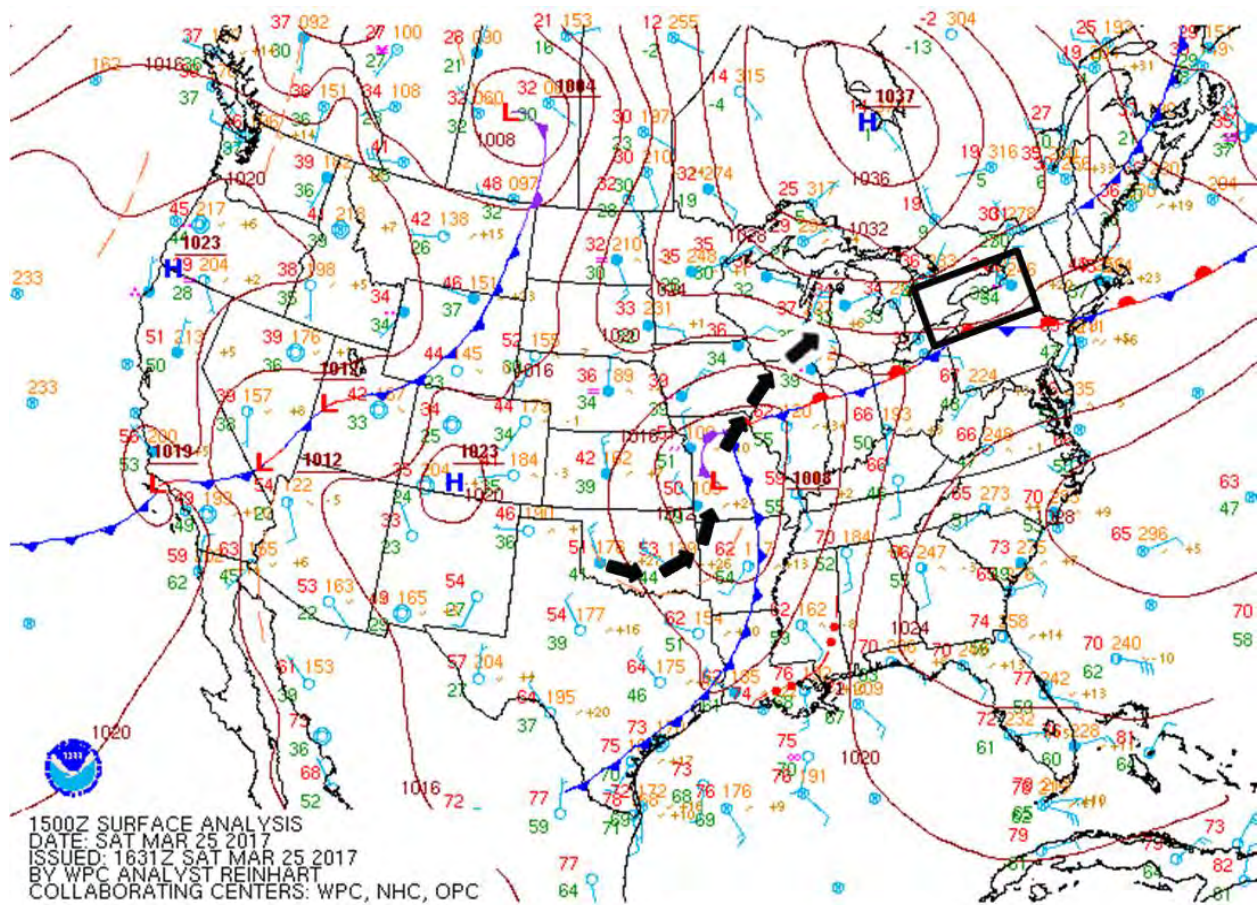


Figure 24. Surface analysis over the continental U.S. valid at 15:00 UTC on 25 March 2017. The large black arrows denote past and future projection of the surface low-pressure center presently located over Missouri. The black rectangle shows the region of interest where in situ measurements were taken during the BAIRS II campaign.

Unlike previous missions where probing was often conducted at altitudes within and just above the ML, the focus on this date was to perform longer transects within fixed altitude blocks between regions where needle ( $-4^{\circ}$  to  $-7^{\circ}\text{C}$ ) and dendritic ( $-9^{\circ}$  to  $-16^{\circ}\text{C}$ ) ice crystal growth zones typically occur. These zones are predominantly classified as dry snow by the HCA and were being targeted to determine the coexistence with supercooled water and whether or not the ice crystals were rimed.

Figure 25 shows the flight path of the Convair-580 during the mission. The original intent was to fly west within the precipitation band over Lake Ontario in the upper portion of the block, and double back over the same line but within the lower portion of the block. However, once the aircraft approached Hamilton on the western shore of the lake, Toronto Center booted the Convair-580 out of Toronto airspace and south into Cleveland airspace due to heavy air traffic congestion. For a short period of time, the aircraft dipped below the ML on its way to Lake Erie while waiting for approval from Cleveland Center to fly back within the intended block. Once the request was granted, porpoising continued on a transect west of the

KBUF radar within some enhanced reflectivity regions that were observed to contain graupel and a sustained period of SLW.

At the same time, an enhanced +ZDR bright band began to develop and the aircraft was directed east of KBUF for a potential intersect. A spiral maneuver was first conducted near Batavia, NY and close to a cell containing reflectivity of 50 dBZ near the ML. Thereafter, the flight segments located south of Lake Ontario and north/northeast of KBUF were flown to probe the +ZDR band. Unfortunately, this band was weaker and less coherent in the KBUF data at this location and the aircraft was also frequently not within any radar beam angle due to the proximity of the aircraft relative to the radar. A detailed description of the key findings along the flight track shown in Figure 25 is found in the next section.

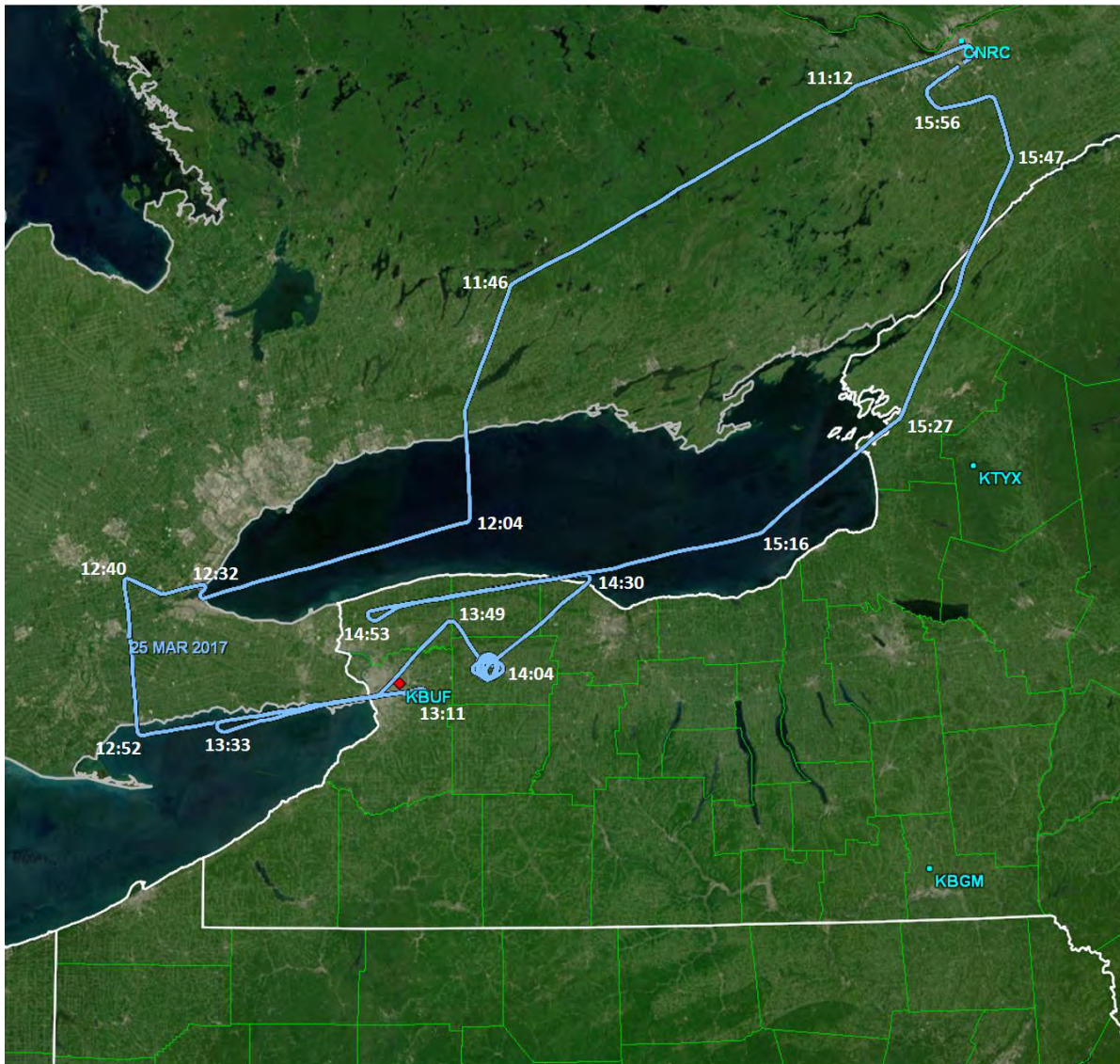


Figure 25. Flight track taken by the Convair-580 aircraft on 25 March 2017 between 11:00–16:00 UTC. The overlays and base map were displayed using the GR2Analyst radar display program developed by Gibson Ridge Software.

## Flight Summary/Overview

This five-hour daytime flight (11:00 to 16:00 UTC) was characterized by the most laterally extensive melting layer/radar bright band with reflectivities reaching 50 dBZ, and by the bumpiest ride of all flights during BAIRS I and II. In contrast to the 24 March flight, porpoising maneuvers on this flight remained above the ML/radar bright band.

The approach to the Buffalo area from Ottawa headed south over mid-Lake Ontario in Toronto airspace. The main target initially was an east–west-oriented line over the Toronto area. Optical sun dogs were reported twice during the initial approach (11:29 and 11:55 UTC) before the aircraft was fully embedded in the storm. A high-altitude ( $-24^{\circ}$  to  $-27^{\circ}\text{C}$ ) porpoising strategy was adopted (11:20–12:00 UTC) for the en route to Buffalo flight portion in response to onboard lidar evidence for a liquid layer in this range in an upper-level anvil cloud with strongly sloped reflectivity features (extending downward to at least 1 km altitude), topped with narrow convective turrets (with tops in the altitude range 5–7 km), and where the ride was bumpy. The pilot reported light rime icing on the windscreen (11:25 UTC) and liquid drops were noted in CPI imagery (11:29 UTC) during this overall period.

This short porpoising sequence ended near the time (11:58 UTC) the radar bright band first appeared in the onboard X-band radar imagery when the plane is descending toward the bright band. After two-hop porpoising ( $-2^{\circ}$  to  $-10^{\circ}\text{C}$ ), the aircraft descends below the ML for the first time, with notable bumpiness just above  $0^{\circ}\text{C}$ . Rain is encountered below  $0^{\circ}\text{C}$  with prevalence of drops  $>1$  mm in diameter. Difficulties with the Toronto ATC Center prevented access to deeper airspace at this time (12:46 UTC). By 12:48 UTC, ATC issued a directive to leave Toronto airspace and attention is then focused on weather targets near Rochester to the east.

The forced exit from Toronto airspace was fortunate in that it initiated a new eastward flight track that led immediately into more interesting weather. Between 12:53–12:54 UTC, the aircraft encountered a pocket of high Nevzorov liquid water content ( $0.7\text{ g/m}^3$ ), the largest value for the flight. This was also the bumpiest ride at any time during this flight. Small graupel particles were evident in the CPI imagery. The broken trace of the ML ( $\sim 2.6$  km altitude) was evident in X-band imagery with maximum reflectivity  $\sim 35$  dBZ. No lightning was noted, but it is likely we were close to a threshold for that occurrence. The bumpy ride extended from at least 12:54–13:02 UTC in this leg of the flight. Rime ice was detected on the windscreen (12:57 UTC).

A small amplitude porpoising strategy with rather narrow temperature amplitude ( $-7^{\circ}$  to  $-12^{\circ}\text{C}$ ) continued from 13:15–14:00 UTC. The radar bright band was discernible beneath the flight track continuously, occasionally showing reflectivity values in the 40–45 dBZ range. The ride was particularly bumpy over the stronger reflectivity segments, where the irregular cloud top reached  $\sim 7$  km. The Nevzorov TWC attained some of the largest values ( $0.8$ – $1\text{ g/m}^3$ ) during any BAIRS flight in the interval 13:17–13:22 UTC, when graupel particles were also noted in the CPI imagery. This last porpoising maneuver ended in a spiral descent (then ascent) between Buffalo and Rochester and through the ML where 1–2 mm diameter spherical drops were evident. Large wet snowflakes were noted during this traverse.

Coming out of this spiral ascent, the aircraft headed northeast and initiated a new longer (14:25–15:40 UTC) porpoising maneuver between temperature limits  $-5^{\circ}$  to  $-12^{\circ}\text{C}$  with a sequence of six separate

ascents/descents. This part of the flight track involved a final westward excursion and then an abrupt reversal of direction for the final leg home to Ottawa. The high temperature limit in these ascents/descents barely reached the traditional needle regime. Dendrites were detected at the low temperature limit ( $T = -12^{\circ}\text{C}$ ), thereby supporting a crystal sandwich structure. In three of the six descents (between 14:30 and 15:27 UTC) for which needles were encountered, supercooled water was also present. In the other three descents (at 14:39, 14:49, and 15:02 UTC), needles were scarce and so was supercooled water. (Further evidence for supercooled water during this porpoising sequence is visible in Figure 60 in Section 4.4.)

The aforementioned porpoising sequence was completed close to the time of the aircraft's crossing of the U.S./Canadian border on the return to Ottawa. A delicate radar bright band is evident beneath the aircraft until 15:20 UTC. Brief supercooled water in drizzle form in the CPI imagery was noted at 15:25 UTC at  $T = -8^{\circ}\text{C}$ .

**This page intentionally left blank.**

## 4. PRINCIPAL FINDINGS AND RESULTS

### 4.1 CHARACTERIZATION OF CLOUD PHASE

In the BAIRS I campaign, the Nevzorov LWC probe was the principal instrument used to characterize the presence of SLW and the aircraft icing hazard condition due to the sensor's excellent sensitivity when the SLW was in cloud droplet form. However, given that the response of the LWC probe may be as much as 10–15% of the measured IWC in ice phase (glaciated) clouds (Korolev *et al.* [40]), a methodology was developed to leverage the measurements collected from a more comprehensive suite of onboard microphysical instruments and particle imaging probes available in the BAIRS II study. The Convair-580 aircraft and earlier versions of some of the same probes used in this study were also used and analyzed by Cober *et al.* [14] in prior icing field experiments to document the observed responses within liquid, glaciated, and mixed-phase cloud conditions. Built upon that effort, an automated rule set approach was developed to assess and assign the cloud phase encountered into six categories: “glaciated”, “mixed”, “liquid below 0°C”, “liquid above 0°C”, “clear” (no ice or liquid particles), and “unknown”. The cloud phase estimates determine the presence or absence of an icing hazard and serve as a verification dataset to validate next generations of the NEXRAD dual polarimetric IHL detection product. Performance results of the current operational IHL algorithm verified with the cloud phase estimates are provided in Section 4.7.

The primary airborne instruments and observations used to characterize cloud phase include temperature; LWC and TWC from the Nevzorov hot-wire probes; particle concentration from the 3–45  $\mu\text{m}$  FSSP scattering probe; and crystal habit classification frequencies of Spheres, Needles, Dendrites, and Irregulars generated by the SNDI algorithm and derived from the 2D-C and PIP OAPs. Secondary observations of frequency oscillation data from the RID icing rod and evaluation of particle imagery from several OAPs, including the CPI, were used to validate the assigned phase, re-categorize unknown phase classifications derived from the primary instruments above, and identify “SLD” environments when drop sizes exceeded 100  $\mu\text{m}$  with few or no ice crystals observed.

A flowchart that details the methodology used to estimate the cloud phase is shown in Figure 26. The three preprocessing steps shown in row 1 synchronize and average the datasets over five-second intervals, and calculations of the LWC/TWC ratios are completed prior to descending through the decision tree logic in rows 2–4. The Nevzorov measurements of LWC, TWC, and calculated ratios are first tested against threshold values and have greater importance in determining the initial cloud phase condition. Thereafter, the presumed phase category may be altered based on whether the FSSP concentration value (third row) was above or below fixed thresholds and the combined frequencies of the SNDI categories was greater than 0, equal to 0, or was not determined (N/A = not available) (fourth row). The choice of selecting a fixed concentration threshold value of 3  $\text{cm}^{-3}$  was based on a thorough review of the 2D-S OAP imagery in BAIRS II in which evidence (absence) of very small cloud droplets were observed consistently when concentration values exceeded (fell short of) this threshold in the majority of the flights. Concentration values less than the threshold value indicates increased likelihood of a glaciated phase type. A combined SNDI frequency exceeding 0 implies some fraction of the sampling area is presumed to contain ice crystals and will change the phase type to mixed or glaciated if the phase type derived from the Nevzorov and FSSP measurements did not indicate the presence of ice. An unknown phase type occurs when the sensor

measurement values or derived SNDI frequencies conflict with each other. Once the phase types have been declared from the test sequences shown in rows 2-4 in the flowchart, all types are assumed to be cold phase (“liquid” refers to liquid droplets in a subfreezing environment).

For instance, if the LWC/TWC ratio exceeds 0.85, a substantial portion of the sampled area is expected to contain liquid water and the initial phase type is presumed to be liquid. If the FSSP concentration exceeds  $3 \text{ cm}^{-3}$ , the initial condition is confirmed and the SNDI frequency value is compared. The phase type will remain liquid if the frequency equals 0 or was not determined, otherwise if some form of ice crystals were observed (SNDI frequencies  $>0$ ), the phase type changes to mixed. An FSSP concentration that does not exceed the threshold value (or is not available) changes the initial type to unknown because the measurement indicates an absence of liquid droplets and a condition opposite from what is inferred from the Nevzorov measurements.

Once all observations are assigned an initial phase type, a few additional steps are performed to determine whether the phase should be revised. If the initial phase type is clear or N/A, the type is not changed. For all other phase types, the type is reassigned to liquid (warm environment) if the measured temperature exceeds  $0^{\circ}\text{C}$ . The last step involves a manual review of the imagery from multiple particle imaging probes to 1) assign a phase type to the unknown category, 2) validate the initial phase determined automatically, 3) identify SLD conditions when some of the drop sizes exceed  $100 \mu\text{m}$  with few or no observed ice crystals, and 4) verify that rapid changes in RID frequency correlate with the liquid or mixed phase type. Phase assessments based on a review of the particle imagery takes into account the particles observed over the entire five-second interval and not at the specific observation time. For situations in which ice crystals were the major hydrometeor type, a mixed-phase condition is designated if liquid droplets were observed for at least two seconds over the interval.

For all five flights, there were a total of 13,391 five-second averaged observations in which the phase was assigned a type other than N/A. Among these, 134 (1%) observations were classified as unknown and 1,348 (10%) were revised from the initial classification type. A summary of the steps taken to estimate cloud phase is outlined below:

- Determine initial phase from the Nevzorov LWC, TWC, and LWC/TWC ratio with the parameter rule set defined by Cober *et al.* [14]
- Modify phase based on FSSP particle concentration indicating the presence or absence of liquid water and SNDI habit classifications indicating presence or absence of ice crystals
- Review particle imaging probes to help determine phase for all unknown cases in which initial phase was not determined in the previous two steps
- Incorporate temperature data to distinguish liquid water phase from SLW
- Identify SLD intervals using temperature and particle sizes imprinted in the CPI imagery
- Confirm rapid changes in RID frequency correlate with mixed or liquid phase intervals
- Validate and adjust cloud phase after performing a review of OAP imagery, particularly from the 2D-S and CPI high-resolution probes, to identify cloud droplet and large droplet episodes that may not have shown an instrument response

### Cloud Phase Estimate Methodology

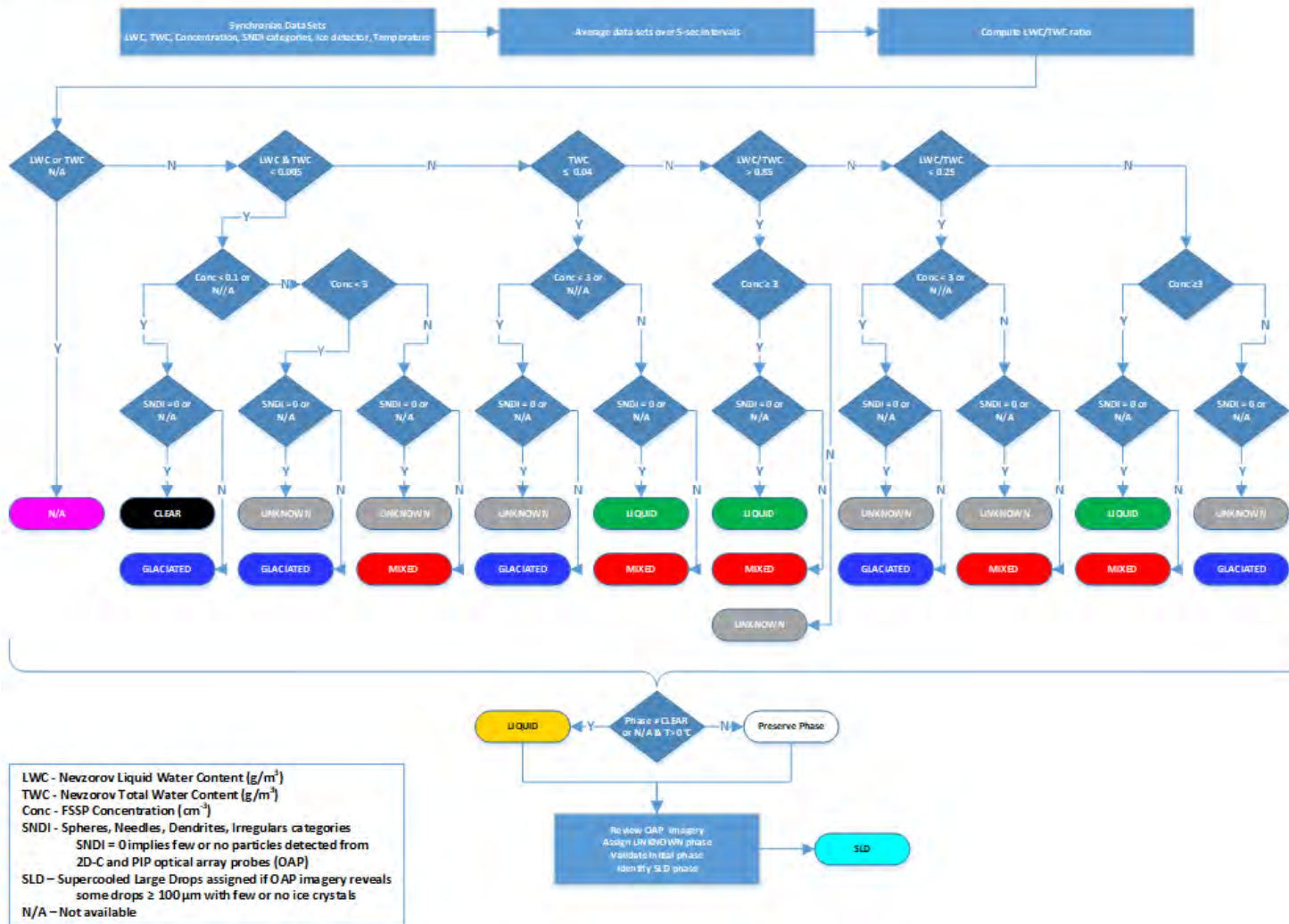


Figure 26. Flowchart illustrating the methodology used to estimate the cloud phase encountered by the Convair-580 aircraft at five-second observation intervals. The data preprocessing steps are shown in row 1. Determination of the initial phase type is based on probe measurements from the Nevzorov LWC, TWC, and LWC/TWC ratio (row 2), the FSSP concentration (row 3), and crystal habit classification frequencies generated by the SNDI algorithm (row 4). Several steps are then performed to assign an unknown phase type, validate the initial type, and identify SLD intervals.

An evaluation tool was developed to help visualize and assess the performance of the cloud phase typing methodology against the defined parameter rule set applied to the sensor measurements. Figure 27 shows a six-panel time series plot generated from this tool for the 10-minute interval 15:30–15:40 UTC on 10 January 2017. The panels show from top to bottom, panel 1) Nevzorov LWC (blue, left axis) and TWC (black, left axis) and LWC/TWC ratio (red, right axis); panel 2) FSSP concentration (black); panels 3) and 4) SNDI classification frequencies of Spheres (burnt red), Needles (cyan), Dendrites (blue), and Irregulars (gold) derived from the 2D-C and PIP OAPs, respectively; panel 5) RID frequency of the raw one-second (black) and five-second averaged (magenta) data; and panel 6) manual assessment of the particle type(s) observed in the CPI imagery (left axis) with in situ temperature (blue, right axis).

The color-coded boxes above most of the panels are provided to show the initial and revised phase type classifications, highlight changes in instrument responses or cloud type particles, and are useful in developing the parameter rule set used to determine the phase. The first and second row of boxes at the top of panel 1 represent the final and initial cloud phase estimates, respectively. The third row is the phase type based strictly on the Nevzorov measurements and ratios. The two red and single black dashed lines in the panel denote the defined Nevzorov threshold values used in the phase estimation. The phase type categories are listed at the top of the panel and are matched in color to the boxes below. In panel 2, the black, blue, and green boxes denote phase types of clear, glaciated, and liquid or mixed, respectively, based on the FSSP concentration measurements. The dashed black line ( $3 \text{ cm}^{-3}$ ) is the threshold value applied in the phase estimation. The color-coded boxes above panel 3 are derived from the combined analysis of the SNDI categories from the 2D-C (panel 3) and PIP (panel 4) probes and show categories of no observed particles (black), greater than 10% frequency of spheres (green), and other non-sphere categories with a low percentage of spheres (blue). The green, gray, and black boxes above panel 5 identify the intervals in which the RID frequency is dropping (indicator of rime ice accumulating on the probe), rising (shedding of rime ice off the probe, but possibly within a rime icing environment), and stable conditions (no riming encountered), respectively. The particle types determined from CPI imagery are shown in panel 6 and categorized/labeled as, “n” (no particles or a data gap in the imagery), “d” (cloud droplets), “dz” (drizzle drops  $>100 \mu\text{m}$ ), “dzd” (drizzle drops, cloud droplets), “dzdc” (drizzle drops, cloud droplets, ice crystals), “dzc” (drizzle drops, ice crystals), “dc” (cloud droplets, ice crystals), and “c” (ice crystals). The color-coded boxes above panel 6 are equivalent to the defined categories above panel 1.

During the interval shown in Figure 27, temperatures ranged from  $-6^\circ$  to  $-12^\circ\text{C}$  and the Convair-580 encountered frequent changes in cloud phase with extended periods of icing hazard shown in red (mixed) and green (liquid) at the top of panel 1. For instance, between 15:35–15:36 UTC, the aircraft encountered a liquid phase cloud. This condition is characteristic of a high LWC/TWC ratio (red line above 0.85 in panel 1), FSSP concentrations above  $3 \text{ cm}^{-3}$  (dashed black line in panel 2), absence of ice crystal habits determined from the SNDI algorithm (panels 3 and 4), and rapid changes in RID frequency in a decreasing-increasing-decreasing pattern (panel 5). Although not used in the initial cloud phase determination, cloud droplets (type d in panel 6) were the predominate particles observed in the CPI imagery and indicative of liquid phase.

Time series plots of the cloud phase estimates spanning the entire mission flight interval for each of the five flights are provided in Appendix C.

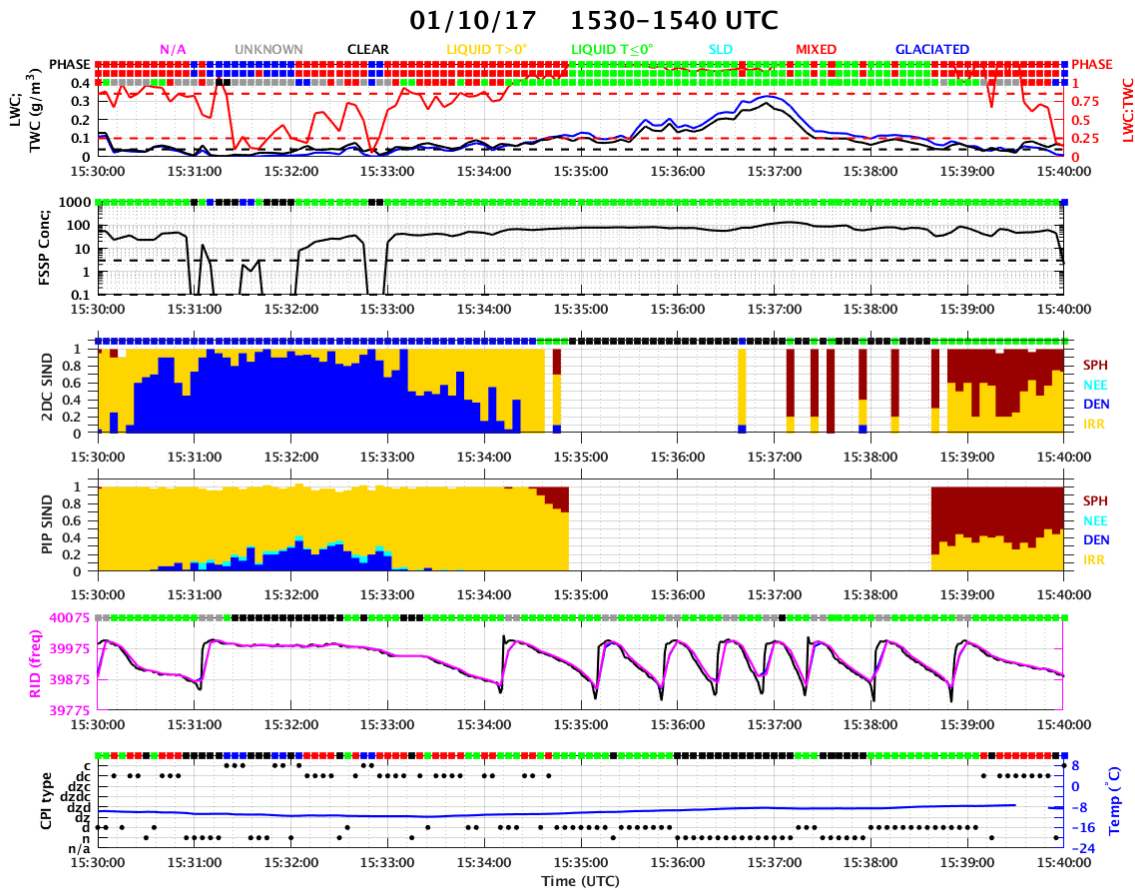


Figure 27. An example of a six-panel time series plot generated from a tool used in the evaluation of the cloud phase estimate methodology for the interval 15:30–15:40 UTC on 10 January 2017. From top to bottom, the panels show probe measurements from the Nevzorov LWC, TWC, and LWC/TWC ratio (panel 1), FSSP concentration (panel 2), SINDI crystal habit classifications derived from the 2D-C and PIP probes (panels 3 and 4), RID frequency (panel 5), and particle types observed in the CPI imagery (left axis) with temperature (right axis)(panel 6).

## 4.2 THE CRYSTAL SANDWICH: A DUAL POL SIGNATURE FOR ICING HAZARD

### 4.2.1 Perspective on Needle Crystals from BAIRS I

The perceived importance of needle crystals in the context of supercooled water, aircraft icing and dual polarimetric radar sensing was greatly expanded from BAIRS I to BAIRS II. Some discussion of the history of learning over the entire period is appropriate to understand why this is so.

In BAIRS I, only one of three flights, on 28 February 2013, showed a great prevalence of needle crystals, along with an abundance of horizontal flat plate crystals. At the time, we viewed this as an anomaly case, set up by exceedingly gentle ascent—the weakest snowstorm possible was our assessment at the time

(Williams *et al.* [83]) and later summarized when the three flights were summarized for the aircraft icing conference in Prague (Williams *et al.* [86]).

When the analysis for the five flights in BAIRS II got underway, the first aircraft dataset to become available (after quality control evaluations) for careful checking was from the CPI probe (received from Alexei Korolev at ECCC). This crisp hydrometeor imagery showed an abundance of needles and columns in all five flights and in a range of temperature generally consistent with laboratory diffusion chamber measurements (Bailey and Hallett [1]). The resolution of the CPI imagery was also sufficiently good that rimed and unrimed needles/columns could be readily distinguished. These observations were presented earlier (Williams *et al.* [87]).

It is worthwhile noting that needle crystals have been previously documented in the temperature range  $-3^{\circ}$  to  $-6^{\circ}\text{C}$  in natural conditions (Heim [31]; Nakaya and Terada [57]; Korolev *et al.* [43]). (According to Weickmann [78], the first measurements of needles in this lower temperature range were reported by Heim [31].) The new finding in the present study is that the needles are frequently collocated with, or in close proximity to, supercooled water, which make the aircraft icing hazard, and form a portion of a “crystal sandwich” radar feature.

Recalling that layers of flat-plate crystals overlaid the needle layers in the earlier flight of BAIRS I, we then began to examine porpoising and spiral ascents in the BAIRS II aircraft dataset whenever a sufficient temperature range was spanned to include both needles and flat-plate crystals, according to the crystal habit diagram. It then became apparent that the weakest snowstorm possible from BAIRS I was not an anomaly, but just one example of systematic behavior. This conclusion was strongly corroborated by a collection of NEXRAD winter cases organized at MIT LL, in which evidence for bright bands in differential reflectivity for both dendrites and needles were apparent, so long as the background reflectivity levels were sufficiently small. These many observations, discussed in greater detail in Section 4.2.3, served as important dual polarimetric evidence for the “crystal sandwich”, to be explained in detail on the basis of the in situ aircraft observations. The latter conditions refocused attention on the “gentle ascent” in a quantitative context, and that is the subject of Section 4.3.

#### **4.2.2 Needles and Dendrites Linked with Water Saturation and Supercooled Water**

A major objective from the outset in the FAA-supported work on aircraft validation of in situ icing conditions has been the identification of S-band dual polarimetric radar signatures for supercooled water. This objective quickly became a search for dual polarimetric-identifiable anisotropic radar targets with which supercooled water is associated. The most conspicuous target was the flat dendritic crystals that had earlier been shown to produce a positive anomaly in differential reflectivity over a relatively narrow range of altitude and in situ temperature (Hogan *et al.* [34]; Kennedy and Rutledge [39]). Later work of the MIT LL group extended the range of meteorological prevalence and named this feature the “positive ZDR bright band” (+ZDR BB; Williams *et al.* [85], [86]).

An important guide for the prevalence of crystal habits with in situ temperature and humidity comes from diffusion chamber measurements in the laboratory (Hallett and Mason [28]; Bailey and Hallett [1]). In this method, the relative humidity with respect to liquid water can be more accurately controlled and measured than one can achieve by measurements of temperature and dew point in the atmosphere. The line of saturation with respect to liquid water can be confidently included (in red) in Figure 28. Two key crystal

types are found rightward of this red line, in water-saturated conditions. First, the dendritic crystals discussed in the previous paragraph in a temperature range of  $-10^{\circ}$  to  $-14^{\circ}\text{C}$  (Williams *et al.* [84]) are apparent. Also conspicuous are the needle crystals in a temperature range  $-3^{\circ}$  to  $-6^{\circ}\text{C}$ . These laboratory conditions are well matched to the in situ aircraft observations pertaining to needle crystals in the BAIRS I flight on 28 February 2013.

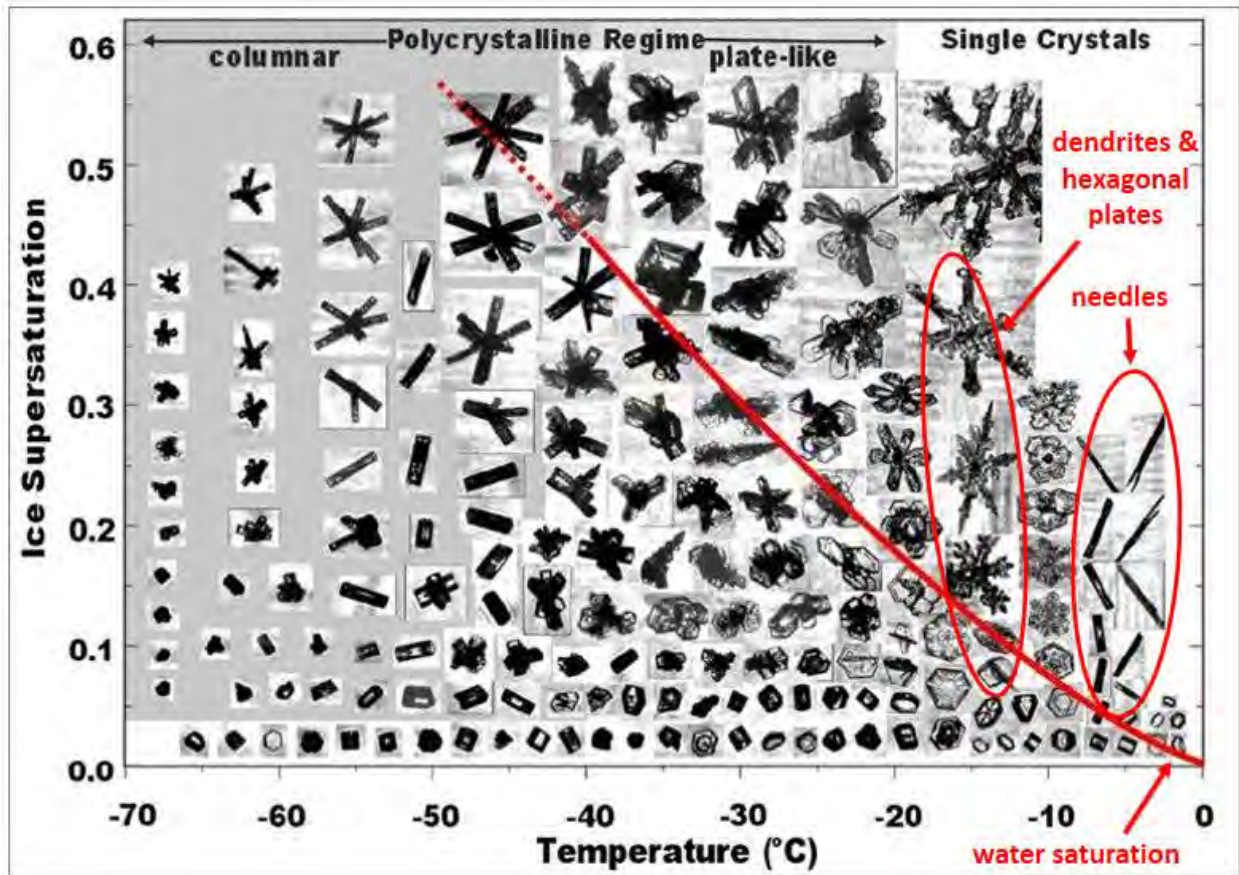


Figure 28. The crystal habit diagram based on laboratory diffusion chamber measurements of Bailey and Hallett [1]. The sloping red line represents the condition of water saturation. Also encircled are the three crystal types of fundamental importance for the crystal sandwich: the flat crystals on the left (including dendrites and flat-plate hexagonal crystals) in a temperature range from  $-9^{\circ}$  to  $-16^{\circ}\text{C}$  and the needle crystals on the right in a temperature range from  $-4^{\circ}$  to  $-7^{\circ}\text{C}$ .

An important objective in BAIRS II has been the inquiry into presence of supercooled liquid water in situ and differential reflectivity by remote sensing wherever flat-plate crystals and needles are prevalent hydrometeors.

#### 4.2.3 Documentation of Crystal Sandwich Structure in Aircraft Measurements

Three separate methods for integrating the Convair-580 aircraft and ground-based NEXRAD radar observations have been devised to document the crystal sandwich cases in BAIRS II. These three methods are here described in turn.

First, time series of a multitude of in situ aircraft observations and radar observations have been organized for every flight in BAIRS II. As shown in Figure 9, these time series include, from top to bottom, the hydrometeor identification results from the SNDI algorithm (Korolev and Sussman [41]), the results from the NEXRAD HCA, the aircraft altitude and in situ air temperature, the Rosemount icing detector output and Nevzorov traces for liquid water content and total water content, the reflectivity for the onboard X-band radar, and the mean value among dual polarimetric radar estimates ( $Z$ ,  $ZDR$ ,  $CC$ , and  $KDP$ ) within the physical-sized window centered at the aircraft location (as discussed in Section 2.3), for the NEXRAD radar (KBUF, KBGM, KTYX) in closest proximity to the aircraft. Time series plots for each of the three BAIRS II case studies are included in Figures 33, 38, and 43.

Second, the aircraft is placed in the context of the vertical profile of temperature and LWC within the crystal sandwich and the hydrometeor populations documented with the aircraft 2D-C probe near the upper and lower boundaries of the crystal sandwich in the representation shown in Figures 29, 34, 39, and 44 for the four separate case studies. The vertical profiles are enabled either by a vertical porpoising maneuver or by a special ascent/descent at one location.

Third, the aircraft is placed in the four-dimensional ( $x$ ,  $y$ ,  $z$ ,  $t$ ) context of the NEXRAD radar with special nine-panel plots for each case study. This plot format was described in greater detail earlier in Section 2.5. Each radar panel represents a portion of a PPI scale centered on the aircraft location. The center column of three panels is taken from the radar volume scan closest to the current aircraft location. The left and right columns of panels represent the volume scans before and after the center column volume scan. The center horizontal row of panels represents the elevation angle closest to the aircraft location, with adjacent panels representing the elevation angles above and below the aircraft location.

Sets of nine-panel plots of  $ZDR$ ,  $Z$ , and  $HC$  for the four respective case studies are shown in Figures 30–32, 35–37, 40–42, and 45–47. The history of the aircraft position is marked in the center panel. For the BAIRS I case (Figures 30–32), this trajectory is color-coded to denote the in situ LWC encountered (black  $<0.005$ ; yellow  $<0.1$ ; red  $\geq 0.1$  g/m<sup>3</sup>), but for the BAIRS II cases, it is color-coded to denote the cloud phase (blue = glaciated, red = mixed, green = liquid below 0 °C, gold = liquid above 0°C, black = clear, cyan = SLD).

## **Case Studies**

### **Case I: 28 February 2013**

This case study from BAIRS I provided the first indications of a crystal sandwich. A long aircraft porpoising episode during this flight from 18:00–19:35 UTC provided alternating access to the needle layer near -4°C and a layer of hexagonal flat-plate crystals near -9°C (Williams *et al.* [83]). Needles are conspicuous in the interval 18:31–18:33 UTC (Figure 29). Then the plane ascends and a rich concentration of hexagonal flat-plate crystals is encountered in the time frame 18:35–18:38 UTC. These crystals show up more strongly as spheres in the sparse SNDI analysis (Korolev and Sussman [41]) of this time interval.

The LWC on the Nevzorov probe maximizes at 18:34:20 UTC (0.57 g/m<sup>3</sup>), in the interval between the needle layer and the layer of hexagonal flat-plate crystals above.

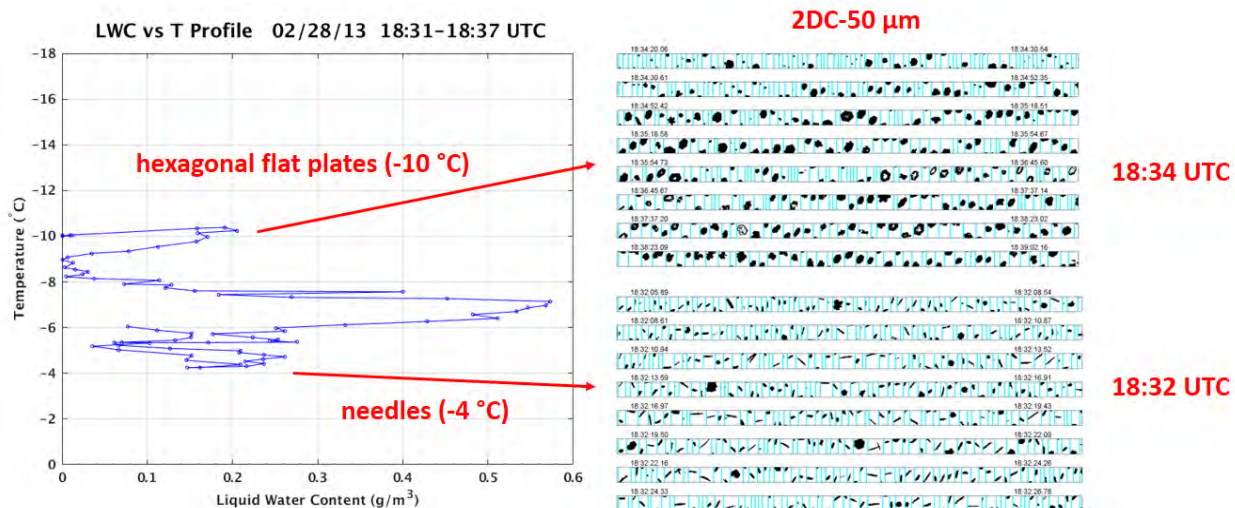


Figure 29. Vertical profile of LWC and samples of the 2D-C hydrometeor imagery at two temperature levels in the profile while porpoising between 18:31–18:37 UTC on 28 February 2013. A maximum in LWC is evident between the two crystal layers.

The most conspicuous feature in the nine-panel plots for this case (Figures 30–32) is found in the differential reflectivity of Figure 30. Here, one sees evidence for the largest +ZDR values ever encountered in either BAIRS I or BAIRS II, with some values reaching +7.8 dB. This special circumstance is in keeping with the theoretical finding (e.g., Hogan *et al.* [34]) that the most anisotropic hydrometeor target known is the hexagonal flat-plate crystal. It is also noteworthy that these extreme +ZDR values were encountered in regions of negative reflectivity values (Figure 31) and within 60 km of the radar. The HC in Figure 32 did not show Ice Crystal for these unusual natural targets, but rather Unknown. This error is attributable to the unusual nature of the targets which the plane sampled by virtue of the onboard dual polarimetric information from the ground for this flight.

In contrast with the large +ZDR values for the flat-plate crystals, the needle crystals at shorter radar range in Figure 30 show positive values in the range of +0.2 to +0.8 dB. These values are consistent with theoretical estimates on horizontally oriented needles with random orientations (Hogan *et al.* [34]).

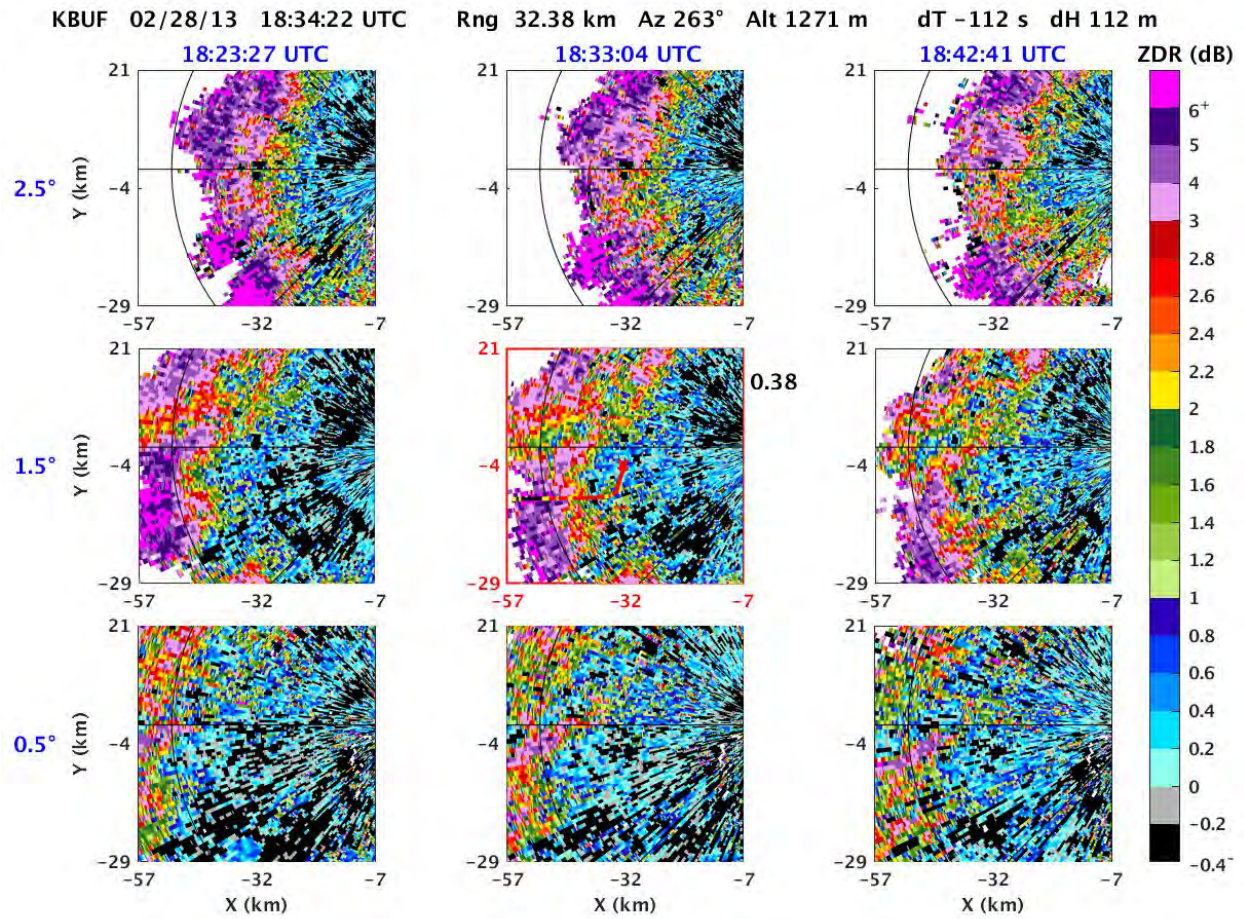


Figure 30. Nine-panel plot of KBUF differential reflectivity (ZDR) with the center plot matched nearest in time and space to the Convair-580 position at 18:34:22 UTC for the crystal sandwich case on 28 February 2013. The row (column) of plots show adjacent elevation angles (volume times) increasing from bottom to top (left to right), respectively.

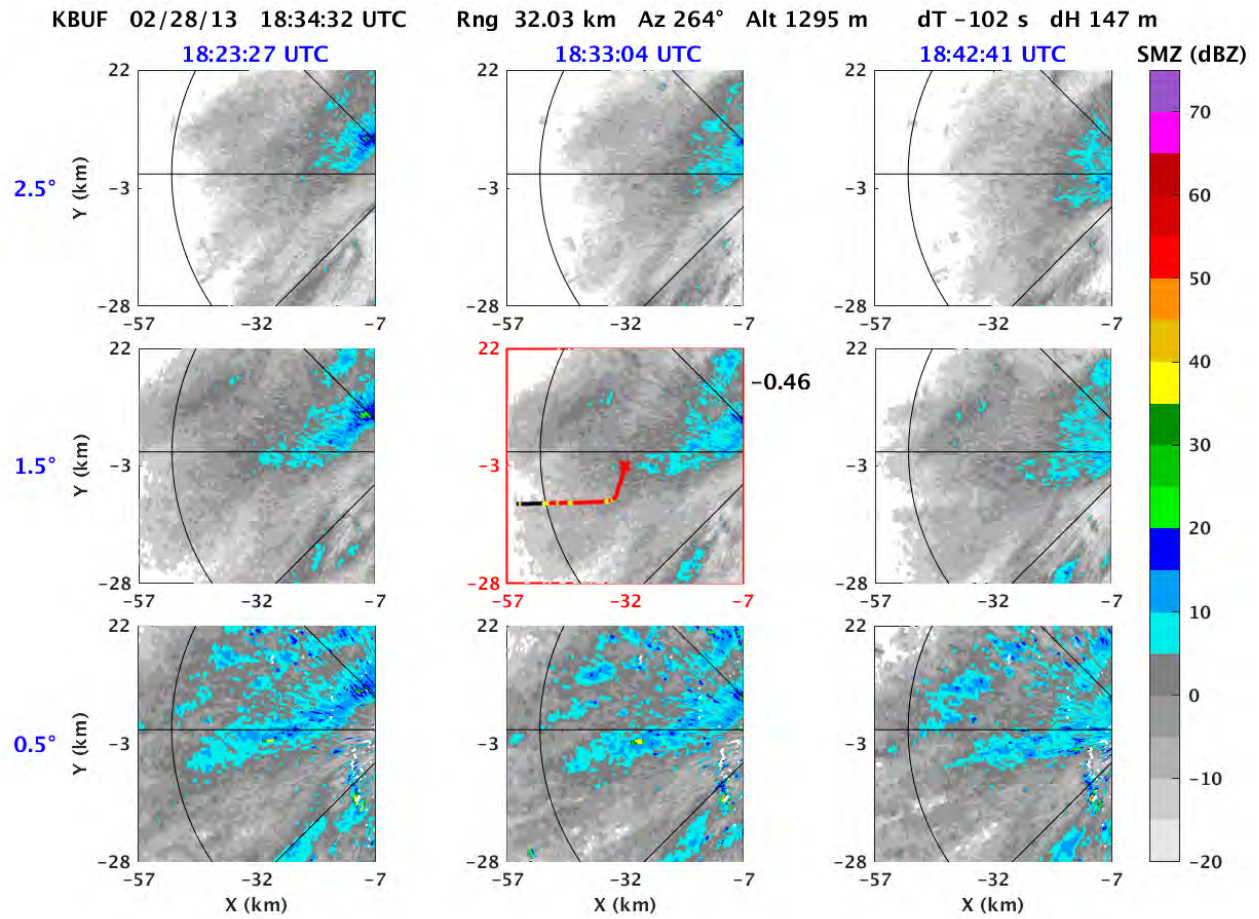


Figure 31. Nine-panel plot of KBUF reflectivity ( $Z$ ) with the center plot matched nearest in time and space to the Convair-580 position at 18:34:22 UTC for the crystal sandwich case on 28 February 2013. The row (column) of plots show adjacent elevation angles (volume times) increasing from bottom to top (left to right), respectively.

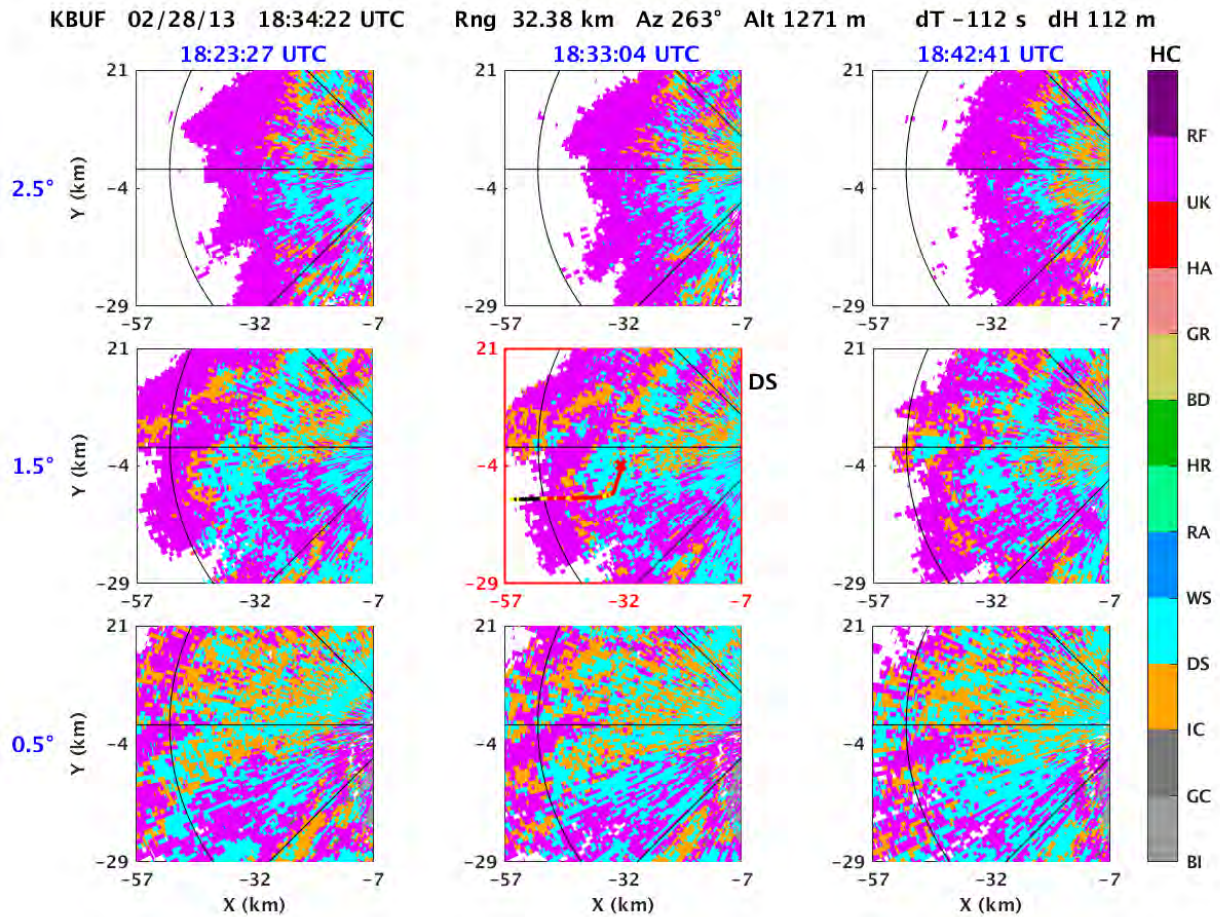


Figure 32. Nine-panel plot of KBUF hydrometeor classification (HC) with the center plot matched nearest in time and space to the Convair-580 position at 18:34:22 UTC for the crystal sandwich case on 28 February 2013. The rows (columns) of plots show adjacent elevation angles (volume times) increasing from bottom to top (left to right), respectively. Abbreviations of the HC categories include Biological (BI), Ground Clutter (GC), Ice Crystals (IC), Dry Snow (DS), Wet Snow (WS), Rain (RA), Heavy Rain (HR), Big Drops (BD), Graupel (GR), Hail-rain mix (HA), Unknown (UK), and Range Folding (RF).

## Case II: 10 January 2017

Evidence for crystal sandwich structure was noted during a spiral ascent of the aircraft in one location. Figure 33 shows the time series plots of aircraft variables over the period 15:20–15:30 UTC that spans the key features. The in situ temperature drops from  $-3^{\circ}$  to  $-10^{\circ}\text{C}$  as the altitude increases from 2.1 to 4 km. Needle crystals (cyan) are conspicuous in the 2D-C imagery only in the interval 15:20–15:21 UTC, but later at lower temperatures, the dominant crystal type shifts to dendrites (blue).

Only a trace of supercooled water is evident in the Nevzorov probe in the needle region (with no response from the Rosemont probe), but the LWC increases systematically into the dendrite layer above (with clear accompanying response from the Rosemount probe), attaining a maximum value of  $0.23 \text{ g/m}^3$  at 15:29 UTC.

The onboard X-band reflectivity in the needle region lies in the range of 10–15 dBZ, consistent with the range expected for “crystal storms” (Lim *et al.* [53]; see also Section 4.5 of this report). This reflectivity level rises to the low 20s dBZ in the dendritic crystal layer. The differential reflectivity from the ground-based radar (KBUF) is marginally sampled in the needle region, but is showing small (tenths of dB) values in the upper dendritic region. Breaks in the dual polarimetric product traces shown in the bottom two panels in Figure 33 indicate the aircraft position did not reside within any KBUF elevation angle. Dashed lines denote a time difference between the aircraft and radar exceeds 120 seconds.

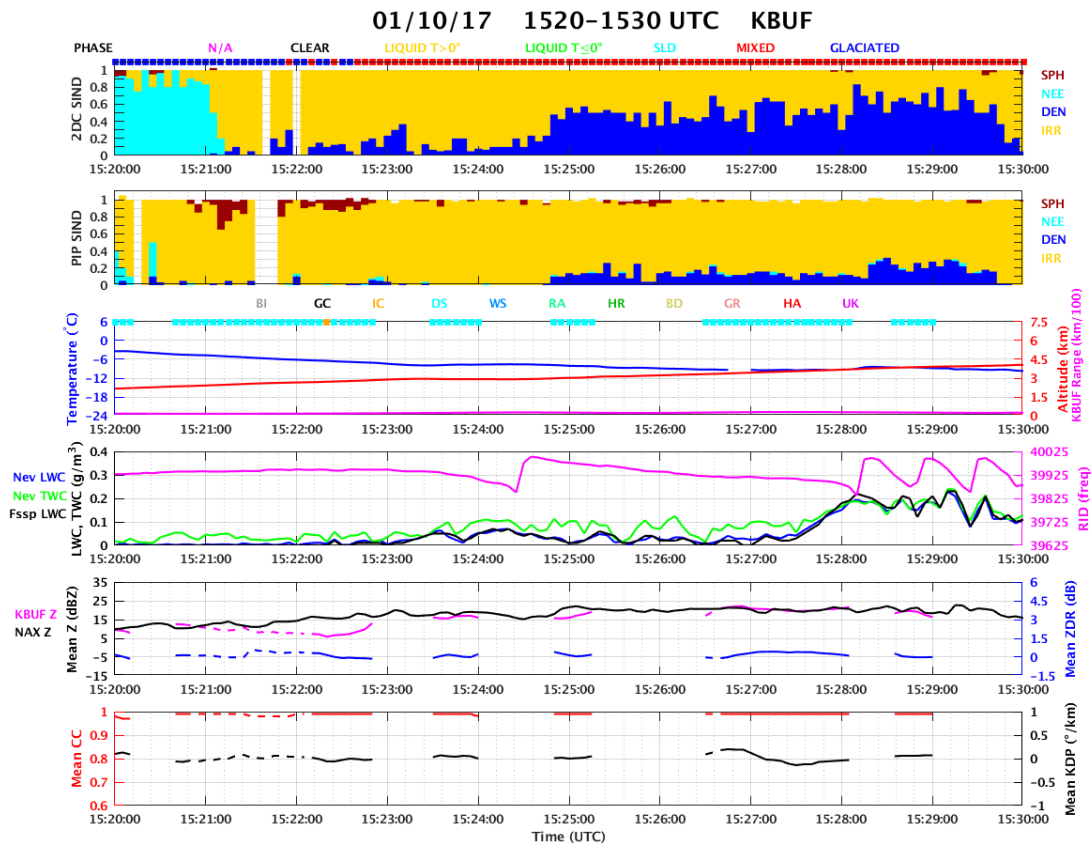


Figure 33. Six-panel plot showing records from the SNDI algorithm (top two panels), in situ temperature, aircraft altitude, Nevzorov LWC and TWC, RID frequency, and FSSP LWC (middle two panels), and onboard X-band radar reflectivity and dual polarimetric quantities from KBUF (bottom two panels) radar for the interval 15:20–15:30 UTC on 10 January 2017.

Figure 34 shows the reconstructed vertical profile of supercooled LWC (in  $\text{g/m}^3$ ) over the same time interval. Sample imagery from the 2D-C probe is shown to verify the presence of needles/columns near the lower boundary and dendrites near the upper boundary of the sandwich. In this case, the largest concentration of SLW is found in the upper part of the sandwich.

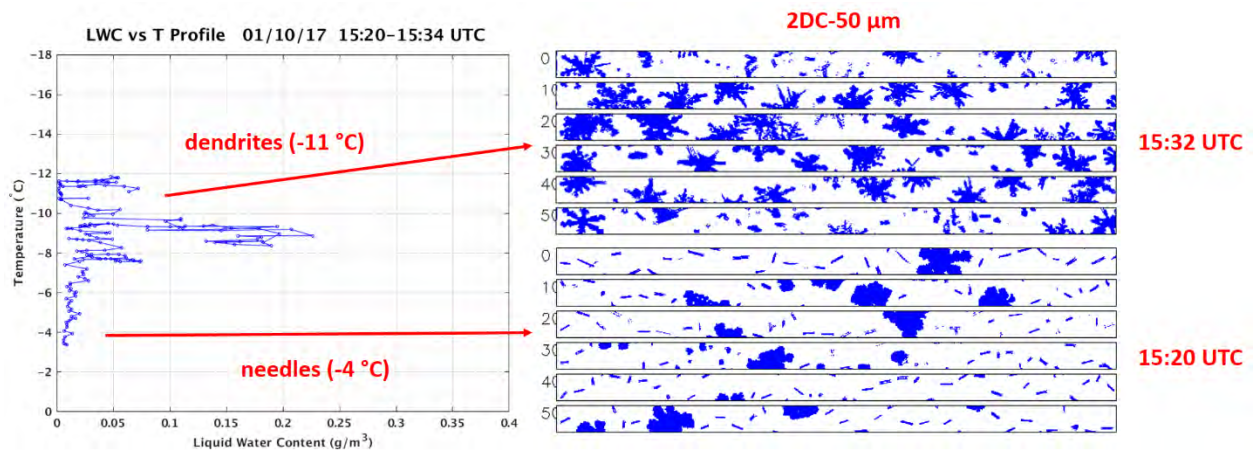


Figure 34. Vertical profile of LWC and samples of the 2D-C hydrometeor imagery at two temperature levels in the profile during a spiral ascent between 15:20–15:34 UTC on 10 January 2017.

Figures 35–37 show the nine-panel plots for differential reflectivity, reflectivity, and hydrometeor classification, respectively, for the same case. From this larger perspective, the +ZDR bright band associated with the dendritic crystals in the upper layer of the sandwich is readily apparent in six of the nine panel plots (Figure 35). The whitened portion of this feature in three of the panels is an indication that the reflectivity is near the noise floor of the radar at this range, but there is little doubt that a small concentration of dendritic crystals resides in these regions. This dendritic layer also shows a clear evolution in time through the three consecutive volume scans, with major diminishing trend, suggesting the possible aggregation of dendrites.

The KBUF radar lies to the west of the region depicted in the nine-panel plots for this case. The history of the aircraft clockwise spiral straddles the sharply defined +ZDR bright band and the stronger reflectivity region beneath it, where aggregation is likely occurring beneath the dendrite layer. This straddling is also evident in the center panel of the HC nine-panel plot (Figure 37), with correctly identified Ice Crystals (orange color) above the Dry Snow (turquoise color) at lower altitudes (leftward of the +ZDR bright band in the PPI), where aggregation of dendrites is inferred to make the snow.

Above the sharply defined dendritic layer is a more diffuse and thicker layer of generally positive differential reflectivity and weaker reflectivity ( $Z < 15$  dBZ) where Ice Crystals also dominate in the HC.

In contrast with the dendritic layer which is consistently identified as Ice Crystals (Figure 37), the layer beneath is less homogeneously Ice Crystals but a mixture of weakly positive (0 to +1 dB) ZDR values. Generally speaking, the Dry Snow and inferred aggregation is associated with stronger reflectivity (up to 30 dBZ), whereas the Ice Crystals (where needles are expected) are detected in the surrounding regions of weaker reflectivity (0 to 15 dBZ).

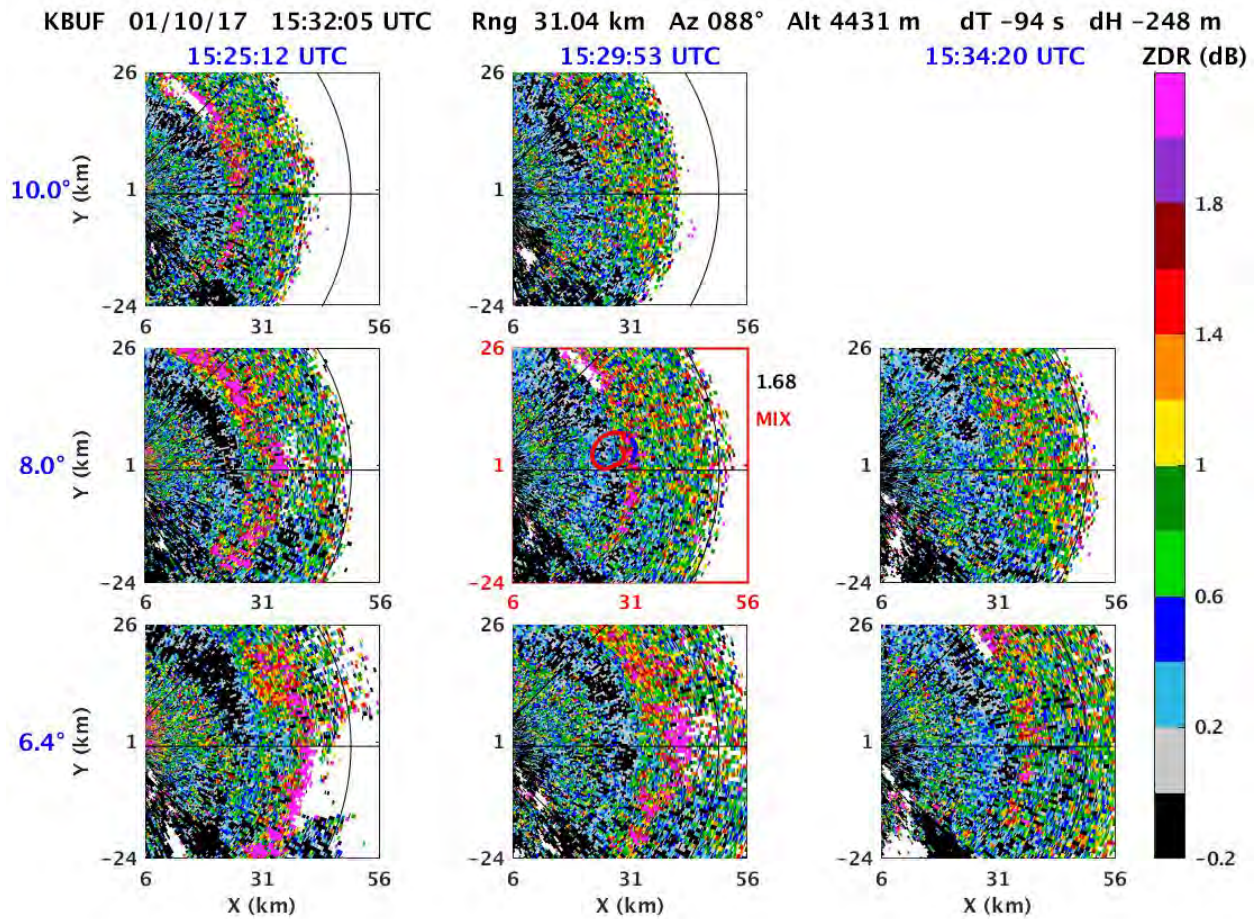


Figure 35. Nine-panel plot of KBUF differential reflectivity (ZDR) with the center plot matched nearest in time and space to the Convair-580 position at 15:32:05 UTC for the crystal sandwich case on 10 January 2017. The row (column) of plots show adjacent elevation angles (volume times) increasing from bottom to top (left to right), respectively.

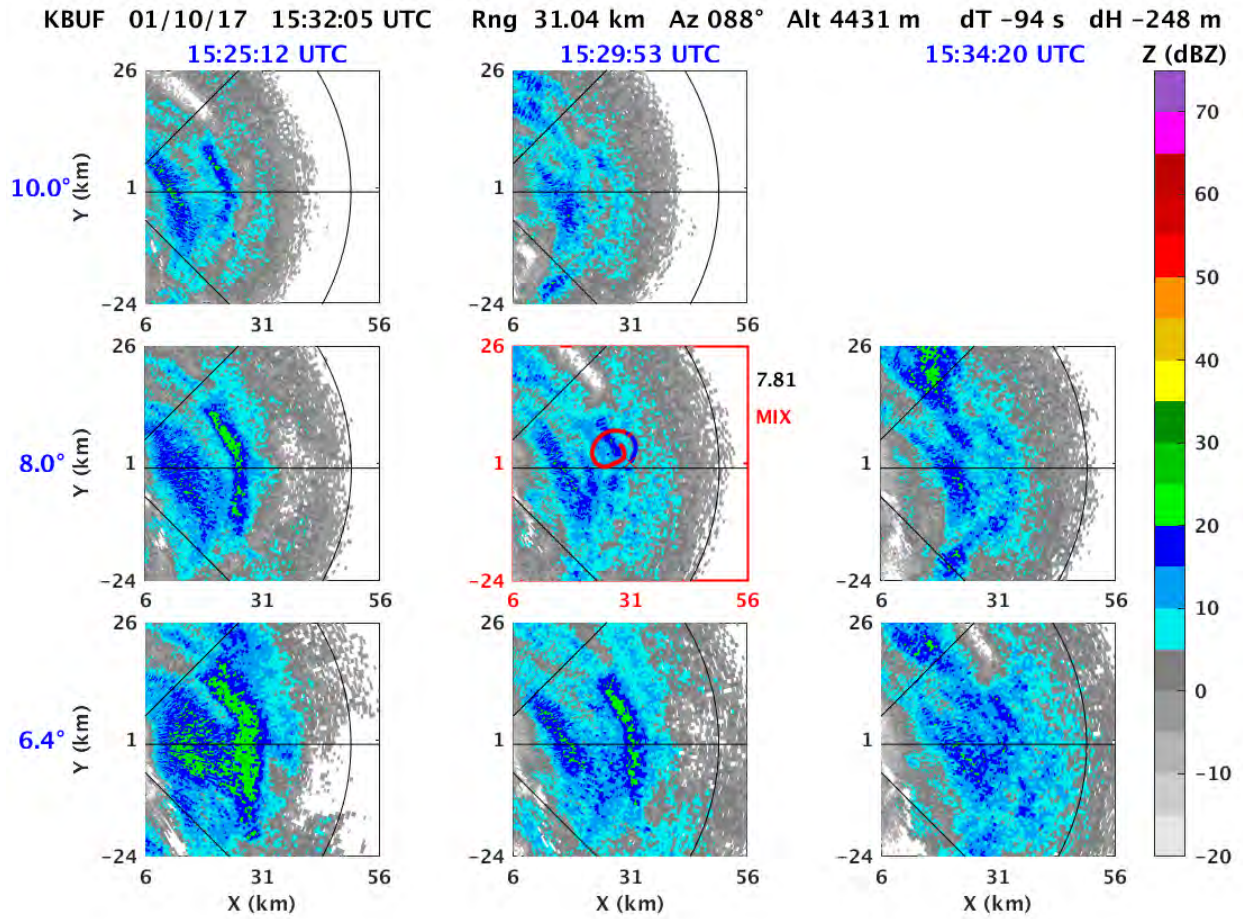


Figure 36. Nine-panel plot of KBUF reflectivity (Z) with the center plot matched nearest in time and space to the Convair-580 position at 15:32:05 UTC for the crystal sandwich case on 10 January 2017. The row (column) of plots show adjacent elevation angles (volume times) increasing from bottom to top (left to right), respectively.

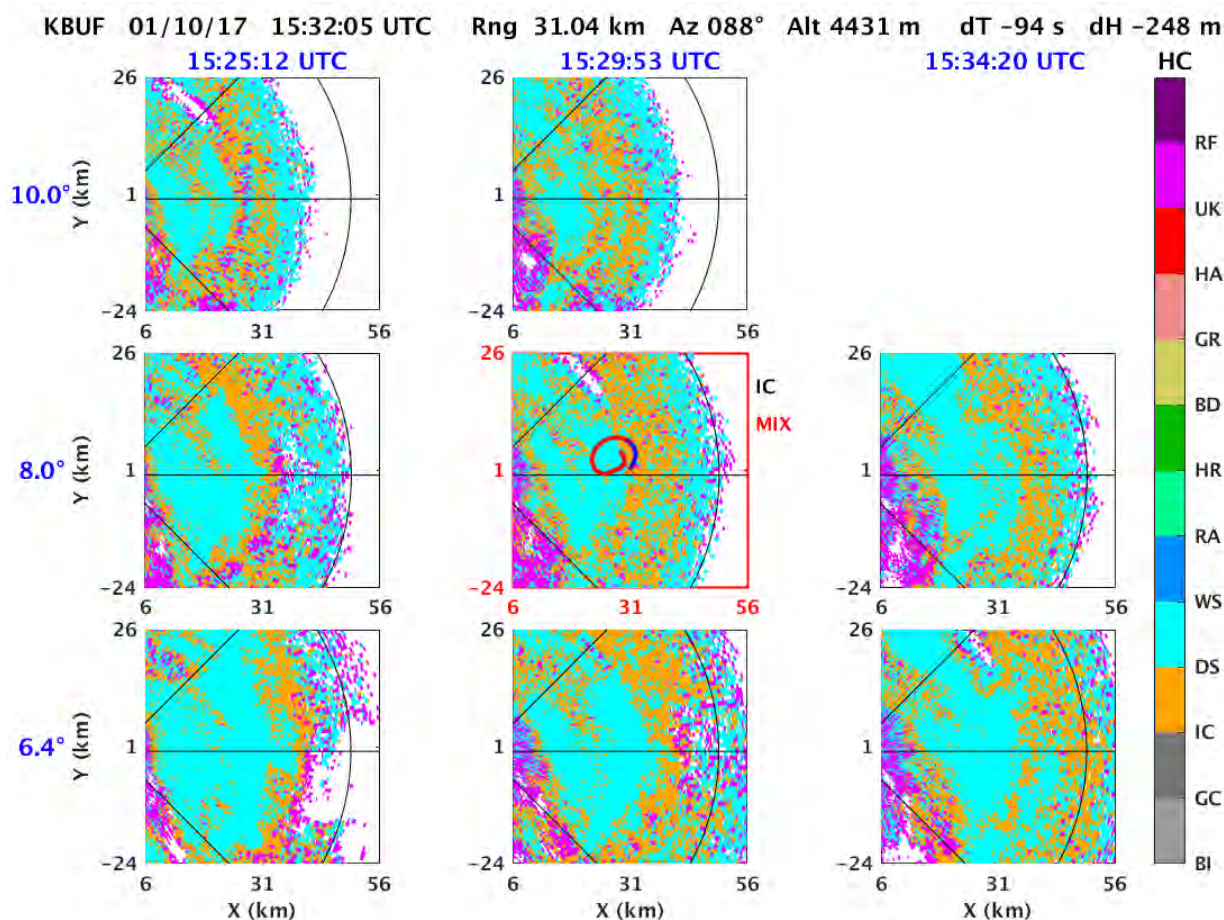


Figure 37. Nine-panel plot of KBUF hydrometeor classification (HC) with the center plot matched nearest in time and space to the Convair-580 position at 15:32:05 UTC for the crystal sandwich case on 10 January 2017. The row (column) of plots show adjacent elevation angles (volume times) increasing from bottom to top (left to right), respectively. Abbreviations of the HC categories include Biological (BI), Ground Clutter (GC), Ice Crystals (IC), Dry Snow (DS), Wet Snow (WS), Rain (RA), Heavy Rain (HR), Big Drops (BD), Graupel (GR), Hail–Rain mix (HA), Unknown (UK), and Range Folding (RF).

### Case III: 24 March 2017

The evidence for this crystal sandwich is diagnosed on the basis of a spiral descent of the aircraft, documented in the time series plots in Figure 38 over the time interval 10:43–10:50 UTC. Irregular shapes dominate the SNDI hydrometeor classifications, but dendrites are evident at the top of the trajectory at 10:43–10:45 UTC (with in situ temperature  $-14^{\circ}$  to  $-12^{\circ}\text{C}$ ) and then needles dominate from 10:48–10:50 UTC (with in situ temperature  $-7^{\circ}$  to  $-5^{\circ}\text{C}$ ). The Nevzorov probe is showing evidence for supercooled water throughout this interval, with maximum value  $>0.2\text{ g/m}^3$  in the dendritic layer and values of the order of  $0.1\text{ g/m}^3$  in the needle layer.

Similar to the situation in Case II, the onboard X-band reflectivity is lowest in the needle region (15–20 dBZ) and somewhat larger (high 20s dBZ) in the dendritic layer. The differential reflectivity is showing positive values throughout the sandwich region, with values up to +1 dB in the dendritic layer and somewhat

smaller positive values,  $<+1$  dB, in the needle layer, all consistent with preferential horizontal orientation of crystal shapes.

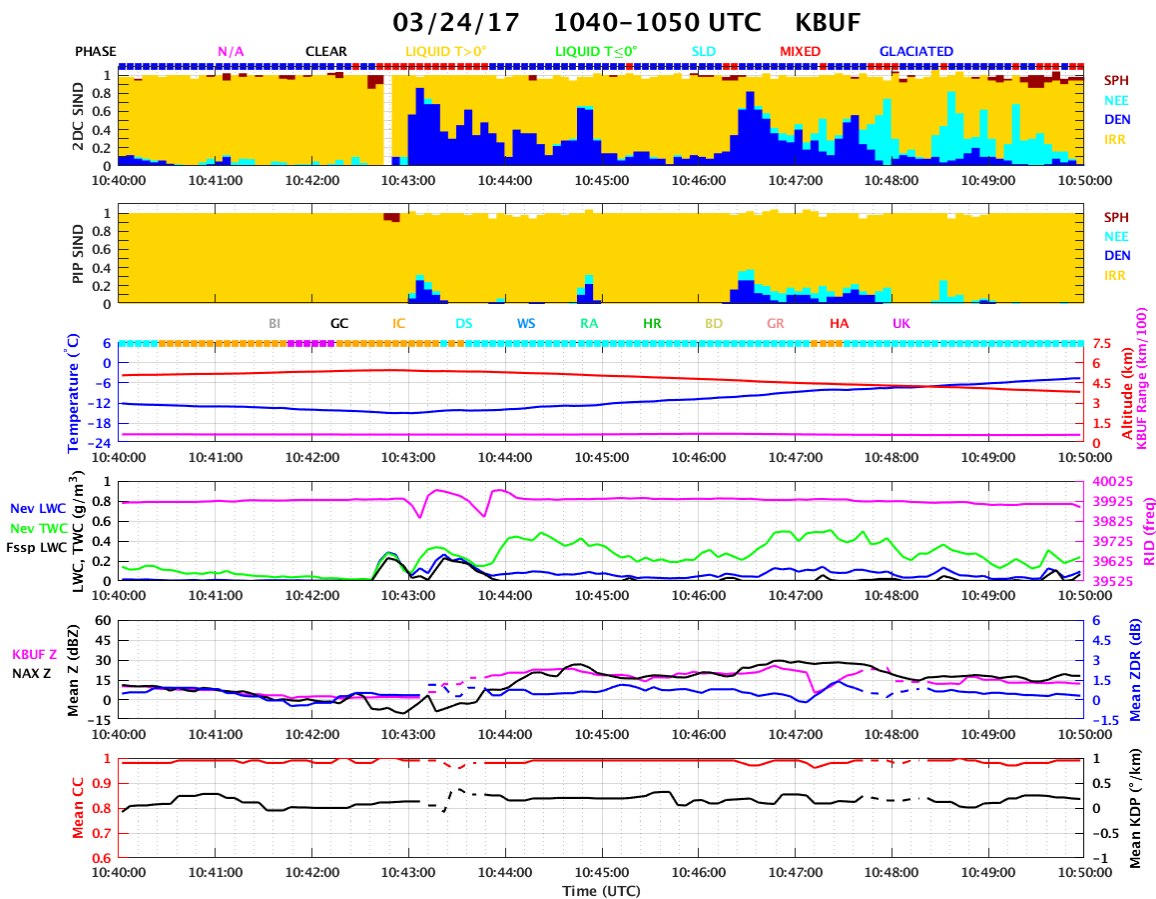


Figure 38. Six-panel plot showing records from the SNDI algorithm (top two panels), in situ temperature, aircraft altitude, Nevzorov LWC and TWC, RID frequency, and FSSP LWC (middle two panels), and onboard X-band radar reflectivity and dual polarimetric quantities from KBUF (bottom two panels) radar for the interval 10:40–10:50 UTC on 24 March 2017.

The reconstructed vertical profile with temperature (Figure 39) shows a broad LWC maximum in the range of  $-6^\circ$  to  $-9^\circ\text{C}$ , with larger values at the upper boundary of the dendritic layer. Samples of 2D-C hydrometeor imagery show that the lower needle layer is co-populated with other shapes that may have descended from higher altitude. The presence of these other shapes is consistent with the somewhat larger reflectivity values, suggestive of aggregation.

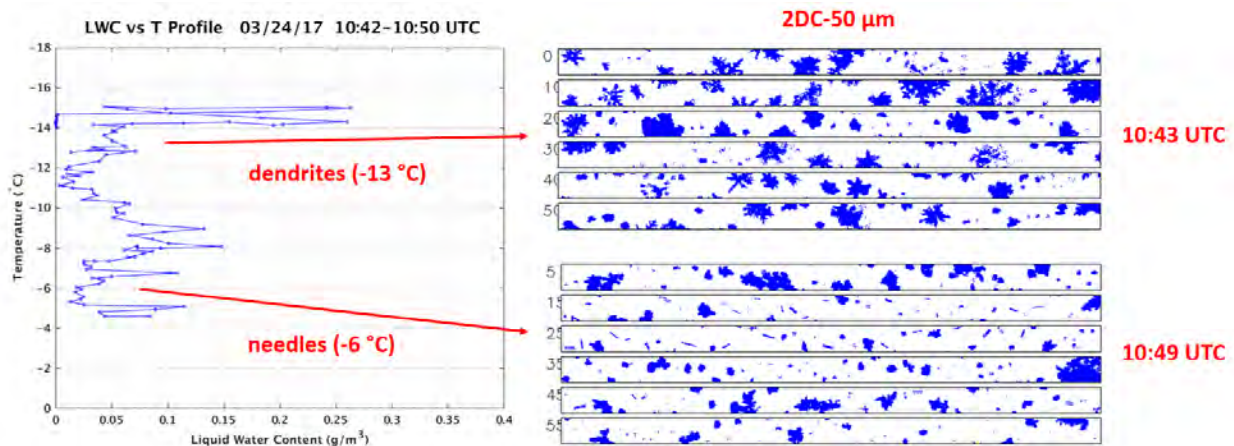


Figure 39. Vertical profile of LWC and samples of the 2D-C hydrometeor imagery at two temperature levels in the profile during a spiral descent between 10:42–10:50 UTC on 24 March 2017.

The flight track shown in the nine-panel plots in Figures 40–42 show the aircraft is spiraling through the lower portion of the crystal sandwich (associated with the needle layer). This layer overlies a ML, associated with markedly enhanced reflectivity, but with a more ragged form than the usual quiescent melting zone. The radar lies southeast of the region depicted in the nine-panel plots, and the ML location is perhaps most easily identified by the presence of the green region of rain beneath it and shown in the lower right-hand corner in each of the  $3.1^\circ$  bottom row panels (Figure 42). In reflectivity (Figure 41), the melting region is characterized by reflectivity generally greater than 35 dBZ and occasionally  $>50$  dBZ. The HCA plots in Figure 42 incorrectly finds graupel (pink color) in such high reflectivity regions, whereas wet aggregates may be more likely. The dominant HC category is again dry snow, consistent with the dominance of the SNDI classification by irregulars rather than distinct crystals.

The expected needle region above the ML is characterized mostly as dry snow in HC (Figure 42) and is evident in a radially-restricted region of enhanced +ZDR in every panel of the nine-panel plots (Figure 40). When ice crystals are apparent in this region, they are generally associated with weak reflectivity ( $<15$  dBZ). The clockwise spiral coincides with this enhanced +ZDR and is primarily shown as blue, indicating glaciated phase with brief intervals shown as red (mixed phase). Unlike in Cases I and II, the +ZDR bright band and upper boundary of the crystal sandwich are not defined in this case due in part to limited radar measurements.

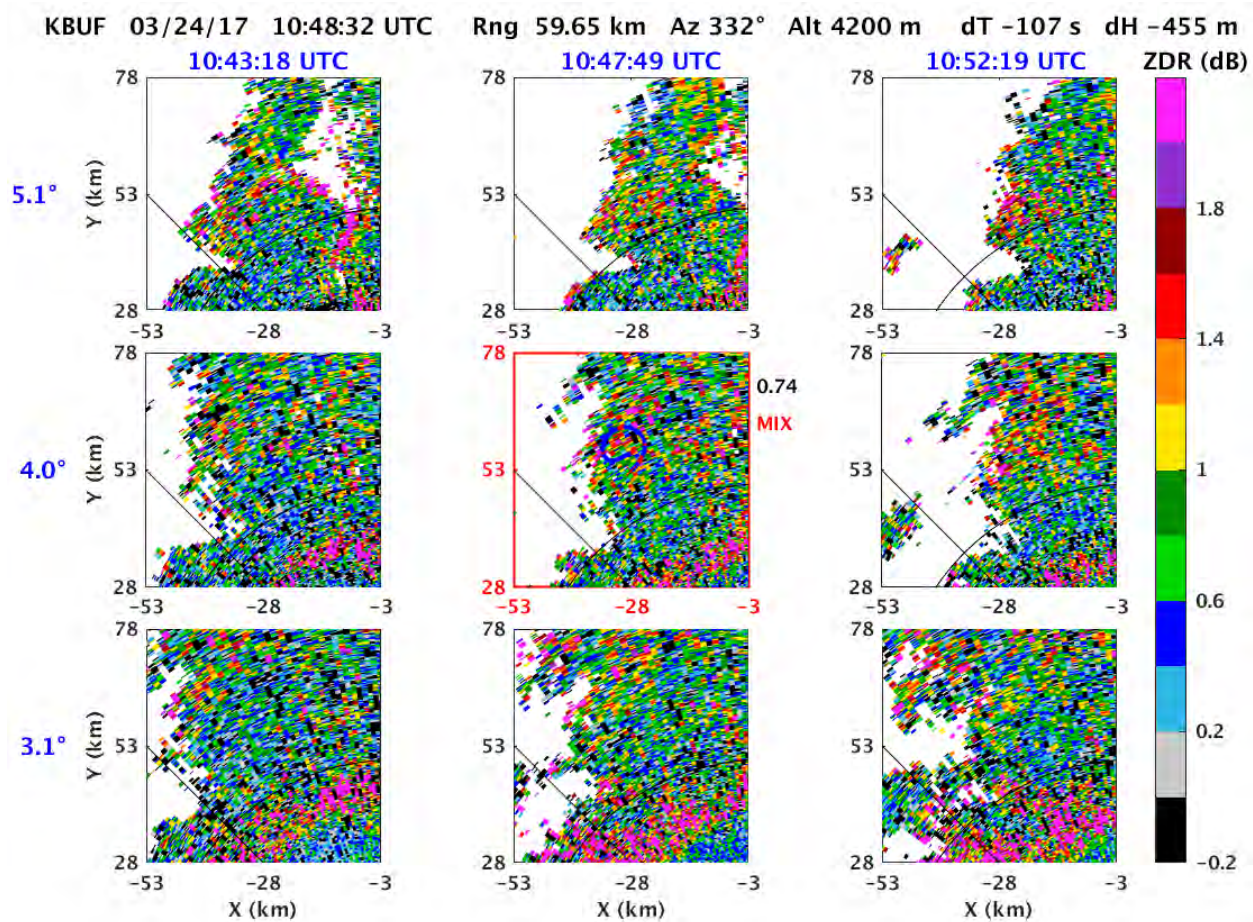


Figure 40. Nine-panel plot of KBUF differential reflectivity (ZDR) with the center plot matched nearest in time and space to the Convair-580 position at 10:48:32 UTC for the crystal sandwich case on 24 March 2017. The row (column) of plots show adjacent elevation angles (volume times) increasing from bottom to top (left to right).

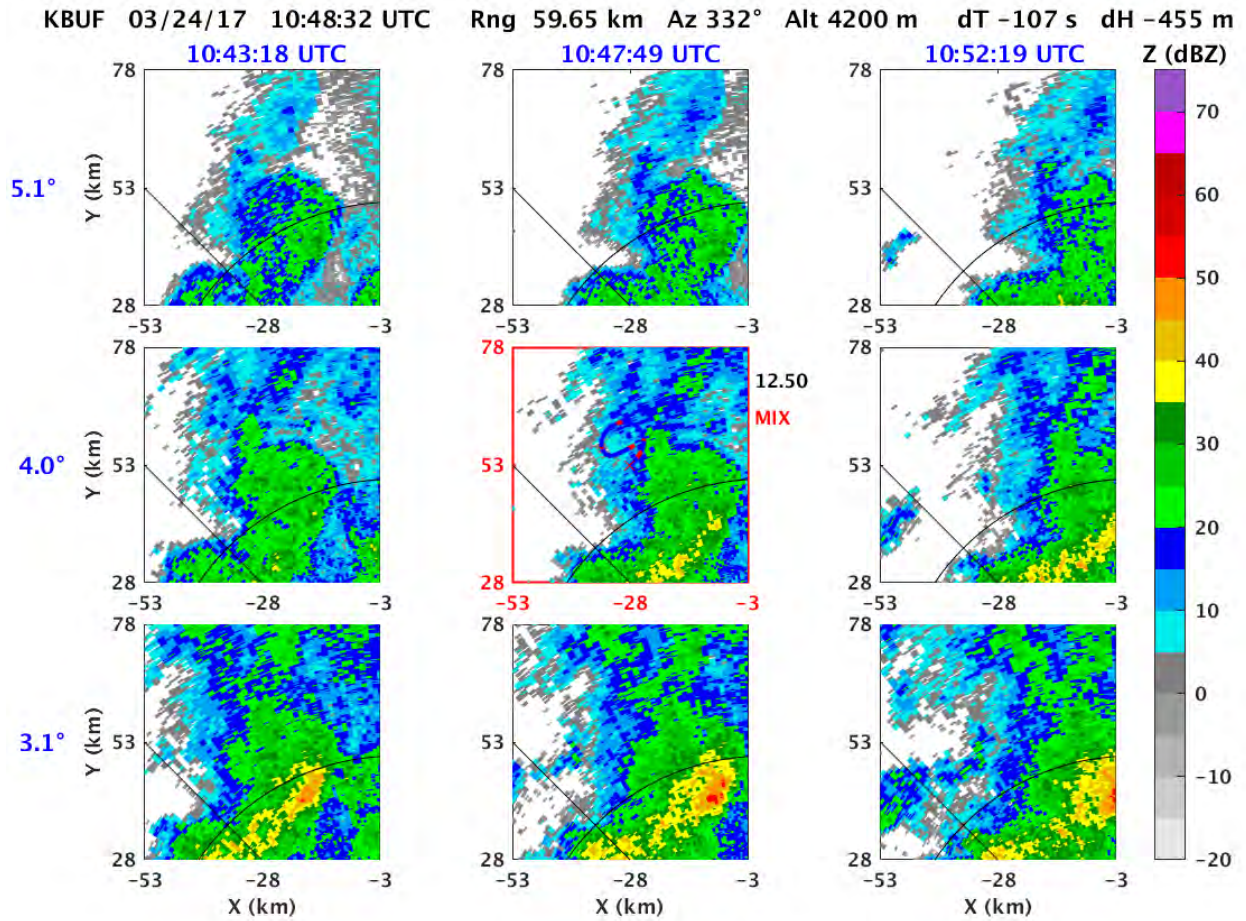


Figure 41. Nine-panel plot of KBUF reflectivity ( $Z$ ) with the center plot matched nearest in time and space to the Convair-580 position at 10:48:32 UTC for the crystal sandwich case on 24 March 2017. The row (column) of plots show adjacent elevation angles (volume times) increasing from bottom to top (left to right), respectively.

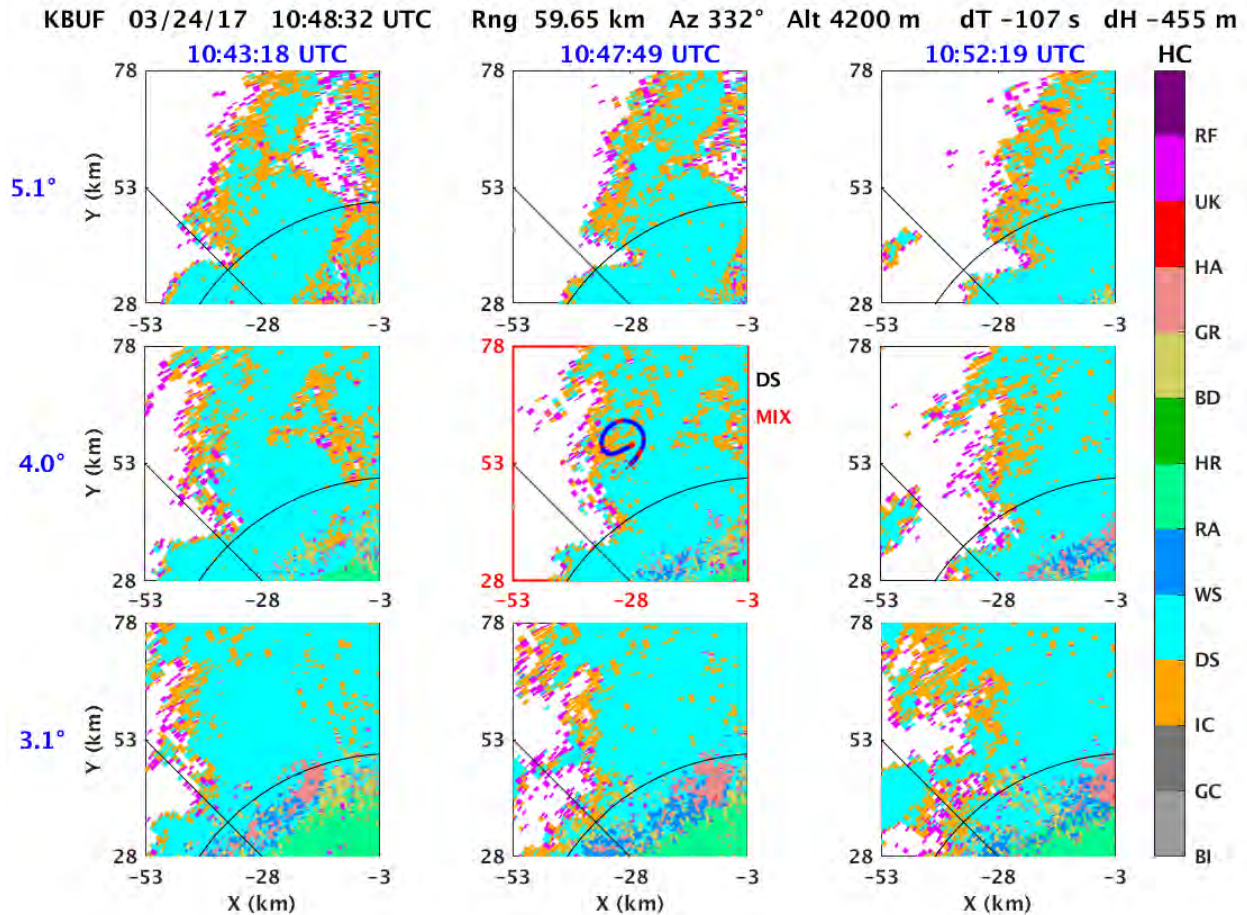


Figure 42. Nine-panel plot of KBUF hydrometeor classification (HC) with the center plot matched nearest in time and space to the Convair-580 position at 10:48:32 UTC for the crystal sandwich case on 24 March 2017. The row (column) of plots show adjacent elevation angles (volume times) increasing from bottom to top (left to right), respectively. Abbreviations of the HC categories include Biological (BI), Ground Clutter (GC), Ice Crystals (IC), Dry Snow (DS), Wet Snow (WS), Rain (RA), Heavy Rain (HR), Big Drops (BD), Graupel (GR), Hail–Rain mix (HA), Unknown (UK), and Range Folding (RF).

#### Case IV: 25 March 2017

The documentation of this crystal sandwich case is shown in the time series plots of Figure 43. The “sandwich” is spanned by the aircraft in a spiral ascent in the time interval 14:15–14:22 UTC. Needles are the dominant crystal type in the SNDI analysis between 14:15–14:16 UTC (where the in situ air temperature is  $T = -5^{\circ}\text{C}$ ), but this changes to a predominance of dendrites between 14:19–14:21 UTC (where in situ air temperature is  $T = -12^{\circ}\text{C}$ ). The Nevzorov LWC is weak in the dendritic layer (with minimal response registered on the Rosemount probe), but increases into the needle layer to maximize at  $0.1\text{ g/m}^3$ .

The onboard X-band reflectivity data show larger values in the needle layer (22–28 dBZ) and smaller values (14–21 dBZ) in the dendrite layer, which is an opposite response to other crystal sandwich cases and likely attributed to aggregation of dendritic crystals descending into the needle layer from above (see 2D-C imagery in Figure 44). The NEXRAD ZDR is near zero to a few tenths of a dB in the needle layer, but is

showing slightly higher positive values ( $\sim 0.6$  dB) at 14:21 UTC in the dendritic layer, consistent with expectations (Williams *et al.* [84]).

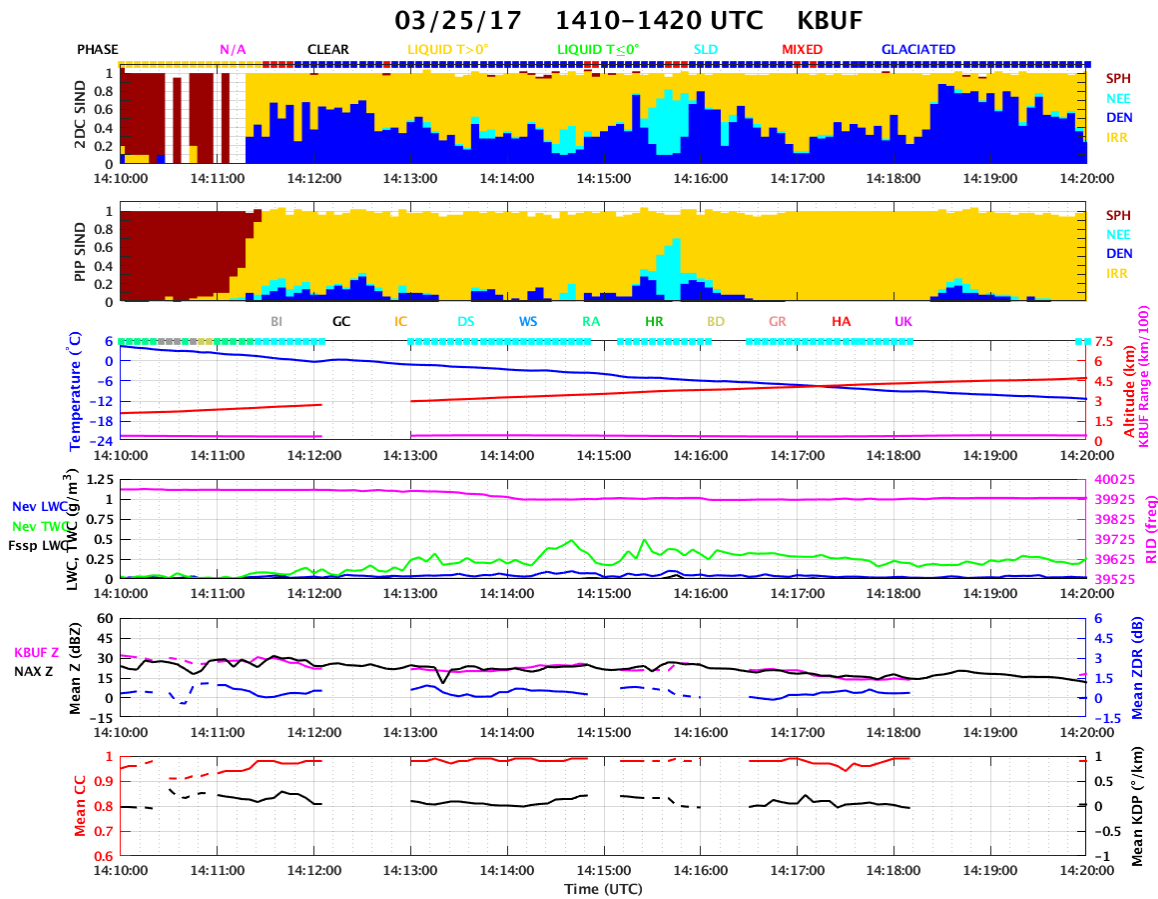


Figure 43. Six-panel plot showing records from the SNDI algorithm (top two panels), in situ temperature, aircraft altitude, Nevzorov LWC and TWC, RID frequency, and FSSP LWC (middle two panels), and onboard X-band radar reflectivity and dual polarimetric quantities from KBUF (bottom two panels) radar for the interval 14:10–14:20 UTC on 25 March 2017.

The reconstructed vertical profile of temperature and LWC is shown in Figure 44 for this case. As noted in the time series plots, the LWC in this case is clearly larger in the lower (needle) portion of the crystal sandwich than in the dendrite layer. The dendritic crystals appear to be mixed in with the needles to some extent, suggesting descent from the region of lower temperature at higher altitude.

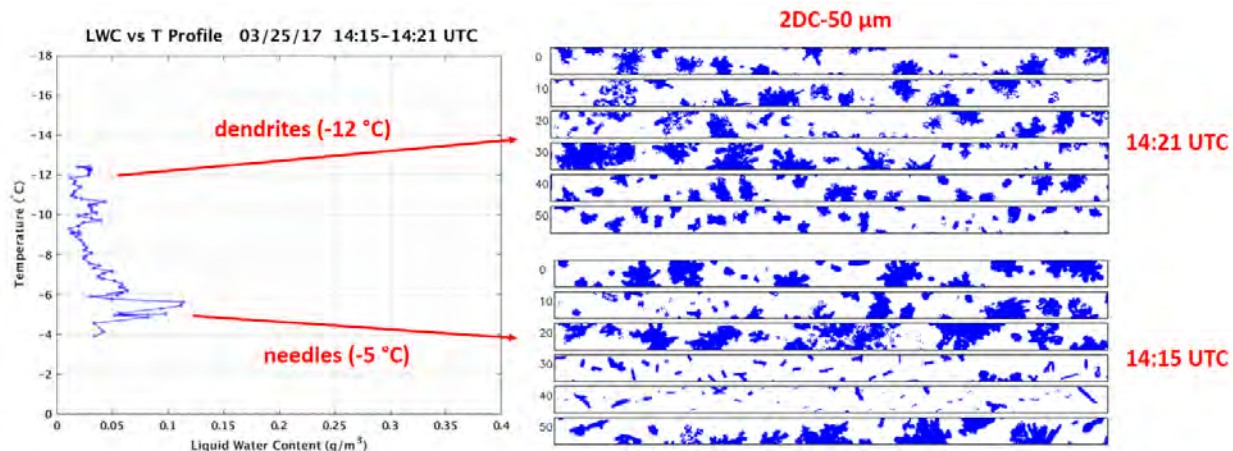


Figure 44. Vertical profile of LWC and samples of the 2D-C hydrometeor imagery at two temperature levels in the profile during a spiral ascent between 14:15–14:21 UTC on 25 March 2017.

The crystal sandwich is perhaps best identified in the radar observations in the nine-panels of HC in Figure 47. The radar lies west of the region depicted here and the ML (rain beneath it) to the left and the ice crystals layer to the right together bound the crystal sandwich, with the aircraft spiral (with red and blue traces indicative of mixed and glaciated phase, respectively) in the inferred needle region, again characterized more often as dry snow than ice crystals. This circumstance is interpreted again as the result of aggregation of the dendritic crystals from the top of the sandwich and the attendant increase in Z (Figure 46) and decrease in ZDR, as the isolated crystal anisotropy is lost in the aggregation.

The nine-panel plot of differential reflectivity in Figure 45 shows two distinct rings (in the majority of panels), the left ring associated with the ML and the right one being the +ZDR bright band associated with the dendritic layer. Localized anomalies of larger positive ZDR (some  $>+2$  dB) are generally associated with smaller reflectivity ( $<20$  dBZ).

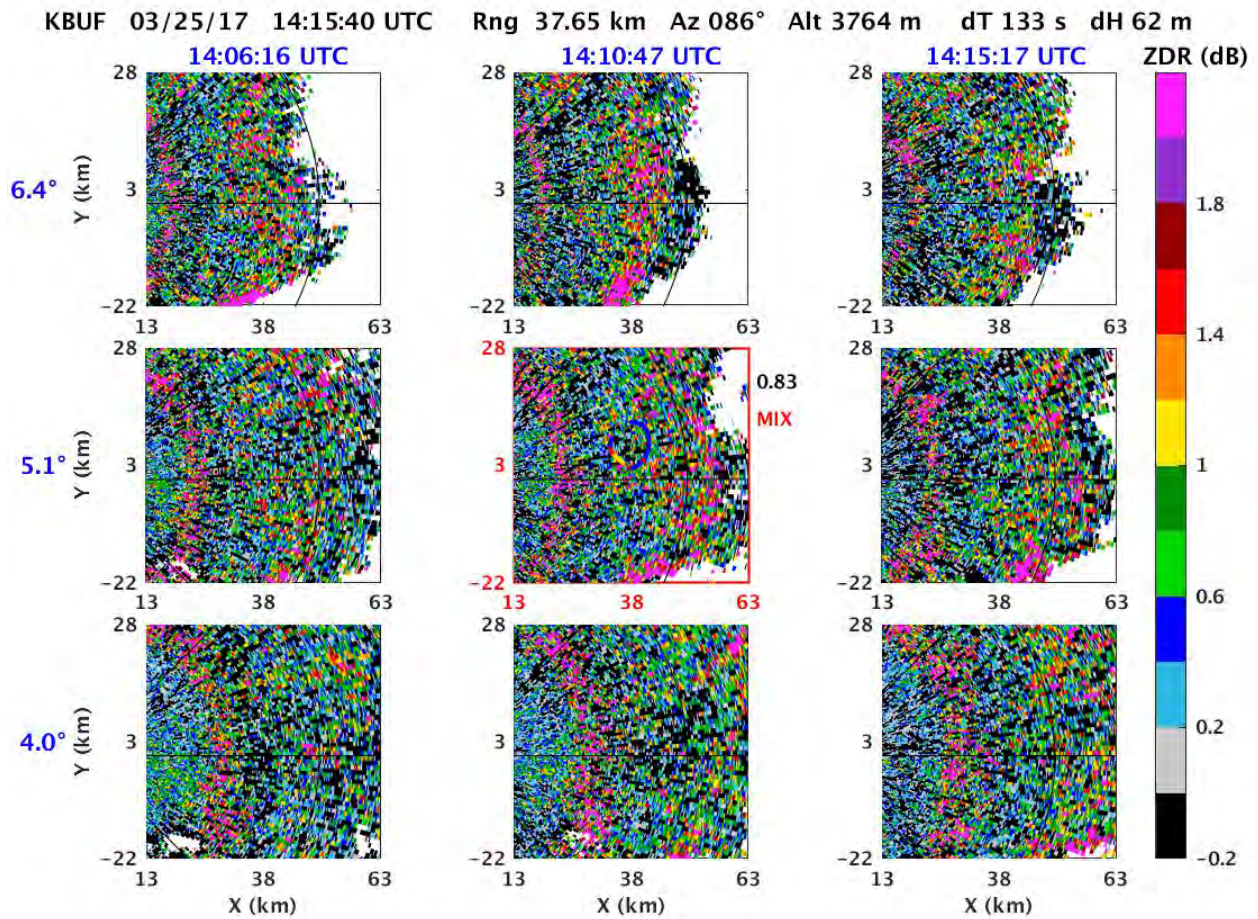


Figure 45. Nine-panel plot of KBUF differential reflectivity (ZDR) with the center plot matched nearest in time and space to the Convair-580 position at 14:15:40 UTC for the crystal sandwich case on 25 March 2017. The row (column) of plots show adjacent elevation angles (volume times) increasing from bottom to top (left to right), respectively.

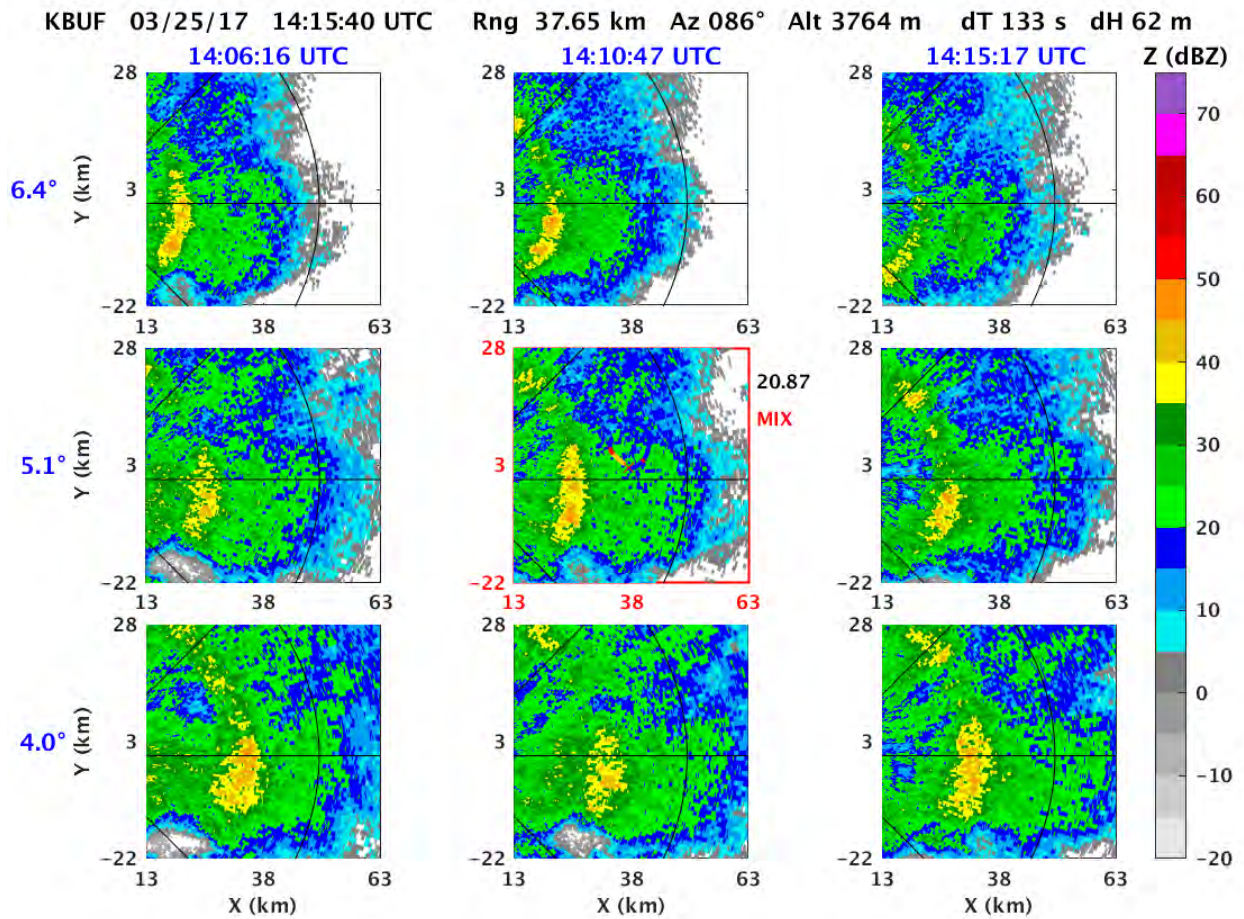


Figure 46. Nine-panel plot of KBUF reflectivity (Z) with the center plot matched nearest in time and space to the Convair-580 position at 14:15:40 UTC for the crystal sandwich case on 25 March 2017. The row (column) of plots show adjacent elevation angles (volume times) increasing from bottom to top (left to right), respectively.

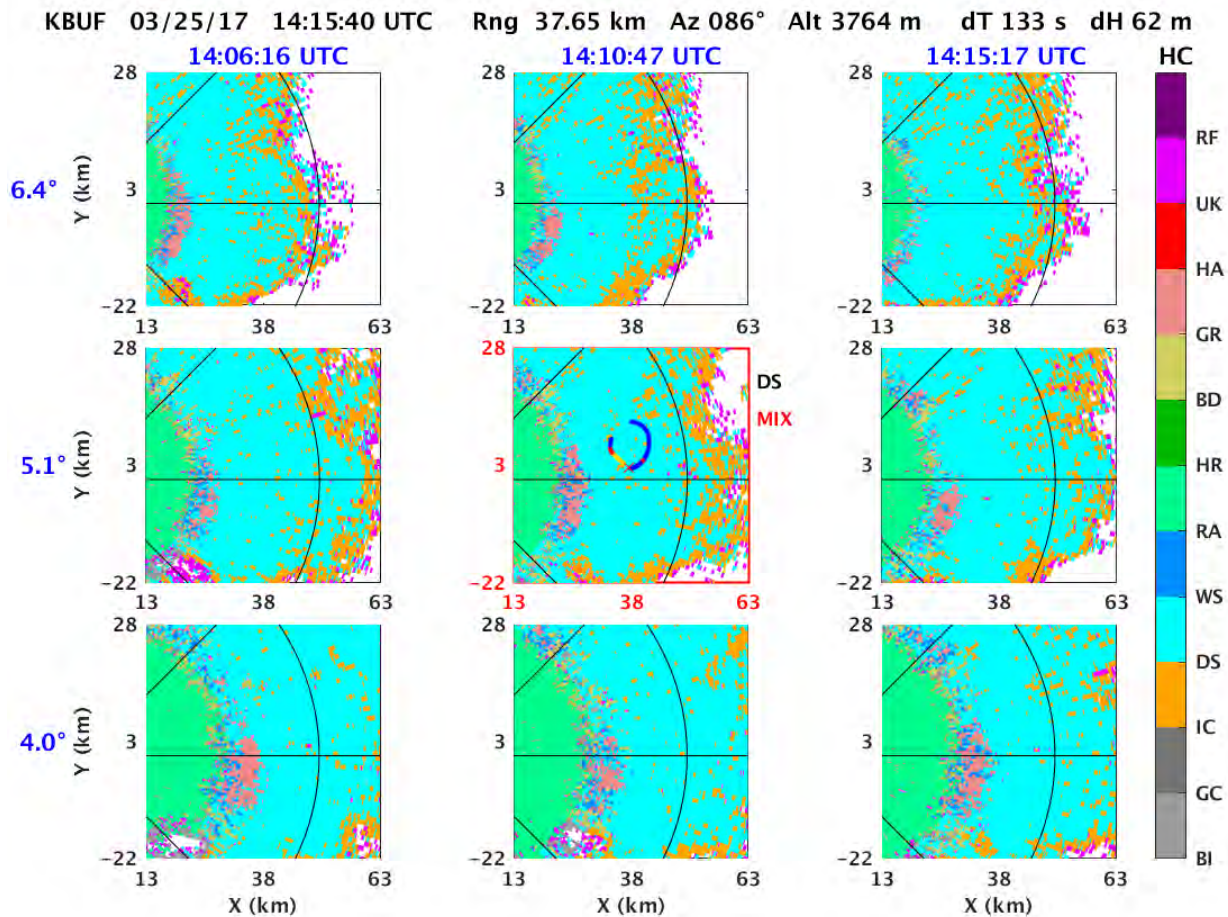


Figure 47. Nine-panel plot of KBUF hydrometeor classification (HC) with the center plot matched nearest in time and space to the Convair-580 position at 14:15:40 UTC for the crystal sandwich case on 25 March 2017. The row (column) of plots show adjacent elevation angles (volume times) increasing from bottom to top (left to right), respectively. Abbreviations of the HC categories include Biological (BI), Ground Clutter (GC), Ice Crystals (IC), Dry Snow (DS), Wet Snow (WS), Rain (RA), Heavy Rain (HR), Big Drops (BD), Graupel (GR), Hail–Rain mix (HA), Unknown (UK), and Range Folding (RF).

### 11 November 2003: An example from AIRS II

One final example of evidence for a robust crystal sandwich in the presence of weak reflectivity is taken from an unpublished presentation by Mengistu Wolde of NRC from 11 November 2003, and summarized in Figure 48. The Convair-580 aircraft was also used for this documentation during the second Alliance Icing Research Study (AIRS II) campaign (Wolde *et al.* [92]). Vertical profiles of LWC, W-band radar reflectivity, and differential reflectivity are all shown, with 100 m averaging of all quantities. The 2D-C imagery is also shown. Dendrites are evident near the top of the profile (4.7 km altitude) in the 20:17 UTC time frame when the ZDR values are maximum and reaching +2 dB. Needles are evident at lower altitude (~3.5 km) in the 20:43–20:46 UTC time frame, and a local maximum in LWC, reaching  $0.2 \text{ g/m}^3$  is present just above the needle region. These observations are entirely consistent with the four cases from BAIRS flights discussed previously.

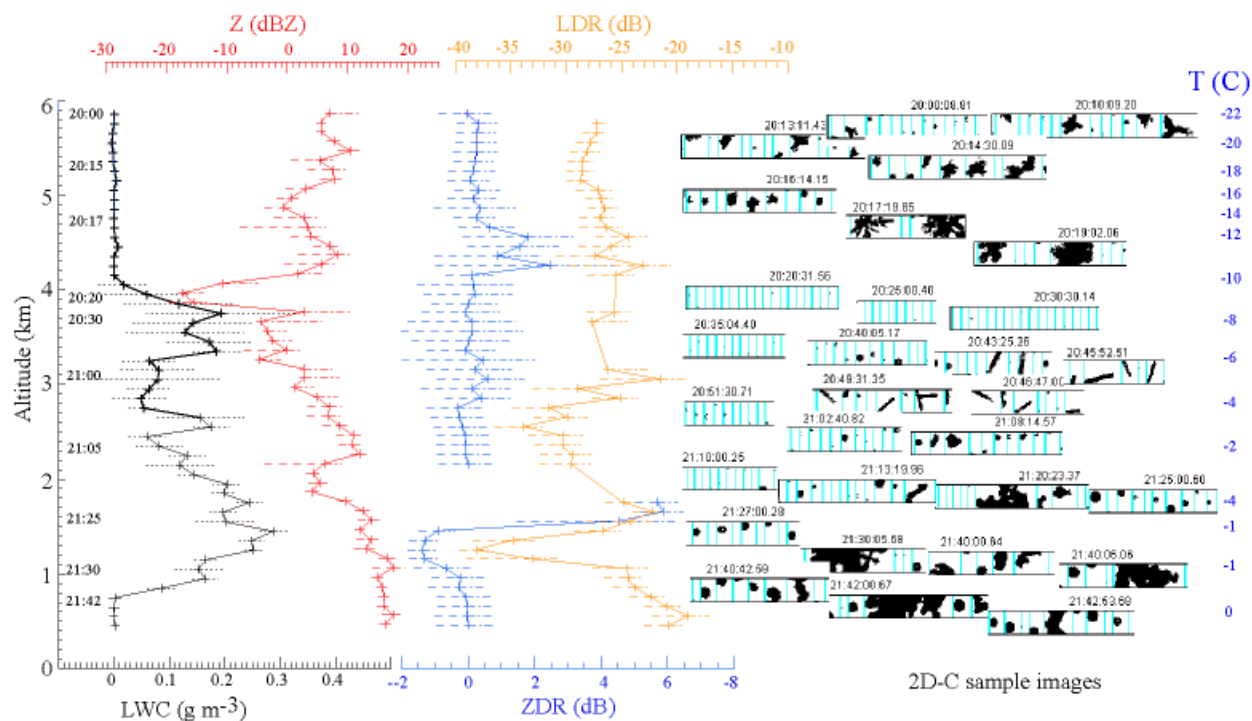


Figure 48. Evidence for crystal sandwich structure in vertical profiles of LWC (black), reflectivity (red), ZDR (blue), and LDR (linear depolarization ratio; orange) from the AIRS-II aircraft campaign on 11 November 2003 (Wolde *et al.* [92]).

#### 4.2.4 Evidence for Crystal Sandwich Structure in NEXRAD PPI Scans in Winter Storms

MIT LL collected a large number of examples of NEXRAD PPI scans in winter storms subsequent to BAIRS II, from a substantial number of separate radars using the Gibson Ridge Software GR2Analyst radar display tool, showing evidence for strong positive differential reflectivity from two distinct altitudes not associated with a ML (and in situ temperatures from a supporting model) and in the presence of gentle ascent. (These data on ZDR were not corrected in the manner described for the BAIRS II NEXRAD data as described in Section 2.4.) These examples constitute additional evidence for the crystal sandwich structure in dual polarimetric radar that has now been documented in situ with the Convair-580 observations, with an upper +d ZDR bright band associated with dendritic crystals at temperatures in the range  $-10^{\circ}$  to  $-14^{\circ}\text{C}$  and a lower +n ZDR bright band associated with needle crystals in a temperature range of  $-3^{\circ}$  to  $-7^{\circ}\text{C}$ . The respective temperature ranges are consistent with laboratory diffusion chamber measurements (Bailey and Hallett [1]) of the growth of flat plate crystals/dendrites and needles. A list of these NEXRAD cases, including dates, times, NEXRAD radar, warm/cold classification (radar evidence/absence of ML), and additional information from proximity soundings showing presence/absence of stable isothermal layers, is shown in Table 2. The common occurrence of crystal sandwich structure is good news from the standpoint of dual polarimetric detection of aircraft icing conditions, since supercooled water is physically linked with the water-saturated conditions needed for these two prevalent crystal types, and that has now been confirmed in the aircraft observations at least once on every one of five flights in BAIRS II (Williams *et al.* [89]).

**TABLE 2**  
**NEXRAD Radar Evidence for Crystal Sandwiches**

<b>Date</b>	<b>Time (UTC)</b>	<b>Radar</b>	<b>Warm (W)/Cold (C)</b>	<b>Temperature Inversion/Isothermal</b>
10 Jan 2017	15:25:13	KBUF	W	Yes
12 Feb 2017	18:56:00	KBOX	C	Yes
9 Dec 2017	08:01:25	KBOX	C	Yes
19 Dec 2017	17:04:03	KRTX	W	No
20 Dec 2017	15:21:02	KMRX	W	No
20 Dec 2017	15:42:00	KRAX	W	No
27 Dec 2017	16:52:55	KMHX	W	Yes
4 Jan 2018	19:09:02	KBOX	C	Yes
12 Jan 2018	15:31:05	KDTX	C	Yes
17 Jan 2018	14:33:00–15:00:00	KBOX	C	Yes
29 Jan 2018	15:05:45	KDTX	C	Yes
7 Feb 2018	15:40:58	KBOX	W	Yes
12 Feb 2018	14:58:31	KOKX	W	Yes
16 Feb 2018	14:10:43	KOKX	W	No
23 Apr 2018	19:07:07	KFCX	W	Yes
18 May 2018	13:58:39	KDOX	W	No

The physical interpretation of the crystal sandwich involves the growth of the two dominant crystals in two distinct temperature ranges by water vapor diffusion in the presence of gentle warm frontal ascent, at a speed earlier estimated in the range of 1 to 5 cm/s. The faster-growing flat-plate crystals will develop fall speeds with respect to still air up to 0.6 m/s (Hobbs [32]) and if present in sufficient numbers, they will begin to aggregate into snowflakes at altitudes below the upper +d ZDR layer. This process will increase the reflectivity, but will also reduce the differential reflectivity since the snowflakes are markedly more isotropic than the original flat-plate crystals. The larger reflectivity of the aggregates may then overwhelm the return from the needle crystals in the lower layer, and may account for the consistent finding in the PPI scans that the azimuthal extent of the flat-plate crystals above is almost invariably greater than the azimuthal extents of the +n ZDR needle layer below. Cases with two contiguous layers of crystals and with azimuthally complete rings at two distinct ranges in the PPI have not been found. An explanation for this is that the (likely) surfaces of sloping gentle ascent are most fully detectable with a favorable combination of slope and combined set of adjacent radar scanning angles.

Certain predictions arise out of this simple picture for the crystal sandwich:

- (i) The differential reflectivity of the upper +d ZDR layer should be generally greater than that of the lower +n ZDR layer, in keeping with theoretical predictions for oblate and prolate shapes, respectively (Hogan *et al.* [34]).
- (ii) The reflectivity associated with pure crystals and without appreciable aggregation will be thresholded at some value that has been previously estimated (Lim *et al.* [53]) at 10 dBZ. Accordingly, very gentle ascent of the air is needed for crystal storms. (In future work, Z/ZDR scatterplots are needed for the entire needle temperature range to look for two clusters of data points: high Z/low ZDR characterizing aggregates and low Z/high ZDR characterizing needles and dendrites.)
- (iii) The presence of aggregation, characterized by larger Z values, may interfere with and even prevent the detection of the +n ZDR layer beneath. Aggregates mixed with needles may mask the needle response.
- (iv) In situ data support the notion that this radar feature is likely associated with supercooled liquid water particularly to an altitude up to or into the +d ZDR layer.

Toward making further analyses of these cases, four-panel radar PPI plots of Z, ZDR, CC, and KDP have been constructed and measured. Four examples (9 December 2017, KBOX radar; 20 December 2017, KMRX radar; 27 December 2017, KMHX radar; and 7 February 2018, KBOX radar) have been included here in Figures 49–52, respectively, and with specific extracted radar quantities shown in Table 3. Included here are estimates for the largest Z and ZDR values in the +d ZDR and the +n ZDR crystal layers, and an estimate of the background Z and ZDR in the altitude range where the lower +n ZDR layer is expected and within regions with no observed positive enhancement in ZDR. The ZDR data were not adjusted in these examples, unlike the adjustments applied to the BAIRS II cases using the method described in Section 2.4.

KBOX 12/09/17 08:01:25 UTC EI 9.9°

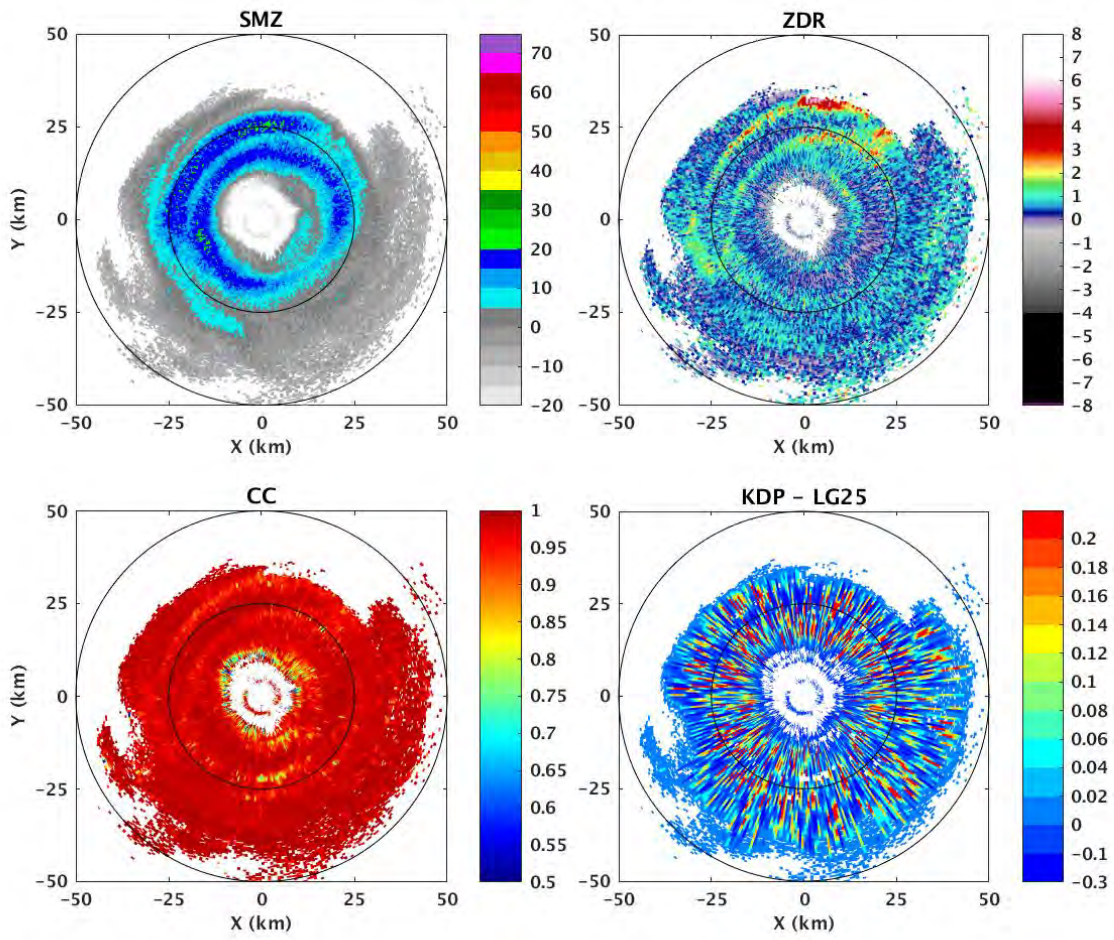


Figure 49. Four-panel PPI plot of reflectivity (upper left), ZDR (upper right), CC (lower left), and KDP (lower right) for the KBOX 9.9° elevation angle at 08:01:25 UTC on 9 December 2017.

KMRX 12/20/17 15:21:02 UTC EI 19.5°

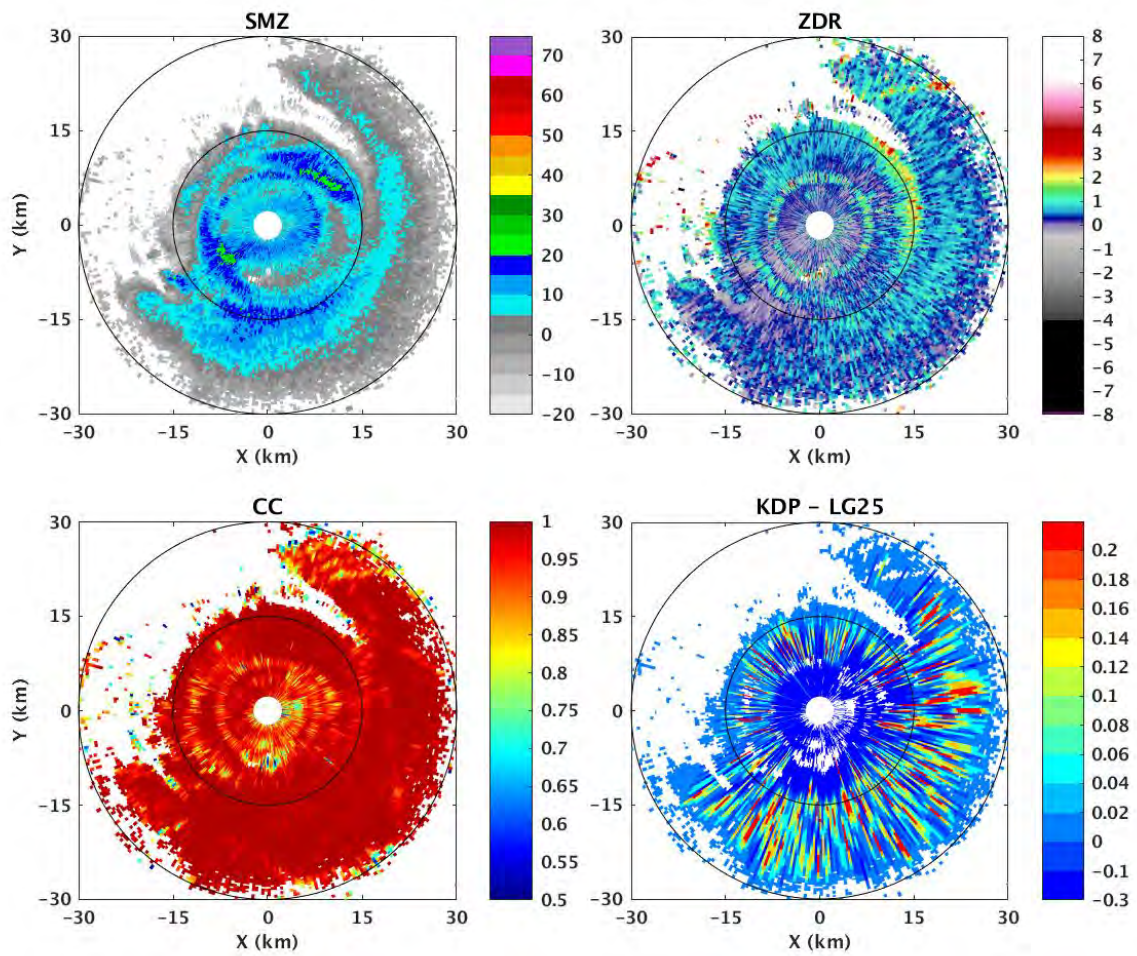


Figure 50. Four-panel PPI plot of reflectivity (upper left), ZDR (upper right), CC (lower left), and KDP (lower right) for the KMRX 19.5° elevation angle at 15:21:02 UTC on 20 December 2017.

KMHX 12/27/17 16:52:55 UTC EI 9.9°

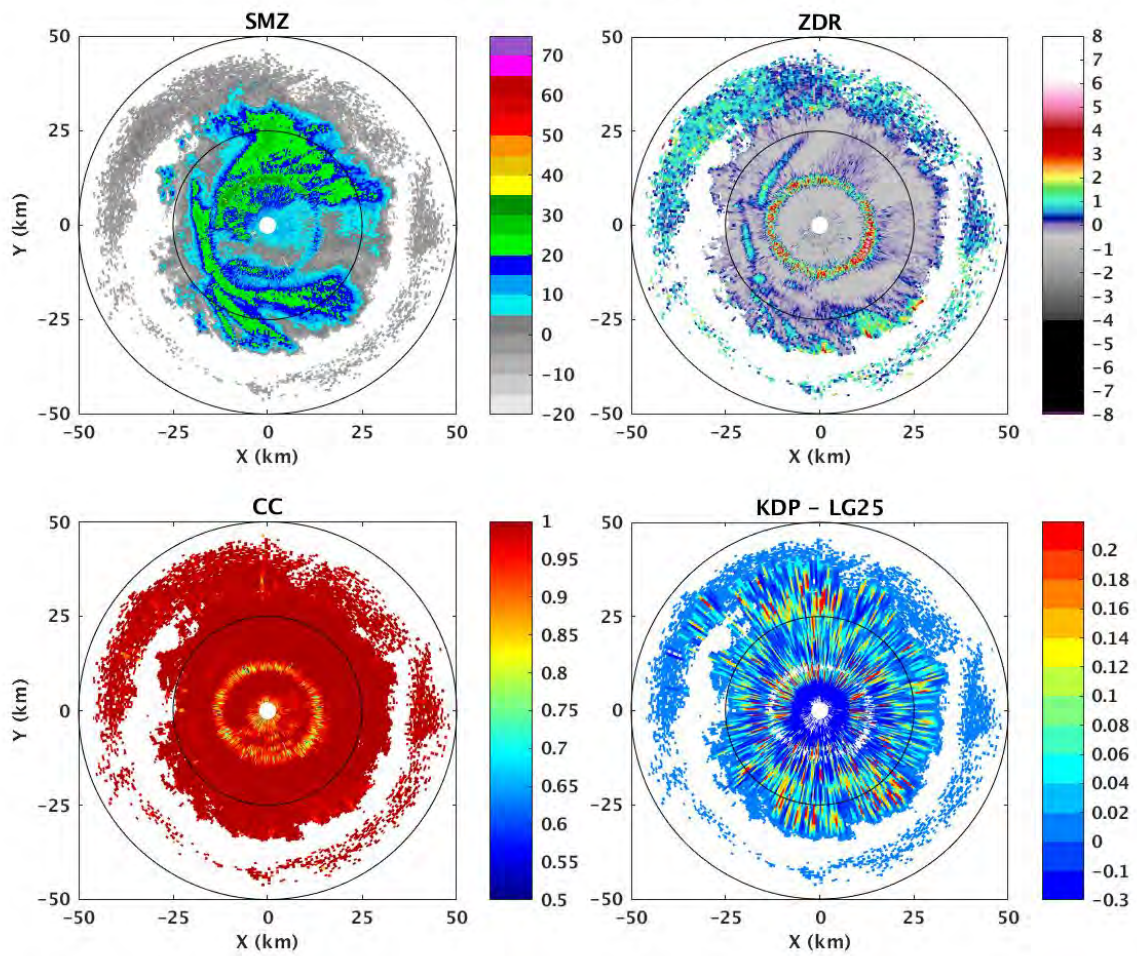


Figure 51. Four-panel PPI plot of reflectivity (upper left), ZDR (upper right), CC (lower left), and KDP (lower right) for the KMHX 9.9° elevation angle at 16:52:55 UTC on 27 December 2017.

KBOX 02/07/18 15:40:58 UTC EI 19.5°

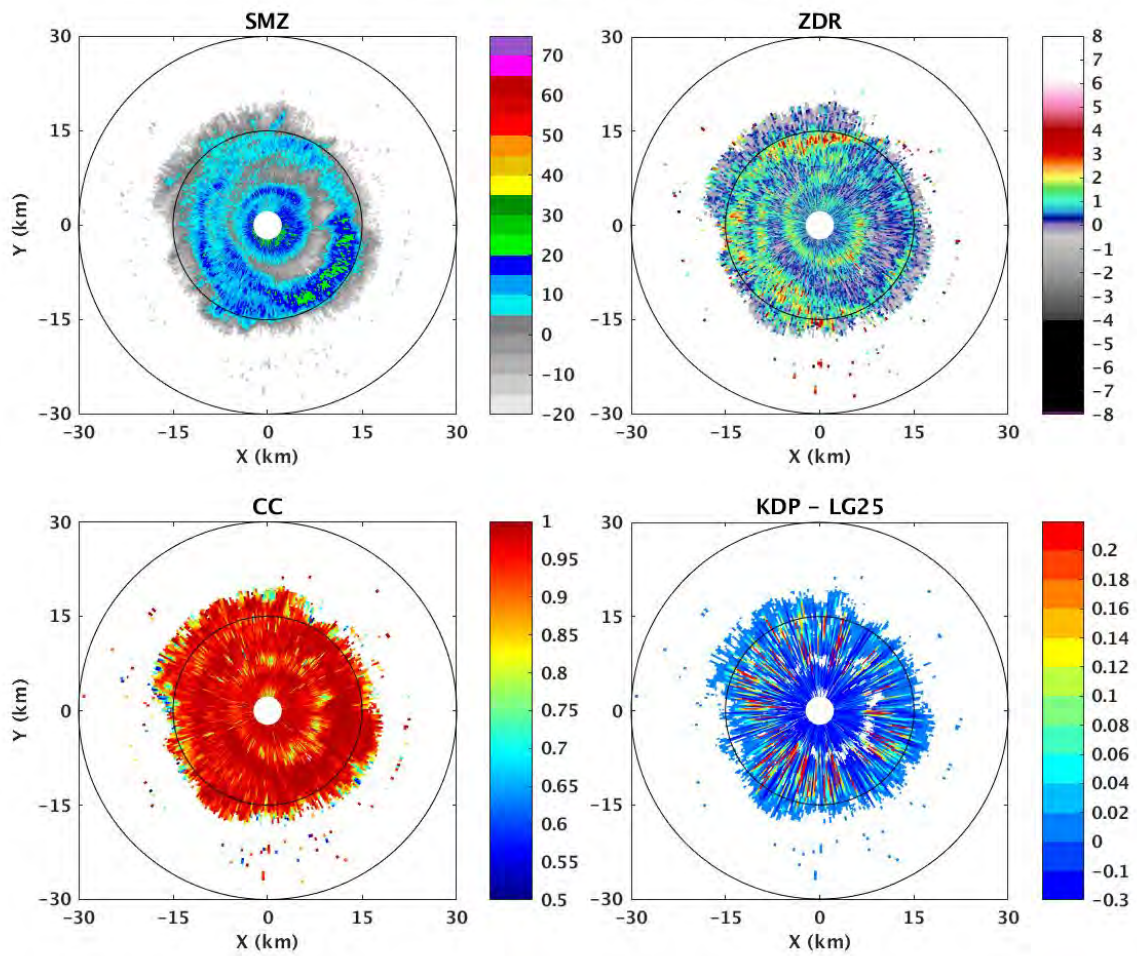


Figure 52. Four-panel PPI plot of reflectivity (upper left), ZDR (upper right), CC (lower left), and KDP (lower right) for the KBOX 19.5° elevation angle at 15:40:58 UTC on 7 February 2018.

**TABLE 3**  
**Dual Polarimetric Parameters for Four Crystal Sandwich Cases on NEXRAD Radars**

Parameter	KBOX 12/09/17		KMRX 12/20/17		KMHX 12/27/17		KBOX 2/7/18	
	Z	ZDR	Z	ZDR	Z	ZDR	Z	ZDR
Dendrite layer max	15	3.8	22	3.1	14.5	2.3	16	5.1
Needle layer max	20	3.3	19.5	2.3	16.5	2.1	18	3
Background max	23	2.1	25.5	1.1	20.5	0.8	19	2.7

These results are generally consistent with the expectations. That is to say that the ZDR values for the upper layer (dendrites) are larger than for the lower layer (needles), though the measured values in both cases are notably smaller than the theoretical predictions (Hogan *et al.* [34]). The maximum ZDR values for the crystal layers are within a few dB of the predicted threshold required for crystal layers. The +n ZDR layer Z values are remarkably consistent from case to case. Toward evaluating the suggestion that the +n ZDR layers may be masked by aggregation, we returned to the 10 +ZDR bright band examples in Williams *et al.* [85], for which no +n ZDR layers were discernible. Now we have a tentative explanation. In most cases, the background levels in the needle range of temperature are ~5 dBZ greater than those found for Table 3. Clearly, more cases are needed to establish meaningful statistics here and eventually the creation of an algorithm for crystal sandwich identification.

#### 4.2.5 The Possible Graupel Factory within the Crystal Sandwich

Fukuta [22] and Fukuta and Takahashi [23] first pointed out that the in situ temperature zone between where needles are prevalent ( $-4^{\circ} < T < -7^{\circ}\text{C}$ ) and where dendrites/plates are prevalent ( $-9^{\circ} < T < -16^{\circ}\text{C}$ ) may be most favorable to a riming process and the formation of graupel. This same temperature zone is by definition the central part of the ice crystal sandwich that has been linked with the presence of supercooled water and hence with aircraft icing conditions (Williams *et al.* [87], [89]). This section is concerned with an alternative physical explanation to the one provided by Fukuta and Takahashi [23] for why the “no-man’s land” between dendrites above and needles below will be more favorable to riming than in the two bounding crystal layers.

This alternative explanation is based on predictions for the fall speeds of crystals in the three temperature regimes of the crystal sandwich: (1) dendrites/plates ( $-9^{\circ} < T < -16^{\circ}\text{C}$ ), (2) needles ( $-4^{\circ} < T < -7^{\circ}\text{C}$ ), and (3) isometric crystals in the no-man’s land ( $-7^{\circ} \leq T \leq -9^{\circ}\text{C}$ ). We will also assume that the crystal growth in these three regimes is by (1) extension of the a-axis of the crystal (lying in the plane of the hexagon) to form a dendrite or plate, (2) extension of the c-axis of the crystal (running perpendicular to the hexagonal plane) to form a long needle, and (3) roughly equal extension of both a-axis and c-axis to form an isometric crystal (to be assumed a sphere in this simplified treatment).

In all these calculations, steady crystal fall speeds are predicted based on the traditional assumption of force balance between gravity and aerodynamic drag.

$$\text{Gravity force} = \text{Aerodynamic force}$$

## Dendrite Crystals

The dendritic crystal is assumed to be accurately represented by a flat disc of radius  $r$ , ice density  $\rho_i$ , and plate thickness  $d$ . The air density is denoted by  $\rho_a$  where  $C_d$  is the drag coefficient.

$$\pi r^2 d \rho_i g = 1/2 \rho_a V^2 C_d \pi r^2 \quad (1)$$

The radius  $r$  drops out on both sides of the equation, leaving the expression for fall speed squared:

$$V^2 = 2 (\rho_i/\rho_a) g d/C_d \quad (2)$$

For dendrites that are enlarging in area by vapor diffusion but remaining with fixed thickness  $d$ , the fall speed is largely clamped, despite the monotonic increase in crystal mass with time. This conclusion is supported by careful observations (Nakaya and Terada [57]).

The drag coefficient  $C_d$  has been tacitly assumed to be constant in the foregoing analysis. In reality, the  $C_d$  value depends on the Reynolds number (Ludlam [55]), and as the dendrite increases in size by diffusional growth (even while  $d$  is fixed), the Reynolds number increases. However, in the range of Reynolds numbers of atmospheric relevance, the decline of  $C_d$  with Reynolds number flattens considerably. Jawaweera and Cottis [37, Figure 5] show the fall speed of plates versus total mass for a fixed thickness of 11  $\mu\text{m}$  and the fall speed increases only modestly (0.2 to 0.3 m/s, or  $\sim 50\%$ ) over a range of mass that amounts to two orders of magnitude. This documented increase is the  $C_d$  effect. In general, the fall speeds of plates remain below 1 m/s over a large range of plate diameters and total masses.

## Needle Crystals

A similar circumstance limiting the fall speed also pertains to needle crystals. Again, balancing forces due to gravity and aerodynamic drag, for a long needle of length  $L$  and diameter  $d$ , we have:

$$\pi (d^2/4) L \rho_i g = 1/2 \rho_a V^2 C_d L d \quad (3)$$

The needle length  $L$  drops out here on both sides of the equation, consistent with fall speeds being independent of needle length. This result for ice needles also pertains to radar chaff fibers (Justo and Eadie [38]; Kurdzo *et al.* [47]).

We are left with an expression for  $V^2$  of similar form to Eq. 2:

$$V^2 = (1/2) (\rho_i/\rho_a) g d/C_d \quad (4)$$

So long as the needle growth is confined to the  $c$ -axis and to an increase of  $L$ , with the diameter  $d$  fixed, the fall speed is independent of the mass increase of the needle by diffusional growth. This result again largely guarantees a colloidal stability of hydrometeors that orient themselves in the gravity field, and a fall speed for needles limited to substantially less than 1 m/s.

Hobbs [32] estimates the fall speeds of needle crystals with lengths varying from 0.5 to 2.5 mm to be in the range of 0.2 to 0.7 m/s. Justo and Eadie [38] estimated fall speeds for chaff at low altitude in the range of 0.5 to 0.7 m/s.

## Isometric Crystals

The final crystal type to consider is the isometric form that appears in the “no-man’s land” between dendrites and needles (Bailey and Hallett [1]). Both the a-axis and the c-axis lengths increase with time in this regime, and accordingly, we treat this barrel-shaped crystal as a sphere with a single radius  $r$ . Again balancing gravity and aerodynamic drag, we have:

$$(4/3) \pi r^3 \rho_i g = 1/2 \rho_a V^2 C_d \pi r^2 \quad (5)$$

For this situation, the size parameter does not drop out on both sides, and we are left with a form that includes the growth parameter  $r$ :

$$V^2 = (8/3) (\rho_i/\rho_a) g r/C_d \quad (6)$$

In contrast with the situation for both dendrites and needles, the dimension that grows by diffusion contributes to an increase in the fall speed and thereby an increase in the tendency for accretion of supercooled water and riming (by liquid water being scoured out in the fall path). In contrast to the dendritic and needle crystals whose fall speeds are naturally stabilized to values less than 1 m/s, regardless of their total mass, the isometric crystals can reach a fall speed substantially exceeding 1 m/s by diffusional growth alone. Appeal to accurate calculations based on Eq. 6 in Ludlam [55] for an altitude of 3 km (700 mb) show that an ice sphere with diameter of only 250  $\mu\text{m}$  is sufficient for a fall speed of 1 m/s, and if the diameter reaches 1 mm, the fall speed is already 5 m/s. The diminishment in the drag coefficient with increasing Reynolds number contributes to this velocity increase with increasing particle diameter. This fall speed is an order of magnitude larger than terminal fall speeds of anisotropic crystals. At 5 m/s, accretion by riming is then strongly enhanced in the presence of supercooled cloud water, also shown to be present within the crystal sandwich.

The important message from the foregoing calculations for the crystal sandwich is that while all crystal shapes considered can grow in size to 1 mm or larger in their maximum dimension by vapor diffusion, only the isometric shape can easily surpass the 1 m/s fall speed threshold needed to accelerate the riming process to graupel. The anisotropic crystals dendrites, plates, and needles (as well as chaff fibers) retain sub-1 m/s fall speeds even while growing in size to serve as readily detectable targets to dual polarimetric radar. This finding addresses one of the questions posed by the NEXRAD community in discussion about why the upper dendritic layer of the crystal sandwich is as stable as it is in the dual polarimetric radar observations: crystal growth by diffusion in the long dimension does not by itself speed up removal of the crystals by fallout, with the sole exception of the isometric shape. In the next section, other possible embryos for graupel will be considered.

### 4.2.6 Investigation of Prevalent Hydrometeors in the “No-Man’s Land” of the Crystal Sandwich

In light of the predictions in the previous section for isometric crystals to be the dominant origins of graupel particles in the temperature range intermediate to that for needles and for dendrites (called here “no-man’s land”), the CPI hydrometeor imagery has been searched in time intervals when the aircraft is within the inferred crystal sandwich. The intervals below were selected from the crystal sandwich case studies in Section 4.2.3. This search was also motivated by earlier observations of the embryos of graupel particles in winter storms in Salt Lake City, Utah and in Sapporo, Japan by Takahashi and Fukuta [73]. The

general findings for the flights in which some indication of a crystal sandwich was apparent are summarized below. The cap column has emerged as a new inhabitant of the internal crystal sandwich, but a variety of hydrometeors have been found, depending on which flight is examined.

#### **10 January 2017**

15:18 to 15:32 UTC: Overall, the dominant hydrometeors encountered in this case within the “sandwich” were small graupel particles and rimed dendrites. No pristine cap columns were noted in this flight, and there is little surprise given the active riming present. From 15:16:47 to 15:18:39 UTC, short (aspect ratio typically 2:1) rimed columns were found in great abundance. This typical aspect ratio is close to the 1:1 value for predicted isometric crystals.

#### **7 February 2017**

17:56 to 18:05 UTC: This is the period mentioned in the flight summary in Section 3.4, indicating the suggestion of a crystal sandwich with abundant needles, but with inadequate aircraft altitude sampling to verify thoroughly the upper dendritic layer. Rimed needles and graupel were the primary larger hydrometeors in this time interval, but roughly equidimensional ice fragments showed the greatest overall abundance. No cap columns were noted at any time in this time interval.

#### **24 March 2017**

10:41 to 10:50 UTC: For the comparisons on both 24 March and 25 March, a 70-second correction (addition) was needed to make the CPI clock match with true UTC time. Cap columns were frequently noted in CPI imagery in the first two minutes of this time interval when the temperature was in the range  $-13^{\circ}$  to  $-14^{\circ}\text{C}$ . This would have been near the base of the layer of flat-plate crystals above, as dendrites were present from 10:43 to 10:45 UTC. Cap columns were then noted as the aircraft descended again through the  $T = -13^{\circ}\text{C}$  level. Within the crystal sandwich, the hydrometeors were observed to be a mixture of columns, assemblage of sector plates, and small ice fragments.

#### **25 March 2017**

14:14 to 14:23 UTC: In this case, the cap columns were evident in two temperature ranges, in one case, roughly matched with the situation on 24 March with  $T = -12^{\circ}\text{C}$  when the aircraft was near maximum altitude in this time interval (14:23 UTC). Cap columns were also noted in this interval when the in situ temperature was near  $-4^{\circ}\text{C}$ , when needles were the predominant crystal type. In between these intervals, sector plates and fragments thereof were the predominate crystals encountered.

### **4.2.7 Discussion**

Based on both in situ aircraft observations of crystal types (Section 4.2.3) and the dual polarimetric radar observations from NEXRAD (Section 4.2.4), the simple illustration of the crystal sandwich in Figure 53 is justified. Dendritic crystals are prevalent in a laterally extensive layer over a temperature range of  $-9^{\circ}$  to  $-16^{\circ}\text{C}$  and needle crystals are prevalent in a layer beneath over a temperature range of  $-4^{\circ}$  to  $-7^{\circ}\text{C}$ . Both layers of the crystal sandwich over a radar bright band near  $0^{\circ}\text{C}$  was a conspicuous feature in the vertical profile of reflectivity in the Convair-580’s onboard X-band radar. The very presence of a well-defined radar bright band is evidence for weak vertical ascent, a circumstance favorable to closely matching

the crystal habit temperature dependence demonstrated in laboratory diffusion chamber measurements (e.g., Bailey and Hallett [1]).

A schematic profile of LWC is also shown in Figure 53, consistent with the observations (in Figures 29, 34, 39) that the maximum value lies somewhere between the two crystal layers, and which may well be influenced by an active Bergeron–Findeisen process (herein referred to as Bergeron) (Bergeron [3], [4]; Findeisen [20]) of LWC depletion within each layer.

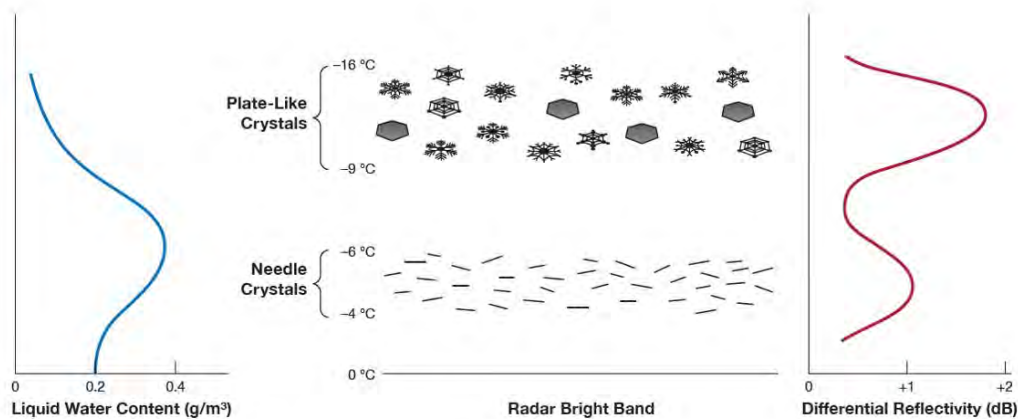


Figure 53. Schematic illustration of the crystal sandwich structure, including profiles of supercooled liquid water (left) and ground-based radar differential reflectivity (right).

It is important to point out that the preferred aircraft documentation of the crystal sandwich structure in Figure 53 is obtained by spiral ascent or descent in place, as was the situation for Cases II, III, and IV. A straight-track porpoising maneuver may provide the evidence for two crystal layers and supercooled water in between, but without guarantee that the three key layers are stacked vertically in one location. We hasten to add here that the aircraft work in both BAIRS I and II has demonstrated the layered nature of crystals and supercooled water, inherently linked with gentle ascent on warm frontal boundaries. With typical frontal slopes of 100 to 1 and along-slope wind speeds of order 10 m/s, the vertical ascent speed is  $\sim 10^{-2} \times 10 \text{ m/s} = 0.1 \text{ m/s} = 10 \text{ cm/s}$ .

A second requirement for thorough documentation of the crystal sandwich is that the cloud temperature sampling by aircraft span the full range of the two prevalent crystal types. Though we had first evidence for the crystal sandwich during the third flight of BAIRS I (Williams *et al.* [84]), we did not then appreciate the robustness of this structure until the end of the BAIRS II campaign and when the other NEXRAD radar examples presented in Section 4.2.4 were collected. As a result, we did not make concerted efforts to porpoise over the necessary temperature range during the aircraft campaign.

Also shown in Figure 53 is a vertical profile of positive differential reflectivity, physically linked with the preferred horizontal orientation of the two anisotropic crystal types, and the expectation (consistent

with the available NEXRAD measurements documented in Section 4.2.4) that the +ZDR values for dendrites will be consistently larger than for needles (e.g., Hogan *et al.* [34]). The “no-man’s land” between needles and dendrites is shown as an empty zone in Figure 53, but the checks for hydrometeors in this range and discussed in Section 4.2.6 have shown the presence of equidimensional ice fragments, graupel particles, and cap columns, all of which are expected to have more isotropic response as indicated by the local minimum in ZDR in the figure.

During the meeting of the NEXRAD Technical Advisory Committee in April 2019, questions were raised about the temporal stability of the crystal sandwich structure shown in Figure 53. One can make use of the fall speed estimates of relevant crystals (Section 4.2.5) to address this question. The sandwich thickness in Figure 53 is of the order of 2 km. For a crystal fall speed of 0.2 m/s, the sandwich transit time would be  $(2000 \text{ m}) / (0.2 \text{ m/s}) = 10^4 \text{ sec}$ , or about 3 hours. This time scale is consistent with the lifetime of +ZDR bright band features in the ground-based radar observations. We also have good evidence that the upper-level dendrites do descend by gravity, as we find them occasionally mixed in with the needles in the lower layer of the sandwich. Examples are shown in Figures 39 and 44.

The crystal sandwich is not always present in situations when we expected it to be. Examples are mentioned in the discussion of flight tracks in Section 3.

### **4.3 REFLECTIVITY LEVEL OF CRYSTAL SNOWSTORMS AND IMPLICATIONS FOR THE PRESENCE OF SUPERCOOLED WATER AND AIRCRAFT ICING CONDITIONS**

#### **4.3.1 Introduction**

In summertime moist convection and in all tropical moist convection, convective updrafts (ascent rates) are many meters per second, up to nearly 100 m/s, and radar reflectivity values populate the upper end of the logarithmic reflectivity scale ( $>30 \text{ dBZ}$ ). Furthermore, a number of empirical fiducial marks have been assigned to this scale in published work in summertime conditions. For example, the 30 dBZ reflectivity needed for initial electrification (Breed and Dye [10]), the nominal 40 dBZ threshold for the first lightning flash in developing storms (Dye *et al.* [18]), a 55 dBZ threshold for hail in New England thunderstorms (Geotis [25]), a  $\sim 63 \text{ dBZ}$  threshold for the hail spike (Wilson and Reum [91]; Lemon [52]) and more complicated thresholds for giant hail (Picca and Ryzhkov [60]).

In winter snowstorms in which ascent speeds are generally less than meters per second (and often substantially less), and which populate the lower portion of the logarithmic reflectivity scale ( $<30 \text{ dBZ}$ ), surprisingly little consideration has been given to quantitative ascent rates or empirical reflectivity thresholds. Part of the reason for this neglect is that the warm frontal ascent in winter is quite small (in the range 1 cm/s to 1 m/s) and impossible to measure with aircraft or balloon probing.

This section of the report is squarely aimed at remedying this shortcoming in winter storm studies. Ascent rate is fundamental to aircraft icing issues because supercooled water is produced by the ascent of saturated air. A simple relationship between ascent rate  $W$  (in the range of 1 cm/s to 1 m/s) is developed for winter storms with large lateral extent. Then on this scale of ascent and radar reflectivity, specific storm types are identified. The crystal storm is the low end-member here and is of considerable interest because of its association with supercooled water (in the context of laboratory diffusion chamber measurements of ice crystal growth), as described and documented in Section 4.2.2.

### 4.3.2 The Role of Ascent Speed in Setting the Precipitation Rate in Snowstorms

It is generally agreed that precipitation rate is strongly influenced by the ascent rate of moist air, simply because the ascent into cooler air is the source of the condensates. This section is concerned with a way to make this connection quantitative by placing a bound on the precipitation rate  $S$  in a stratiform snowstorm experiencing a uniform rate of ascent  $W$  (as for example on a gently sloping warm frontal surface). In an atmosphere saturated with moisture and undergoing reversible ascent, the greatest precipitation rate is achieved by depositing the entirety of the precipitable water ( $PW$ ) (i.e., all the condensing water vapor) in the column over a time scale given by the column transit time by the ascent speed ( $= H/W$ ). This calculation assumes that the precipitation efficiency is 100%. This assertion is reasonable for laterally extensive snowstorms lacking dry boundaries to drive entrainment and the loss of cloud water (ice) to evaporation (sublimation). The total precipitable water is dependent on the initial lifting temperature and is available in published tables (U.S. Department of Commerce [77]). Following these assumptions, the maximum precipitation rate  $S$  is given by:

$$S = PW / (H/W) \text{ kg/m}^2/\text{s} \quad (7)$$

It is no surprise that the precipitation rate  $S$  is a linear function of the ascent rate  $W$ . For lifting from  $0^\circ\text{C}$ , typical of many winter storms, the  $PW = 8.5$  mm (liquid water equivalent) and a typical value for  $H = 5000$  m (U.S. Department of Commerce [77]). Figure 54 shows the predicted relationship between precipitation rate  $S$  in mm/hr and ascent rate  $W$  (in m/s) (after appropriate units conversion) over three decades of ascent rate.

$$S = 6.1 W \text{ mm/hr} \quad (8)$$

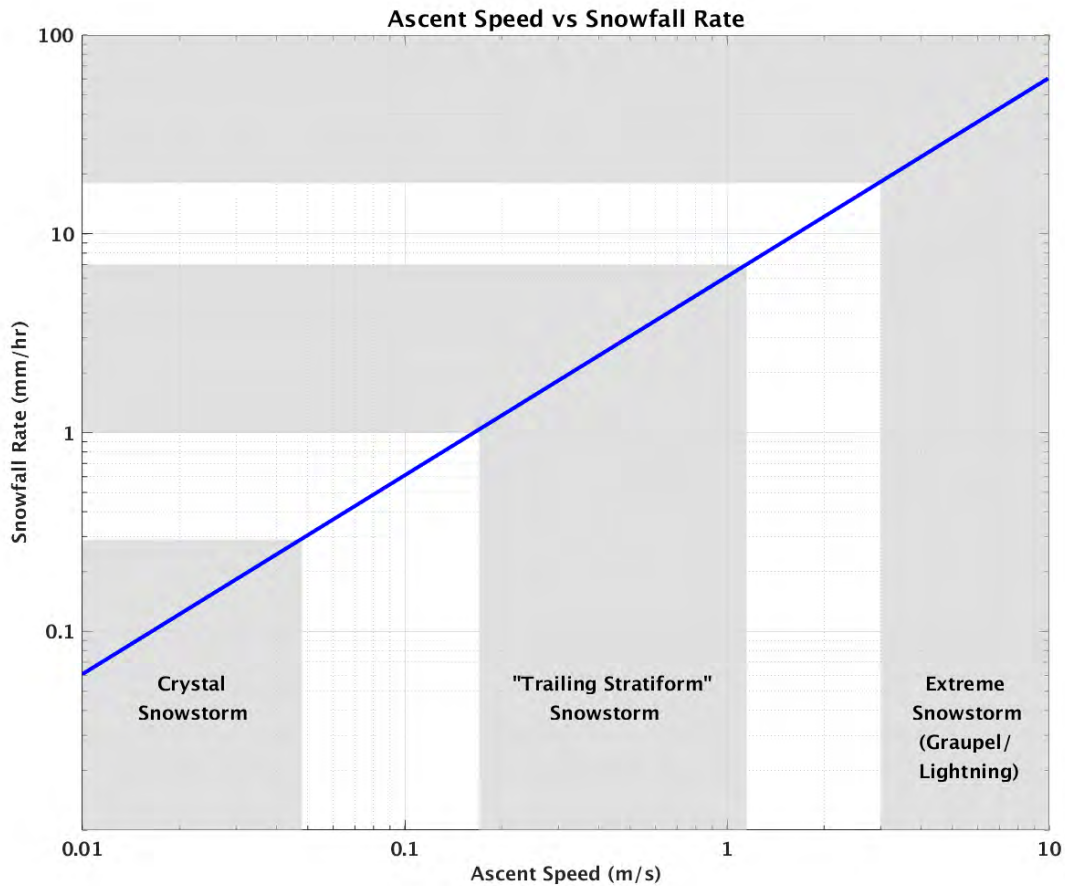


Figure 54. Relationship between snowfall rate  $S$  (mm/hr) and ascent speed  $W$  (m/s) based on Eq. 7. Rough boundaries on three snowstorm regimes discussed in the text are also shown. The snowfall rate along the ordinate is liquid water equivalent.

A useful reference check here are the snowstorms occurring aloft in summertime in the trailing stratiform regions of squall lines, and in which the mesoscale ascent is frequently occurring at and above the radar bright band near  $0^{\circ}\text{C}$ . Typical precipitation rates in such systems are 1–5 mm/hr (Tokay and Short [76]; Russell *et al.* [66]). These values are reasonably well matched to values in Figure 54 for ascent rates that are typical of trailing stratiform regions ( $\sim 1$  m/s or less). It is well-known that aggregation is an important process for precipitation formation above the radar bright band toward making precipitation rates of order 1–5 mm/hr and with maximum rates of  $\sim 10$  mm/hr. Here, radar reflectivity values are in the range of 20–30 dBZ. The fall speeds of aggregates can exceed 1 m/s. It should also be noted here that supercooled water is often small or non-existent in these situations (A. Heymsfield, personal communication, 2018).

A second important reference check for Eq. 7 is the high end of the scale of snowfall rate in Figure 54. With a 3 m/s ascent rate, the predicted snowfall rate is 18 mm/hr, or in actual snow depth (with the usual rough factor-of-10 conversion), 18 cm/hr or  $\sim 7$  inches per hour. This is a reasonable upper limit for a  $0^{\circ}\text{C}$

initial lifting temperature. It is also useful to point out that with ascent rates of 3 m/s in winter, small lump graupel may form, and then lightning is possible in snowstorms (by the same mechanism recognized in summer thunderstorms). The existence of lightning and graupel are both meaningful markers for extreme snowstorms, with the acknowledgement that the commonly used term “thunder snow” may be a misnomer (Williams [88]).

#### 4.3.3 Reflectivity–Precipitation Rate Relationships in Snow and the Threshold for Crystal Storms

Many studies have considered reflectivity–snowfall (Z-S) relationships (Hogan *et al.* [33]; Huang *et al.* [35]; Bukovcic *et al.* [11]) in winter weather (Table 4). Examples are included here with good sampling in the low end of the dynamic range of snowfall rate. These results are important in the present context toward estimating the ascent rate and corresponding snowfall rate when one has a storm dominated by ice crystals.

**TABLE 4**  
**Z-S Relationships for Snowfall and Precipitation Rate (mm/hr Liquid Water Equivalent) for 10 dBZ, and Corresponding Ascent Value based on Figure 54**

Study	Z-S relationship	S value for 10 dBZ	W value from Figure 54
Hogan <i>et al.</i> [33]	$Z = 170 S^{1.5}$	0.15 mm/hr	2.5 cm/s
Huang <i>et al.</i> [35]	$Z = 204.1 S^{1.5785}$	0.15 mm/hr	2.4 cm/s
Bukovcic <i>et al.</i> [11]	$Z = 120 S^2$	0.29 mm/hr	4.8 cm/s

From a purely empirical standpoint, the measured radar reflectivity has been small (<20 dBZ, and frequently <10 dBZ) in several situations relevant to crystal storms: when +ZDR bright bands have been documented (Williams *et al.* [85], [85]), when predominant hexagonal flat-plate crystals have been verified (Williams *et al.* [83]), when predominant needle crystals have been documented (Williams *et al.* [87], [89]), and more recently when evidence for large +ZDR anomalies beneath the +ZDR bright band are present in winter weather. It seems physically plausible that when crystal concentrations are both small and quasi-monodisperse (expected in the assumed conditions of uniform ascent), that aggregation will be strongly suppressed and the full anisotropic expression of the crystals (several dB) will be apparent in differential reflectivity. Radar Z will also be reduced when aggregation is suppressed. Relevant here is the work of Lim *et al.* [53], who, on the basis of observations in snowstorms, assign a 10 dBZ reflectivity boundary between ice crystals and aggregates. This finding is broadly consistent with the other observations noted above.

A consideration of Z-S relationships in Table 4 allows estimates of the snowfall rate for a crystal snowstorm, assuming the validity of a 10 dBZ reflectivity threshold. The computed precipitation rates from these Z-S relations are included in Table 4, and are also used to mark boundaries in Figure 54. The values are of the order 0.1 mm/hr and correspond with ascent speeds of the order of centimeters per second, some one to two orders of magnitude smaller than the mesoscale ascent rate in the trailing stratiform region of summer squall lines (where +ZDR bright bands are seldom detected, Williams *et al.* [85]).

Following the suggestion in Williams *et al.* [86] that hydrometeor fall speeds in winter storms will adjust to the rate of ascent which is the moisture supply, it is interesting to contrast the fall speeds of needle and dendrite crystals (Hobbs [32]) with the larger fall speeds of aggregates composed of the same crystals. Since the measured fall speeds of radar-detectable crystals are generally greater than the ascent rates inferred from Figure 54 for crystal snowstorms, one can conclude that the crystals fall out of the regions of ascent. This is consistent with the finding of some occasional hexagonal flat-plate crystals mixed in with the layer of needle crystals below.

#### **4.3.4 The Role of $N^*r$ as Sink for Supercooled Liquid Water**

Now that some rough estimates are available for the ascent rates appropriate for crystal snowstorms, it is valuable to consult the predictions for ice crystal populations needed for the suppression of supercooled water in the presence of uniform ascent. Korolev and Mazin [42] have identified  $N^*r$  as the cloud physics parameter representing the sink for liquid water by way of the Bergeron process: vapor diffusion onto the ice particles and transferred from the liquid phase. Williams *et al.* [85, Figure 3] made use of the theoretical calculations and some aircraft-measured values of  $N^*r$  to infer that ascent speeds of 5 cm/s would be needed to maintain supercooled water at  $T = -5^\circ\text{C}$ , where needles are prevalent, and 50 cm/s at  $T = -15^\circ\text{C}$ , where dendrite crystals are expected. These calculations are consistent with our findings in BAIRS II that supercooled liquid water is substantially more likely in the presence of needle crystals than in the presence of dendrites. These estimated threshold ascent speeds are somewhat larger than the inferred values in a crystal storm based on Figure 54. It is clear that accurate estimates of  $N^*r$  are needed with the aircraft hydrometeor imagery to make these comparisons, and we have some suspicion that  $N^*r$  has been underestimated in earlier trials.

#### **4.3.5 Summary**

Ascent speed and snowfall rate are closely related in winter storms. The foregoing calculations and observations suggest that supercooled water in small droplet form may be more prevalent in regions of weak ascent (and low radar reflectivity) than in strong ascent (and stronger reflectivity). We are finding more SLW in association with ice crystals than what others have found in the trailing stratiform regions of squall lines, where reflectivity and ascent speeds are notably larger. A prime example is the “crystal storm” case in BAIRS I in which a layer of SLW was encountered within a crystal sandwich with peak SLW concentration reaching  $0.6 \text{ g/m}^3$ , but with background reflectivity of generally less than 10 dBZ. This is good news for efforts to use dual polarimetric radar methods to identify possible regions of supercooled water.

### **4.4 SLD IN A MARITIME SYNOPTIC REGIME: COMPARISONS WITH FLIGHTS IN A CONTINENTAL REGIME**

#### **4.4.1 Introduction**

The dramatic contrast in concentrations of CCN between continental and maritime boundary layers (e.g., Williams *et al.* [82]) has been shown to play a key role in the formation and distribution of supercooled liquid water particles that pose an icing hazard to aircraft. With smaller CCN concentrations, typical of maritime conditions, the available condensate is shared amongst a smaller number of particles, thereby promoting drizzle formation and with sufficiently deep clouds at temperatures above freezing, warm rain.

This effect now has numerous demonstrations in summertime conditions (Williams and Stanfill [81] Rosenfeld *et al.* [65]; Braga *et al.* [9]), but also with drizzle in winter storms (Rasmussen *et al.* [63]; Bernstein *et al.* [6]). Icing conditions associated with SLD are generally considered to be most hazardous, more so than small droplet riming icing (Cober *et al.*[12]; Rasmussen *et al.* [63]; Bernstein *et al.* [8]).

This section is concerned with the identification of runaway coalescence to drizzle conditions in one of five BAIRS II flights (24 January 2017) with distinct maritime characteristics. It should be emphasized that these characteristics are clearly manifest despite the fact that the storm probing by Convair-580 took place more than 500 km inland from the Atlantic Ocean. The conspicuous maritime characteristics will also be contrasted with those on the other four flights, all of which showed distinct continental character.

#### **4.4.2 Cloud Droplet Diameters**

The initial evidence for the maritime regime in the flight on 24 January 2017 was the anomalous nature of drop sizes. This aspect was identified in real time during the flight and was expressed in the debrief afterward. The comparative anomaly is best expressed by the MVD from the aircraft FSSP as shown in Figure 55 for all five flights of BAIRS II.

A critical threshold diameter for runaway coalescence and the formation of drizzle from smaller cloud droplets have long been recognized near  $D = 25 \mu\text{m}$  (Rosenfeld and Gutman [64]; Gerber [26]; Rangno and Hobbs [62]; Freud and Rosenfeld [21]). This fundamental threshold is shown as a red horizontally dashed lines in each of five flight records in Figure 55.

In all four records pertaining to flights in the continental regime (10 Jan, 7 Feb, 24 Mar, and 25 Mar panels in Figure 55), the MVD barely attains the  $D = 25 \mu\text{m}$  threshold, with a few occasional spikes to large values. In contrast, the MVD for the maritime case (24 Jan panel) exceeds the  $25 \mu\text{m}$  threshold in a sustained manner (i.e., several minutes duration) more than seven times. The sustainment pattern is likely somewhat an artificial response to flight path operations. The reality is likely that the over-threshold condition was more consistent and widespread. These episodes will be discussed in Section 4.4.8.

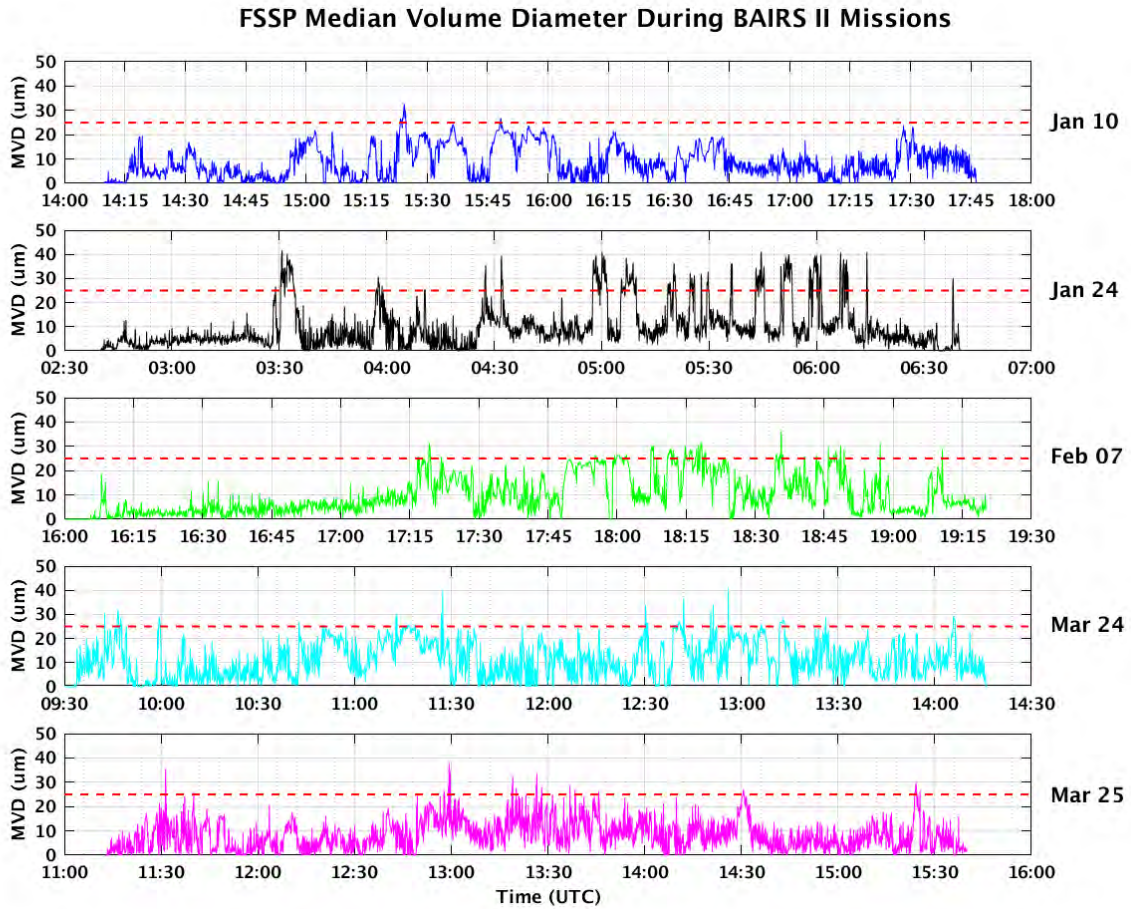


Figure 55. Five flight history of MVD derived from the FSSP. The red dashed line denotes the critical threshold diameter for runaway coalescence and the formation of drizzle from smaller cloud droplets.

#### 4.4.3 Concatenated Hydrometeor Size Distributions

Important evidence for the transformation of supercooled water in cloud droplet form to drizzle, most prevalent in maritime conditions (Dai [16]; Rosenfeld *et al.* [65]), is found in the concatenated hydrometeor size distributions discussed earlier in Section 2.5. Such distributions are included in Figures 56–60 for the entirety of each of five flights. Each of these figures contains information chosen from a combination of five separate aircraft hydrometeor probes available (FSSP from 3.5 to 45.5  $\mu\text{m}$ , 2D-S from 55 to 2090  $\mu\text{m}$ , 2D-C from 50 to 1000  $\mu\text{m}$ , PIP from 1000 to 12,800  $\mu\text{m}$ , and HVPS from 600 to 38,400  $\mu\text{m}$ ) to span a total size range of four decades (1 to  $10^4$   $\mu\text{m}$ ). The units for hydrometeor concentrations are #particles/liter/ $\mu\text{m}$  and have been consistent from probe to probe.

The anomaly of the maritime case (Figure 57) is again readily apparent in comparison with the other four continental cases (Figures 56, 58–60). In all of the latter cases, the droplet concentrations in the FSSP range attain the high end of the scale (red and orange colors) where values are consistent with continental concentrations of CCN of  $10^3$  per cc. These large concentrations virtually guarantee the presence of supercooled liquid droplets in the FSSP observations, as they are large in comparison with the empirical

threshold concentrations for small ice particles (Korolev *et al.* [43]). In contrast, for the maritime case (Figure 57), the droplet concentrations in the FSSP range are generally reaching 10–100 per liter per  $\mu\text{m}$  (yellow color) and on occasion 100–1000 per liter per  $\mu\text{m}$  (orange color). These lower concentrations are consistent with the smaller CCN concentrations typical of clean maritime boundary layer air (1–100 per cc).

A more important contrast in the concatenated size distributions between maritime and continental cases, because it pertains to the process for drizzle formation and SLD icing conditions, is found in the transition region between the FSSP (cloud droplets) region and the range of the 2D-C beginning at 50  $\mu\text{m}$  size. For the continental case of 10 January 2017, for example, this transition is abrupt, amounting to a drop off in concentration by 4–5 orders of magnitude, and indicative of a colloidally stable droplet population, with no obvious tendency to bridge over to the larger sizes.

In contrast, for the sole maritime case in Figure 57, strong yellow tails in the size distribution serve to bridge the FSSP range with the 2D-C range at larger size. The particle concentrations are quasi-continuous from the small droplets to the large drizzle tails ( $D > 100 \mu\text{m}$ ), and represent a highly efficient coalescence process strongly promoted by the notable exceedance of the 25  $\mu\text{m}$  diameter threshold.

A comparison of the maritime case in Figure 55 (panel 2) and the concatenated spectra in Figure 57 shows that the episodes with enhanced MVD coincide with the episodes of strong yellow tailing into the drizzle size range ( $D > 100 \mu\text{m}$ ). Enhancements in onboard X-band reflectivity (not shown) are also associated with the episodes of substantial drizzle production, consistent with other published observations showing that drizzle is a detectable radar target (e.g., Ikeda *et al.* [36]).

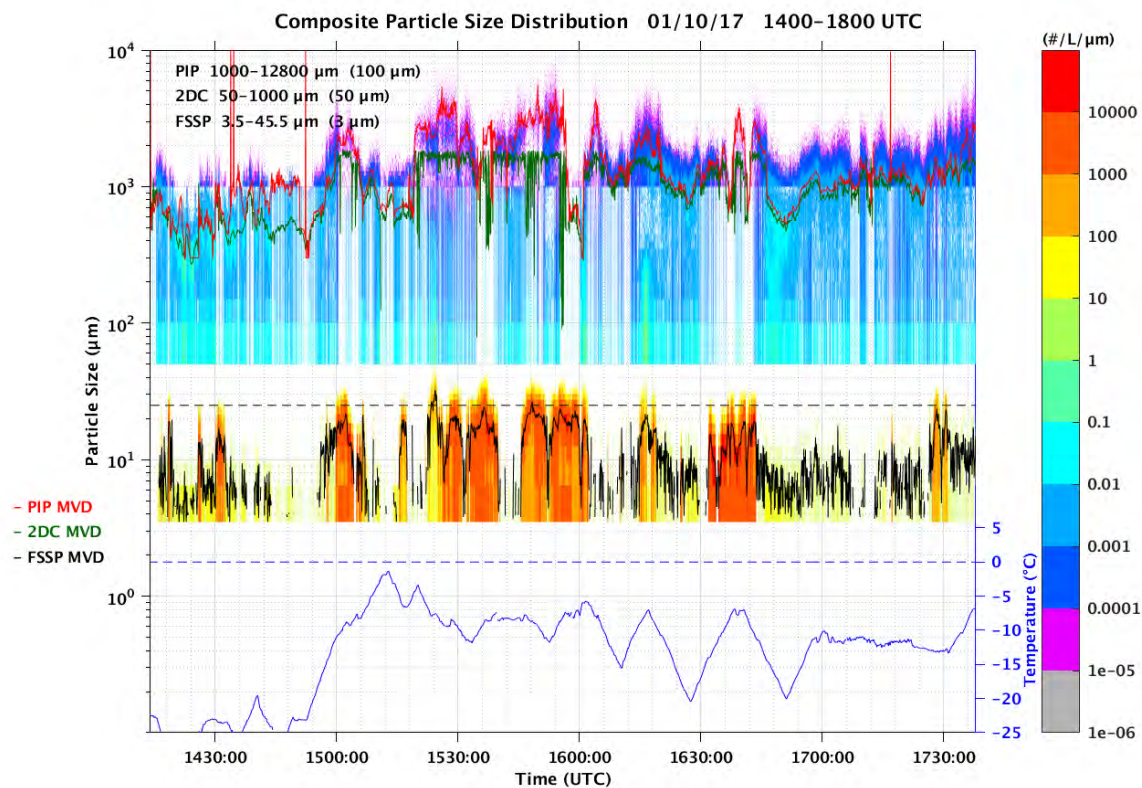


Figure 56. Concatenated hydrometeor size distributions showing particle concentrations derived from the FSSP, 2D-C, and PIP probes on 10 January 2017 for the interval 14:00–18:00 UTC. Timelines of MVD are shown in black (FSSP), green (2D-C), and red (PIP). Five-second averages of the in situ temperature are shown in blue.

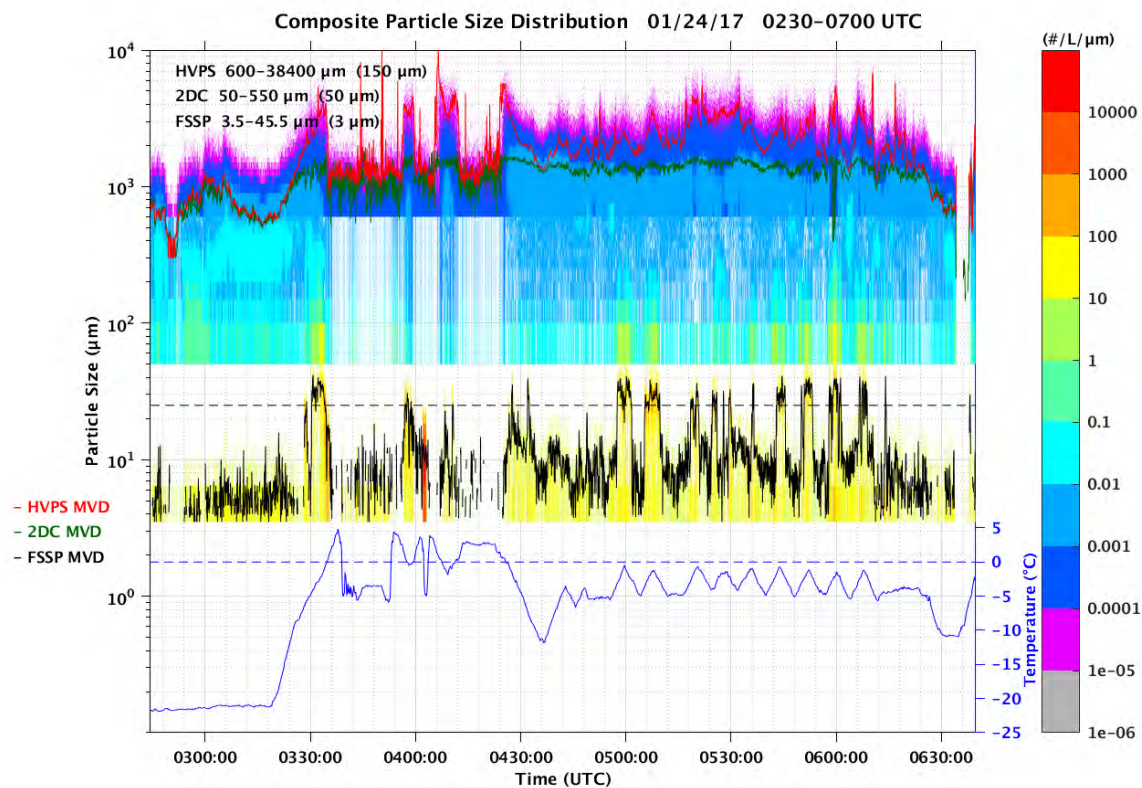


Figure 57. Concatenated hydrometeor size distributions showing particle concentrations derived from the FSSP, 2D-C, and HVPS probes on 24 January 2017 for the interval 02:30-07:00 UTC. Timelines of MVD are shown in black (FSSP), green (2D-C), and red (HVPS). Five-second averages of the in situ temperature are shown in blue.

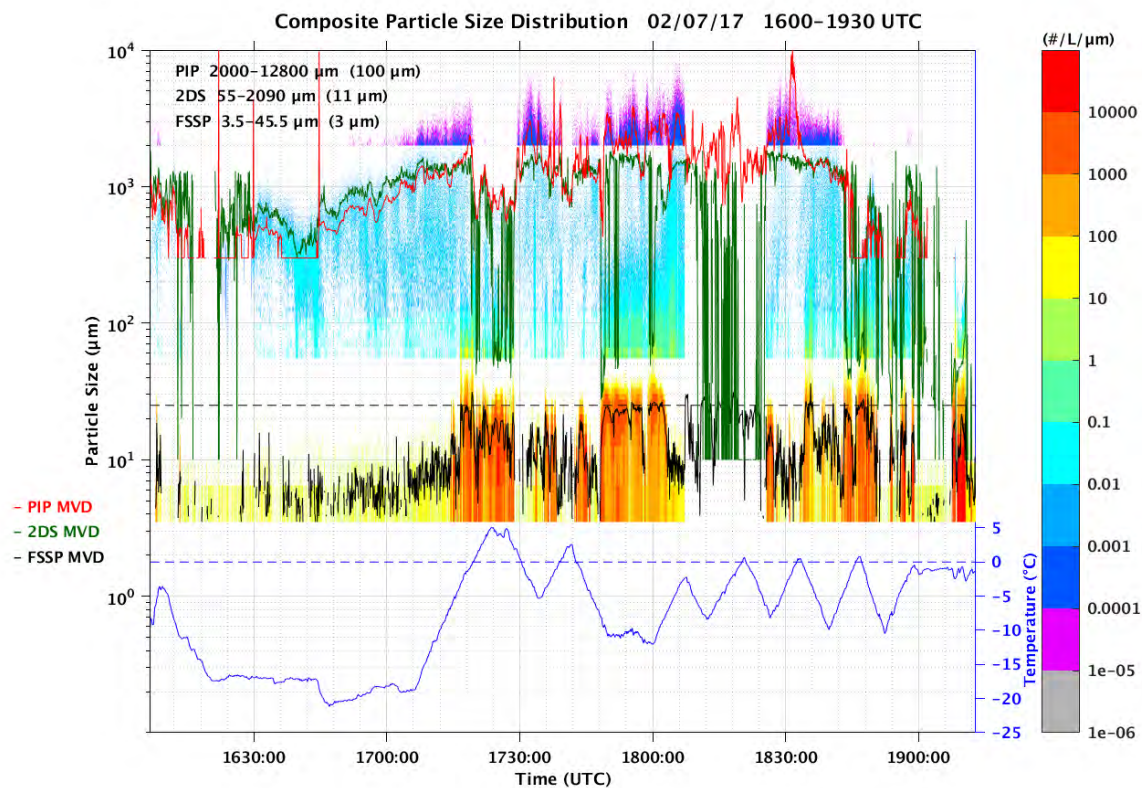


Figure 58. Concatenated hydrometeor size distributions showing particle concentrations derived from the FSSP, 2D-S, and PIP probes on 7 February 2017 for the interval 16:00–19:30 UTC. Timelines of MVD are shown in black (FSSP), green (2D-S), and red (PIP). Five-second averages of the in situ temperature are shown in blue.

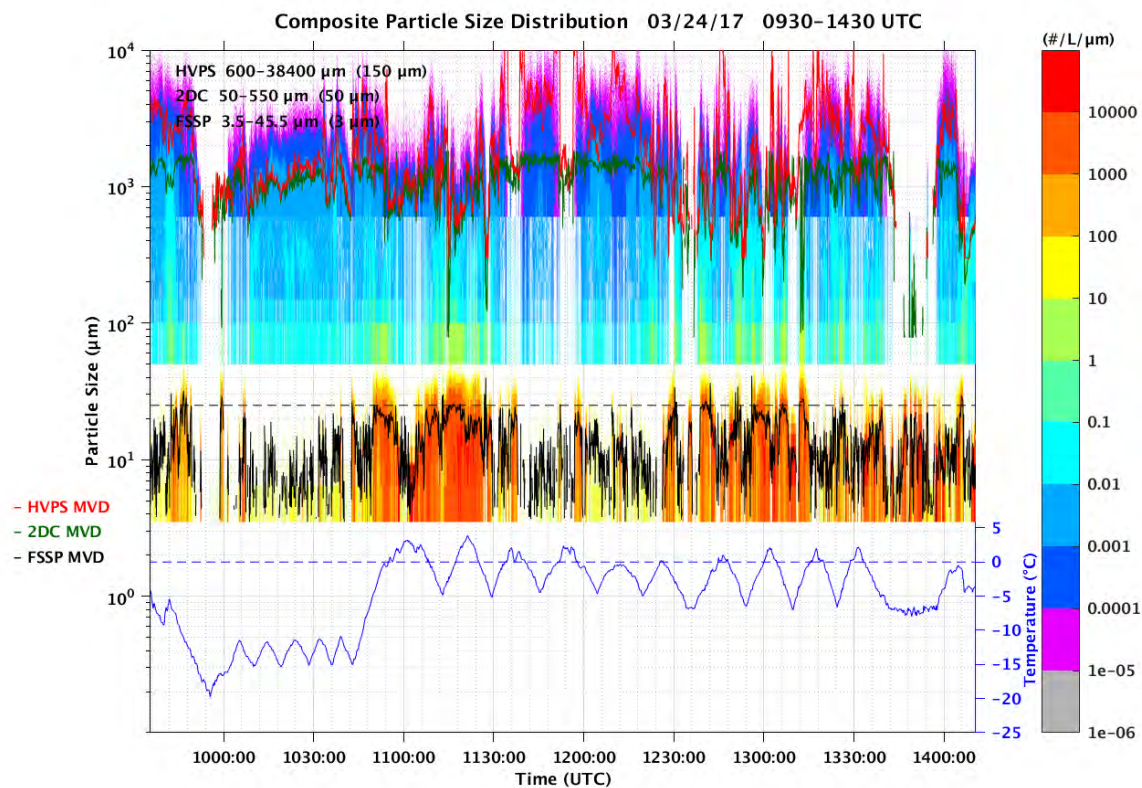


Figure 59. Concatenated hydrometeor size distributions showing particle concentrations derived from the FSSP, 2D-C, and HVPS probes on 24 March 2017 for the interval 09:30–14:30 UTC. Timelines of MVD are shown in black (FSSP), green (2D-C), and red (HVPS). Five-second averages of the in situ temperature are shown in blue.

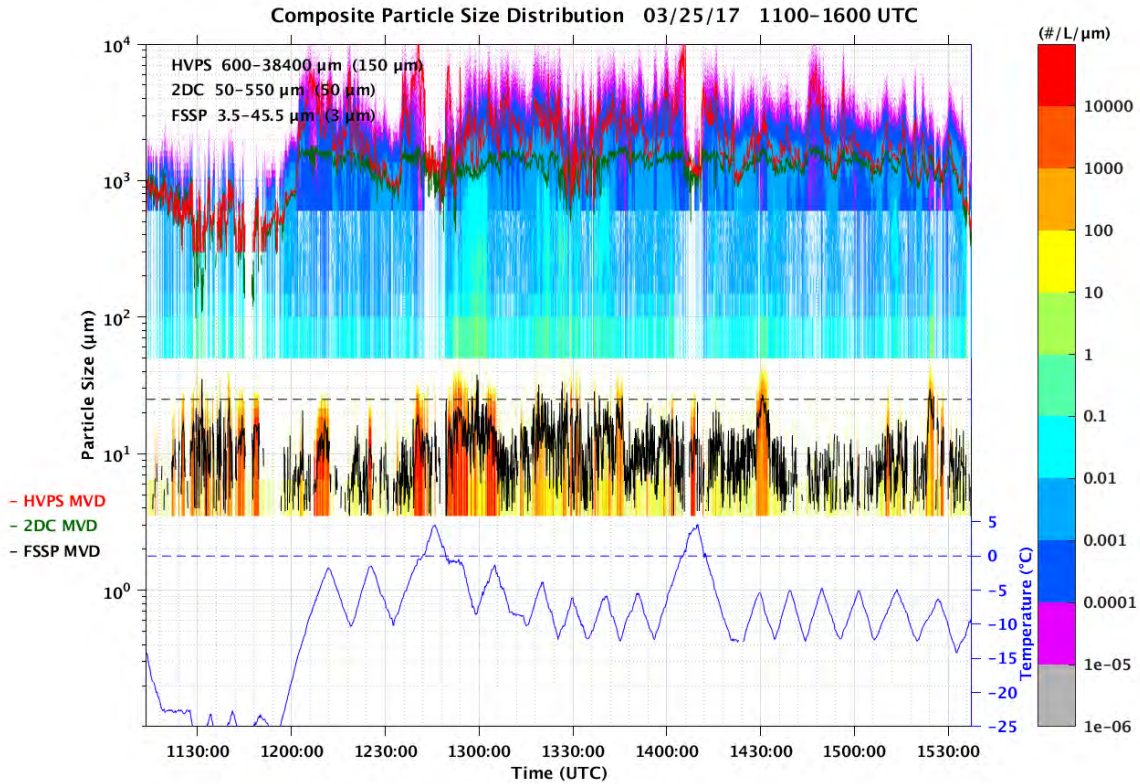


Figure 60. Concatenated hydrometeor size distributions showing particle concentrations derived from the FSSP, 2D-C, and HVPS probes on 25 March 2017 for the interval 11:00–16:00 UTC. Timelines of MVD are shown in black (FSSP), green (2D-C), and red (HVPS). Five-second averages of the in situ temperature are shown in blue.

#### 4.4.4 Anomalous Optical Extinction in the Maritime Regime

Optical extinction through air populated by water particles is an additional aircraft measurement that affords a clear distinction between a continental and a maritime regime, and which also showed the 24 January flight to be anomalous among the four others. To understand why this is so, the following simple calculations with a monodisperse cloud of water droplets are relevant.

In the wavelength limit of geometrical optics ( $\lambda \ll 2\pi r$ ):

Consider water clouds with  $N$  droplets per cubic meter and radius  $r$ :

$$\text{Projected area per droplet} = \pi r^2 \quad (9)$$

$$\text{Droplet area (blocking light) per unit volume} = N \pi r^2 \text{ m}^2/\text{m}^3 \quad (10)$$

Mean free path through cloud of droplets by dimensional analysis is:

$$L = 1/(N \pi r^2) \text{ m} \quad (11)$$

The cloud liquid water content is  $LWC = \rho N (4/3 \pi r^3)$  kg/m<sup>3</sup>, where  $\rho$  is the density of water.

Solving for  $N \pi r^2$  gives  $3/4\rho LWC/r$ .

Plugging into Eq. 9 gives

$$L = 4\rho/3 LWC * r \quad \text{m} \quad (12)$$

This is to say that for fixed total LWC, the mean free path for light through a cloud is linear in radius.

Consider three typical drop sizes: cloud (20 microns), drizzle (200 microns) and rain (2000 microns = 2 mm).

Following Eq. 10, the extinction (inverse mean free path) in cloud will be 10× that in drizzle and the extinction in drizzle is 10× that in rain. This is the basis for the expectation that the extinction in continental (water) clouds will be greater than in maritime clouds. When ice is present, the situation is more complicated and one cannot be certain when liquid water alone is present to produce the extinction.

The distributions of aircraft-measured optical extinction (km<sup>-1</sup>) with the ECCC extinction probe for four of five flights are shown in Figure 61 (extinction data were not available on the 10 January flight). The observed values range from 0 to 80 km<sup>-1</sup>. Clearly the lowest values (0–15 km<sup>-1</sup>) are noted for the maritime case, consistent with the foregoing simple calculations.

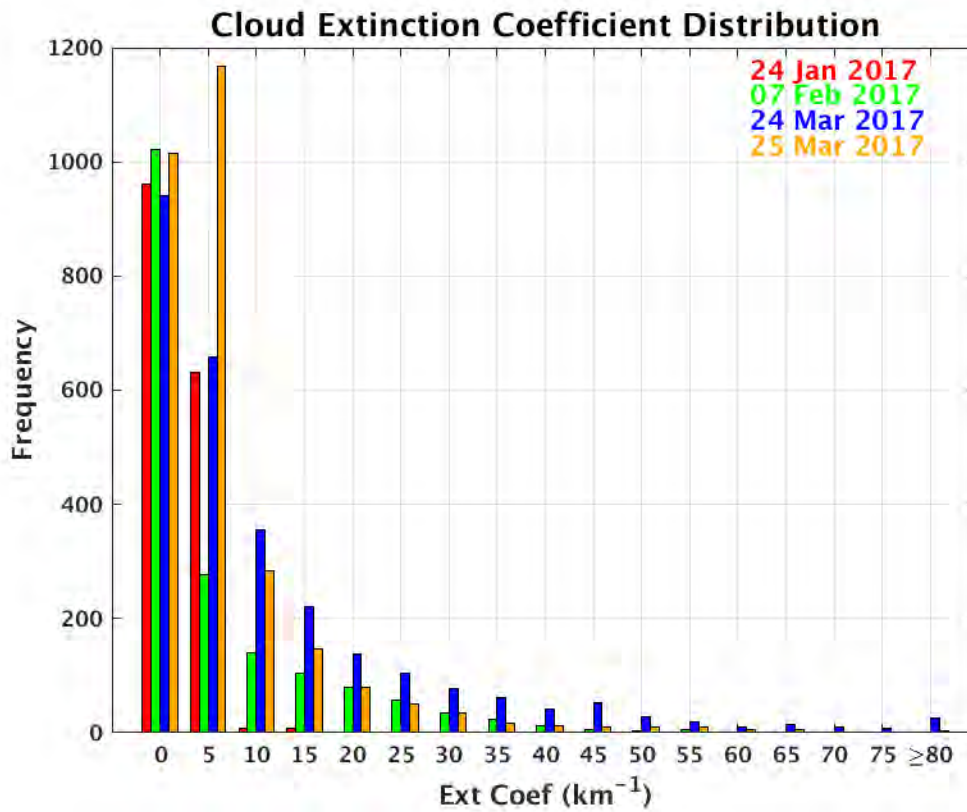


Figure 61. Distributions of cloud extinction coefficient measured during four of five flights. The extinction meter was not operable on the 10 January flight.

Spot check comparisons of the onboard polarimetric lidar (not shown here) also showed systematically longer optical paths in the maritime case compared to the other four continental cases. These findings point up the possible use of ground-based lidar measurements for diagnosing drizzle and SLD icing conditions.

Additional comparisons pertaining to extinction were made possible by an examination of values in supercooled cloud in the lower mixed-phase region and also containing needle crystals. This aspect guaranteed an in situ range of temperature from  $-4^{\circ}$  to  $-7^{\circ}\text{C}$ . These results are shown in Figure 62 for four of the five flights. Each plotted point represents the maximum extinction value and usually coincides with the maximum value of supercooled LWC recorded with the Nevzorov probe. The two main takeaways from Figure 62 are that the extinction is positively correlated with LWC, and the smallest values of extinction are evident for the maritime case. When SLD is involved in addition to small droplets, the situation is more complicated (for one, the Nevzorov probe does not respond well to SLD).

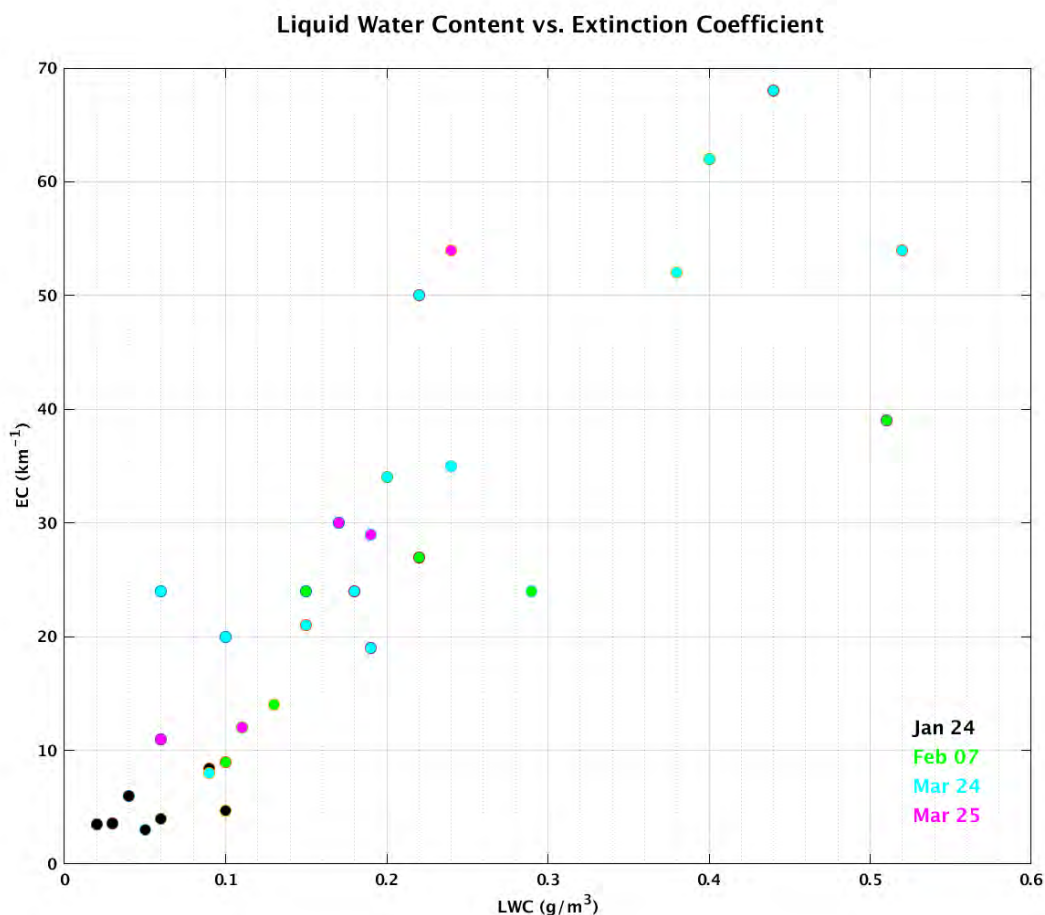


Figure 62. Scatterplot of LWC versus extinction coefficient with evidence of needle crystals for four of five flights. The extinction meter was not operable on the 10 January flight.

#### 4.4.5 Ubiquitous Presence of Size Spectral Broadening in the Presence of Small Supercooled Droplets in FSSP Observations

The concatenated hydrometeor size distributions shown earlier in Figures 56–60 provide graphic evidence for the production of larger particles ( $D > 25 \mu\text{m}$ ) from smaller ones ( $D < 25 \mu\text{m}$ ). The rich concentrations of supercooled cloud droplets are most commonly indicated by orange/red colored regions, with corresponding concentrations in the range of  $10^2$  to  $10^4$  per liter per micron over the size range of 3.5 to 45.5  $\mu\text{m}$ . The evidence that these particles are supercooled droplets rather than ice particles comes from the simultaneous increase in readings from the Nevzorov LWC probe and with the evidence that they are supercooled comes from in situ temperature. In every flight, one can find examples of size broadening and presence of yellow tails (in the concentration range 10 to  $10^2$ ) into the size range  $D = 20$  to 100  $\mu\text{m}$  and beyond (herein referred to as the “size gap”). (Numerous specific examples will be presented and discussed in Section 4.4.8.) Over all five flights, the most likely location for these paired observations of supercooled cloud droplets and the yellow tails into the size gap is near the  $0^\circ\text{C}$  isotherm, at the lower limit of the mixed phase zone in winter storms. The main reason for the interest in this phenomenon in the present study is

that SLD and drizzle are often the dominant hydrometeors in these yellow tails. SLD is often viewed as the most serious aircraft icing hazard because of the much longer freezing times of large supercooled drops when they come into contact with the aircraft surface (Sand *et al.* [68]; Polotovich [61]; Bernstein *et al.* [6]).

#### 4.4.6 Mechanisms for Spectral Broadening and the Formation of SLD and Drizzle

The widespread evidence for spectral broadening in the BAIRS II dataset deserves special attention. This is particularly important for understanding the in situ conditions that promote the formation of SLD and drizzle from smaller supercooled cloud droplets. However, a number of mechanisms other than runaway coalescence for spectral broadening must be considered and distinguished from the one deemed most hazardous in the icing context. (Specific examples will be shown later in Section 4.4.8.) In these other categories, the hydrometeors in the yellow tail may be solid rather than liquid hydrometeors. These scenarios do not pose icing hazards.

At least five different mechanisms have been previously identified for the development of large hydrometeors (in the yellow tail region) from supercooled cloud droplets and are summarized here and in Table 5.

1. Formation of SLD and drizzle by collision and coalescence of cloud droplets

Growth of supercooled cloud droplets by vapor diffusion in super-saturated conditions has long been recognized as an inadequate explanation for the development of liquid-phase precipitation. The key role for droplet coalescence in collisions is now recognized as a mechanism for runaway development when a critical threshold size near  $D = 25 \mu\text{m}$  is attained. The runaway is the result of two strong size dependences: the collision efficiency and the  $D^2$  fall speed dependence pertaining to the Stokes regime. The overall size dependence of the collection kernel has been shown to be  $D^5$  (Freud and Rosenfeld [21]).

2. Ice particle growth by the Bergeron mechanism

Any ice particle seeds within a cloud of supercooled cloud droplets will grow at the expense of the supercooled water by the Bergeron process. This has not been recognized as the predominant process for precipitation formation in the extratropics, and has much applicability in the winter storm observations in BAIRS II.

3. Graupel formation by accretion of supercooled droplets

Any ice particle growing by the Bergeron process will begin to descend at a greater rate than the supercooled droplets surrounding it. This ice particle will then encounter cloud droplets in its path. The smaller the droplets, the faster they will freeze in contact with the evolving graupel particle, and the more fragile will be the rime surface. The continued “dry growth” of the graupel by accretion will enhance the yellow tail.

#### 4. Ice fragmentation by collision of graupel particles

Collisions between graupel particles falling at different speeds with respect to the air around them can produce ice particle fragments from the delicate rimed surfaces. This process has been demonstrated in laboratory experiments (Takahashi *et al.* [74]). The fragments can contribute to the yellow tails in the concatenated spectra and examples will be shown in Section 4.4.8.

#### 5. Secondary ice production

Viable mechanism for producing ice particles in concentration far larger than can be explained by ice nucleus concentrations begin with the Hallett–Mossop process (Hallett and Mossop [29]). This process involves the ejection of ice splinters (of column and needle form) when supercooled drops with  $D > 24 \mu\text{m}$  freeze. These new ice particles can then continue to grow by the Bergeron process (in the same manner as mechanism (2) above) to broaden the overall size distribution. The Hallett–Mossop process and its important droplet threshold are cited here specifically as they link strongly with an alternative mechanism for the creation of SLD near the melting layer, as discussed in the next section.

#### 4.4.7 An Alternative Hypothesis for Supercooled Droplets near the Melting Layer

The foregoing discussion on producing SLD and drizzle as an icing hazard has focused on the mechanism of collision/coalescence of small supercooled droplets. An entirely different mechanism for establishing SLD and drizzle near the melting layer has been proposed by Korolev *et al.* [40]. Droplets larger than the  $D = 25 \mu\text{m}$  threshold are transported upward from the melting zone below the  $0^\circ\text{C}$  isotherm. This obviates any need for mixed-phase coalescence, which, according to Korolev *et al.* [40], is suppressed by glaciation. In effect, products of melting are introduced as supercooled elements to produce the yellow tail in the concatenated size distributions.

Now we have two hypotheses to account for SLD and drizzle in the lower mixed-phase region, one set forth by Korolev *et al.* [45] and one based on runaway coalescence of cloud droplets. A major challenge in distinguishing these two hypotheses is that possibly coincidental matching of the  $D = 25 \mu\text{m}$  size threshold: one as a diagnostic for runaway coalescence and the other as a diagnostic for secondary ice production. (If the matching is not coincidental, the message on the matching is clear: secondary ice production is stimulated just as colloidal instability of a droplet cloud is occurring.) Table 5 contrasts the explanations of the two hypotheses for a range of observations, many of which have already been mentioned in the discussion on the maritime/continental contrast in Sections 4.4.2 to 4.4.4.

**TABLE 5**  
**Two Hypotheses for Presence of Large Droplets (>24  $\mu\text{m}$ ) Just Above the 0°C Level for Purposes of Enabling an Ice Multiplication Process**

Observation	Collision/Coalescence of Smaller Droplets	Upward Transport from Melting Layer
FSSP concentration contrast	Large CCN in continental regime	No explanation to offer
Abundance of small droplets above 0°C altitude	Ascent of air above 0°C isotherm	Not applicable
Exceedance of 25 $\mu\text{m}$ threshold	Essential for runaway coalescence	Needed for secondary ice production
Supercooled drizzle at -2°C	Collision/coalescence	No explanation to offer
Supercooled drizzle far above 0°C altitude	Collision/coalescence	No explanation to offer
Continuity of size spectra far from FSSP region (and through the size gap)	Collision/coalescence; Graupel formation; ice particle growth by Bergeron process; needle creation by secondary ice production	No explanation to offer or would not expect size continuity
Absence of SLW far above melting layer	Bergeron depletion by ice particles	Insufficient updraft speeds to transport drops
Drizzle drop concentration and ice particle concentration	Collision/coalescence	Effective transport of liquid drops from below melting layer
Absence of small drops aloft	Depletion by collision/coalescence; Bergeron depletion by ice particles	Glaciation of the cloud
Surplus of small ice particles	Fragmentation of graupel surface in graupel collisions	Secondary ice production
Drizzle drops in Continental regime	Air gets cleansed in condensate removal; collision/coalescence with larger LWC or with deeper cloud layer	Upward transport from warm region

The list of observations noted here may not pertain to both hypotheses, and when it is so, it is noted in the right-hand column.

The various explanations for observations following each hypothesis will be addressed in the discussion of specific observations in each of five flights in BAIRS II, in the next Section 4.4.8.

#### **4.4.8 Investigation of Spectral Broadening, Flight by Flight**

With an aim to disclose conditions favorable to SLD and drizzle, and to distinguish the two hypotheses summarized in Table 5 for SLD, specific episodes when yellow tailing of the concatenated hydrometeor distributions is present will be explored for selected time intervals. In making the assessments

about the nature of the hydrometeors, extensive use is made of the CPI particle imagery on account of the unambiguous identification of hydrometeor types. As a measure of the relative numbers of different hydrometeor types, and to ascertain which hydrometeors in CPI are making up the yellow tails, 2D-S imagery was also examined.

### **10 January 2017**

This continental flight is noteworthy for a minimum number of yellow tails in the concatenated hydrometeor observations in Figure 56. This is consistent with the FSSP distributions that just barely attain the  $D = 25 \mu\text{m}$  threshold for runaway coalescence. Noteworthy here are the white spaces (absence of any larger hydrometeors) coincident with the majority of rich FSSP populations (orange and red color). One episode of yellow tailing is evident at 16:16:03 UTC, when the FSSP concentration is showing orange ( $10^2$  to  $10^3$  particles per liter per micron). The CPI imagery (Figure 63) for the interval 16:17:07 to 16:17:40 UTC shows no evidence for SLD or drizzle, but only a multitude of ice fragments predominant in the size gap ( $D = 20$  to  $100 \mu\text{m}$ ).



The main message for this case is that the supercooled droplets remain largely in colloidally stable form, without progression to larger size. It is also noteworthy that the aircraft was close to the ML at 15:12 UTC ( $T = -2^{\circ}\text{C}$ ) but neither cloud droplets nor SLD was evident.

### **24 January 2017**

This solitary maritime case was previously discussed in Sections 4.4.2 to 4.4.4. The FSSP concentrations are two to three orders of magnitude smaller than for the other four flights, all characterized as continental. On the face of it, this evidence is consistent with a contrast in CCN between this case and the others. The median droplet diameters exceed substantially the  $D = 25\ \mu\text{m}$  threshold for runaway coalescence. However, in fairness to the hypothesis requiring proximity to the ML, all major yellow tail episodes in this case are time correlated with in situ temperatures and are within  $1\text{--}2^{\circ}\text{C}$  of the melting level.

Regarding the population of the yellow tails, one of the strongest examples is found at 05:59:00 UTC and examined in the CPI imagery for the time interval 05:59:12–05:59:21 UTC in Figure 64. A dominance of both small and large supercooled drizzle drops is evident, underscoring the icing hazard in the maritime regime.



Figure 64. CPI imagery for 05:59:12–05:59:21 UTC on 24 January 2017. Each image is labeled with a time stamp (above) and particle size (bottom; in  $\mu\text{m}$ ).

## **7 February 2017**

The BAIRS II flights in February and March showed evidence for MLs at higher altitude and were decidedly more convective in nature than the two January cases. The first pronounced yellow tailing associated with elevated FSSP concentration of supercooled cloud droplets is evident in Figure 58 during aircraft descent toward the ML at ~17:15 UTC. The Nevzorov LWC record shows evidence for SLW within the layer between 3500 m ( $T = -6^{\circ}\text{C}$ ) and 2400 m ( $T = 0^{\circ}\text{C}$ ), for a total layer thickness of 1100 m. The CPI imagery for the 17:18:11-17:18:47 UTC interval in Figure 65 shows evidence for numerous large supercooled droplets and one drizzle drop ( $D = 124\ \mu\text{m}$ ). Evidence for active riming is also apparent. The corresponding 2D-S imagery in Figure 66 for the 17:18–17:19 UTC interval also shows a predominance of drops exceeding the  $D = 25\ \mu\text{m}$  threshold for runaway coalescence.



02072017 171800 Buffer width = 1280 microns.  
 Project: BAIRS2-WERVEX Probe: 2DS\_H Resolution: 10,0000 microns  
 This image represents one minute of flight time, one panel every 5 seconds.  
 Many more images are not shown. Contact NRC (Mengistu Wolde) or ECCC (Alexei Korolev) for complete images.

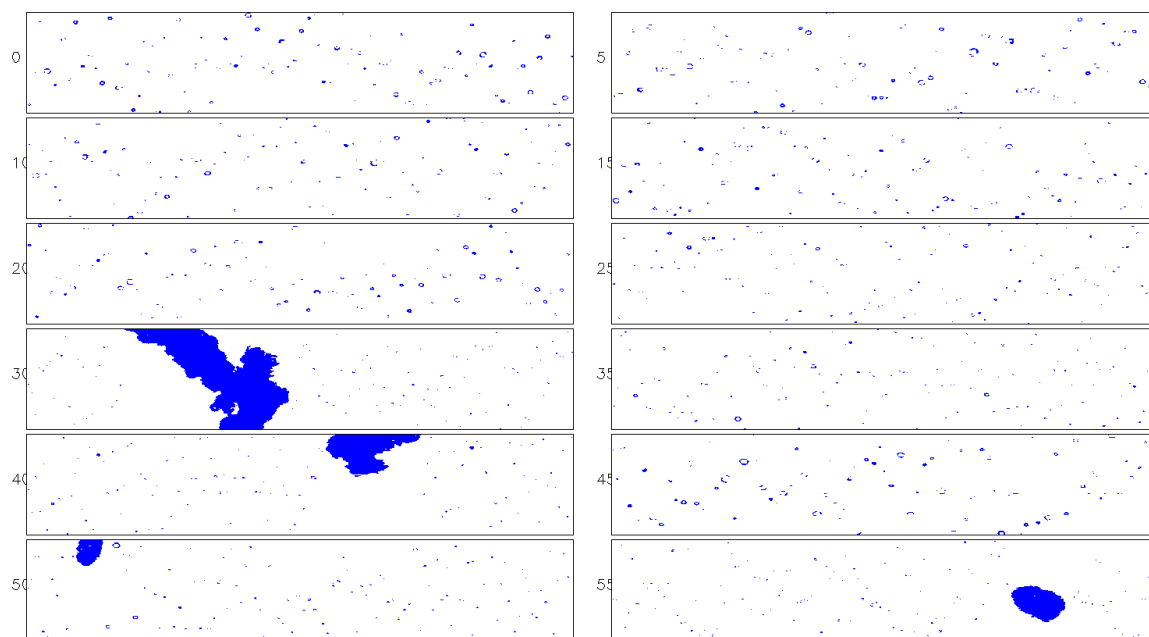


Figure 66. 2D-S imagery for 17:18–17:19 UTC on 7 February 2017. The number of seconds past the minute is shown to the left of each image.

During a later porpoising episode (18:40–18:52 UTC), another elevated concentration of supercooled droplets in FSSP ( $10^3$  to  $10^4$  particles per liter per  $\mu\text{m}$ ) is evident in a layer extending from 3200 m ( $T = -4^\circ\text{C}$ ) to 2400 m ( $T = 0^\circ\text{C}$ ) and back up to 3700 m ( $T = -8^\circ\text{C}$ ), for a layer thickness varying from 800 to 1300 m. The CPI imagery in Figure 67 obtained in the interval 18:48:16–18:48:45 UTC ( $T = -3^\circ\text{C}$ ) shows 18 examples of drops exceeding the SLD threshold ( $D = 100 \mu\text{m}$ ). The Nevzorov evidence for a layer of SLW with thickness 800 m to 1300 m is supportive of a coalescence mechanism for the SLD, but the proximity to the ML and the existence of columns and needles in the CPI imagery is supportive of the hypothesis for secondary ice production by Korolev *et al.* [44].

02/07/2017 18:48:16-18:48:45  
 Time is not synced. Time is CPI's original time.

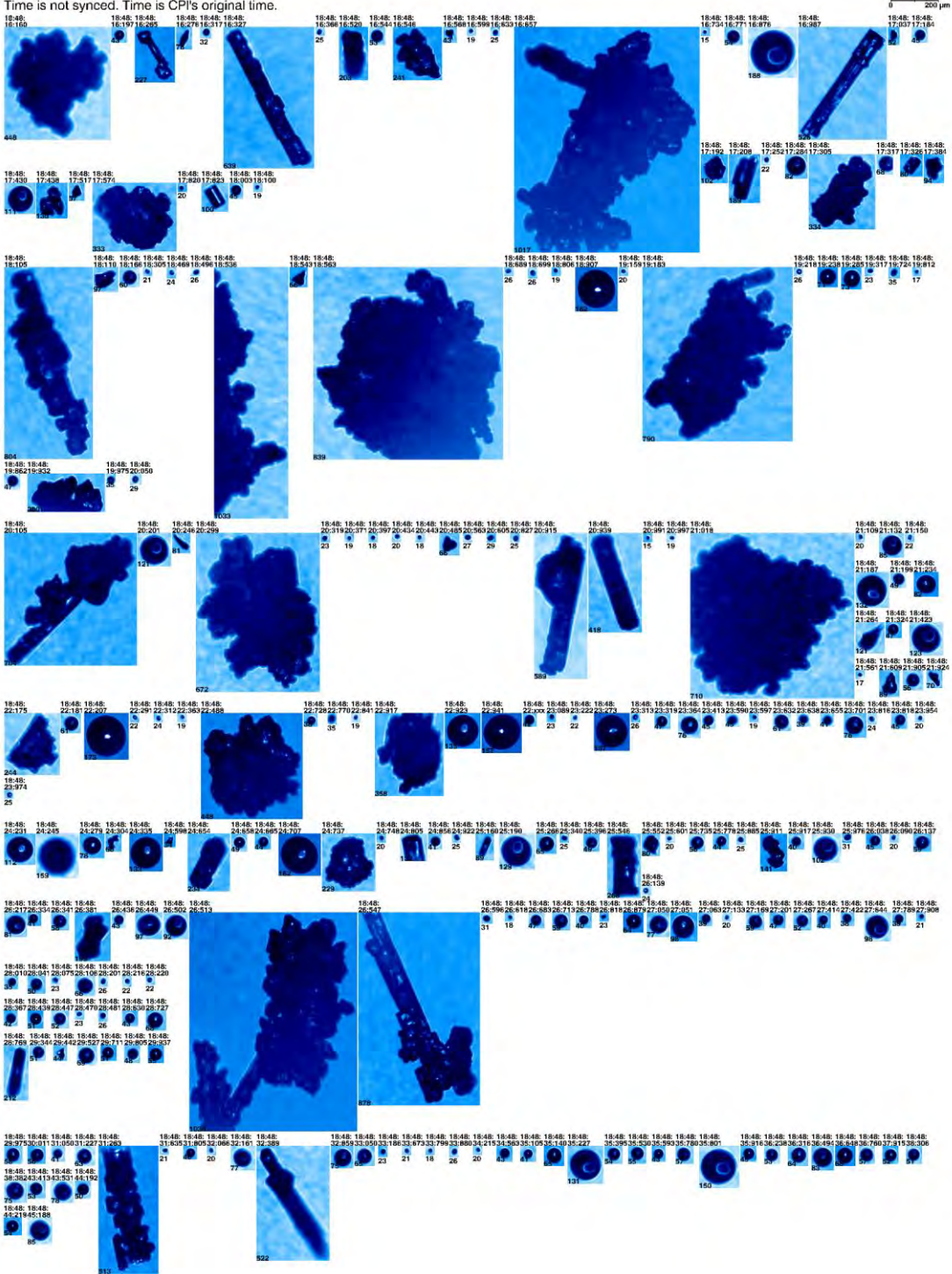


Figure 67. CPI imagery for 18:48:16–18:48:45 UTC on 7 February 2017. Each image is labeled with a time stamp (above) and particle size (bottom; in  $\mu\text{m}$ ).

## 24 March 2017

In the descent of the aircraft toward the ML in the 10:45 UTC time frame, a layer of supercooled water was encountered at 10:42:30 UTC at an altitude of 5500 m ( $T = -13^{\circ}\text{C}$ ). High concentration of supercooled water droplets are evident in FSSP observations (Figure 59) and with a distinct yellow tail beyond the  $D = 25 \mu\text{m}$  threshold. The aircraft was near the  $0^{\circ}\text{C}$  isotherm at 10:53 UTC at an altitude of 3200 m. The approximate SLW layer thickness is therefore 2300 m.

The CPI imagery in the interval 10:51:51 to 10:52:14 UTC is shown in Figure 68. Ten examples of droplet diameters exceeding the SLD threshold are shown, as well as a multitude of droplets whose diameters exceed the  $D = 25 \mu\text{m}$  threshold for runaway coalescence. The observations together with the thick layer of SLW above are supportive of the collision/coalescence mechanism for SLD near the  $0^{\circ}\text{C}$  isotherm. Maritime conditions (as with 24 January 2017) with small populations of larger droplets are evidently not essential for effective coalescence and SLD so long as the LWC and the layer thickness are sufficiently large.



A second example of an encounter with SLD near the lower boundary of a layer of supercooled water can be seen in Figure 59 during porpoising in the 12:54–12:59 UTC time interval. The FSSP concentration of supercooled cloud droplets is enhanced and yellow tailing is evident beyond the  $D = 25 \mu\text{m}$  threshold. The LWC on the Nevzorov probe is sustained from an altitude of 4100 m ( $T = -6^\circ\text{C}$ ) at 12:54 UTC to 3000 m ( $T = 0^\circ\text{C}$ ) at 12:59 UTC, for an estimated layer thickness of 1100 m. CPI imagery in the 12:57:20–12:57:40 UTC interval ( $T = -1^\circ$  to  $-2^\circ\text{C}$ ) in Figure 69 shows 12 examples of SLD together with a larger population of droplets with  $D > 25 \mu\text{m}$ . The proximity of the ML allows the possible transfer of larger droplets from below, but the substantial layer of SLW in cloud droplet form also allows for collision and coalescence.

03/24/2017 12:57:20-12:57:40

Time is not synced. Time is CPI's original time.

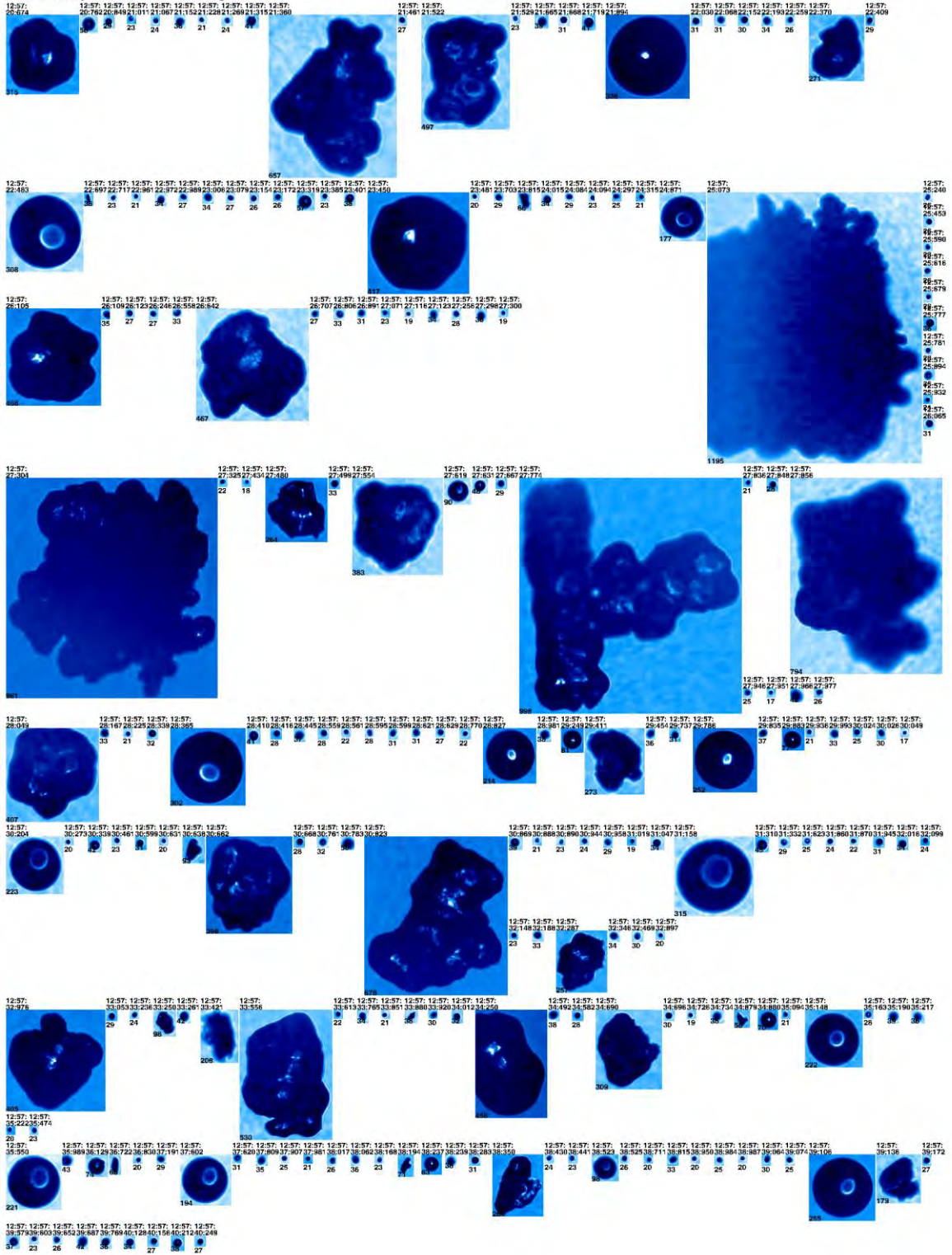


Figure 69. CPI imagery for 12:57:20–12:57:40 UTC on 24 March 2017. Each image is labeled with a time stamp (above) and particle size (bottom; in  $\mu\text{m}$ ).

## 25 March 2017

This was another “warm” case with elevated radar bright band, and the clouds on this day were sampled primarily with the porpoising maneuver (as evident with the oscillation in temperature shown in Figure 60) but with only two excursions below the melting level (12:42–12:50 UTC and 14:05–14:12 UTC). The partial disappearance of FSSP observations during both episodes is evidence that the ascent of air was not prevalent beneath the ML, when radar bright bands were evident during both episodes.

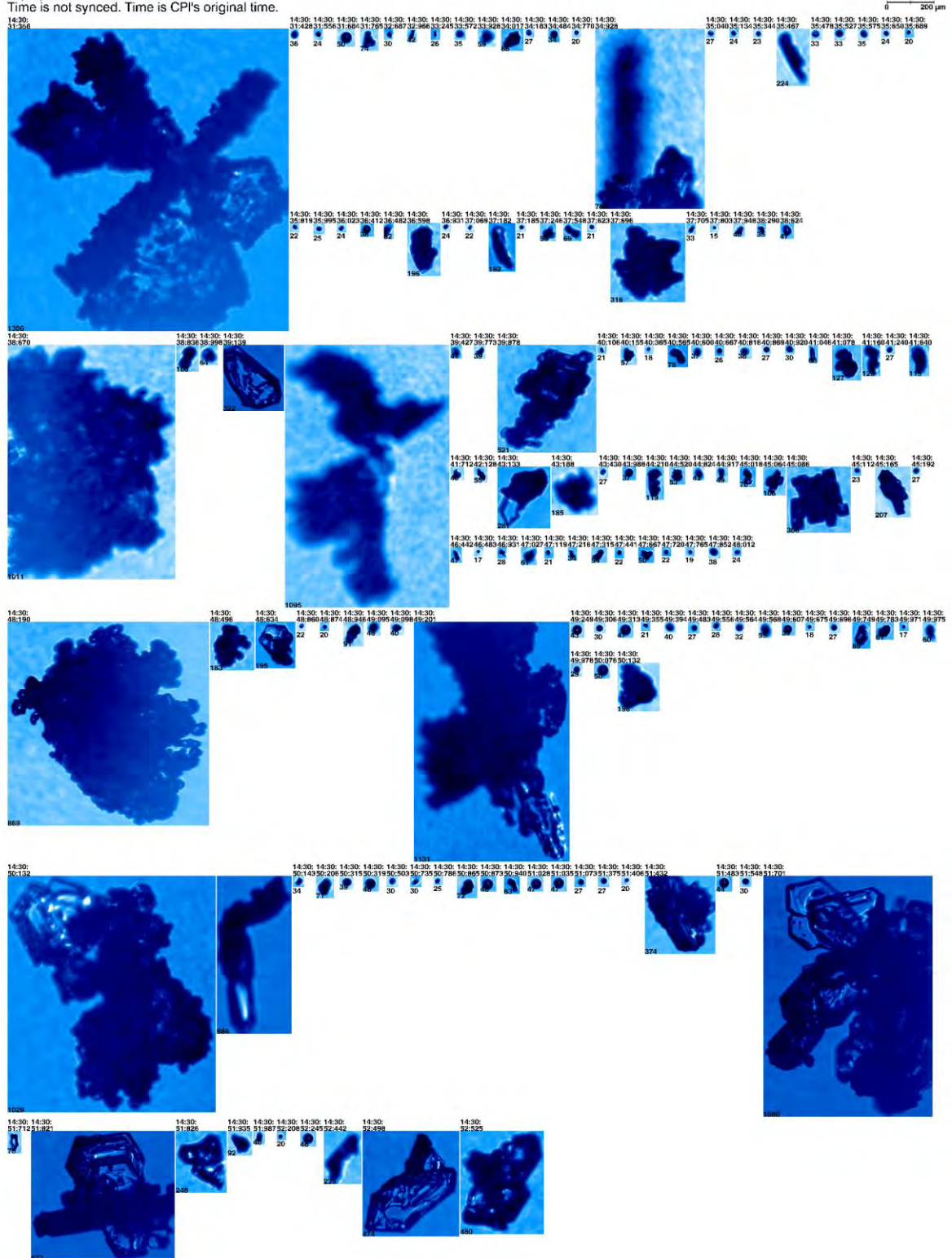
Above the ML, several episodes of enhanced FSSP concentration are evident, with tails exceeding  $D = 25 \mu\text{m}$  size in the yellow range of concentration (10 to 100 particles per liter per  $\mu\text{m}$ ). In general, SLD was not the main constituent in these tails, but instead size gap droplets, graupel, and possibly graupel fragments were. This description was upheld even when the aircraft was in proximity to the ML, as in the first example discussed below.

Figure 60 shows aircraft proximity to  $0^\circ\text{C}$  (near  $T = -1^\circ\text{C}$ ) over the 12:50–12:55 UTC interval. The FSSP droplet concentration is large and sustained. The aircraft ascent immediately afterward shows evidence for a layer of SLW from  $T = 0^\circ\text{C}$  (4300 m) to  $T = -8^\circ\text{C}$  (6000 m), for a total thickness of 1700 m. The CPI imagery in Figure 70 for the 12:53:59–12:54:11 UTC interval ( $T = -1^\circ\text{C}$ ) shows an abundance of supercooled cloud droplets with size  $D > 25 \mu\text{m}$ , but no drizzle drops. Millimeter-sized graupel particles are also evident together with larger numbers of fragments that may have been produced by hydrometeor collisions. Therefore, in this continental case, accretion of cloud water is dominating over coalescence in creating larger hydrometeors.



A second example of FSSP enhancement and yellow tailing later in the flight and further ( $T = -5^{\circ}\text{C}$ ) from the ML is examined near 14:30 UTC. The LWC on Nevzorov (not shown) was enhanced from 14:29–14:33 UTC, consistent with enhanced FSSP concentrations evident in Figure 60. The CPI imagery from 14:30:31–14:30:52 UTC in Figure 71 shows an abundance of supercooled droplets in the size gap range, but no SLD drizzle drops. Riming and graupel are evident, as are ice fragments that may have been produced by collisions.

03/25/2017 14:30:31-14:30:52  
 Time is not synced. Time is CPI's original time.



Both examples drawn from this more convective continental case provide evidence that the preferred mode of growth to larger hydrometeors is accretion to form graupel rather than SLDs. This microphysical mode is preferred in this case even within 1°C of the ML, casting doubt on a robust transfer of drops into the mixed-phase region from below.

#### **4.4.9 Discussion**

Observations from five separate flights have been examined for conditions favorable to the production of SLD, a long-recognized icing hazard (Sand *et al.* [68]; Polotovich [61]; Bernstein *et al.* [6]). Concurrently, efforts have been made to distinguish a collision/coalescence hypothesis from the idea proposed by Korolev *et al.* [44], [45] that larger drops may arise from transport back up through the ML. The common presence of rich concentrations of supercooled cloud droplets immediately above the ML and in the lower reaches of the mixed-phase region is evidence for lifting at and above 0°C in these warm winter systems, in agreement with the more extensively investigated mesoscale ascent above 0°C (with descent beneath and inflow jet at 0°C to compensate the upward and downward motions) in summertime mesoscale convective systems (MCSs). These winter storms are not glaciated above 0°C, but instead exhibit layers of supercooled water that can exceed 1000 m in thickness. (Similar observations were noted earlier in BAIRS I (Williams *et al.* [84]). Other studies (Cober *et al.* [12]; Rasmussen *et al.* [63]; Rosenfeld *et al.* [65]) have shown that this thickness is sufficient to support a collision/coalescence process adequate to form SLDs near the 0°C level without any need for transport from below. The identification of times when the aircraft is in proximity to 0°C and no large drops are present casts some doubts on the robust nature of this process, as discussed by Korolev *et al.* [44], [45]).

These findings underline the importance of the radar bright band in winter storms as a flag for the presence of both SLW in small droplet form and in SLD form, immediately above the ML bright band. When large ice particle fluxes from above are absent (in contrast to summertime MCS stratiform regions), the minimal role of ice nuclei at these warmest mixed phase temperatures, together with the strong tendency for ascent make this region particularly hazardous to aviation.

### **4.5 FURTHER CONSIDERATIONS OF ICE MULTIPLICATION AND THE ASSOCIATION OF NEEDLE CRYSTALS WITH SUPERCOOLED WATER**

#### **4.5.1 Introduction**

The ice multiplication process is also of considerable importance to aircraft icing for two main reasons. First and foremost, a number of mechanisms rely on the presence of supercooled water in large droplet form. These mechanisms for ice multiplication include the Hallett–Mossop process (Hallett and Mossop [29]), requiring a threshold droplet diameter of 25 µm, and ice shattering mechanisms that operate more effectively with larger supercooled drops (Wildeman *et al.* [79]; Lauber *et al.* [49]). The Hallett–Mossop process is of considerable interest because it operates in a temperature range in which needle crystals are the dominant crystal habit (Bailey and Hallett [1]), and needles are abundant in the BAIRS II dataset. The second reason for ice multiplication’s importance is the proliferation of ice particles that serve as sinks for supercooled water by the Bergeron process. In this sense, ice multiplication can ameliorate the icing hazard. Another interest in the association of supercooled water with ice crystals is the claim (e.g., Takahashi [72]) that dramatic reductions in charge transfers in ice particle collisions are evident when supercooled water and water-saturated conditions are absent.

The availability of observations on needle crystal concentrations in a dataset in which the yes/no condition on supercooled water has become increasingly stringent motivated some tests when needle crystals were the predominant hydrometeor.

#### **4.5.2 Selection of Flight Time Periods with Rich Needle Concentrations**

To test these ideas about ice multiplication in the needle region that is so prevalent in the BAIRS II flights, one needs measurements of needle concentration. The SNDI algorithm in use with the Convair-580 hydrometeor measurements provides estimates of the relative concentrations of needles (in comparison with classified Spheres, Dendrites, and Irregulars) but not absolute concentrations. Accordingly for this study, we have selected all time intervals on all five flights for which the needle population is equal to or greater than 90% of the total and then assume that the total hydrometeor concentration  $N$  and the  $N*r$  parameter from Korolev and Mazin [42] will represent needle crystals alone.

Fifteen five-second time intervals have been selected from five BAIRS II flights and eight intervals from one BAIRS I flight for which the 90% abundance criterion for needles was satisfied for either the 2D-C or the PIP SNDI analysis (see Section 2.5). The substantially more stringent rules for presence/absence of supercooled water, elaborated on earlier in Section 4.1, were implemented to make yes/no decisions on the presence of supercooled water and mixed-phase conditions. These conditions include consideration of FSSP droplet concentrations and the ratio of liquid water content to total water content on the Nevzorov probe. Eight cases with no supercooled water (“no-SLW”) and 15 cases with supercooled water (“yes-SLW”) were identified. The five-second averaged crystal concentrations for the two scenarios are plotted in Figure 72, along with the mean value of particle size  $r$ , extracted from simultaneous values of  $N$  and  $N*r$  from the five-second data sample. Among the BAIRS II cases, the greatest number of samples was found on 24 March 2017, likely because of the extensive porpoising performed on that day through the temperature region of most importance for needles.

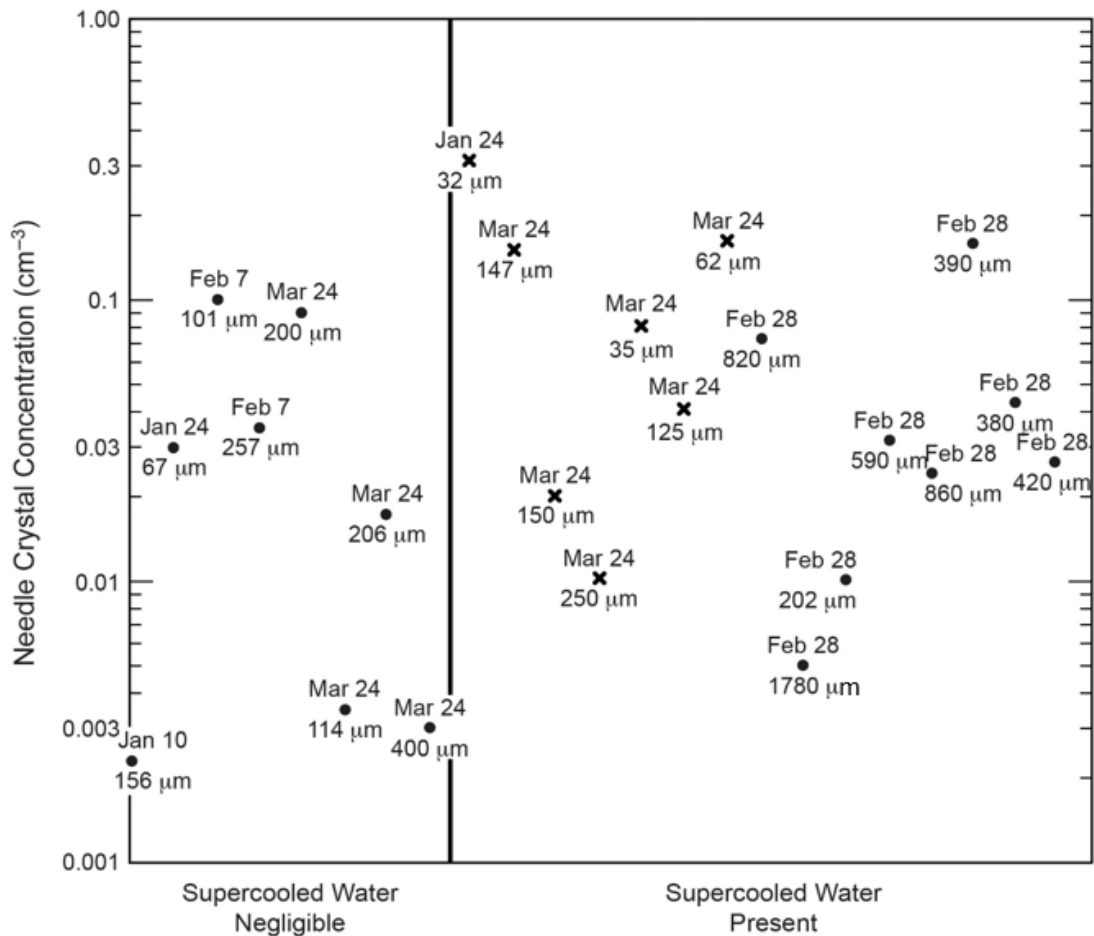


Figure 72. Needle crystal concentrations for dates and times when the fraction of needle crystals in the SNDI algorithm exceeded 90%. Data points are labeled by the date of the BAIRS II flight and by mean crystal size. Data from one flight in BAIRS I (28 February 2013) were also added. The placement of the points along the abscissa is not indicative of the amount of SLW present.

The needle concentrations in Figure 72 range from  $10^{-3}$  to  $0.3 \text{ cm}^{-3}$ . The smallest concentrations are already two to three orders of magnitude larger than what measured ice nuclei concentrations would account for (e.g., Ladino *et al.* [48]). Accordingly, ice multiplication mechanisms are of immediate interest to account for the substantial needle concentrations in the temperature range  $-4^{\circ}$  to  $-7^{\circ}\text{C}$ .

The contrast in concentrations between no-SLW and yes-SLW scenarios is discernible, but less dramatic than preliminary analysis showed with a smaller number of data points. The contrast in mean values between no-SLW ( $0.035 \text{ cm}^{-3}$ ) and yes-SLW ( $0.075 \text{ cm}^{-3}$ ) is about a factor of two. This contrast falls short in explaining by itself the more marked contrast in charge transfer per collision in laboratory simulations of ice particle charge transfer in the presence/absence of supercooled water. The very smallest needle concentrations are clearly in the no-SLW group, and the very largest concentrations clearly in the

yes-SLW group, but some cases are also found with large needle concentrations in the apparent absence of supercooled water. In the flight on 7 February 2017, some large needle concentrations were noted in the absence of SLW, but in both cases, a layer of supercooled drizzle overlaid the sample altitudes, possibly serving as a source for ice multiplication.

The general absence of the large supercooled drops needed to account for ice multiplication within the sampled needle population is a bit puzzling, but of course the actual ice multiplication process may have taken place elsewhere and still served to supply the observed needle crystals, or the Convair-580 may have arrived in these areas after all the SLD were already depleted.

#### **4.5.3 Characterization of the Needle Environment**

The immediate microphysical environment of the rich needle populations documented in Figure 72 has been examined by consulting the CPI imagery among the BAIRS II cases for the same time frames (the CPI probe was not installed for BAIRS I). Consistent with the 2D-C and PIP analysis, when SNDI documents a high percentage of needles, this crystal type is also predominant in CPI. One can also look for supercooled droplets in the size range exceeding 18  $\mu\text{m}$  diameter in CPI. In general, all possible combinations of rimed/unrimed needles and presence/absence of supercooled droplets are apparent in these comparisons for the 15 five-second intervals selected for Figure 72 as expected given the spread of the data cases. However, in the yes-SLW category, rimed needles were most commonly observed. In the no-SLW category, the occurrence of rimed and unrimed needles was comparable. Examples of CPI imagery in each category are shown in Figure 73 (no-SLW, rimed columns, then unrimed needles) and in Figure 74 (yes-SLW, rimed needles).

01/10/2017 15:18:39-15:20:45  
 Time is not synced. Time is CPI's original time.

0 200  $\mu$ m

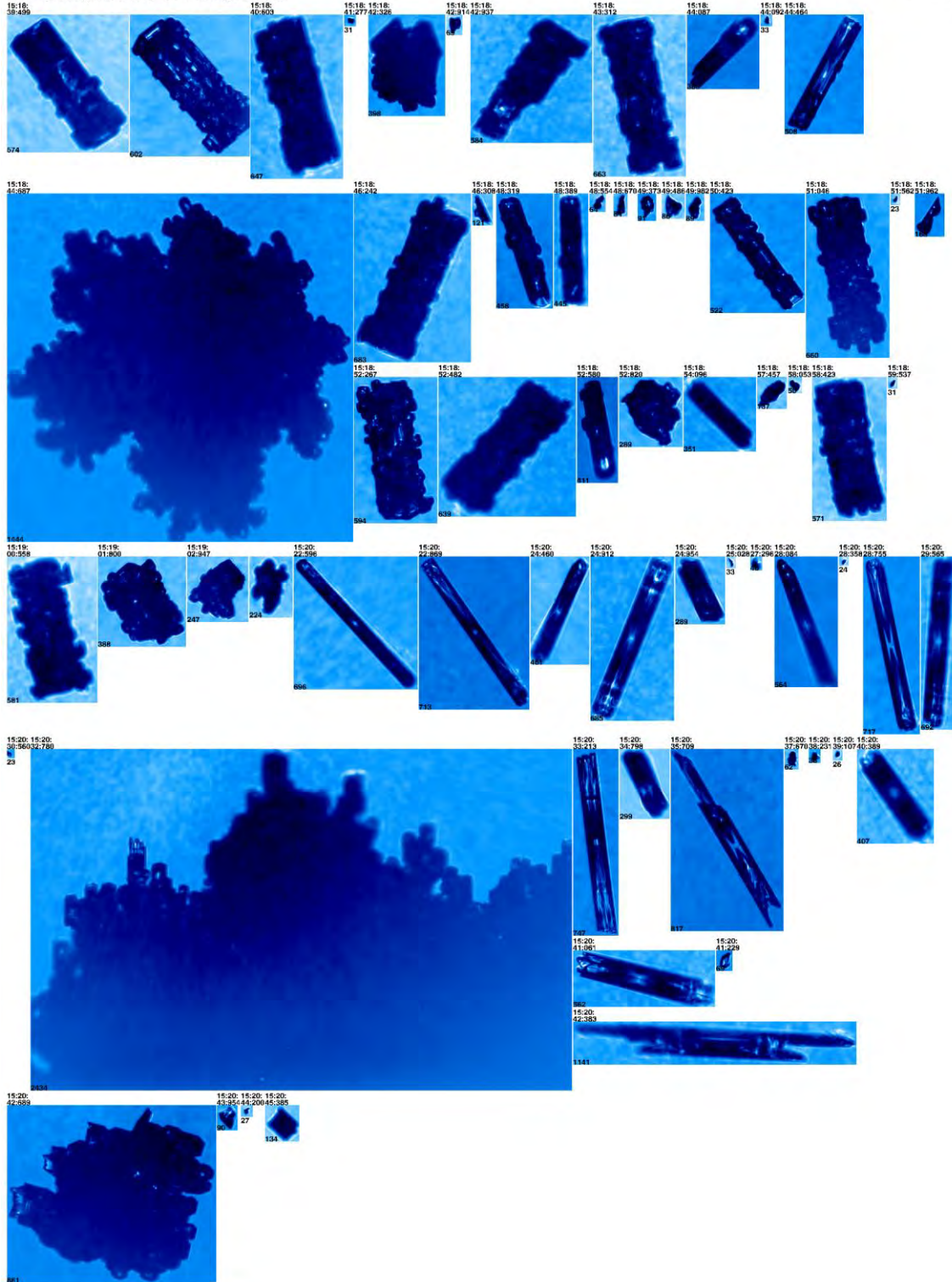


Figure 73. CPI imagery covering a transition from rimed columns (and small graupel particles) (15:18:39–15:19:02 UTC) to unrimed needles (15:20:22–15:20:45 UTC) on 10 January 2017.



The presence of unrimed needles and unrimed dendrites has long presented an apparent contradiction with the laboratory diffusion chamber results (Bailey and Hallett [1]), since in the cloud medium a water-saturated condition must be maintained by the presence of supercooled water. (In the laboratory, the water-saturated condition can be maintained through the artifice of imposed temperature and moisture gradients.) One way around this paradox is to have the supercooled water in sufficiently-small droplet form that no riming is possible by virtue of negligible collision efficiency. The FSSP instrument used in this study has a lower limit of  $D = 3 \mu\text{m}$ , so the smallest cloud droplets with the smallest collision efficiencies cannot be observed. Another contributing factor to this suppressed riming may be the modest fall speeds achieved by needle shapes, as estimated in Section 4.2.5.

Droplets with sizes greater than the Hallett–Mossop threshold ( $D = 25 \mu\text{m}$ ) were rare in the CPI imagery for these cases and larger drizzle-size droplets suitable for making ice multiplication by freezing/shattering were also absent. So generally speaking the nature of the supercooled water (in small droplet form) was not suitable for exploring the observed crystal concentrations by generally recognized ice multiplication mechanisms. However, it is quite possible that suitable supercooled water was available outside these special volumes characterized by largely pure needle populations to account for the ice multiplication. One possible example of that is the case of 7 February 2017 with drizzle overlying the needle observation altitude as has already been mentioned.

#### **4.5.4 Comparisons of Distributions of $N^*r$ for Dendrites and for Needles**

The empirical information from the laboratory diffusion chamber measurements (Bailey and Hallett [1]) is that water-saturated conditions are required for both needle and dendritic crystals, but in distinct temperature ranges. However, the collective experience from BAIRS I and II, particularly the analysis of “crystal sandwich” scenarios in BAIRS II (see Section 4.2), supports the view that supercooled liquid water is more likely to be collocated with or in close proximity to needles than is the case for dendrites. One possible explanation for this result is that the sink for supercooled water in the Bergeron process,  $N^*r$  (Korolev and Mazin [42]), is larger in general for dendrites than for needles. As a test of this prediction, all values for  $N^*r$  for conditions with “pure” crystal concentrations (again defined as SNDI percentages exceeding 90% in either 2D-C or PIP category) in both the Dendrite and the Needle categories are shown in Figures 75 and 76, respectively. Contrary to hypothesis, the  $N^*r$  values for needles (mean value  $3.1 \mu\text{m}/\text{cm}^3$ ) are larger than for dendrites (mean value  $1.0 \mu\text{m}/\text{cm}^3$ ). It should be noted, however, that the  $N^*r$  values for needles are inflated by a factor of approximately two relative to the true values because the Feret diameter is computed rather than the capacitive length. If the needle values of  $N^*r$  in Figure 76 are adjusted downward by a factor of around two, the values for dendrites and needles come into closer parity. This still leaves the explanation for why SLW is more common among needles than among dendrites in the BAIRS observations incomplete.

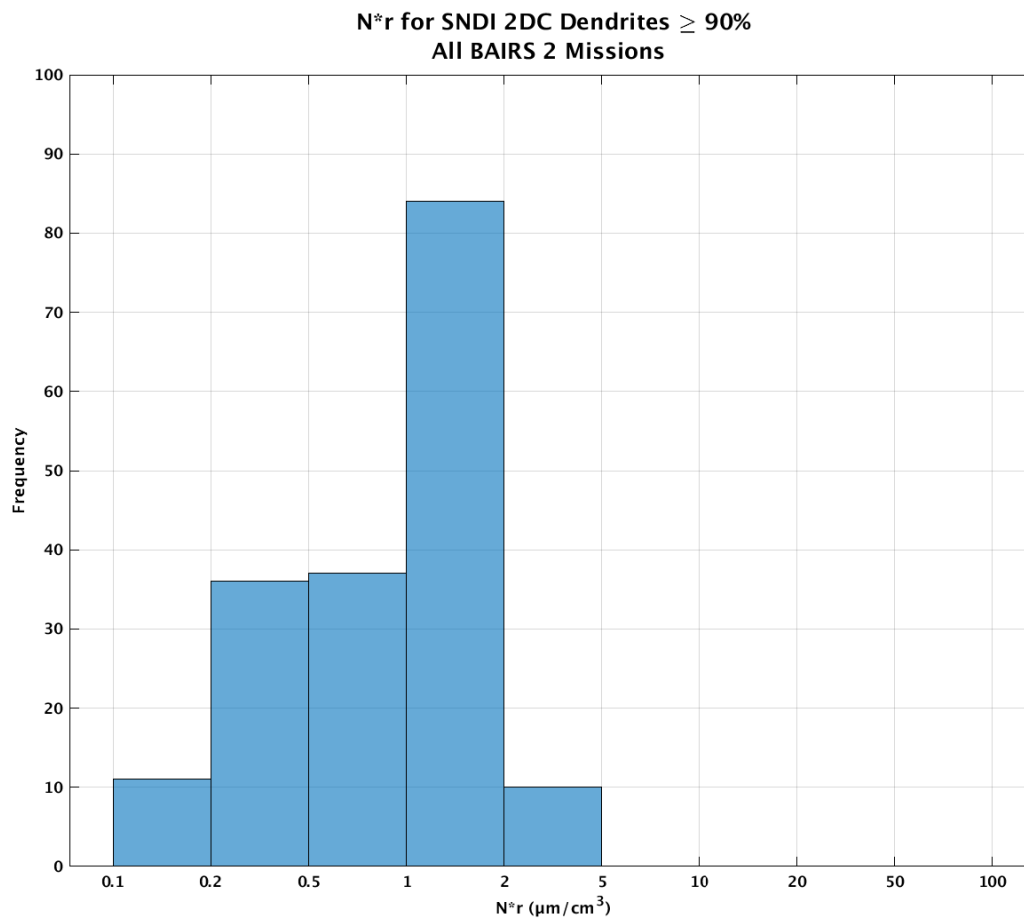


*Figure 75. Histogram of  $N^*r$  values for all dendrite crystals under the condition that  $>90\%$  of crystals in the SNDI algorithm are Dendrites.*

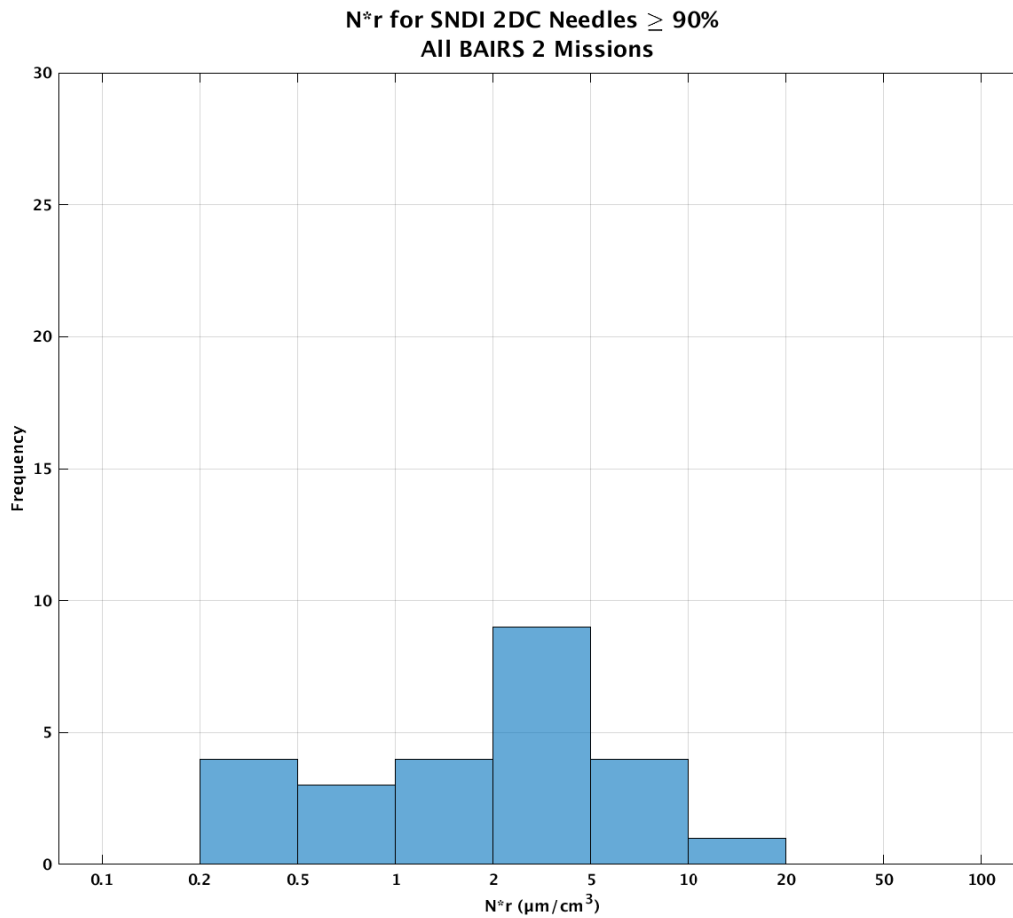


Figure 76. Histogram of  $N^*r$  values for all needle crystals under the condition that  $>90\%$  of crystals in the SNDI algorithm are Needles.

## 4.6 SEARCH FOR DUAL POLARIMETRIC DISTINCTIONS BETWEEN GLACIATED AND SUPERCOOLED ENVIRONMENTS

### 4.6.1 Introduction

In keeping with the overriding objective of this study, which is the use of dual polarimetric radar to diagnose the presence of supercooled water and icing hazard, this section of the report is concerned with a comparison of NEXRAD dual polarimetric response to storm volumes characterized on the basis of the in situ aircraft observations in BAIRS II as either glaciated or mixed phase. The approach taken here was intended as a shortcut procedure for a more elaborate machine-learning approach whose findings remain incomplete at press time for this report.

### 4.6.2 Classification of Glaciated and Mixed Phase Environments

The use of the aircraft observations to distinguish between storm regions in a glaciated and a mixed phase category was based on the methods described in Section 4.1 and is an improvement on such methods

from BAIRS I. The mixed phase regions of interest here (also referred to here as “SLD” phase) include observations verified to contain supercooled water in SLD form (on the basis of CPI hydrometeor imagery) with evidence of drizzle-sized drops ( $\geq 100 \mu\text{m}$ ) mixed with either cloud droplets, ice crystals, or both. The glaciated regions were devoid of supercooled water in any form (small or large drops). The goal of these comparisons is to identify appreciable differences in the distributions of measured dual polarimetric variables for mixed and glaciated phase regions in the storms. Results of these comparisons are provided in the following section.

### 4.6.3 Comparisons between Glaciated and SLD Phase

The observables considered here for comparison between glaciated phase and SLD phase are mean X-band reflectivity (Figure 77), mean NEXRAD reflectivity (Figure 78), NEXRAD Hydrometeor Class mode (Figure 79), mean NEXRAD differential phase (Figure 80), mean NEXRAD correlation coefficient (Figure 81), mean NEXRAD differential reflectivity (Figure 82), and in situ mean temperature (Figure 83). All X-band, NEXRAD, and temperature observations are averaged over five seconds. The NEXRAD values (mean and mode) were computed among all valid values within the physical-sized window (Section 2.3) matched in time and space to the aircraft location. The comparisons for each quantity are discussed here in turn.

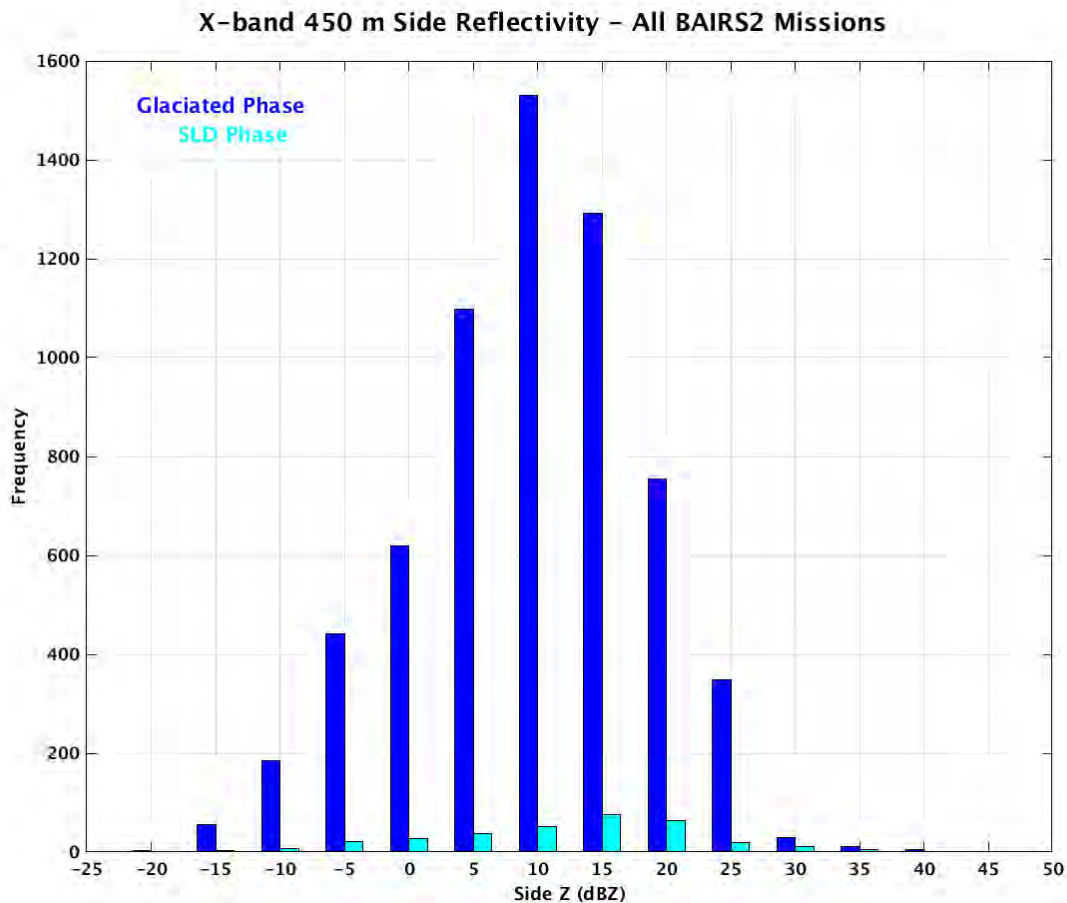


Figure 77. Convair-580 X-band 450 m mean reflectivity (side) for all BAIRS II missions separated by glaciated (blue) and SLD (cyan) phases.

With regard to the X-band radar reflectivity in Figure 77, the reflectivity values for the SLD cases are clearly enhanced, by what looks like about 5 dB. For example, the maximum frequency of the SLD distribution in Figure 77 is at 15 dBZ and the maximum in the glaciated distribution is at 10 dBZ, 5 dB smaller. This offset is what we expect to have based on the effective difference in dielectric constant between liquid and solid phase of ice (Battan [2]; pages 38–40). The  $IKI^2$  quantity is 0.93 for water and 0.197 for ice, a contrast of 6.7 dB, and so the results in Figure 77 (coarsely resolved at the 5 dBZ level) are quite reasonable.

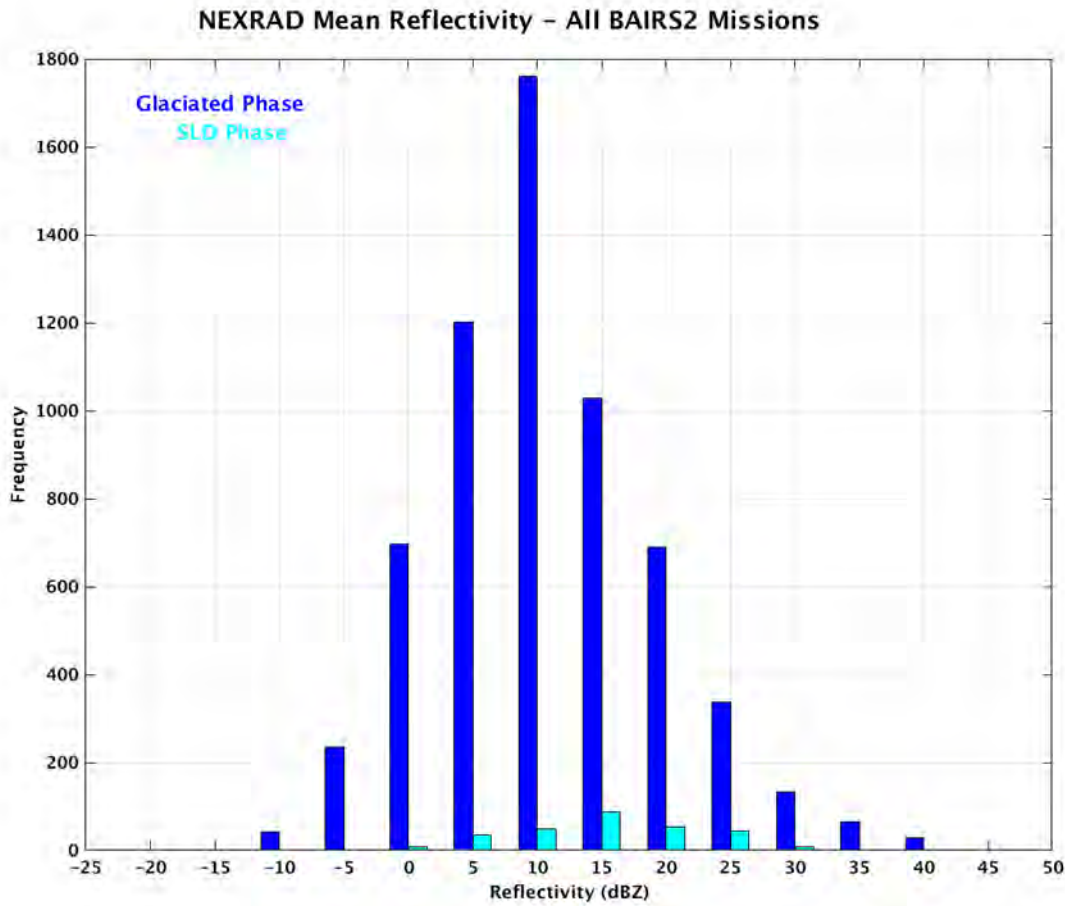


Figure 78. NEXRAD mean reflectivity for all BAIRS II missions separated by glaciated (blue) and SLD (cyan) phase.

Figure 78 shows the distributions for the glaciated phase and mixed phase (SLD) for NEXRAD S-band radar reflectivity instead of the onboard X-band radar. Thankfully, we have the same situation here that we had with the X-band comparisons in Figure 77. The SLD cases involving liquid water are offset to the right by ~5 dB, consistent with the difference expected based on the dielectric constant contrast between liquid and solid ice (Battan [2]).

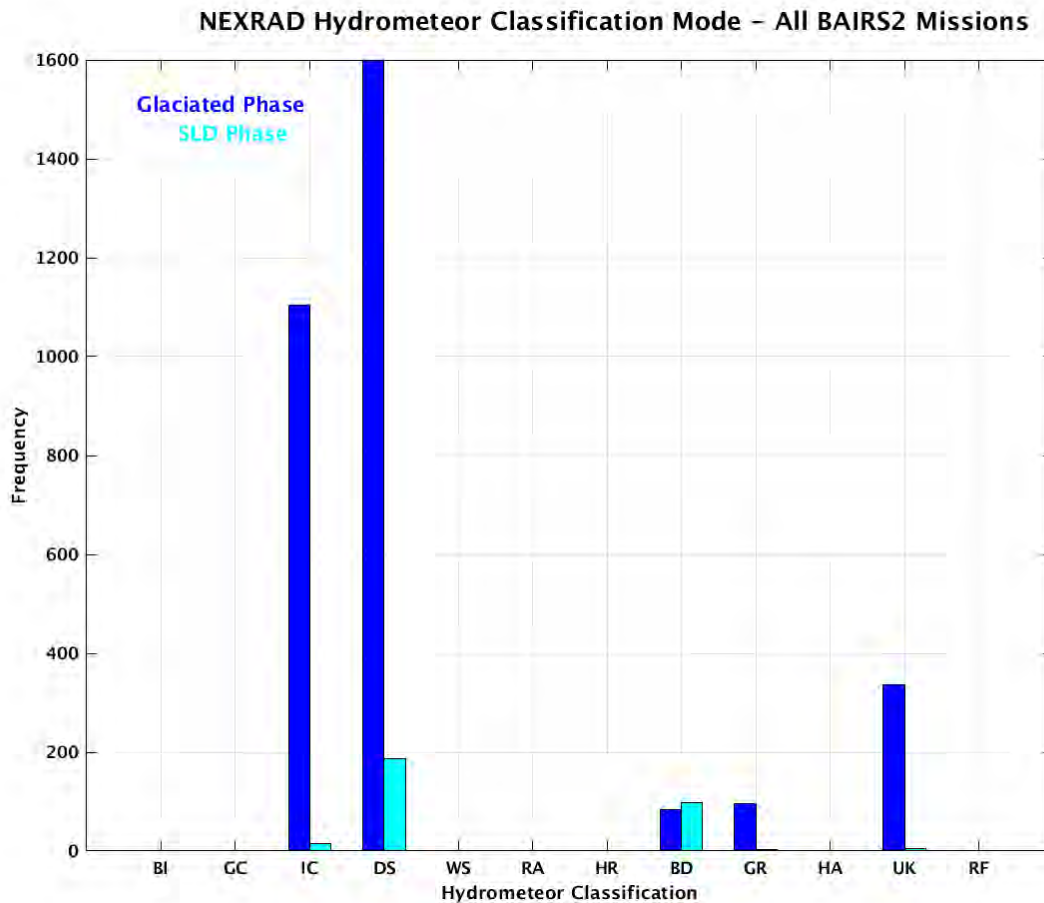


Figure 79. NEXRAD hydrometeor classification (HC) mode for all BAIRS II missions separated by glaciated (blue) and SLD (cyan) phases. Abbreviations of the HC categories include Biological (BI), Ground Clutter (GC), Ice Crystals (IC), Dry Snow (DS), Wet Snow (WS), Rain (RA), Heavy Rain (HR), Big Drops (BD), Graupel (GR), Hail-Rain mix (HA), and Unknown (UK).

Figure 79 shows how the two categories, glaciated and SLD phases, are distributed with the hydrometeor class mode. Cases were chosen based on the smallest slant range distance to the Convair-580 among the three NEXRAD radars scanning in the BAIRS II domain (KBUF, KBGM, KTYX). The most prevalent categories in the BAIRS II winter storms are DS and IC, as one might expect. Here, there is evidence for supercooled liquid water masquerading as DS, a finding first noted from BAIRS I. This is attributable to comparable Z values and to ZDR values that are not markedly different from zero. One also sees SLD showing up in the BD category in 30% and 1% of the SLD (mixed phase) and glaciated cases, respectively. Remember that SLD (liquid water) is not allowed in this hydrometeor classification's log anywhere above the ML altitude. Accordingly, it is forced to pick a different class even if it somehow wanted a liquid water designation (RA or HR). The BD findings would be within the ML zone.

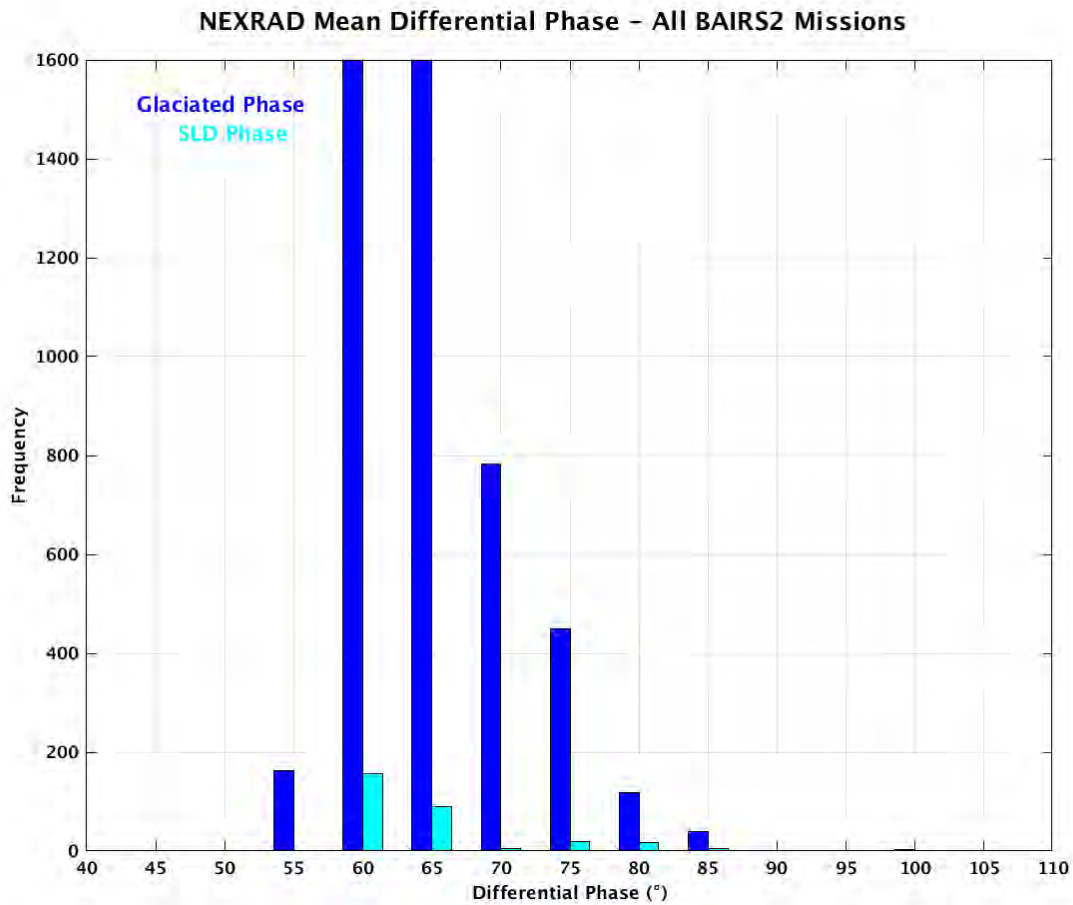


Figure 80. NEXRAD mean differential phase for all BAIRS II missions separated by glaciated (blue) and SLD (cyan) phases.

Comparisons for NEXRAD PHI are shown in Figure 80. The two maxima in differential phase for glaciated agree with the two maxima in SLD phase, so no significant distinction is evident here in dual polarimetric response at this level of resolution ( $5^\circ$ ). It should also be noted that responses in PHI at operational radar sites begin at  $55\text{--}60^\circ$  and this is reflected in the absence of observations below this interval within the figure. The distribution bin count has been capped at 1600, but the actual maxima for glaciated phase exceeds 2200 in both bins.

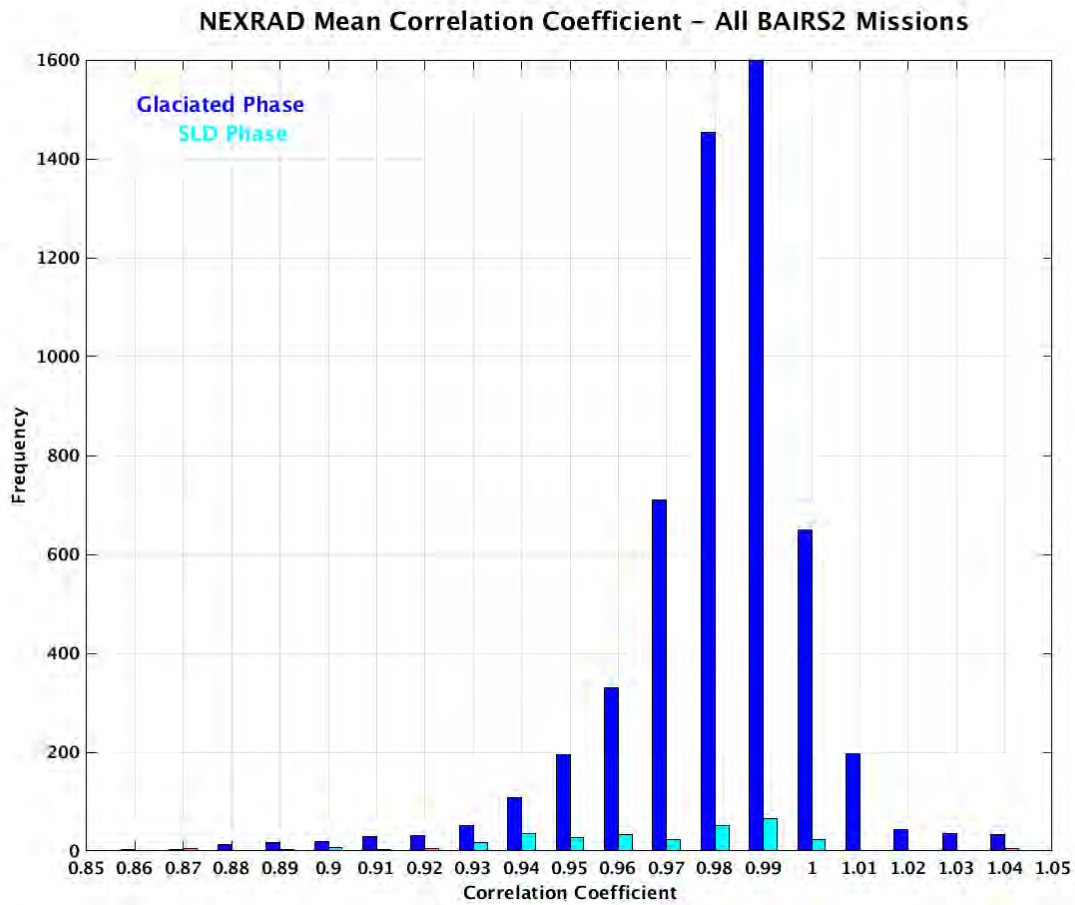


Figure 81. NEXRAD mean correlation coefficient for all BAIRS II missions separated by glaciated (blue) and SLD (cyan) phases.

With regard to the NEXRAD correlation coefficient in Figure 81, the maximum frequency in the glaciated phase category coincides with the maximum frequency in the SLD category, and no obvious offsets in values are evident for the two regimes here. The bin count maximum at 0.99 for the glaciated category is 2289.

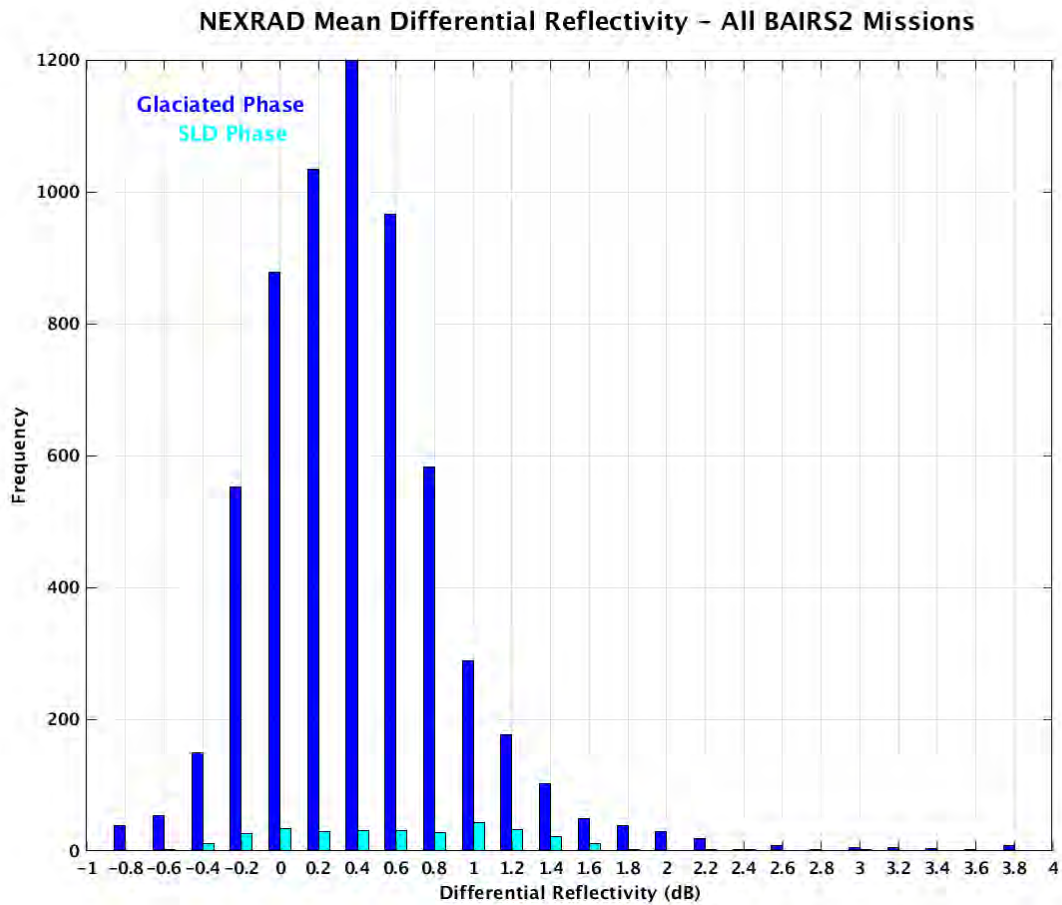


Figure 82. NEXRAD mean differential reflectivity for all BAIRS II missions separated by glaciated (blue) and SLD (cyan) phases.

Comparisons in NEXRAD differential reflectivity for SLD (mixed phase) and glaciated categories are shown in Figure 82. Here, we have a significant offset of the two distributions, with larger mean ZDR associated with the SLD category than with the glaciated category. The mean ZDR for SLD is roughly twice the values for glaciated cases. This finding is puzzling because the ZDR for real drizzle should be zero, so in the absence of contributions from supercooled raindrops and aggregates mixed in, we should have 0 dB in the mean for SLD and we do not. A review of the CPI imagery showed that drizzle drops of at least 100  $\mu\text{m}$  were present among all SLD intervals, with drop sizes between 200–500  $\mu\text{m}$  common.

The full distribution plots in Figures 73 to 83 show that the mixed-phase category (with the condition of SLD present) was less prevalent than glaciated by one to two orders of magnitude over the five flights. Accordingly, twice the number of glaciated samples were randomly selected at comparable levels of radar reflectivity (measured by the Convair-580 X-band radar) to make the comparisons between the two distributions of dual polarimetric variables. Six sets of six-panel NEXRAD (Z, ZDR, CC, PHI, HC) and in situ temperature distribution plots (not shown here) that contain a random sample of glaciated cases equal to twice the number of SLD cases all show evidence of the offset of the mixed-phase distribution relative to the glaciated distribution in each set for the reflectivity intervals at 10, 15, 20, and 25 dBZ. No offset is

apparent in the distributions for reflectivity intervals with lower values. The tentative overall conclusion here is that this offset is real and may be attributable to the presence of drops larger than the drizzle category and which may exhibit significant positive ZDR values. According to Teschi *et al.* [75], a discernable positive ZDR on raindrops begins at  $D = 500 \mu\text{m}$  diameter.

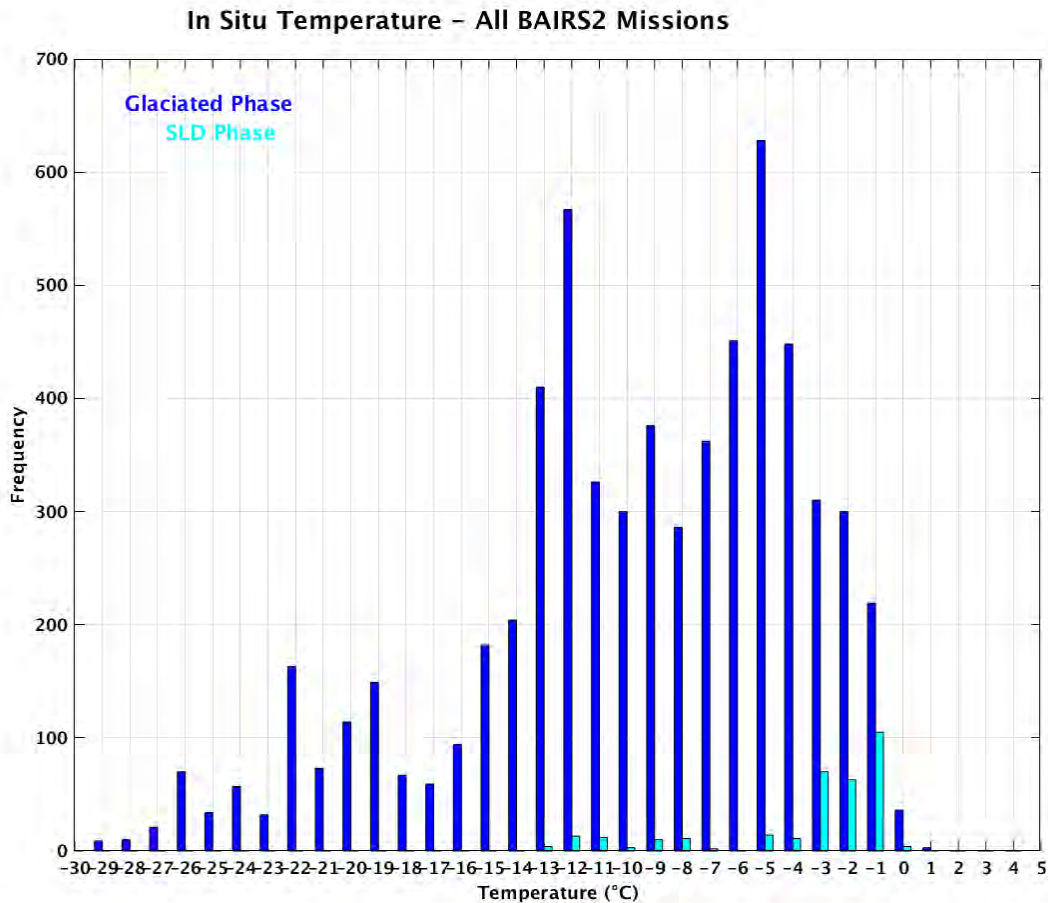


Figure 83. In situ temperature for all BAIRS II missions separated by glaciated (blue) and SLD (cyan) phases.

Regarding the comparisons for glaciated phase and SLD phase for the in situ aircraft temperature measurements in Figure 83, we have a significant offset here, with SLD much more likely at higher (warmer) temperature. On average, we can expect lower probability for SLW at lower temperatures. A possible alternative explanation is that we have supercooled droplets mixed upward through the ML by turbulent eddy diffusion, a hypothesis addressed in Korolev *et al.* [45].

## 4.7 IHL PERFORMANCE USING CLOUD PHASE ESTIMATES FOR VERIFICATION

### 4.7.1 Introduction

The operational NEXRAD IHL algorithm (Hallowell *et al.* [30]) produces a top and bottom icing hazard altitude product that defines the bounds of the icing layer derived at each radar range–azimuth bin. The products are generated once per radar volume with a 1 km spatial resolution. The algorithm determines the vertical extent of the icing layer by searching for the HCA Graupel class among each range bin in all elevation angles of the radar volume. Once complete, the altitudes of the highest and lowest angles containing graupel are calculated for each bin (total beam width included). As a final step, gridded one-hour forecast fields of temperature and relative humidity from the NWP RAP model are used to identify layers in which atmospheric conditions are conducive for icing, as developed at the National Center for Atmospheric Research and implemented within the Current Icing Potential algorithm (Bernstein *et al.* [7]). These probabilistic, model-derived icing layers are used to extend vertically the IHL icing top altitude up to the model icing height only if they reside above and are co-located with the range–azimuth bins that contained graupel. Upon completion, the IHL top and bottom products are created. Appendix B of the BAIRS I report (Williams *et al.* [84]) and an earlier study (Donovan *et al.* [17]) describes an analysis of IHL performance vs. aircraft icing pilot reports.

### 4.7.2 BAIRS II Assessment

In situ data collected during the BAIRS II campaign were used to evaluate the performance of the IHL algorithm. The evaluation methodology was very similar to an earlier study (Donovan *et al.* [17]) in which IHL detections were validated using icing PIREPs. However for BAIRS II, a multi-probe assessment of the cloud phase (Section 4.1) was used as a substitute for the PIREPs to verify the presence or absence of an icing hazard. A second major difference was a considerable reduction in the spatial area used in the comparisons. In the PIREP study, the icing and null (absence of icing) reports were represented by 50 and 10 km radius cylinders centered at the PIREP location, respectively, with the vertical thickness determined by the flight altitude(s) where icing (no icing) was encountered. These cylinders encompass the icing airspace (or lack thereof) associated with each report and help to account for spatial and temporal uncertainties in reporting. In the present evaluation, each five-second aircraft observation is represented with a radar range-dependent physical-size kernel (with dimensions in range and azimuth) centered at the Convair-580 position. The kernel size approximates the physical distance traversed by the aircraft at a nominal speed of 100 m/s (see Section 2.3). In both evaluations, an outline of the cylinder and kernel geometries are projected onto the two-dimensional polar grid surface creating a footprint from which IHL detections can be compared.

For the purposes of determining the IHL performance, an icing observation was characterized when the cloud phase type was either liquid (temperature  $< 0^{\circ}\text{C}$ ) or mixed, and a no-icing observation was characterized when the cloud phase type was glaciated. No other cloud phase types (observations) were used in the evaluation. Several scoring categories were tabulated in order to evaluate IHL in terms of probability of detection (POD) and false alarm rate (FAR). The POD was computed twice, among all observations in which graupel was detected within the kernel footprint and for all observations regardless of the HC detections associated with the aircraft location.

The scoring categories related to icing observations are defined as follows:

- H (Hit): IHL detection(s) reside in the kernel footprint and the altitude layer overlaps the aircraft altitude
- MAB (Miss Above or Below): IHL detection(s) reside in the kernel footprint but the altitude layer does not overlap the aircraft altitude
- M (Miss): no IHL detections reside in the kernel footprint
- NS (No Signal): no HCA classifications detected in the kernel centered on the aircraft location
- NBI (No Beam Intersection): aircraft position did not reside within any elevation beam angle

The scoring categories related to the no-icing observations are defined as follows:

- FD (False Detection): IHL detection(s) reside in the kernel footprint and the altitude layer overlaps the aircraft altitude
- CND (Correct No Detect): no IHL detections reside in the kernel footprint or IHL detection(s) reside in the kernel footprint but the altitude layer does not overlap the aircraft altitude
- NS (No Signal): no HCA classifications detected in the kernel centered at the aircraft location
- NBI (No Beam Intersection): aircraft position did not reside within any elevation beam angle

The formulas used to compute POD and FAR are shown below.

$$\text{POD-graupel} = H / (H + \text{MAB}) \quad (13)$$

$$\text{POD-all} = H / (H + \text{MAB} + \text{M} + \text{NS} + \text{NBI}) \quad (14)$$

$$\text{FAR-all} = \text{FD} / (\text{FD} + \text{CND} + \text{NS} + \text{NBI}) \quad (15)$$

Table 6 shows the number of icing (liquid phase when  $T < 0^{\circ}\text{C}$  and mixed phase) and no-icing (glaciated phase) observations when the Convair-580 aircraft position was within 200 km of each radar within the BAIRS II domain. These results are very similar to the evaluation performed using PIREPs, despite the methodology differences outlined above. Performance based on the graupel cases (POD-graupel) is excellent for KBGM and KTYX and very good for KBUF (82%). Since the current version of the IHL algorithm will only issue detections in the presence of graupel classifications (with model augmentation described earlier), this is the best indicator of the performance in its current form. However, when all observations are considered (POD-all), the POD is significantly lower and only 2% and 3% for KBGM and KTYX, respectively. The number of icing and no-icing observations for these two sites are less than half that for KBUF due to the proximity of the Convair-580 to KBUF for a majority of the flights combined. The FARs for KBGM and KTYX are consistent with the FAR computed PIREP study (5%), but substantially higher (16%) for KBUF. However, unlike the PIREP study, the NBI category was included in the FAR calculations here attributing in part to the higher FARs.

**TABLE 6**  
**Number of Observations Characterized as Icing and No-Icing based on an Assessment of Cloud Phase when the Convair-580 Aircraft was within 200 km of each Radar and the Performance of the IHL Algorithm Measured in Terms of POD and FAR**

<b>Radar</b>	<b>Icing Obs.</b>	<b>POD-all</b>	<b>POD-graupel</b>		<b>No-Icing Obs.</b>	<b>FAR-all</b>
<b>KBUF</b>	2981	16%	82%		5898	16%
<b>KBGM</b>	1327	2%	100%		2773	6%
<b>KTYX</b>	1478	3%	100%		3462	5%

A categorical breakdown of all aircraft–radar beam comparisons for the icing phase observations (top row) and no-icing or glaciated observations (bottom row) for KBUF, KBGM, and KTYX (left, middle, and right columns, respectively) is provided in Figure 84. The black and gray sectors in both rows represent the fraction of observations in which there was no aircraft–radar beam intersection (NBI) and the fraction where there was an intersection, but no radar signal (no HC) within the kernel comparison region (NS), respectively. All other sectors in the icing charts represent the fraction of observations in which GR was classified in the spatial footprint or the mode of other HCs within the aircraft–radar beam comparison region (IC = Ice Crystals; DS = Dry Snow; UNK = Unknown; and Other = any other HC). As noted in the PIREP study and similarly found here, a significant portion of the icing hazard is being masked by other hydrometeor classifications and most notably, Dry Snow. The no-icing charts show the fraction of FD and the portion of observations in which IHL correctly did not issue a detection (CND). The latter is a new finding that expands on describing the performance of the current IHL.

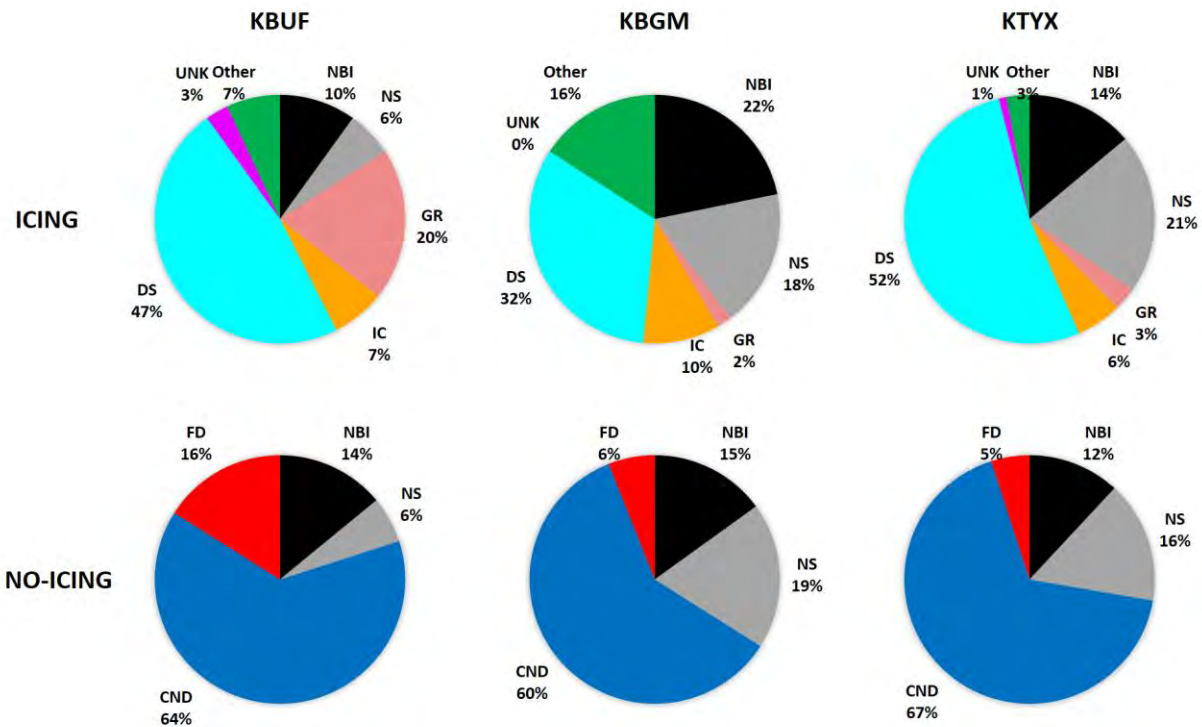


Figure 84. Categorical breakdown of all aircraft–radar beam comparisons for observations categorized as an icing hazard (top row) and no-icing (bottom row) encountered by the Convair-580 relative to the KBUF (left column), KBGM (center column), and KTYX (right column) radars.

The incidence of the Convair-580 to encounter a cloud phase of SLD when the IHL algorithm issued detections within the kernel footprint was also studied. In all instances among the three radars, this situation did not occur. The good news is that when the HCA detects graupel, it has been manifested through the riming and accretion of supercooled liquid droplets and not SLD as would be expected. Conversely, this exposes a limitation in the current algorithm to detect SLD situations that can pose a significant icing hazard.

## 5. DISCUSSION

The overriding motivation of the FAA-supported work in both BAIRS I and BAIRS II has been identifying dual polarimetric methods for locating icing hazard in winter storms. Some success has been achieved in an indirect approach. The IHL algorithm currently in operation infers an icing hazard with the indirect approach by exploiting the graupel hydrometeor classification as a sentinel for riming via supercooled cloud droplets. In BAIRS II, the crystal sandwich is introduced as a potential radar feature appropriate to focus on for icing hazard identification. Before discussing further aspects of the indirect approach, it is worthwhile first to review the basic challenges of the direct approach. Supercooled water is often present in small cloud droplet form (of the kind measured with the FSSP probe on the aircraft), which is not detectable by S-band radars because of the fundamental  $D^6$  dependence of the droplet radar cross section. SLD (and larger drizzle drops) have larger cross sections that move drizzle into the S-band detectable range, but are too small to show measureable departures from isotropy in ZDR measurements. Very important in this regard, and touched on in Section 2.4, is that it is paramount for dual polarimetric radars to be as well calibrated as possible and maintained as such, especially given the isotropy challenges in the direct approach.

There was a lack of success in finding any obvious discriminator between mixed (with SLD present) and glaciated phase regimes in Section 4.6 of this study. That is attributable to the weak and isotropic nature of the supercooled water target focused on. The only noteworthy distinction here, shown in Figure 82, is for the mixed phase to show larger +ZDR returns, on average. This finding may be attributable to a tendency for some drizzle drops to coalesce to larger oblate raindrops with measureable departure from isotropy (0 dB). That does not render the data necessarily ineffective, but suggests that algorithms for dual polarimetric icing hazards will need to focus on more sophisticated characterizations than the histogram binnings used here (especially if in a machine-learning context).

Greater success has been achieved in this study with an indirect approach to the use of dual polarimetric radar. In this approach, anisotropic targets (ice crystals) are selected that have a thermodynamic connection with supercooled water. The appearance of both needles and dendrites in laboratory diffusion chamber measurements (e.g., Bailey and Hallett [1]) require water-saturated conditions and hence in a cloud context, the presence of supercooled cloud water. This quest began with the dendritic crystals of the +ZDR bright band (Williams *et al.* [85], [86]), but the 28 February 2013 “crystal storm” in BAIRS I provided the important hint that a two-layered crystal sandwich with supercooled water somewhere in between might be a robust feature in winter storms with sufficiently gentle ascent. The cases documented in Section 4.2 support this idea, leading to a crystal sandwich structure depicted in Figure 53. Still other situations during the five flights when complete documentation of both crystal layers was unavailable suggested that both crystal layers were really present.

By considering the full range of possible background reflectivity below the dendrite layer, we have come to identify three fairly distinct scenarios:

1. Full sandwich: Two quasi-homogeneous layers of dendrites (or flat plates) and needles are present. This situation is illustrated schematically in Figure 53 and is well-represented by the 28 February 2013 case in which the background reflectivity is generally <10 dBZ.

2. Partial sandwich: This configuration is well illustrated by the various NEXRAD cases in Figures 49 to 52. The upper dendritic layer is reasonably contiguous, but evidence for the needle crystals generally with smaller +ZDR values in the lower layer is more scattered and discontinuous. This condition has been tentatively attributed to the larger background reflectivity associated with aggregation of dendritic crystals in the upper crystal layer and then subsequent descent when they dominate the returns from unaggregated needles. This situation is prevalent when the background reflectivity is substantially larger than the 10 dBZ values for “crystal storms” and more often in the range of 10–25 dBZ (see Table 3).
3. Dendritic layer only (half-sandwich): When aggregation of dendritic crystals is vigorous and the background reflectivity is larger still than the situation in (2) above, there is little or no chance to detect the anisotropic return from isolated needle crystals in the lower (warmer) layer. Then only the +d ZDR bright band remains. A number of examples of this situation can be found in Williams *et al.* [85]. Based on the documentation of these results alone, and with the findings in 28 February 2013 in BAIRS I, the discovery of the crystal sandwich might not have been achieved.

Fundamental cloud microphysical questions remain in conjunction with the two crystal types of the crystal sandwich. If supercooled water (and water-saturated) conditions are required for the formation of these crystal types, why don't we find more often in the crisp CPI hydrometeor imagery that these crystals are unrimed? Could this be a function of crystal “age” with respect to interception by the Convair-580? (Needles encountered in a rimed state as they fall away from their inception “birth” layer.) Some discussion on this point is found in Section 4.5.3. The fall speeds of dendritic and needle crystals have been shown to be modest (Section 4.2.5), and this will suppress the tendency to rime. It may also be the case that a quasi-equilibrium is established between moisture made available in ascent and the moisture transfer to ice crystals by the Bergeron process. The finding that the layer of supercooled water (or a maximum) often does not coincide with either the upper dendritic layer or the lower needle layer is consistent with the erosion of cloud droplets by the Bergeron process.

Turning now to the maritime case on 24 January 2017, this may well be the first example of a winter storm in a collection of winter storms in the same location that stands out so dramatically on the basis of the onboard aircraft observations. All of this is surely to be expected when one has order-of-magnitude (or more) differences in CCN populations between maritime and continental air. In this case, we lack the CCN observations, but the marked differences in FSSP droplet concentrations (see concatenated drop spectra in Figures 56–60) and the median volume diameters of cloud droplets tell essentially the same story.

The distinct differences between maritime and continental cases here in the aircraft observations is without debate. An important related question arises in the same context: how can one distinguish a maritime from a continental winter storm on the basis of the dual polarimetric observations alone? (Notwithstanding obvious challenges for maritime conditions to occur thousands of kilometers from oceans.) In conditions of summertime convection, one can look for radar first echo heights with more polluted continental conditions (Ludlam [55]; Williams *et al.* [80]). In winter time, however, the ascent is not localized to a convective scale updraft, but instead occurs on gently sloping frontal surfaces with mesoscale ascent. Furthermore, in many locations on the frontal surface, the primary growth of radar targets is by Bergeron enlargement of ice crystals. Only in localized regions will growth of reflectivity occur by coalescence of drizzle drops. Such regions are hard to find, again because of the isotropic nature of the supercooled droplet targets. For the moment, there is not an easy answer to the question posed above.

Section 4.5 further examines needle crystals in the context of ice multiplication. The conclusions here are not definitive. A dramatic contrast in needle concentrations when supercooled water was present was not found. Given that supercooled drops are needed for certain ice multiplication processes, we had some expectation for a larger contrast in Figure 72. With the present compilation of data points, only three of them stand out as showing low concentrations when supercooled water is absent. However, it should be noted again that the conditions for these tests, namely that needles were the predominant crystal present in the sample volume, may have been too specialized. It is also possible that the main ice multiplication events were not collocated with the locations where the needles and the supercooled water were identified. On the basis of these comparisons, one cannot make any great claims to understand better the complex process of ice multiplication, and its role in modulating the icing hazard.

**This page intentionally left blank.**

## 6. CONCLUSIONS

Winter storms are often characterized by large scale ascent on frontal boundaries with slopes of order 1%. Ascent is essential for the formation of both supercooled water and ice crystals (dendrites and needles, with temperature-dependent habits) with anisotropic response to dual polarimetric radar. The key finding with the aircraft and radar observations in this study is the crystal sandwich, a dual polarimetric target with clear relevance to the FAA's interest in the use of the NEXRAD radars for the identification of icing hazard to aircraft. Though the complete two-layer crystal sandwich appears to be most prevalent in conditions of weakest ascent, the presence of the more robust upper dendritic layer, earlier referred to as the +ZDR bright band, is a strong suggestion that some semblance of a needle crystal layer will also be present below, in a predictable temperature range and associated with a layer of supercooled water somewhere within the sandwich. Importantly, evidence is provided to show the layer of supercooled water (in any size spectra) can be as extensive as a couple of kilometers thick and not necessarily be in thin layers. Such layer thicknesses can be especially notable for general aviation and, possibly, operation of the National Airspace System.

Referring back to Figure 1, the five BAIRS II in situ icing missions were focused on the aforementioned crystal sandwich zone up to and somewhat above the dendritic growth zone and down into the melting layer zone environment. There were excursions beneath the melting layer. Notably, the maritime case of 24 January 2017 had a higher than normal melting layer zone with a refreeze zone below. The refreeze zone was probed in a limited fashion, but not sufficiently to study aspects of refreezing and ice multiplication processes specific to there. It was an environment rich with SLDs.

An important aspect of this study was to first make an accounting of system bias as reasonably possible with the differential reflectivity (ZDR) data of the three NEXRADs. Currently, the NEXRAD network is working towards a standard operating procedure to maximize maintaining radar performance with respect to ZDR in this context. The current IHL does not have a bias-adjusted functionality. Our studies have shown that in the context of relying on the graupel hydrometeor classification this has not been debilitating. To move forward with advancing the IHL, the radar network is ideally calibrated as the bias uncertainty noted is on the order of the ZDR isotropy.

Another key finding in this study was the development of a multi-sensor cloud phase algorithm to distinguish between liquid phase, mixed phase, and glaciated (no icing) conditions. For future IHL development, the cloud phase designation database will continue to be an essential resource. It was used in this study to further evaluate the IHL performance and characterize IHL. With respect to graupel-associated icing hazard detection, the results were consistent with prior studies. Additionally, as configured now, IHL properly did not report an icing hazard in glaciated conditions generally with false alarm rates below 10% and correctly not detected from 60% to 67%. Importantly, in SLD environments IHL was not reporting an icing hazard. This is consistent with the microphysical scenario of supercooled cloud droplets being the key to graupel formation. IHL development focuses on maintaining this performance in these circumstances, extend icing hazard detectability beyond graupel, and identify its limits.

**This page intentionally left blank.**

## 7. SUGGESTIONS FOR FUTURE WORK

The work completed in this study is not without loose ends, and a number of areas have been identified where additional work is needed for further progress and understanding. Some additional thinking along these lines was also addressed in a document prepared on the eve of the In-Cloud Icing and Large-drop Experiment (ICICLE) (Williams *et al.* [90]) and can be consulted. These areas are summarized in turn.

### 7.1 CRYSTAL SANDWICH

The crystal sandwich is well connected with the established microphysics of the laboratory diffusion chamber (e.g., Bailey and Hallett [1]), but the number of well-documented cases in this study is too few to render complete confidence in a robust phenomenon in winter storms. Nor is there a sufficient number of well-documented cases to generalize about where the supercooled water is located relative to the two crystal layers. Additional work with aircraft spirals over the full temperature range for crystals and dendrites is needed here. Some of the later flights in the recent ICICLE study, also with the Convair-580, may be useful for this purpose. A far larger collection of cases may be needed for effective development of an algorithm aimed at exploitation of the crystal sandwich for operational icing identification.

Scan-to-scan PPI analysis is also needed to understand the physical basis for the features identified in many cases in winter storms and shown in Figures 49 to 52. If these anisotropic targets are needles, these regions should exhibit smaller reflectivity than the +ZDR bright band above, believed to be caused by dendrites with greater anisotropy. If these zones represent descent of upper-level dendrites to lower levels, the transition needs to be consistent with reasonable estimates for ice crystal fall speeds. When these regions disappear, is that disappearance plausibly related to the aggregation of the dendritic crystals and the corresponding reduction in differential reflectivity and increase in reflectivity?

### 7.2 UNRIMED DENDRITIC AND NEEDLE CRYSTALS

Needle and dendritic crystals are fundamental constituents of the crystal sandwich and are linked with water-saturated conditions by virtue of the laboratory diffusion chamber results (e.g., Bailey and Hallett [1]). Given the latter conditions, the question remains why these two key crystal types are not more often rimed, now that we have the CPI imagery to make an unambiguous determination. Numerical models with detailed microphysics should be checked to address this puzzling issue.

### 7.3 ASCENT RATES ALONG FRONTAL BOUNDARIES

Ascent rates are some meters per second along a warm frontal boundary in summertime convection, but only some centimeters per second in winter storms. This situation places cloud microphysics in winter storms in a different regime. Despite the evidence in Section 4.3 that ascent rates in winter storms are closely tied to the snowfall rate, which in turn influences the regime of the crystal sandwich (see discussion in Section 4), the actual values for both frontal slopes and ascent rates have remained elusive to direct observation and in extraction from numerical mesoscale models. Efforts should be made to assess the ascent rate in snowstorms by checking warm frontal slopes (with slope  $\tan \theta$ , where  $\theta$  is the angle between the frontal slope and the horizontal) in the models and using the wind speed  $V$  along the frontal slope to estimate

ascent rate  $W$ . If both these quantities are provided with reasonable accuracy, the mean ascent rate  $W$  should be determinable with reasonable accuracy from the following simple relationship:

$$W = V \tan \theta \quad (16)$$

Progress here is needed if deeper understanding of the relationship between the synoptic scale and the in situ microphysics pertaining to icing conditions is to be achieved.

#### **7.4 RADAR BRIGHT BAND AND THE ENVIRONMENT BELOW THE MELTING LAYER IN WINTER STORMS**

Some evidence of a melting level with radar bright band was evident during all five flights of BAIRS II, and this feature is a consistent underlying feature of the crystal sandwich (Figure 53). In some cases, the presence of an inversion resulted in supercooled raindrops in a zone beneath the melting layer, and this is also an icing hazard. Dual polarimetric methods should be developed to distinguish these hazardous situations from those in which no inversion is present and the melting ice remains in liquid form all the way to the ground. The investigation and temporal evolution of these processes in a time versus height format could be made possible with the quasi-vertical profile (QVP) approach described by Ryzhkov *et al.* [67].

#### **7.5 CLOUD CONDENSATION NUCLEI**

The supercooled cloud droplet number concentrations are dictated by the concentrations of CCN. For the 24 January 2017 flight, we inferred the presence of clean air of maritime origin, with low CCN, and the aircraft microphysical observations revealed a major impact, as shown in Section 4.4. Even better would have been the documentation of low values of CCN associated with air of maritime origin and also experiencing frontal ascent. Data collected from an aircraft equipped with a CCN counter should be used to help characterize the differences between maritime and continental winter storms that are discernible with dual polarimetric radar observations alone. The presence of cleaner air may be a major factor in distinguishing conditions when the supercooled water is in small droplet form and when it is in SLD and drizzle form, generally deemed more hazardous to aviation.

#### **7.6 COMPARISON OF $N^*r$ IN SNOWSTORMS AND IN THUNDERSTORMS**

A current puzzlement in thunderstorm research is how large stratiform regions can produce lightning but without the presence of supercooled water. (This problem is addressed by a recent paper by Dye and Bansemer [19]). The answer may lie in the large numbers of ice particles available for collision in stratiform regions in comparison with thunderstorms. The charge transfer per collision may be much reduced, but the number of collisions per unit time may compensate. To get additional insights here, it would be interesting to compare  $N^*r$  in the situation of strongest vertical development and turbulence in snowstorms in BAIRS II with typical numbers in other summertime stratiform situations.

#### **7.7 EMBRYOS FOR GRAUPEL PARTICLES**

The embryos for graupel particles have been much debated in the literature (Knight and Knight [46]; Takahashi and Fukuta [73]). Earlier investigation of wind tunnel observations (Fukuta and Takahashi [23]) and the calculations in Section 4.2.5 strongly support equidimensional particles (isometric in the case of

crystals) as embryos, because of their expected larger fall speeds. Small graupel were abundant during BAIRS II flights on 10 January, 24 March, and 25 March 2017. The high-quality CPI imagery could be used to isolate the rimed particles in very early stages when the substructure is still visible toward identifying possible embryos.

**This page intentionally left blank.**

## **APPENDIX A**

### **INTER-COMPARISON OF AIRCRAFT AND RADAR VARIABLES FOR FIVE FLIGHTS**

Complete distributions of the Convair-580 aircraft measurements and the NEXRAD radar products matched to the aircraft position in space and time were compiled for the duration of each flight and are provided in chronological order in Figures 85 to 89. Each six-panel figure contains distributions of temperature, LWC, and MVD in the top row with mean reflectivity, mean ZDR, and HC mode in the bottom row. In four of the five figures, the radar product values shown were derived from the KBUF NEXRAD due to the close proximity of the aircraft for a considerable portion of each flight. However, radar data from KBGM are shown in Figure 86 for the 24 January flight due to the late onset of precipitation to reach the KBUF region.

Comparisons among the distributions for each of the five flights are provided below in bullet format in a left to right, top to bottom sequence as shown in the distribution figures.

#### **TEMPERATURE**

- Bimodal distributions with colder temperatures recorded during en route transects to the target regions
- 10 January—only flight in which the aircraft did not descend through ML
- Significant probing just above ML and within needle layer during 24 January, 7 February, and 24 March flights
- Needle and dendrite layers probed extensively on 25 March flight

#### **LWC**

- Counts shown with log scale
- Lowest values on 24 January flight (maritime case) with minimal cloud droplets observed
- Highest values and largest distributions observed on 24 March and 25 March flights, the two longest flights of the campaign

#### **MVD**

- Little distinction in distributions for the 10 January, 7 February, 24 March, and 25 March flights; synoptic conditions were similar on these dates
- Bimodal distribution for larger sizes in 21-42  $\mu\text{m}$  interval evident in the 24 January flight

### **MEAN Z**

- Lowest values observed on 10 January flight
- Higher Z observed on 24 March and 25 March flights where stronger Z cores were probed; graupel encountered on 24 March flight
- Mean of distributions slightly higher on 7 February, 24 March, and 25 March flights; highest on 24 March (~23 dBZ)

### **MEAN ZDR**

- Very little distinction among 10 January, 7 February, 24 March, and 25 March flights with distribution mean near 0.5 dB
- Higher ZDRs observed on 24 January due in part to the extended probing of oblate drops within an SLD layer

### **HC MODE**

- Dry Snow predominate class in all flights
- Graupel class encountered on 24 March and 25 March flights
- Large encounter with Big Drops class on 24 January flight within subfreezing layer beneath the ML for which the HCA is unaware; Big Drops encounters in the other flights were primarily observed beneath the ML

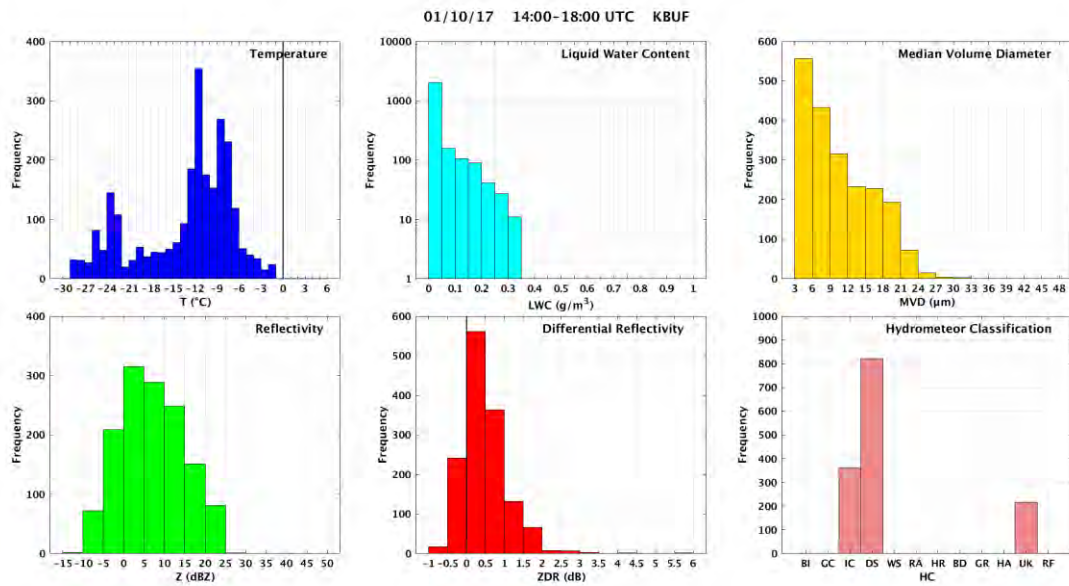


Figure 85. Select distributions of Convair-580 measurements (top row) and spatial-temporal matched KBUF radar estimates (bottom row) for the duration of the 10 January 2017 flight. The top row shows temperature (left), Nevzorov LWC (center; log scale), and FSSP MVD (right). The bottom row shows mean reflectivity (left), mean ZDR (center), and HC mode (right). Abbreviations of the HC categories include Biological (BI), Ground Clutter (GC), Ice Crystals (IC), Dry Snow (DS), Wet Snow (WS), Rain (RA), Heavy Rain (HR), Big Drops (BD), Graupel (GR), Hail-Rain mix (HA), Unknown (UK), and Range Folding (RF).

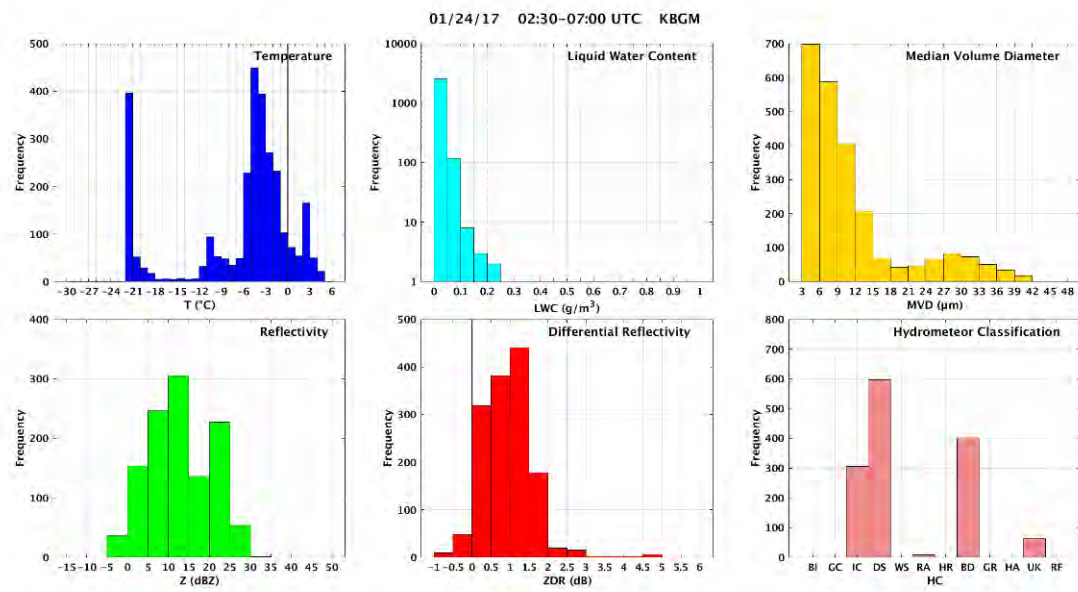


Figure 86. Select distributions of Convair-580 measurements (top row) and spatial-temporal matched KBGM radar estimates (bottom row) for the duration of the 24 January 2017 flight. The top row shows temperature (left), Nevzorov LWC (center; log scale), and FSSP MVD (right). The bottom row shows mean reflectivity (left), mean ZDR (center), and HC mode (right). Abbreviations of the HC categories include Biological (BI), Ground Clutter (GC), Ice Crystals (IC), Dry Snow (DS), Wet Snow (WS), Rain (RA), Heavy Rain (HR), Big Drops (BD), Graupel (GR), Hail-Rain mix (HA), Unknown (UK), and Range Folding (RF).

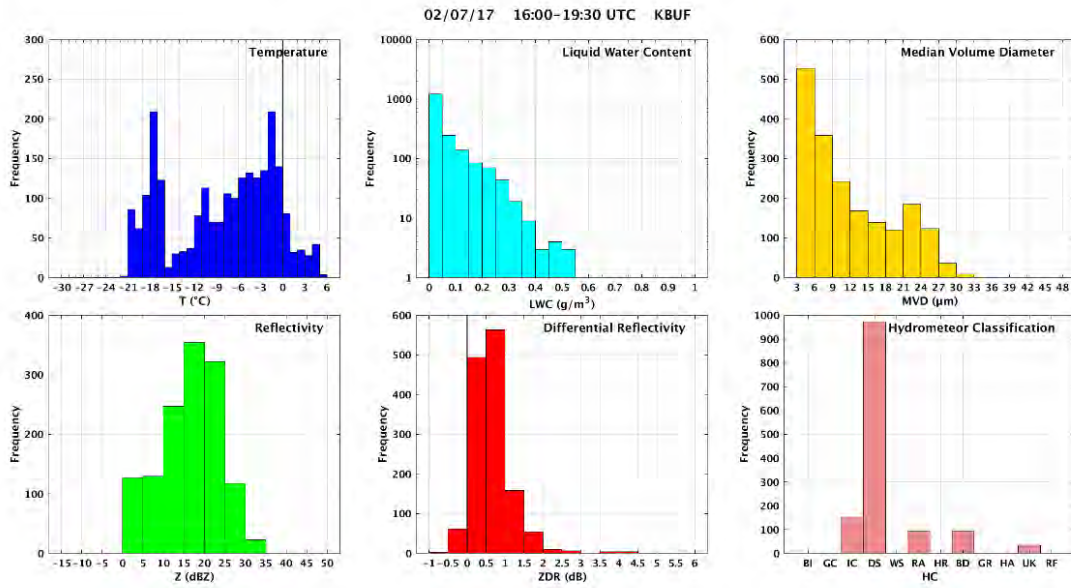


Figure 87. Select distributions of Convair-580 measurements (top row) and spatial-temporal matched KBUF radar estimates (bottom row) for the duration of the 7 February 2017 flight. The top row shows temperature (left), Nevzorov LWC (center; log scale), and FSSP MVD (right). The bottom row shows mean reflectivity (left), mean ZDR (center), and HC mode (right). Abbreviations of the HC categories include Biological (BI), Ground Clutter (GC), Ice Crystals (IC), Dry Snow (DS), Wet Snow (WS), Rain (RA), Heavy Rain (HR), Big Drops (BD), Graupel (GR), Hail-Rain mix (HA), Unknown (UK), and Range Folding (RF).

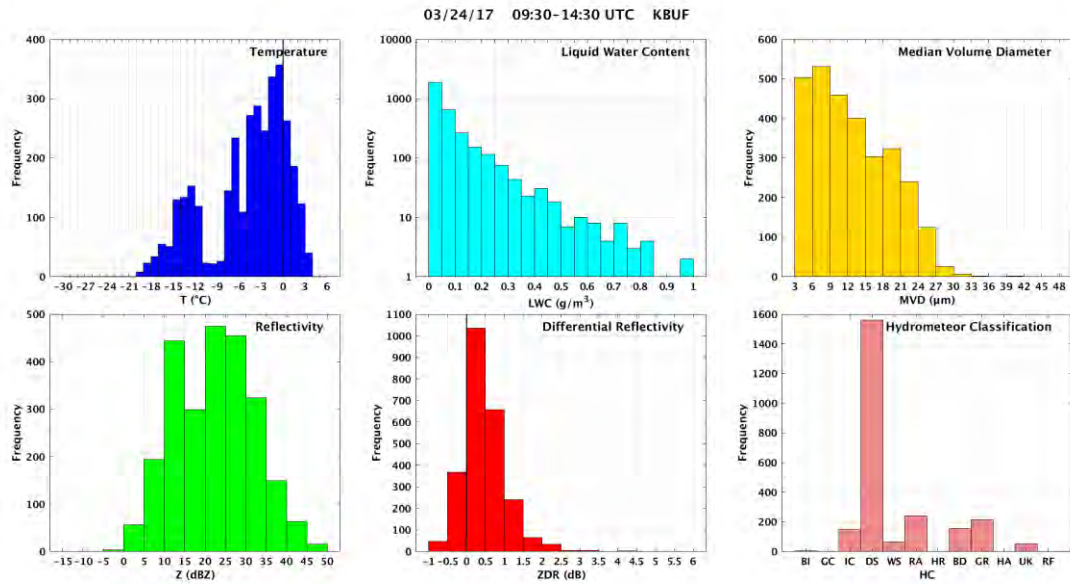


Figure 88. Select distributions of Convair-580 measurements (top row) and spatial-temporal matched KBUF radar estimates (bottom row) for the duration of the 24 March 2017 flight. The top row shows temperature (left), Nevzorov LWC (center; log scale), and FSSP MVD (right). The bottom row shows mean reflectivity (left), mean ZDR (center), and HC mode (right). Abbreviations of the HC categories include Biological (BI), Ground Clutter (GC), Ice Crystals (IC), Dry Snow (DS), Wet Snow (WS), Rain (RA), Heavy Rain (HR), Big Drops (BD), Graupel (GR), Hail-Rain mix (HA), Unknown (UK), and Range Folding (RF).

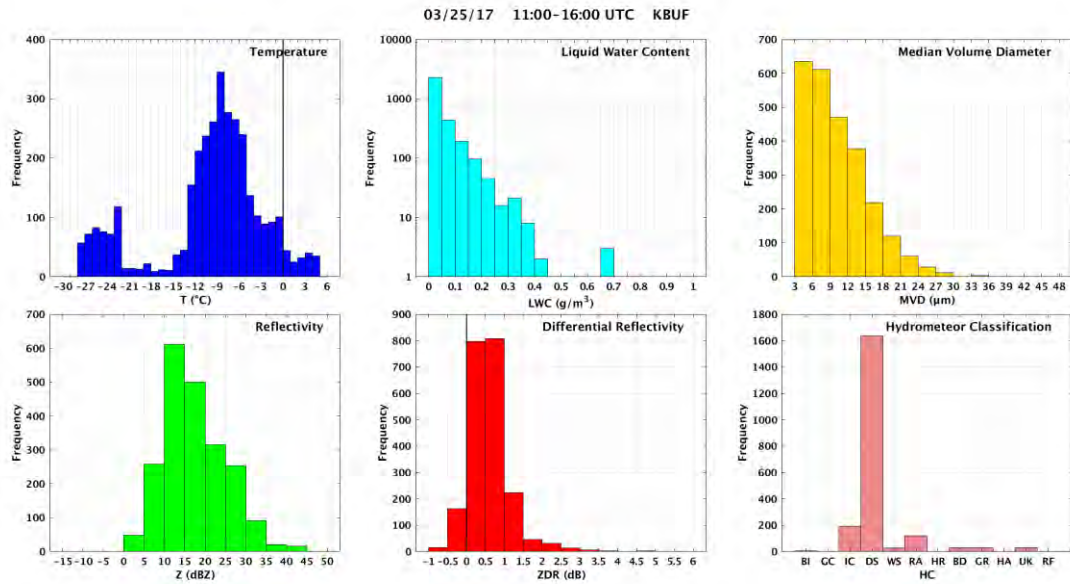


Figure 89. Select distributions of Convair-580 measurements (top row) and spatial-temporal matched KBUF radar estimates (bottom row) for the duration of the 25 March 2017 flight. The top row shows temperature (left), Nevzorov LWC (center; log scale), and FSSP MVD (right). The bottom row shows mean reflectivity (left), mean ZDR (center), and HC mode (right). Abbreviations of the HC categories include Biological (BI), Ground Clutter (GC), Ice Crystals (IC), Dry Snow (DS), Wet Snow (WS), Rain (RA), Heavy Rain (HR), Big Drops (BD), Graupel (GR), Hail-Rain mix (HA), Unknown (UK), and Range Folding (RF).

**This page intentionally left blank.**

## APPENDIX B

### SYNOPTIC ANALYSIS OF RADAR SITUATION WITH +ZDR BRIGHT BANDS

The interest in the pair of crystal layers of the crystal sandwich addressed earlier in Section 4.2 followed earlier work focused only on the upper dendritic crystal layer (Williams *et al.* [84], [85], [86]), especially based on aircraft observations in BAIRS I (Williams *et al.* [86]). In both circumstances, the interest in the FAA context lay in identifying systematic dual polarimetric radar signatures linked with supercooled water and aircraft icing hazard. This Appendix presents an investigation of synoptic conditions favorable to the occurrence of widespread layers of specific ice crystal types. A wide variety of previous case studies have been investigated and are summarized in Table 7. Frontal lifting is fundamental in nearly all cases, as expected, but the role of cold fronts is more prevalent than earlier assessed.

Toward gaining more insight into the physical mechanisms of lifting that serve to create +ZDR bright bands with accompanying supercooled water and icing conditions, we have gathered together a variety of cases studied previously in other contexts on this project. These cases are all listed below in Table 7 (along with associated lifting mechanism and maximum composite reflectivity), and include the “crystal sandwich” cases outside of BAIRS II documented with other NEXRAD radars, the cases studied earlier by Williams *et al.* [85] also under FAA-sponsorship, and the cases from the flights in BAIRS I and II. For synoptic context, we make use of the website below with an archive of frontal locations and composite reflectivity maps over the CONUS, with 3-hourly time resolution.

[https://www.wpc.ncep.noaa.gov/archives/web\\_pages/sfc/sfc\\_archive.php](https://www.wpc.ncep.noaa.gov/archives/web_pages/sfc/sfc_archive.php)

For the crystal sandwich cases, there are nearly as many clear-cut cold front cases (6) as warm fronts (7). This would seem to underline the fact that some form of lifting on the mesoscale is needed for +ZDR bright band formation, but it is not necessary that this lifting be of the warm frontal type. It is also clear that the maximum values in the composite reflectivity, for the majority of cases, are substantially greater for the cold frontal cases than the warm frontal ones, consistent with the notion that ascent is stronger on cold fronts, and the occurrence of lightning is also deemed more likely in such cases. The “Dry Snow” case on 19 February 2013 (BAIRS I) is one good example of cold frontal lifting when substantially larger reflectivity was present (Williams *et al.* [86]) and no obvious +ZDR bright band was present. In contrast with this frontally forced case is the 28 February 2013 crystal storm case from BAIRS I in which no fronts are discerned but only a low pressure center in which the weak ascent may be the result of low level convergence in the low. This case is conspicuously the case of weakest ascent in the entire list and curiously also showed a predominance of hexagonal flat plate crystals.

It is also noteworthy here that the maximum values for composite reflectivity for crystal sandwich cases in category (1) in Table 7 tend to be smaller than for the collection of +ZDR bright band cases in category (2) in Table 7 (albeit in a different set of meteorological scenarios including hurricanes), none of which showed any evidence for a needle layer. This finding is broadly consistent with the notion that when the snowfall is sufficiently intense, the differential reflectivity of the needle layer will be dominated by aggregates falling from above, and not be detectable.

The slopes of the fronts documented in Table 7 were not determined in this analysis.

The widths of the composite reflectivity regions (measured perpendicular to the frontal boundary) away from the warm fronts show considerable variability in this dataset. These zones are important in the icing context. The temperature of the air on the warm side of the front is likely an important player here, with warmer air allowing a larger total range of temperature as it ascends moist adiabatically along the sloping frontal surface. For the same reason, warm fronts at lower latitude should exhibit greater widths of composite reflectivity, on average, generally consistent with the available data.

**TABLE 7**  
**Summary of Cases Examined for Lifting Mechanism with Associated Maximum Composite Reflectivity**

Date	Time (UTC)	Radar	Lifting Mechanism	Composite Reflectivity (dBZ)
<b>(1) Cases from NEXRAD radars with evidence of +d and +n ZDR “bright bands”</b>				
10 Jan 2017	15:25:13	KBUF	Warm front	25
12 Feb 2017	18:00	KBOX	Warm front	25
9 Dec 2017	08:01	KBOX	Warm front	20
19 Dec 2017	17:04:03	KRTX	Cold front	35
20 Dec 2017	15:21:04	KMRX	Cold front	40
20 Dec 2017	15:42	KRAX	Behind cold front	35
27 Dec 2017	16:52:57	KMHX	Low on stationary front	35
4 Jan 2018	19:09:02	KBOX	Atlantic bomb	20
12 Jan 2018	15:31:05	KDTX	Cold front	35
17 Jan 2018	14:33–15:00	KBOX	Short warm front	20
29 Jan 2018	15:05:45	KDTX	Convergence in low	20
7 Feb 2018	15:41	KBOX	Warm front	30
12 Feb 2018	14:58:31	KOKX	Cold front	35
16 Feb 2018	14:10:43	KOKX	Cold front	20
23 Apr 2018	19:07:07	KFCX	Warm front	40
18 May 2018	15:00	KDOX	Stationary front	45
15 Nov 2018	19:14	KDIX	Warm front	50
11 Dec 2018	21:00	KRTX	Recent warm frontal passage	30

<b>(2) Cases from Williams <i>et al.</i> (2015a) JAMC article</b>				
8 Dec 2009	23:57	Valpo	Warm front	50
24 Feb 2010	18:59	Valpo	Cold front	15
8 Jan 2010	16:25	Valpo	Lake effect (no +ZDR BB)	10
5 Nov 2010	05:14	Valpo	Lake effect (no +ZDR BB)	10
1 Feb 2011	19:12	Valpo	Stationary front (blizzard)	40
27 Aug 2011	00:43	KMHX	Hurricane Irene	45
3 Jul 2012	11:30	KATX	Warm front from Pacific Ocean	40
31 Aug 2012	12:30	KLSX	Hurricane Isaac	40
17 Jun 2012	06:08	Valpo	Cold front (squall line)	40
20 May 2011	13:50	KOUN	Cold front (squall line; no +ZDR BB)	50
<b>(3) Cases from BAIRS I</b>				
19 Feb 2013	15:00	KBUF	Cold front (fast moving; no +ZDR BB)	15
27 Feb 2013	00:00	KBUF	Warm front	45
28 Feb 2013	19:00	KBUF	Convergence in low (no fronts)	5
<b>(4) Cases from BAIRS II</b>				
10 Jan 2017	15:00	KBUF	Warm front	25
24 Jan 2017	06:00	KBUF	Warm front (airflow from Atlantic)	35
7 Feb 2017	18:00	KBUF	Warm front	35
24 Mar 2017	12:00	KBUF	Warm front	35
25 Mar 2017	12:00–15:00	KBUF	Stationary front/cold front	35

Note: Valpo indicates the Valparaiso University dual polarization radar. Other radars are NEXRAD ICAO designations readily found through an internet search.

**This page intentionally left blank.**

## APPENDIX C

### CLOUD PHASE ESTIMATE TIMELINES FOR FIVE FLIGHTS

A complete timeline of the cloud phase encountered by the Convair-580 aircraft as determined from a multi-probe assessment of microphysical measurements, particle classifications generated by the SNDI algorithm, and analysis of particle types observed in OAP imagery are shown for each of the five BAIRS II flights in Figures 90–94. Each figure contains, from top to bottom, initial and revised cloud phase estimates (top of panel 1), measurements of Nevzorov LWC, Nevzorov TWC, and ratio of LWC/TWC (panel 1), particle concentrations from the FSSP (panel 2), SNDI particle habit classifications derived from the 2D-C and PIP OAPs (panels 3 and 4), frequency oscillation from the RID (panel 5), and manual assessment of particle types observed in CPI imagery and in situ temperature (panel 6). Refer to Section 4.1 for a description of the algorithm and the sequence of decisions performed to estimate the cloud phase.

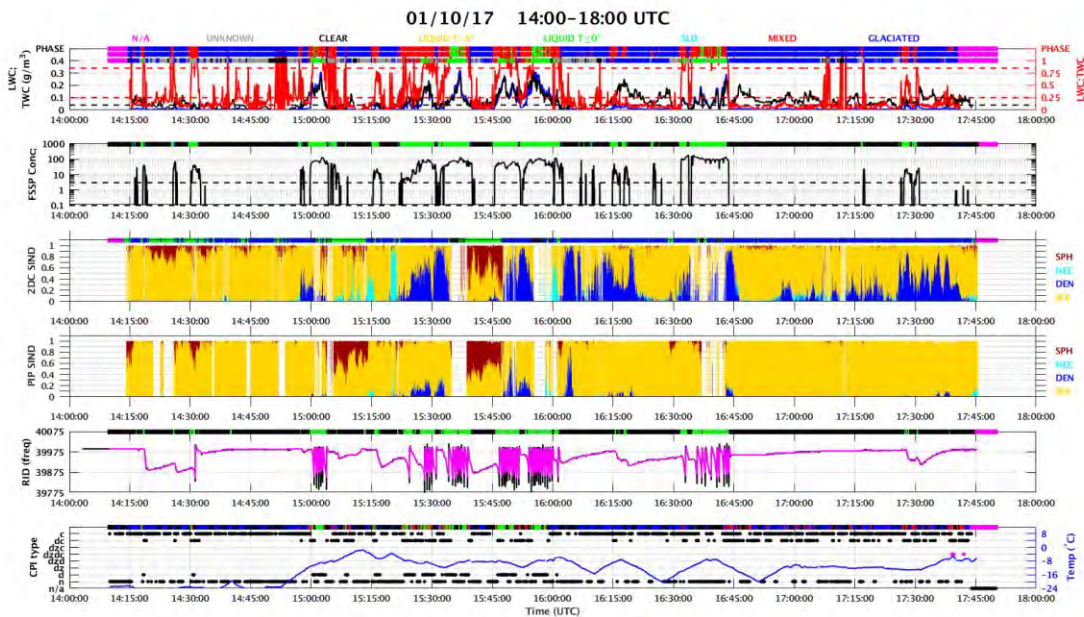


Figure 90. Time series plot of cloud phase (above panel 1) estimated from the data components displayed in the six panels for the 14:00–18:00 UTC interval on 10 January 2017. From top to bottom, the panels show probe measurements from the Nevzorov LWC, TWC, and LWC/TWC ratio (panel 1), FSSP concentration (panel 2), SNDI crystal habit classifications derived from the 2D-C and PIP probes (panels 3 and 4), RID frequency (panel 5), and particle types observed in the CPI imagery (left axis) with temperature (right axis)(panel 6).

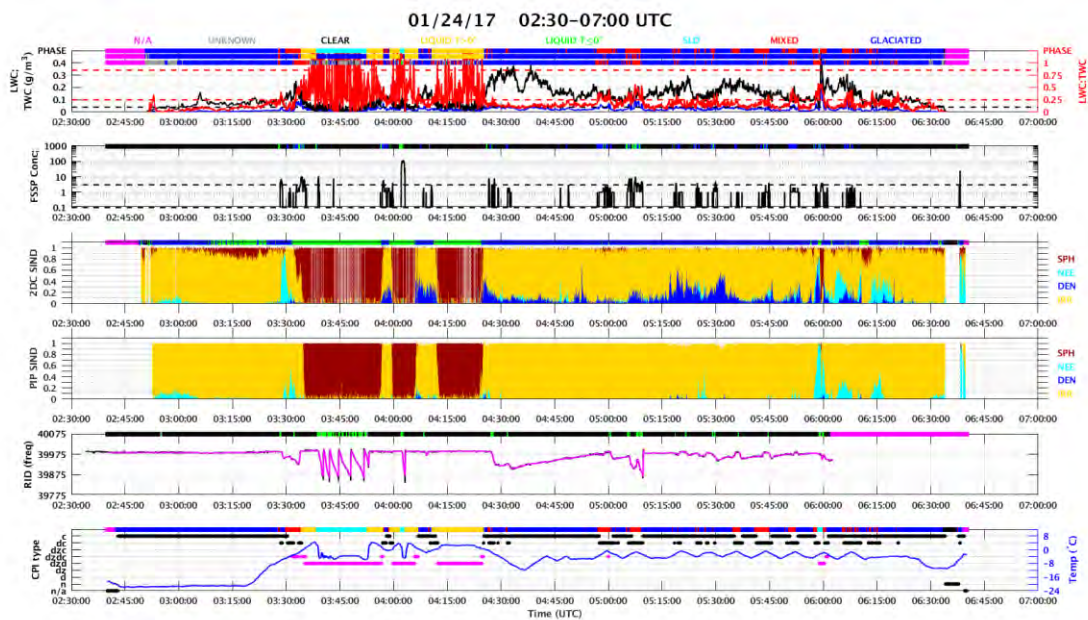


Figure 91. Time series plot of cloud phase (above panel 1) estimated from the data components displayed in the six panels for the 02:30–07:00 UTC interval on 24 January 2017. From top to bottom, the panels show probe measurements from the Nevzorov LWC, TWC, and LWC/TWC ratio (panel 1), FSSP concentration (panel 2), SNDI crystal habit classifications derived from the 2D-C and PIP probes (panels 3 and 4), RID frequency (panel 5), and particle types observed in the CPI imagery (left axis) with temperature (right axis)(panel 6).

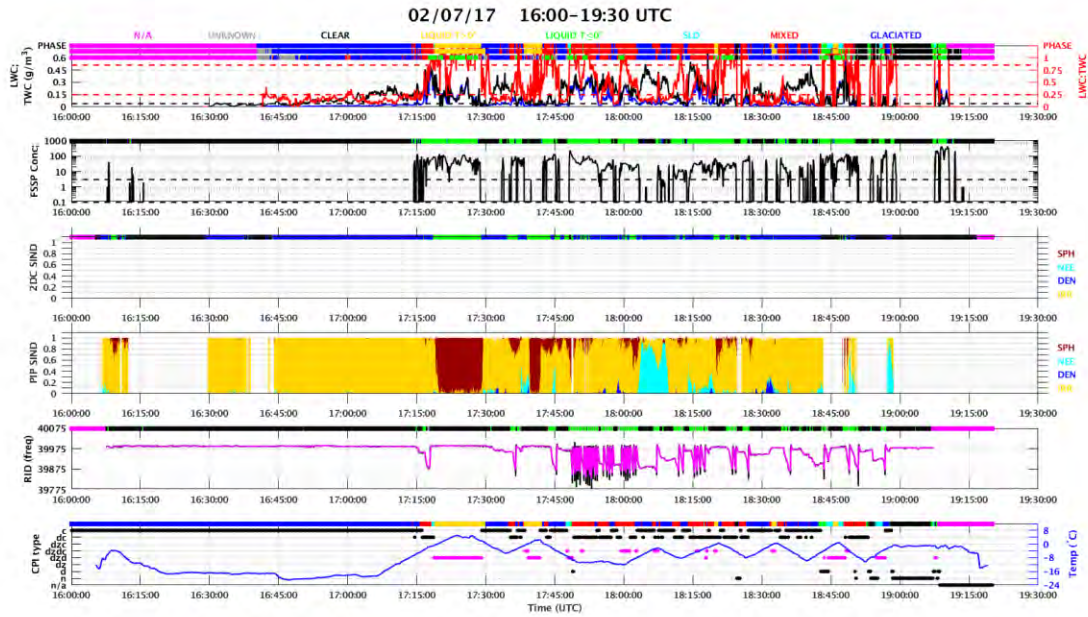


Figure 92. Time series plot of cloud phase (above panel 1) estimated from the data components displayed in the six panels for the 16:00–19:30 UTC interval on 7 February 2017. From top to bottom, the panels show probe measurements from the Nevzorov LWC, TWC, and LWC/TWC ratio (panel 1), FSSP concentration (panel 2), SINDI crystal habit classifications derived from the 2D-C and PIP probes (panels 3 and 4), RID frequency (panel 5), and particle types observed in the CPI imagery (left axis) with temperature (right axis)(panel 6).

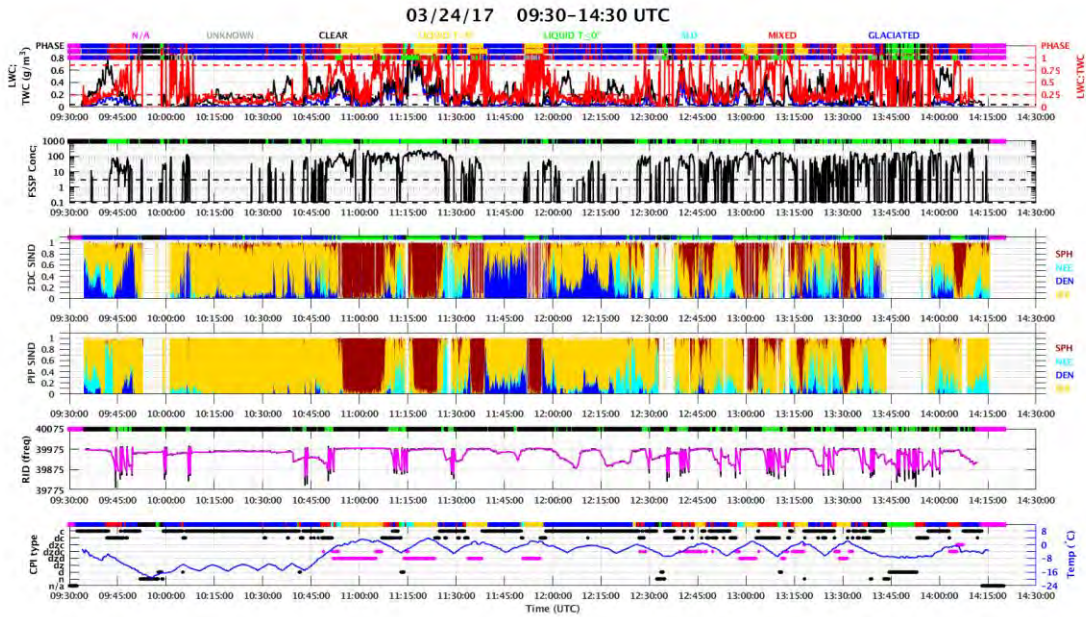


Figure 93. Time series plot of cloud phase (above panel 1) estimated from the data components displayed in the six panels for the 09:30–14:30 UTC interval on 24 March 2017. From top to bottom, the panels show probe measurements from the Nevzorov LWC, TWC, and LWC/TWC ratio (panel 1), FSSP concentration (panel 2), SINDI crystal habit classifications derived from the 2D-C and PIP probes (panels 3 and 4), RID frequency (panel 5), and particle types observed in the CPI imagery (left axis) with temperature (right axis)(panel 6).

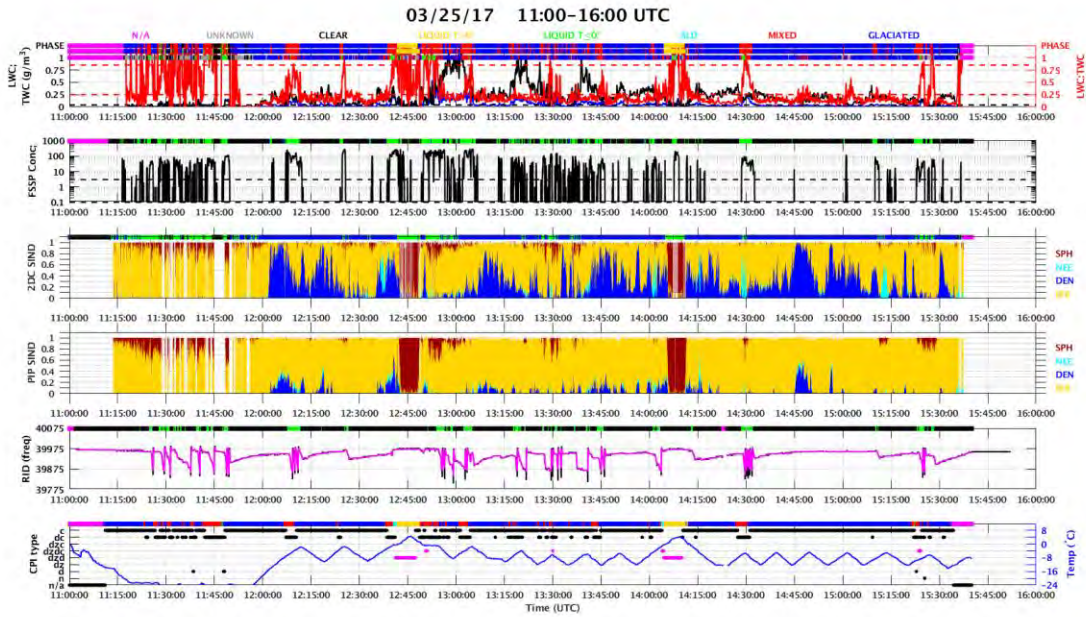


Figure 94. Time series plot of cloud phase (above panel 1) estimated from the data components displayed in the six panels for the 11:00–16:00 UTC interval on 25 March 2017. From top to bottom, the panels show probe measurements from the Nevzorov LWC, TWC, and LWC/TWC ratio (panel 1), FSSP concentration (panel 2), SNDI crystal habit classifications derived from the 2D-C and PIP probes (panels 3 and 4), RID frequency (panel 5), and particle types observed in the CPI imagery (left axis) with temperature (right axis)(panel 6).

**This page intentionally left blank.**

## GLOSSARY

+ZDR	Positive Differential Reflectivity
2D-C	Two-Dimensional Cloud Probe
2D-P	Two-Dimensional Precipitation Probe
2D-S	Two-Dimensional Stereo Probe
AIRS	Alliance Icing Research Study
ATC	Air Traffic Control
BAIRS	Buffalo Area Icing and Radar Study
BB	Bright Band
BD	Big Drops
BI	Biologicals
CC	Correlation Coefficient
CCN	Cloud Condensation Nuclei
CDP	Cloud Droplet Probe
CIP	Cloud Imaging Probe
CPI	Cloud Particle Imager
DMT	Droplet Measurement Technologies
DS	Dry Snow
ECCC	Environment and Climate Change Canada
FAA	Federal Aviation Administration
FAR	False Alarm Rate
FSSP	Forward Scattering Spectrometer Probe
GC	Ground Clutter
GR	Graupel

HA	Hail–Rain Mix
HC	Hydrometeor Classification
HCA	Hydrometeor Classification Algorithm
HR	Heavy Rain
HVPS	High Volume Precipitation Spectrometer
IC	Ice Crystals
IWC	Ice Water Content
ICICLE	In-Cloud Icing and Large-Drop Experiment
IHL	Icing Hazard Levels
KBGM	Binghamton, NY NEXRAD
KBUF	Buffalo, NY NEXRAD
KTYX	Montague, NY NEXRAD
KDP	Specific Differential Phase
LL	Lincoln Laboratory
LWC	Liquid Water Content
MATLAB	Matrix Laboratory
MCS	Mesoscale Convective System
MIT	Massachusetts Institute of Technology
ML	Melting Layer
MVD	Median Volume Diameter
NE	No Echo
NEXRAD	Next Generation Weather Radar
NRC	National Research Council of Canada
NWP	Numerical Weather Prediction
OAP	Optical Array Probe

ORPG	Open Radar Product Generator
PHI	Differential Phase
PIP	Precipitation Imaging Probe
PIREP	Pilot Report
PLANET	Plane Network for Weather Data Exchange
PMS	Particle Measuring System
POD	Probability of Detection
PPI	Plan Position Indicator
PW	Precipitable Water
RA	Rain
RAP	Rapid Refresh
RID	Rosemount Icing Detector
SLD	Supercooled Large Drops
SLW	Supercooled Liquid Water
SNDI	Spheres, Needles, Dendrites, and Irregulars
SPEC	Stratton Park Engineering Company
TWC	Total Water Content
UK	Unknown
UTC	Universal Time Coordinated
VCP	Volume Coverage Pattern
WERVEX	Weather Radar Validation Experiment
WS	Wet Snow
Z	Reflectivity
ZDR	Differential Reflectivity

**This page intentionally left blank.**

## REFERENCES

- [1] Bailey, M. P., and J. Hallett, A comprehensive habit diagram for atmospheric ice crystals: Confirmation from the laboratory, AIRS II, and other field studies. *J. Atmos. Sci.*, 66, 2888–2899, 2009.
- [2] Battan, L.J., *Radar Observations of the Atmosphere*, University of Chicago Press, 1973.
- [3] Bergeron, T., Uber die dreidimensional verknupfende Wet-teranalyse, *Geophys. Norv.*, 5 (6), 1-111, 1928.
- [4] Bergeron, T., On the physics of clouds and precipitation, Proces Verbaux de l'Association de Meteorologie, International Union of Geodesy and Geophysics, 156-178, 1935.
- [5] Bernstein, B.C., T.A. Omeron, F. McDonough, and M.K. Politovich, The relationship between aircraft icing and synoptic conditions, *Weather and Forecasting*, 12, 742-762, 1997.
- [6] Bernstein, B.C., F. McDonough and C. Wolff, Diagnosis of supercooled large drop conditions using cloud water content and drop concentration, AMS, Preprints 111th Conf. on Aviation Range and Aerospace, Hyannis, MA, CD-ROM, 8.6, 2004.
- [7] Bernstein, B.C., F. McDonough, M.K. Politovich, B.G. Brown, T.P. Ratvasky, D.R. Miller, C.A. Wolff and G. Cuning, Current icing potential: algorithm description and comparison with aircraft observations, *J. Appl. Meteor.*, 44, 969-986, 2005.
- [8] Bernstein, B.C., C.A. Wolff and F. McDonough, An inferred climatology of icing conditions aloft, including supercooled large drops. Part I: Canada and the Continental United States, *J. Appl. Meteorol. Climatol.*, 46, 1857-1878, doi:10.1175/2007JAMC1607.1, 2007.
- [9] Braga, R.C., D. Rosenfeld, R. Weigel, T. Jurkat, M.O. Andreae, M. Wendisch, U. Poschl, C. Voigt, C. Mahnke, S. Borrmann, R.I. Albrecht, S. Molleker, D.A. Vila, L.A.T. Machado and L. Grulich, Further evidence for CCN aerosol concentrations determining the height of warm rain and ice initiation in convective clouds over the Amazon basin, *Atmos. Chem. Phys.*, 17, 14433-14456, 2017.
- [10] Breed, D.W. and J.E. Dye, The electrification of New Mexico thunderstorms, 2. Electric field growth during initial electrification, *J. Geophys. Res.*, 94, 14841-14854, 1989.
- [11] Bukovcic, P., A. Ryzhkov, D. Zrnica and G. Zhang, Polarimetric radar relations for quantification of snow based on disdrometer data, *J. Appl. Met. Clim.*, 57, 103-120, 2018.
- [12] Cober, S.G., J.W. Strapp and G.A. Isaac, An example of supercooled drizzle drops formed through a collision-coalescence process, *J. Appl. Met.*, 35, 2250-2260, 1996.

- [13] Cober, S.G., G.A. Isaac and A. Korolev, Assessing the Rosemount icing detector with in situ measurements, *J. Atmos. Ocean Tech.*, 18, 515-528, 2001a.
- [14] Cober, S.G., G.A. Isaac, A.V. Korolev and J.W. Strapp, Assessing cloud-phase conditions, *J. Appl. Met.*, 40, 1967-1983, 2001b.
- [15] Cunningham, J.G., W.D. Zittel, R.R. Lee and R.L. Ice, Methods for identifying systematic differential reflectivity ( $Z_{DR}$ ) biases on the operational WSR-88D network, 36<sup>th</sup> Conference on Radar Meteorology, Breckenridge, CO, *Amer. Meteor. Soc.*, 2013.
- [16] Dai, A., Global precipitation and thunderstorm frequencies. Part I: Seasonal and interannual variations, *J. Clim.*, 14, 1092-1111, 2000.
- [17] Donovan, M.F., E.R. Williams, D.J. Smalley, R.G. Hallowell and B.J. Bennett, Evaluation of the baseline NEXRAD icing hazard product, AMS 37<sup>th</sup> Conference on Radar Meteorology, Norman, OK, 2015.
- [18] Dye, J.E., W.P. Winn, J.J. Jones and D.W. Breed, The electrification of New Mexico thunderclouds 1. Relationship between precipitation development and onset of electrification, *J. Geophys. Res.*, 94, 8643-8656, 1989.
- [19] Dye, J. and A. Bansemer, Electrification in mesoscale updrafts of deep stratiform and anvil clouds in Florida, *J. Geophys. Res. (Atmospheres)*, 124, 1021-1049, 2019.
- [20] Findeisen, W., Kolloid-meteorologische Vorgänge bei Neiderschlags-bildung, *Meteor. Z.*, 55, 121-133, 1938.
- [21] Freud, E. and D. Rosenfeld, Linear relation between convective cloud drop number concentration and depth for rain initiation, *J. Geophys. Res.*, 117, D-2207, doi:10.1029/2011JD016457, 2012.
- [22] Fukuta, N., Development of fast falling ice crystals in clouds at -10°C and its consequences in ice phase processes, Proc. Eighth Int'l. Conf. on Cloud Physics, Clermont-Ferrand, France, Int'l Association of Met. and Atmos. Physics, 97-100, 1980.
- [23] Fukuta, N. and T. Takahashi, The growth of atmospheric ice crystals: A summary of findings in vertical supercooled cloud tunnel studies, *J. Atmos. Sci.*, 56, 1963-1979, 1999.
- [24] Gayet, J.F., G. Febvre and H. Larsen, The reliability of the PMS FSSP in the presence of small ice crystals, *J. Atmos. Oceanic Tech.*, 13, 1300-1310, 1996.
- [25] Geotis, S.G., Some radar measurements on hailstorms, *J. Appl. Met.*, 2, 270-275, 1963.
- [26] Gerber, H., Microphysics of marine stratocumulus clouds with two drizzle modes, *J. Atmos. Sci.*, 53 (12), 1649-1662, doi:10.1175/1520-0469(1996)053<1649:MOMSCW>2.0.CO;2, 1996.

- [27] Greenler, R., *Rainbows, Halos and Glories*, Cambridge University Press, 1980, 195 pp.
- [28] Hallett, J. and B.J. Mason, The influence of temperature and supersaturation on the habit of ice crystals grown from the vapour, *Proc. Roy. Soc.*, A247, 440, 1958.
- [29] Hallett, J. and S.C. Mossop, Production of secondary ice particles during the riming process, *Nature*, 249, 26-28, 1974.
- [30] Hallowell, R.G., M.F. Donovan, D.J. Smalley and B.J. Bennett, Icing hazard detection with NEXRAD IHL, AMS 36<sup>th</sup> Conference on Radar Meteorology, Breckenridge, CO, 2013.
- [31] Heim, F., Diamantstaub und Schneekristalle in der Antarktis, *Meteor. Zeitung*, 31, 232, 1914.
- [32] Hobbs, P.V., *Ice Physics*, Clarendon Press, Oxford, 1974.
- [33] Hogan, R.J., A.J. Illingworth and H. Sauvageot, Measuring crystal size in cirrus using 35- and 84-Ghz radars, *J. Atmos. Ocean. Tech.*, 17, 27-37, 2000.
- [34] Hogan, R. J., P. R. Field, A. J. Illingworth, R. J. Cotton, and T. W. Choullarton, 2002: Properties of embedded convection in warm-frontal mixed-phase cloud from aircraft and polarimetric radar data. *Quart. J. Roy. Meteor. Soc.*, 128, 451–476, 2002.
- [35] Huang, G.-J., V.N. Bringi, R. Cifelli, D. Hudak and W.A. Petersen, A methodology to derive radar reflectivity –liquid equivalent snowfall rate relations using C-band radar and a 2D video disdrometer, *J. Atmos. Ocean. Tech.*, 27, 637-651, 2010.
- [36] Ikeda, K., R.M. Rasmussen, E. Brandes and F. McDonough, Freezing drizzle detection with WSR-88D radars, *J. Appl. Met. Clim.*, 48, 41-60, 2009.
- [37] Jayaweera, K.O.L.F. and R.E. Cottis, Fall velocities of plate-like and columnar ice crystals, *Quart. J. Roy. Met. Soc.*, 95, 703-709, 1969.
- [38] Justo, J.E. and W.J. Eadie, Terminal fall velocity of chaff, *J. Geophys. Res.*, 68, 2858-2861, 1963.
- [39] Kennedy, P. C., and S. A. Rutledge, S-band dual polarization radar observations in winter storms. *J. Appl. Meteor. Climatol.*, 50, 844–858, doi:10.1175/2010JAMC2558.1, 2011.
- [40] Korolev, A.V., J.W. Strapp, G.A. Isaac and A.N. Nevzorov, The Nevzorov airborne hot-wire LWC-TWC probe: Principle of operation and performance characteristics, *J. Atmos. Ocean Tech.*, 15, 1495-1510, 1998.
- [41] Korolev, A. and B. Sussman, A technique for habit classification of cloud particles, *J. Atmos. Ocean. Tech.*, 17, 1048-1057, 2000.
- [42] Korolev, A. and I.P. Mazin, Supersaturation of water vapor in clouds, *J. Atmos. Sci.*, 60, 2957-2974, 2003.

- [43] Korolev, A., G.A. Isaac, S.G. Cober, J.W. Strapp and J. Hallett, Microphysical characterization of mixed phase clouds, *Quart. J. Roy. Met. Soc.*, 129, 39-65, 2003.
- [44] Korolev, A., I. Heckman, J. Milbrandt, L. Ladino, E. Williams, M. Donovan and D. Smalley, A new look at the environmental conditions favorable to secondary ice production: The melting layer as a potential source, AMS Cloud Physics Conference, 9-13 June, Vancouver, Canada, 2018.
- [45] Korolev, A., I. Heckman, A. Ackerman, M. Donovan, A. Fridland, L. Ladino, P. Lawson, J. Milbrandt, D. Smalley and E. Williams, A new look at the environmental conditions favorable to secondary ice production: The melting layer as a potential source, Manuscript in preparation, June, 2019.
- [46] Knight, C.A. and N.C. Knight, Conical graupel, *J. Atmos. Sci.*, 30, 118-124, 1973.
- [47] Kurdzo, J. M., E. R. Williams, D. J. Smalley, B. J. Bennett, D. C. Patterson, M. S. Veillette, and M. F. Donovan, Polarimetric observations of chaff using the WSR-88D network, *J. Appl. Met. Clim.*, 57 (5), 1063-1081, 2018.
- [48] Ladino, L.A., A. Korolev, I. Heckman, M. Wolde, A. Fridlind and A.S. Ackerman, On the role of ice-nucleating aerosol in the formation of ice particles in tropical convective systems, *Geophys. Res. Lett.*, 44, doi:10.1002/2016GL072455, 2017.
- [49] Lauber, A., A. Kiselev, T. Pander and P. Handmann, Secondary ice formation during freezing of levitated droplets, *J. Atmos. Sci.*, 75, 2815-2826, 2018.
- [50] Lawson, P., B. A. Baker and C. G. Schmitt, An overview of microphysical properties of Arctic clouds observed in May and July 1998 during FIRE ACE R., *J. Geophys. Res.*, 106, 14,989-15,014, 2001.
- [51] Lawson, R.P., D. O'Connor, P. Zmarzly, K. Weaver, B. Baker and Q. Mo, The 2D-S (Stereo) Probe: Design and preliminary tests of a new airborne, high-speed, high-resolution particle imaging probe, *J. Atmos. Ocean. Tech.*, 23, 1462-1477, 2006.
- [52] Lemon, L.R., The radar "three-body scatter spike": An operational large-hail signature, *Weather and Forecasting*, 13, 327-340, 1998.
- [53] Lim, S., D. Moisseev, Y. Chandrasekar and D.-R. Lee, Classification and quantification of snow based on spatial variability of radar reflectivity, *J. Meteor. Soc. Japan*, 91, 763-774, 2013.
- [54] Ludlam, F.H., The heat economy of a rimed cylinder, *Quart. J. Roy. Meteor. Soc.*, 77, 663-666, 1951.
- [55] Ludlam, F.H., *Clouds and Storms: The Behavior and Effect of Water in the Atmosphere*, Pennsylvania State University Press, 1980.
- [56] Mason, B.J., *The Physics of Clouds*, Clarendon Press, Oxford, 1971.

- [57] Nakaya, U. and T. Terada, Simultaneous observations of the mass, falling velocity and form of individual snow crystals, *J. Fac. Sci., Hokkaido Univ. Ser. II*, 1, 191-201, 1935.
- [58] Nevzorov, A.N. and V.F. Shugaev, Observations of the initial stage of ice phase evolution in supercooled clouds, *Sov. Meteor. Hydro.*, N8, 41-51, 1992.
- [59] Park, H.S., A.V. Ryzhkov, D.S. Zrnica, and K.E. Kim, The hydrometeor classification algorithm for the polarimetric WSR-88D: Description and application to an MCS, *Weather and Forecasting*, 24, 730-748, 2009.
- [60] Picca, J. and A. Ryzhkov, Polarimetric radar discrimination between small, large, and giant hail at S band (.pdf 518 kB), NOAA/NSSL report, 13 pp., 2011.
- [61] Polotovich, M.K., Aircraft icing caused by large supercooled droplets, *J. Appl. Met.*, 28, 856-868, 1989.
- [62] Rangno, A.L. and P.V. Hobbs, Microstructures and precipitation development in cumulus and small cumulonimbus clouds over the warm pool of the tropical Pacific Ocean, *Quart. J. Roy. Met. Soc.*, 131, 639-673, 2005.
- [63] Rasmussen, R.M., I. Geresdi, G. Thompson, K. Manning and E. Karplus, Freezing drizzle formation in stably stratified layer clouds: The role of radiative cooling of cloud droplets, cloud condensation nuclei and ice initiation, *J. Atmos. Sci.*, 59, 837-860, 2002.
- [64] Rosenfeld D. and G. Gutman, Retrieving microphysical properties near the tops of potential rain clouds by multispectral analysis of AVHRR data. *Atmos. Res.*, 34, 259-283, 1994.
- [65] Rosenfeld, D., R. Chemke, P. DeMott, R.C. Sullivan, R. Rasmussen, F. McDonough, J. Comstock, B. Schmid, J. Tomlinson, H. Jonsson, K. Suski, A. Cazorla and K. Prather, The common occurrence of highly supercooled drizzle and rain near the coastal regions of the western United States, *J. Geophys. Res.*, 118, 9819-9833, doi:10.1002/jgrd.50529, 2013.
- [66] Russell, B., E.R. Williams, M. Gosset, F. Cazanave, L. Descroix, N. Guy, T. Lebel, A. Ali, F. Metayer and G. Quantin, Radar/rain-gauge comparisons on squall lines in Niamey, Niger for the AMMA, *Quart. J. Roy. Met. Soc.*, 136, 289-303, 2010.
- [67] Ryzhkov, A., P. Zhang, H. Reeves, M. Kumjian, T. Tschallener, S. Tromel and C. Simmer, Quasi-vertical profiles – a new way to look at polarimetric radar data, *J. Atmos. Ocean. Tech.*, 33, 551-562, 2016.
- [68] Sand, W.R., W.A. Cooper, M.K. Polotovich and D.L. Veal, Icing conditions encountered by a research aircraft, *J. Clim. Appl. Met.*, 23, 1427-1440, 1984.
- [69] Schuur, T.J., A.V. Ryzhkov and D.S. Zrnica, A statistical analysis of 2D-video-disdrometer data: impact on polarimetric rainfall estimation, 30<sup>th</sup> International Conference on Radar Meteorology, Munich, Germany, Amer. Meteor. Soc., 2001.

- [70] Schuur, T.J., A.V. Ryzhkov and D.R. Clabo, Climatological analysis of DSDs in Oklahoma as revealed by 2D-video disdrometer and polarimetric WSR-88D radar, 32<sup>nd</sup> Conference on Radar Meteorology, Albuquerque, NM, *Amer. Meteor. Soc.*, 2005.
- [71] Sinnott, R.W., Virtues of the Haversine, *Sky and Telescope*, 68, 159, 1984.
- [72] Takahashi, T., Riming electrification as a charge generation mechanism in thunderstorms, *J. Atmos. Sci.*, 35, 1536-1548, 1978.
- [73] Takahashi, T. and N. Fukuta, Observations of the embryos of graupel, *J. Atmos. Sci.*, 45, 3288-3297, 1988.
- [74] Takahashi, T., Y. Nagao and Y. Kushiyama, Possible high ice particle production during graupel-graupel collisions, *J. Atmos. Sci.*, 52, 4523-4527, 1995.
- [75] Teschi, F., W.L. Randeu, M. Schonhuber, and R. Teschi, Simulation of polarimetric radar variables in rain at S-, C- and X-band wavelengths, *Adv. Geosci.*, 16, 27-32, <http://www.adv-geosci.net/16/27/2008/>, 2008.
- [76] Tokay. A. and D.A. Short, Evidence from tropical raindrop spectra of the origin of rain from stratiform versus convective clouds, *J. Appl. Met.*, 35, 355-371, 1996.
- [77] U.S. Department of Commerce, Tables of Precipitable Water and Other Factors for a Saturated-Pseudoadiabatic Atmosphere, Technical Paper No. 14. Washington, 1951.
- [78] Weickmann, H., The ice phase in the atmosphere, Royal Aircraft Establishment, Library Translation No. 273, Volkenrode R & T No. 716, Issued by Ministry of Supply, Millbank, London, September, 1948.
- [79] Wildeman, S., S. Sterl, C. Sun and D. Lohse, Fast dynamics of water droplets freezing from the outside-in, *Physical Review Letters*, January, 2017.
- [80] Williams, E., D. Rosenfeld, N. Madden, C. Labrada, J. Gerlach and L. Atkinson, The role of boundary layer aerosol in the vertical development of precipitation and electrification: Another look at the contrast between lightning over land and over ocean, 11<sup>th</sup> Int'l. Conf. on Atmospheric Electricity, NASA/CP-1999-209261, 754-757, June, 1999.
- [81] Williams, E. and S. Stanfill, The physical origin of the land-ocean contrast in lightning activity, *Comptes Rendus—Physique*, 3, 1277-1292, 2002.
- [82] Williams, E.R., D. Rosenfeld, N. Madden, J. Gerlach, N. Gears, L. Atkinson, N. Dunnemann, G. Frostrom, M. Antonio, B. Biazon, M. Camargo, H. Franca, A. Gomes, M. Lima, R. Machado, S. Manhaes, L. Nachtigall, H. Piva, W. Quintiliano, L. Machado, P. Artaxo, G. Roberts, N. Renno, R. Blakeslee, J. Bailey, D. Boccippio, A. Betts, D. Wolff, B. Roy, J. Halverson, T. Rickenbach, J. Fuentes, and E. Avelino, Contrasting convective regimes over the Amazon: Implications for cloud electrification, *J. Geophys. Res.*, LBA Special Issue, 107, D20, 8082, doi:10.1029/2001JD000380, 2002.

- [83] Williams, E., D. Smalley, M. Donovan, K. Hood, B. Bennett, E. Griffin, M. Wolde, M. Bastian and A. Korolev, Validation of NEXRAD radar differential reflectivity in snowstorms with airborne microphysical measurements: Evidence for hexagonal flat plate crystals, 36<sup>th</sup> Conference on Radar Meteorology, American Meteorological Society, Breckenridge, Colorado, September, 2013.
- [84] Williams, E.R., M.F. Donovan, D.J. Smalley, R.G. Hallowell, E. Griffin, K.T. Hood and B.J. Bennett, The 2013 Buffalo Area icing and Radar Study, Project Report ATC-419, 2015.
- [85] Williams, E.R., D.J. Smalley, M.F. Donovan, R.G. Hallowell, K.T. Hood, B.J. Bennett, R. Evaristo, A. Stepanek, T. Bals-Elsholz, J. Cobb, J. Ritzman, A. Korolev and M. Wolde, Measurements of differential reflectivity in snowstorms and warm season stratiform systems, *J. Appl. Met. Clim.*, 54, 573-595, 2015a.
- [86] Williams, E.R., D.J. Smalley, R. Hallowell, E. Griffin, K. Hood, B.J. Bennett, M. Wolde and A. Korolev, Aircraft insitu validation of hydrometeors and icing conditions inferred by ground-based NEXRAD polarimetric radar, SAE 2015 Int'l Conf. on Icing of Aircraft, Engines and Structures, Prague, Czech Republic, 22-25 June, 2015b.
- [87] Williams, E.R., M.F. Donovan, D.J. Smalley, J.M. Kurdzo, B.J. Bennett, M. Wolde, N. Bastiaqn, K. Baibakov, C. Nguyen, and A. Korolev, In situ verification of aircraft icing conditions involving needle crystals and supercooled water in winter storms, AMS 38th Conference on Radar Meteorology, Chicago, Illinois, August, 2017.
- [88] Williams, E., Lightning activity in winter storms: A meteorological and cloud microphysical perspective, *IEEJ*, 2018.
- [89] Williams, E., D. Smalley, M. Donovan J. Kurdzo, M. Wolde, M. Bastian, K. Baibakov, C. Nguyen, A. Korolev, Stacked layers of dendrites and needles linked with supercooled cloud water in winter storms, AMS Conference on Cloud Physics. Vancouver, B.C., July 9-13, 2018a.
- [90] Williams, E.R., D.J. Smalley and M.F. Donovan, Recommendations for ICICLE and other future icing hazard campaigns based on experience with in situ validation and NEXRAD dual polarimetric radar assessments of icing conditions, MIT Lincoln Laboratory, Lexington, MA., Document 43PM-Wx-0182, November 29, 2018b.
- [91] Wilson, J.W. and D. Reum, The flare echo: Reflectivity and velocity signature, *J. Atmos. Ocean Tech.*, 5, 197-205, 1988.
- [92] Wolde, M., Airborne W-band radar and in situ data comparison during AIRS II: Nov 11, 2003 case, Annual Meeting of the American Meteorological Society, Atlanta, GA, January 2006.
- [93] Wolde, M., A. Battaglia, C. Nguyen, A. L. Pazmany and A. Illingworth, Implementation of polarization diversity pulse-pair technique using airborne W-band radar, *Atmos. Meas. Tech.*, 12, 253-269, 2019.

- [94] Zittel, W.D., J.G. Cunningham, R.R. Lee, L.M. Richardson, R.L. Ice and V. Melnikov, Use of hydrometeors, bragg scatter, and sun spikes to determine system  $Z_{DR}$  biases in the WSR-88D fleet, 8<sup>th</sup> European Conference on Radar in Meteorology and Hydrology, Garmisch-Partenkirchen, Germany, 2014.